UILU-ENG-90-2001

L ENGINEERING STUDIES

ral Research Series No. 549

key words:
1- cyclic loading
2- lateral buckling
3- bracing, buildings

ISSN: 0069-4274

LATERAL BUCKLING OF SHORT I-BEAMS UNDER CYCLIC LOADING

By
Keith D. Hjelmstad — principal author
and
Sang-Gab Lee

A report to sponsors:
The National Science Foundation
The American Institute of Steel Construction

Department of Civil Engineering
University of Illinois at Urbana-Champaign
Urbana, Illinois

April 1990

Lateral Buckling of Short I-Beams Under Cyclic Loading

By

Keith D. Hjelmstad

and

Sang-Gab Lee

A report to sponsors:
The National Science Foundation
and
The American Institute of Steel Construction

Department of Civil Engineering
University of Illinois at Urbana-Champaign
Urbana, Illinois

April 1990

50272-101

REPORT DOCUMENTATION PAGE	1. REPORT NO. UILU-ENG-90-2001	2.	3. Recipient's Accession No.
4. Title and Subtitle: Lateral Buckling of Short I-Beams Under Cyclic Loading			5. Report Date: April 1990 6.
7. Author(s): Keith D. Hjelmstad and Sang-gab Lee			8. Performing Organization Rept. No.: SRS 549
9. Performing Organization Name and Address: Department of Civil Engineering University of Illinois 205 N. Mathews Avenue Urbana, Illinois 61801			10. Project/Task/Work Unit No. 11. Contract (C) or Grant (G) No. (C) CEE 84-04865 (G) CES 86-58019
12. Sponsoring Organization Name and Address: National Science Foundation, Washington D.C. American Institute of Steel Construction, Chicago, IL			13. Type of Report & Period Covered 14.

15. Supplementary Notes

16. Abstract (Limit 200 words)

This report concerns the inelastic lateral buckling and post-buckling behavior of short I-beams subjected to cyclically reversing loads. The eccentrically braced frame, used in the earthquake resistant design of building structures, provides an application in which lateral buckling of short I-beams under cyclic loading is relevant. Our main purpose is to establish some benchmarks with which to assess the consequences of lateral buckling of active link beams in eccentrically braced frames.

A geometrically nonlinear beam model, capable of analyzing lateral buckling of short I-beams under cyclic loading, is formulated in terms of stress components. The novel kinematic model includes a geometrically exact representation of the primary torsional warping as well as secondary warping due to torsion and transverse shear. A new cyclic plasticity model, incorporating many of the most compelling features of existing phenomenological models, is developed and implemented with a consistent return mapping algorithm. The new model represents cyclic metal plasticity well and is suitable for large-scale computation.

The experimental research program comprised five tests of propped cantilever beams subjected to a cyclically reversing point load acting near the fixed end. The experiments include both braced and unbraced beams subjected to similar loading histories. The effects of constitutive parameters, residual stresses, load placement, geometric imperfections, flexible boundary conditions, and lateral bracing are examined using the analytical model developed herein. Most of the parameter studies are carried out using the propped cantilever arrangement used in the experiments.

17. Document Analysis a. Descriptors

Lateral buckling, Rod, Beams, Stability, Experiments, Finite elements, Finite deformation

b. Identifiers/Open-Ended Terms

c. COSATI Field/Group

18. Availability Statement	19. Security Class (This Report): Unclassified	21. No. of Pages: 148
	20. Security Class (This Page): Unclassified	22. Price

(See ANSI-Z39.18) see instructions on reverse

OPTIONAL FORM 272 (4-77)
(Formerly NTIS-35)
Department of Commerce

Table of Contents

Chapter 1

Introduction

This report concerns the inelastic lateral buckling and post-buckling behavior of short I-beams subjected to cyclically reversing loads. The eccentrically braced frame, used in the earthquake resistant design of building structures, provides an application in which lateral buckling of short I-beams under cyclic loading is relevant. Our main purpose is to establish some benchmarks with which to assess the consequences of lateral buckling of active link beams in eccentrically braced frames. As such, our goal is practical and our scope narrow. We have, however, endeavored to investigate the problem in a manner independent of the eccentric bracing context, with the hope of illuminating the general issues of the lateral buckling problem.

While the methods used to investigate the problem may seem extravagant, we did not wish to be encumbered or biased by questionable mechanics when interpreting the complex phenomena inherent to the lateral buckling phenomena. The tools which we bring to bear on the problem of lateral buckling of short beams include nonlinear rods theories, cyclic metal plasticity, numerical analysis of systems with limit loads, and experimental methods. Each of these topics has its own history of development, each has its own interest and research challenges, and each has its own literature. In many of these areas we strive to make a new contribution to the state of knowledge. However, we have tried to maintain harmony and balance in our approach at the risk of failing to excite the specialists in any one of the topical subjects. The main contribution of the present work is our synthesis of the topics and the results that issue from the synergy.

The following sections are presented to allow the uninitiated reader to examine the pure strands from which the fabric is woven. The introductory comments are largely historical, if not somewhat philosophical, and are offered as an aid in establishing a context for the study. We begin by motivating the research with a discussion of the eccentric bracing concept. Subsequently we comment on the origins and issues related to lateral buckling of beams, nonlinear rod theories, and the modeling of cyclic metal plasticity. Finally, we indicate the scope of the present work and give a brief outline of the content of the chapters that follow.

1.1 Eccentrically Braced Frames: A Motivation for the Study of Lateral Buckling

The design of earthquake resistant systems is philosophically different from traditional design practice. Excursions into the inelastic range are accepted for rare but extreme overloads, and hence must be anticipated in the design process. Many of the members of the structure might repeatedly reach or exceed their limit capacity under cyclically reversing loads. Under these circumstances, the strength, stability, and toughness of the energy dissipating members is fundamental to the integrity of the system. Roeder and Popov (1978) were the first to demonstrate that eccentrically braced steel frames were well suited to meet the difficult demands of an earthquake environment.

The economy of the eccentric bracing scheme is achieved by anticipating large local inelastic deformations in the eccentric elements, facilitating energy dissipation, and thereby endowing the system with

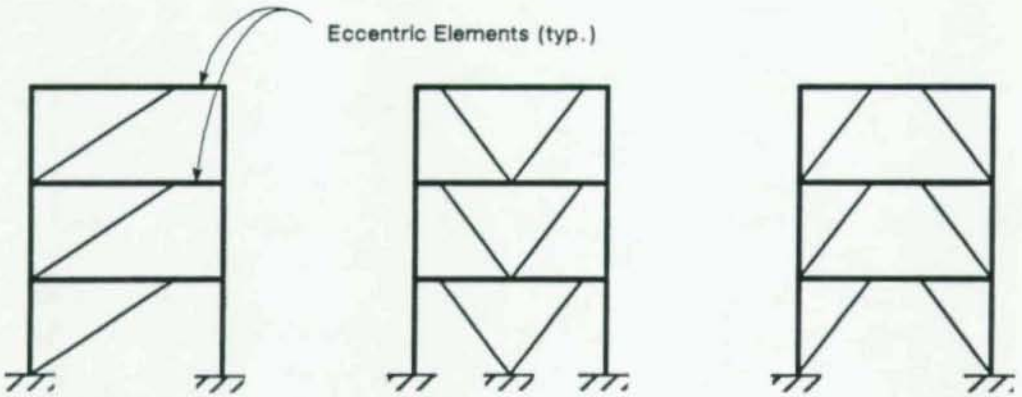

Fig. 1.1 Typical eccentrically braced frames

ductility and toughness. Several possible configurations of eccentrically braced frames are shown in Fig. 1.1. The inelastic deformations are forced to occur in short beam segments (sometimes called *active link beams)* which connect the axial force transmitting members (*i.e.* braces or columns). Large amounts of energy can be dissipated through inelastic shearing of these short beams. The short length of the eccentric elements is important both to promote a high elastic structural stiffness and to insure that shear yielding occurs rather than flexural yielding since shear yielding is considerably more efficient. Integrity of the structure is maintained by providing details which lend the structure ductility (Hjelmstad and Popov, 1983). The need for lateral bracing of the eccentric elements was recognized in the experiments of Manheim (1982) in which lateral buckling of the beams was first observed. All of the recent research on eccentrically braced frames has been concerned with laterally braced systems and, for lack of better information, recommendations for detailing have conservatively required complete lateral bracing at the ends of the active link beam. No research has been done on laterally unbraced or partially braced systems.

The present research is concerned with the nonlinear response of beams, with and without lateral support, subjected to cyclically reversing loads in the inelastic range. Such conditions occur in eccentrically braced frames under earthquake excitation. Consequently, the topic is important to the understanding of eccentrically braced frames. While the report is not really about eccentrically braced frames, they provide an important motivational example.

1.2 Lateral Buckling of Beams

Owing to their open thin-walled geometry, I-beams have a relatively low resistance to lateral buckling. The tendency for beams to buckle torsionally when subjected to loads in the plane of their strong axis has been known for over a hundred years. The need to safely and economically proportion structures has sustained a steady research effort aimed at better understanding the phenomena associated with the lateral buckling of beams.

The technical literature contains hundreds of papers and books devoted to the subject of lateral buckling of beams. An extensive summary of the literature is contained in the works of Bleich (1952), Lee (1960), Chen and Atsuta (1977), and Galambos (1988). Much of the research reported in the

literature on lateral buckling of beams is tangential to the developments reported here. Other research results are subsumed by the generality of our approach. We cannot hope to give an accurate account of the many accomplishments of researchers studying lateral buckling of beams, but we do wish to provide a historical context for the present study, if only a modest one. The following paragraphs contain a brief account of some of the pivotal developments related to the lateral buckling of beams.

The formal theoretical study of lateral-torsional buckling began in 1899 when L. Prandtl and A. G. M. Michell independently published equations describing the elastic lateral buckling of a thin rectangular strip. Over a decade later, S. P. Timoshenko formulated equations governing the elastic lateral-torsional buckling of a beam having an I-type cross section, recognizing that a significant amount of torsional resistance accrues from the restraint of cross-sectional warping in thin-walled open sections (*loc. cit.* Bleich, 1952). The literature on lateral buckling is clearly skewed toward elastic beams. Following the lead of the founders of the subject, latter-day researchers have focussed on determining the fundamental linearized buckling eigenvalue as an estimate of the capacity of the system.

In 1950, Neal published the first analysis of elastoplastic lateral buckling, treating beams of rectangular cross section (Neal, 1950). Horne (1950) soon followed with the important extension to the I-type cross section. Since that time, extensive efforts have been expended toward the goal of estimating the maximum load that an elastoplastic beam can sustain. Most of the analytical studies of inelastic systems are based upon some variation of the tangent modulus approach, widely used for axially loaded columns, to compute a bifurcation load from a linearized theory†. The analytical models have been useful in identifying the important geometric and material properties which affect the buckling response of beams. They have also been used extensively to develop design formulas.

Most of the published results concern the determination of the linearized bifurcation load for systems with various configurations and properties. A great deal of attention has been placed upon formulating and solving certain simple cases such as a simple beam subjected to end moments about its minor axis or a cantilever beam subjected to a single point load at its end. Most of the formulas used in design result from the investigation of these simple systems. Some of the problem parameters that have been considered include the relative position of the load with respect to the beam, flexible boundary conditions, monosymmetry of the cross section, warping restraint, residual stresses, initial imperfections and lateral bracing.

Horne (1954) obtained numerical solutions for beams with unequal end moments and developed an approach whereby the solution to the problem of buckling under unequal end moments could be obtained from that of a beam with equal end moments simply by multiplying the latter by a dimensionless function of the moment ratio. The practice of using such functions to account for variations in load form is ubiquitous in modern design specifications. Zuk (1956) performed analyses of bracing forces at buckling, based upon an assumption about the initial lateral geometric imperfection of the beam. He found that a brace strength of 2% of the compression flange capacity would generally be sufficient to resist buckling. The so-called "two percent rule" was thus born. Winter (1960) determined the axial stiffness of the brace required to prevent simultaneous buckling of the brace and beam. The general issue of lateral bracing requirements remains largely unresolved today, particularly for inelastic buckling. Galambos (1963) was the first to include the effects of residual stresses on the elastoplastic capacity of

† To be more specific, the theories generally represent strains up to second order in the generalized kinematic variables and the equilibrium equations contain terms linear in the kinematic variables. These *second order* theories lead to an eigenvalue problem from which the critical load factor can be estimated.

beams, and established the importance of their consideration. Woolcock and Trahair (1974) considered the post-buckling behavior of elastic beams and found that they can sustain loads in excess of the linearized bifurcation load. They correctly indicated that the additional capacity would seldom be realized due to the onset of yielding. Analysis of the post-buckling response of *inelastic* systems has not been found in the literature for either monotonic or cyclic loading conditions.

Considerable effort has been directed toward formulating theories and toward developing methods of solution to the governing equations. Most of the theories that have evolved are complicated and do not submit to classical solution methods. Various numerical methods have been proposed to deal with such cases, including finite difference methods (Vinnakota, 1977), finite integral methods (Brown and Trahair, 1968), and finite element methods (Barsoum and Gallagher, 1970).

A relatively modest number of experimental investigations have been reported in the literature. The first known tests were reported by A. G. M. Michell in 1899 (*loc. cit.* Bleich, 1952). The results of 123 tests performed in Japan, Great Britain, Australia, and the United States have been summarized and analyzed by Hollinger and Mangelsdorf (1981), wherein the original references are cited.

Experimental results are often difficult to interpret because important properties such as initial imperfections, end restraints, residual stresses, and material properties are difficult to measure and document. Consequently, correlation between analysis and experiment has been relatively superficial. Since most experimental investigations have been oriented toward verifying the predictions of analytical models, and since most analytical models predict only the buckling load, reporting of experimental data in the post buckling range is scarce. However, some data have been reported on the post-buckling response of monotonically loaded beams (Augusti, 1964; Kitipornchai and Trahair, 1975*a*,*b*; Fukumoto, *et. al.*, 1980). No cyclic load tests have been found in the literature.

1.3 Nonlinear Rod Theories

While the theories behind the investigations of lateral buckling of beams and the modern theory of rods have common roots, the theory of rods has developed almost independently of the research in lateral buckling of beams. Lateral buckling research seems to have focussed on the linearized bifurcation problem in the quest for formulae to support the design of structures, almost to the complete exclusion of other approaches. Rod theory, on the other hand, is generally viewed as a branch of mathematical elasticity theory and has grown more from the inspiration of mathematical aesthetics than for practical engineering design needs.

The foundations of nonlinear rod theories go back to Kirchhoff (*circa* 1859) who based his theory on an essentially kinematic argument (*loc. cit.* Love, 1944). The kinematic hypothesis, as employed by Kirchhoff, has become firmly established as the fundamental building block of a reduced theory of structural mechanics. The classical nonlinear theory of rods, called the Kirchhoff-Love rod model, is presented by Love (1944). Extensions of the classical model to include finite extension and shearing are due to Reissner (1973), Antman (1974), and Simo (1985*a*), in different contexts. These rod theories are often called *geometrically exact* because the equations of kinematics and equilibrium hold for all values of the generalized kinematic variables.

One of the principal difficulties inherent in three dimensional rod theories is the parameterization of the rotation field for numerical computations. Simo and Vu-Quoc (1986) presented a variational formu-

lation of the geometrically exact rod model discussed by Simo (1985*a*). They used quaternions to parameterize the rotation field, and develop a novel approach to the configuration update based upon the exponential map. One of the main contributions of Simo and Vu-Quoc is the recognition that the configuration space of rotations is SO(3), rather than the usual linear space, and hence the notion of an admissible variation must reflect the structure of SO(3). Because their model is cast in variational form, it is quite suitable for numerical analysis by the finite element method.

For certain classes of beams, most notably those with thin-walled open cross sections, warping out of the plane of the cross section represents an important mode of deformation, a mode precluded by the Kirchhoff hypothesis that plane sections remain plane. While the inclusion of warping in thin-walled beams goes back much further, Vlazov (1961) is largely responsible for formulating the thin-walled beam theory based upon the *sectorial areas* kinematic hypothesis for torsion. Warping deformations due to transverse shearing are important for beams which have a ratio of length to typical cross sectional dimension on the order of unity. Warping deformations can also be important for anisotropic beams with a small ratio of shear modulus to Young's modulus. Cowper (1966) incorporated the effects of warping deformations in a planar beam through a systematic definition of the so-called *shear coefficient*. Simo (1982) extended the idea of Cowper to a geometrically nonlinear beam theory. Hjelmstad and Popov (1983) incorporated the effects of warping in problems involving inelastic bending and shearing. Simo and Vu-Quoc (1989) extended their earlier model to include the effect of torsional warping deformations in a geometrically exact rod model.

Most of the work done in the theory of rods, as well as in the lateral buckling of beams, has been carried out in the context of *stress resultants*. The concept of the resultant force and resultant bending moment acting at a cross section is a natural consequence of the kinematic hypothesis underlying rod theories. Although the kinematic hypothesis is not necessary to define the stress resultants (they can be defined as integrals of the stress field over the cross section), it motivates the definition in the following sense. The generalized displacement quantities do not depend upon the cross sectional coordinates. This decoupling allows explicit integration of the internal work over the cross section, leading to the definition of conjugate stress and strain resultants. The stress and strain resultants can also be viewed as projections of the stress and strain fields on a low order polynomial basis (Hjelmstad, 1987).

One of the difficulties of operating in stress resultant space is the representation of inelastic constitutive behavior (Hjelmstad and Popov, 1983). It is difficult to construct a suitable yield surface, let alone develop models of strain hardening, for a beam which can experience multiaxial states of stress (*e.g.* combined shear and normal stresses). Pinsky and Taylor (1980) formulated a finite deformation elastic planar beam theory in which the integration over the cross section is accomplished by numerical quadrature rather than by explicit integration. The numerical integration over the cross section allows the theory to be expressed in terms of stress and strain components rather than resultants. The kinematic hypothesis provides a constraint on the deformation map and thereby preserves the essence of the rod theory. Pinsky, Taylor, and Pister (1980) extended the finite deformation plane beam theory to one with viscoplastic constitution. Simo, Hjelmstad, and Taylor (1984) used this approach again for planar beams in which cross sectional warping due to transverse shear is important. Hjelmstad and Popov (1983) applied the technique to short I-beams undergoing planar deformations (in the major plane of inertia) to overcome the problems associated with modeling moment-shear interaction. The real advantage of working with a stress component formulation is that any local constitutive model can be used. Much more is

known about the behavior of materials at the local level than is known about them at the resultant level. The price of representing the constitutive equations locally is computational tedium.

1.4 Cyclic Metal Plasticity

In most research on the inelastic lateral buckling behavior of beams, a highly idealized model of constitutive behavior is employed. In particular, the stress state is assumed to be uniaxial, the material is assumed elastoplastic with linear strain hardening, and unloading in not allowed. The main motivation for using such a model is the prospect of making analytical progress in solving the linearized buckling eigenvalue problem. The simple model is arguably valid for mild steel in the virgin state and has led to many useful formulas for the design of steel beams. The simple constitutive models do not manifest the complex mechanisms of strain hardening known to exist in metals and hence are not valid for generalized loadings.

Phenomenological models of metal plasticity have been under development since the early work of R. von Mises. The origins of the idea of adding isotropic strain hardening (simple expansion of the yield surface) to the equations of elastoplasticity go back at least to Hill (1950) and Hodge (1955). While there is little experimental evidence supporting the isotropic hardening model, it has proven useful in computations. The kinematic hardening rule proposed by Prager (1956)† represented the first attempt at modeling the Bauschinger effect, important in metal plasticity, in the context of a continuum model with a multiaxial stress state. Prager's model was subsequently modified by Ziegler (1959) and others, but retained the basic feature of a single loading surface translating in stress space.

It has long been known that the simple hardening models do not represent the phenomena inherent to cyclic metal plasticity well because they do not allow for a gradual transition from the elastic state to the plastic state. The first attempt to rectify the shortcomings of these models is attributed to Duwez (1935) who proposed the *mechanical sublayer* model in which the material is idealized as a parallel arrangement of friction elements with different slip coefficients. The sublayer concept was extended to multiaxial stress states by Iwan (1967) and independently by Mroz (1967). Both employed a multi-surface model, endowing each surface with different properties as well as an evolutionary rule for its translation. The mechanical sublayer model and its progeny are purely phenomenological models and bear little relation to the underlying physics. However, these models imitate experimental data well, and have proven useful in numerical simulations. More recent developments in phenomenological models include the two-surface models of Kreig (1975), Dafalias (1975), and Dafalias and Popov (1975, 1976). Rees (1984, 1987) proposed the idea of using a multi-surface model in strain space to represent hardening.

Efforts have been made to base cyclic metal plasticity models on the dislocation structure and glide plane slip mechanisms of the polycrystalline structure of the material (Ortiz and Popov, 1982). Such models have been quite successful in representing the material behavior, but have not achieved the popularity of the phenomenological models in computational plasticity.

Large-scale numerical computations with rate-independent plasticity models are generally carried out with return mapping algorithms. At any stage of loading, a trial stress state is computed elastically. If the stress state lies outside the yield surface it is *returned* to an admissible state on the yield surface. The

† As is typical of technical literature, Russian contributions are often overlooked in the English literature. We admit to not being able to read Russian, however, it would appear that the first proposal of the idea of kinematic hardening is due to A. Ishlinskii in 1954 (*loc. cit.* Dafalias and Popov, 1975).

radial return algorithm, initially proposed by Wilkins (1964), is the most popular of the return mapping algorithms. Simo and Taylor (1984, 1985) have recently introduced the concept of the *consistent tangent* moduli for plasticity computations carried out with a return mapping. The use of the consistent tangent reflects the finite steps taken in the numerical integration of the constitutive equations and preserves the asymptotic quadratic convergence rate of Newton's method. Modern numerical algorithms have not yet been applied to cyclic metal plasticity models.

1.5 Scope of the Present Study

A significant portion of the work reported here is the development of an analytical model capable of analyzing lateral buckling of short I-beams under cyclic loading. A geometrically nonlinear beam model is formulated in terms of stress components. Transverse warping and torsional warping deformations are included in the model to treat problems involving high shear and torsion. The kinematic constraint imposed in this model is appropriate for a thin-walled I-section geometry. The novel kinematic model includes a geometrically exact representation of the primary torsional warping as well as secondary warping due to torsion and transverse shear. A new cyclic plasticity model, incorporating many of the most compelling features of existing phenomenological models, is developed and implemented with the consistent return mapping algorithm developed by Simo and Taylor (1985). The new model represents cyclic metal plasticity well and is suitable for large-scale computation.

The experimental research program comprised five tests of propped cantilever beams subjected to a cyclically reversing point load acting near the fixed end. The experiments include both braced and unbraced beams subjected to similar loading histories. The number of specimens tested in the present program was small relative to the large number of parameters that are important to the complex response of these cyclically loaded systems. Therefore, we examine the importance of constitutive parameters, residual stresses, load placement, geometric imperfections, flexible boundary conditions, and lateral bracing using the analytical model developed earlier. Extensive parameter studies are conducted both to assess the performance of the analytical model and to gain further insight into the lateral buckling problem. Once validated, the analytical model is used to extend, interpret, and generalize the results of the experimental investigation through the parameter studies. Most of the parameter studies are carried out using the propped cantilever arrangement used in the experiments.

1.6 Overview of the Report

Chapter 2 begins with the development of the kinematic hypothesis used to describe the nonlinear deformation of an I-beam. The model includes warping deformations due to transverse shear and torsion. The equilibrium equations, cast in terms of stress components, are expressed in weak form and reflect the kinematic hypothesis developed earlier. The resulting nonlinear equations are treated numerically with Newton's method using a finite element discretization of the spatial domain.

A cyclic plasticity model is developed in chapter 3. The basic rate equations are presented first, with subsequent review of existing hardening rules. After past research on cyclic plasticity is reviewed, the new cyclic plasticity model is proposed. Numerical aspects related to the treatment of the constitutive equations are then considered. These aspects include the development of a return mapping algorithm with

algorithmically consistent tangent moduli. Finally, several examples of the proposed cyclic plasticity model are presented in support of the validity of the model.

In chapter 4, five experiments on lateral buckling of propped cantilever beams are described, giving results and general observations on cyclic lateral buckling for these elements. The parameters of the analytical model to be used as the control case in the subsequent analytical studies are presented. A cyclic analysis of the control model is done to demonstrate the ability of the theoretical model to reproduce the important phenomena observed in the experiments.

Various parameter studies affecting the response of the test specimens are performed in chapters 5, 6, and 7. The parameters studied in chapter 5 include constitutive parameters, geometric imperfections in load placement, geometric dimensions of the test piece, boundary conditions, and residual stresses. The effect of flexibility of the fixed end is examined in chapter 6 and the influence of lateral bracing is studied in chapter 7. The linearized buckling load, the inelastic (post-limit) monotonic response, and the inelastic cyclic response are examined to assess the effects of the parameters for each study. The parameter studies are summarized at the end of each chapter.

Chapter 8 gives a summary and the general conclusions of this study.

1.7 Acknowledgements

This report was supported by the National Science Foundation under grants CEE 84-04865 and CES 86-58019, with S. C. Liu as program director. Additional support came from the American Institute of Steel Construction. The support of these organizations is gratefully acknowledged. The results, opinions, and conclusions expressed in this report are solely those of the authors and do not necessarily represent those of the sponsors.

The authors thank James M. Lafave, Christie M. Elliott, and Mark S. Eckhoff, former students in the Department of Civil Engineering at the University of Illinois, for their contributions to the laboratory experiments reported herein. Support from the Department of Civil Engineering administration and the technical staff of Newmark Civil Engineering Laboratory is also gratefully acknowledged.

Thanks are extended to Professors I. Dennis Parsons, David A. W. Pecknold, Arthur R. Robinson, and James E. Stallmeyer for patiently sitting on Sang-gab Lee's doctoral committee, and for at least trying to read the Korean-English version of this report.

Special thanks are due to Ruth E. Downs for reading drafts of the report and making valuable suggestions for its improvement.

Chapter 2

Finite Deformation I-Beam Model

A large majority of the past research on the *inelastic* lateral-torsional buckling of I-beams has employed an *elastic core* type of approach with a second order approximation to the equilibrium equations (see, for example, Galambos, 1963; Rajasekaran, 1971; Chen and Atsuta, 1977). The elastic core approach is generally carried out entirely with stress and strain resultants. The inelastic constitutive equations for the stress resultants are obtained by using a kinematic hypothesis to directly integrate the local tangent modulus of the uniaxial stress-strain curve over the cross-section. Such a process is feasible only if the stress state is uniaxial and the loading monotonic since the kinematic hypothesis gives an unambiguous state of stress for these conditions. The results of this type of analysis have been found to agree well with experiments and have demonstrated the importance of various effects, such as the effects of residual stresses, on buckling. Unfortunately, this method is not readily applicable to short beams where the effects of shear are expected to be important.

Considerable progress has been made in recent years toward understanding the differential geometry of finite beam deformations. Simo and Vu-Quoc (1986) have presented a numerical formulation for a geometrically exact, elastic, stress resultant beam model reflecting the Bernoulli-Kirchhoff kinematic assumption that plane sections remain plane. Simo and Vu-Quoc (1989) have also extended their model to include the effect of torsional warping. The pertinent literature in this area has been cited in the above named references, and will not be repeated here. Because of the restriction to elastic material, these models have not been applied to study the lateral buckling of beams.

Previous efforts to understand the lateral buckling behavior of beams have concentrated almost exclusively on applications involving longer beams subjected to monotonic loading. The particular problems associated with the eccentrically braced frame system have not yet been adequately treated. The purpose of the present chapter is to develop an analytical model which is capable of accounting for the effects of shear and generalized loading on the inelastic buckling of short beams subjected to cyclic loading.

The deformation map has often been restricted to a second order approximation of the deformations. One assumption that has often been used is that the transverse deflections of a beam are small when compared to the lateral deflections. This assumption decouples the transverse equilibrium equation for flexure from the lateral bending and twisting equations. Research has shown that the transverse deflections of short beams in an eccentrically braced frame may be large (Hjelmstad and Popov, 1983). Thus, the simplifying assumption is not appropriate for the current application, particularly since our main interest is in the post-buckling regime. The model developed here considers finite displacement and rotation of the beam with superposed infinitesimal warping deformations.

It has been demonstrated by many researchers that the effects of residual stresses on the buckling of beams is important. Usually, the residual stresses are taken to approximate the distribution that exists after the rolling and cooling processes have been completed. The residual stress pattern is generally taken to be a polynomial function which satisfies self equilibrium requirements (Kitipornchai and Trahair, 1975*b*). However, a beam subjected to cyclic loading may or may not buckle on the virgin loading, and

inelastic action may alter the residual stress pattern. Hence, the initial distribution may not accurately reflect the state of residual stress in a beam with loading history.

In most of the research into the lateral buckling behavior of beams, a highly idealized constitutive assumption is used for the material. Often, a perfect trilinear, uniaxial strain hardening stress–strain curve typical of virgin ductile steel is assumed. Under this assumption the stress–strain curve is trilinear and only three possible values of tangent modulus can be realized (*i.e.* the initial elastic value, zero for the plastic plateau, and a strain–hardening value). The main motivation for using such an idealized model is to make analytical progress in achieving a solution. For monotonic loadings the ideal behavior is often justified. However, it is well known that under generalized loadings this ideal behavior degenerates into nonlinear behavior exhibiting Bauschinger's effect and strain hardening. In our model we implement a more general multiaxial cyclic plasticity model.

The advantage of the computational point of view taken here is that the nonlinear constitutive equations are exactly satisfied at the local level within each global iteration of each time step (Simo, Hjelmstad, and Taylor, 1984). Hence any general constitutive model can be accommodated. Even within the scope of the restricted kinematics, inelastic lateral–torsional problems can accurately be solved for difficult cross–sectional geometries like the I–beam. Also, the local treatment of constitutive equations completely obviates the need for keeping track of the location of the shear center, which plays a fundamental role in the lateral buckling response of stress resultant models.

The analytical model is constructed by imposing a kinematic constraint typical of a *thin–walled beam* theory, but generalized to account for finite deformations. It also includes shearing deformations and warping due to transverse shearing (Hjelmstad, 1987). A (locally) plane stress condition is assumed for the web and flange elements, in the spirit of the thin–walled beam approximation, and the general inelastic constitutive equations reflect this assumption. The equilibrium equations are cast in weak (virtual work) form and treated numerically with the finite element method. Numerical treatment of the problem is accomplished through an iterative procedure of first linearizing the equilibrium equations about an intermediate configuration and then solving the linear problem for the incremental motions. The updated configuration determines the state of strain in a body, for which the corresponding state of stress can be found by solving the nonlinear constitutive equations. The implications of the formulations discussed here are examined carefully in chapters 5, 6 and 7 through a set of numerical simulations which represent a thorough parameter study of the experiments presented in chapter 4.

2.1 Kinematic Description

For an I–beam, the classical torsion warping function, based on *sectorial areas* (Vlazov, 1961), is equivalent to a generalized Bernoulli–Kirchhoff (plane sections remain plane) assumption for each of the elements in the cross–section. Such an assumption is inadequate to treat problems involving high shear since the constant distribution of shear stresses obtained from this hypothesis precludes the possibility of a yield zone propagating from the interior of the cross–section. It also violates the condition that shear stresses vanish at the extreme boundaries.

In this section we discuss the geometry of deformation of the nonlinear beam model. Transverse and torsional warping degrees of freedom are introduced to allow better representation of the variation in shear strains over the cross–section. The kinematic description is an extension of the formulation of Simo

and Vu-Quoc (1986) to account for finite torsional warping deformations superposed with infinitesimal transverse and torsional warping deformations due to transverse shearing. Such an extension is possible because of the particular cross-sectional geometry of the I-beam. In common with the geometric model of Simo and Vu-Quoc, finite extension and finite shearing of the beam are accommodated, even in the presence of large rotations.

A configuration of the beam is described by a vector field giving the position of the current line of centroids and a three-dimensional orthogonal moving frame which models the orientation of the cross-section. The configurations of the beam are completely defined by specifying the evolution of an orthogonal matrix, the position vector of the line of centroids, and the intensity of warping.

We will focus our attention here on a beam model with I-type cross-section. The model will treat the cross-section as a thin-walled open section. In contrast with classical approaches to thin-walled beams, the assumption of vanishing contour shear is not made here. Rather, the kinematic hypothesis is suitably generalized, in the spirit of the Timoshenko beam, such that transverse shearing deformations can accrue. Such a generalization is important in the present application to short beams because of the predominating influence of shear. The geometric assumptions implicit in the present formulation are as follows:

(*i*) The length of the cross-sectional contour remains approximately unchanged during deformation. The changes in length are of second order and are caused by the linear approximation to the warping effects due to shearing along the contour. The kinematics are formulated such that the primary torsion warping deformation does not induce a change in contour length.

(*ii*) The shear strain *across* the thickness of the cross sectional contour is constrained to be zero. This assumption is justifiable if the thickness of the cross-section is small in comparison with the cross-sectional dimensions.

(*iii*) The shear strain along the contour of the section is represented by the average values through the plate thickness. St. Venant torsion is introduced by adding a stress couple which is proportional to the rate of twist of the beam. The constitutive equation for the St. Venant torsion is not coupled with the in-plane stress components.

Notation.- The present development is concerned with an initially straight beam having length L and cross-section Ω which has a piecewise smooth boundary $\partial\Omega$. Coordinates in the reference configuration $B \equiv (0, L) \times \Omega \subset \mathbb{R}^3$, occupied by the beam at time $t = 0$, are designated by $\{X_I\}$ with the standard (material) reference basis $\{\hat{\mathbf{E}}_I\}$. The spatial coordinate system $\{x_i\}$, along with the associated basis $\{\hat{\mathbf{e}}_i\}$, is taken as collinear with $\{X_I\}$. The deformation map is denoted by $\phi : B \subset \mathbb{R}^3 \to \mathbb{R}^3$ and the deformation gradient by $\mathbf{F} = \partial\phi/\partial\mathbf{X}$. The points $X \in B$ and $x \in \phi(B)$ will be identified by their position vectors $\mathbf{X}$ and $\mathbf{x}$ respectively. We adopt the convention that the line of centroids of the cross-sections is initially oriented along the X_1 axis and the principal axes of inertia are oriented along the $\{X_2, X_3\}$ axes. For notational convenience, we will denote the axial coordinate as $X_1 \equiv S$. The summation convention is in force throughout, unless explicitly excepted. Latin indices take values in $\{1,2,3\}$, while Greek indices take values in $\{2,3\}$.

2.1.1 Kinematic hypothesis

The kinematic hypothesis represents a restriction on the deformation map, and is central to the formulation of a beam theory (or any reduced engineering theory). In the present case we wish to capture finite deformation and rotation of the beam cross-section as well as warping. To develop the kinematics which accomplish these goals, we will proceed with a sequential argument. The development will start with a kinematic model proposed by Simo (1985). The model will then be augmented to account for finite warping due to torsion and infinitesimal warping due to transverse shearing. As demonstrated by Simo (1985) finite motion and rigid rotation of the beam cross-section are implicit in the following expression for the deformation map

$$\phi(\mathbf{X}) = \phi_0(S) + X_\alpha \mathbf{t}_\alpha(S) \tag{2.1}$$

where

$$\phi_0(S) = [S + u(S),\ v(S),\ w(S)]^t \tag{2.2}$$

represents the position vector of the centroid of the cross-section. The generalized displacements $u(S)$, $v(S)$, and $w(S)$ represent the components of the displacement of the line of centroids with respect to the basis $\{\hat{\mathbf{E}}_I\}$.

The orientation of the cross-section is represented by the orthonormal moving basis $\{\mathbf{t}_I(S)\}$ attached to the centroid of a typical cross-section. The vectors are oriented such that $\mathbf{t}_1(S)$ remains normal to the *average rotated section*, $\mathbf{t}_2(S)$ describes the major principal direction, and $\mathbf{t}_3(S)$ describes the minor principal direction, as shown in Fig. 2.1. The orientation of the moving basis can be expressed in terms of the fixed basis vectors through an orthogonal transformation $\Lambda(S) = \Lambda_{ij}\hat{\mathbf{e}}_i \otimes \hat{\mathbf{E}}_j$ such that

$$\mathbf{t}_i(S) = \Lambda(S)\hat{\mathbf{E}}_i = \Lambda_{ji}(S)\hat{\mathbf{e}}_j\ , \qquad (i,j = 1,2,3) \tag{2.3}$$

Consider now a warping deformation from the deformed position described by Eq. (2.1) in which the top flange rotates rigidly about its center by an amount γ in the clockwise direction, while the bottom flange rotates rigidly about its center the same amount in the anticlockwise direction. For later clarity of description we refer to this mode of warping as *primary torsional warping*. A new orthogonal frame, shown in Fig. 2.1, can now be defined for both the top flange and the bottom flange as

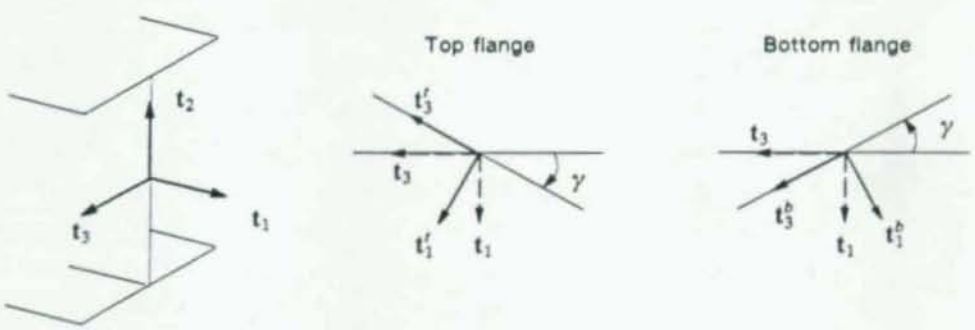

Fig. 2.1 Flange rotation due to primary torsional warping

$$\mathbf{t}_i^t = Q_{ij}(\gamma)\mathbf{t}_j \ , \qquad \mathbf{t}_i^b = Q_{ji}(\gamma)\mathbf{t}_j \ , \qquad i,j \in \{1,3\} \tag{2.4}$$

where the $Q_{ij}(\gamma)$ are the components of the orthogonal transformation matrix

$$\mathbf{Q}(\gamma) = \begin{bmatrix} \cos\gamma & \sin\gamma \\ -\sin\gamma & \cos\gamma \end{bmatrix} \tag{2.5}$$

The presence of shear stresses along the contour of the cross section tends to cause an out-of-plane deformation of the cross section known as warping. The existence of this warping deformation has been recognized for a long time, but was accounted for only in elasticity approaches to beam problems. The justification for neglecting warping due to transverse shear when constructing a beam theory generally relies on the argument that shearing deformations are small compared with flexural deformations. Such an assumption fails to be valid for short beams (where the depth is on the same order as the length) or for beams with extremely low shear modulus. Cowper (1966), was among the first to try to systematically treat the influence of warping in beam theory by developing a method for computing the so-called *shear coefficient* which appears in Timoshenko's beam theory. Simo (1982) demonstrated that a kinematic assumption could be constructed which lead directly to Cowper's consistent shear coefficient. With an explicit expression for the kinematic hypothesis, Simo was able to develop a second order beam theory which consistently accounted for the effect of warping due to transverse shear. Hjelmstad (1987) developed a theory, motivated by this kinematic hypothesis, in which the warping was allowed to accrue as an independent degree-of-freedom. In the sequel we introduce additional warping modes into the kinematic hypothesis to account for the warping caused by the nonuniform shear flow. These additional warping modes are the extension to three dimensions of the ideas implicit in the aforementioned works.

We now superpose on the previous deformation field a distortional warping deformation which is infinitesimal and *normal* to the primary warped cross-section, as shown in Fig. 2.2. Distortional warping deformations will accrue from shearing of the elements caused by transverse resultant shears and torsion. The intensity of warping will be expressed as an expansion of warping basis functions and generalized warping intensities (Hjelmstad, 1987). In the present case, the distortional warping can be expressed in the form $\psi_i(X_2, X_3)\beta_i(S)$, i=1,...,3. Note that the summation convention is in effect.

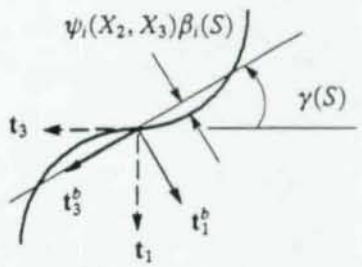

Fig. 2.2 Distortional warping (bottom flange)

The functions $\beta_1(S)$, $\beta_2(S)$, and $\beta_3(S)$ represent the intensity of warping characterized by the warping basis functions $\psi_1(X_2, X_3)$, $\psi_2(X_2, X_3)$ and $\psi_3(X_2, X_3)$, respectively. The specific character of the warping functions for the I-beam will be discussed later.

The deformation map can now be written in terms of the defined objects as follows:

$$\phi(\mathbf{X}) = \phi_o(S) + X_2\mathbf{t}_2 + X_3\begin{Bmatrix}\mathbf{t}_3^t\\ \mathbf{t}_3\\ \mathbf{t}_3^b\end{Bmatrix} + \psi_i(X_2, X_3)\beta_i(S)\begin{Bmatrix}\mathbf{t}_1^t\\ \mathbf{t}_1\\ \mathbf{t}_1^b\end{Bmatrix} \tag{2.6}$$

where the curly bracket notation indicates that the top component applies to the top flange, the middle component applies to the web, and the bottom component applies to the bottom flange. When a term does not have a curly bracket it applies to all three regions. Using the expressions relating the warped base vectors to the unwarped base vectors, we can rewrite the above expression in the form

$$\phi(\mathbf{X}) = \phi_o + X_2\mathbf{t}_2 + X_3[h(\gamma)\mathbf{t}_1 + g(\gamma)\mathbf{t}_3] + \psi_i\beta_i[g(\gamma)\mathbf{t}_1 - h(\gamma)\mathbf{t}_3] \tag{2.7}$$

The functions $g(\gamma)$ and $h(\gamma)$ are defined as

$$g(\gamma) = \begin{Bmatrix}\cos\gamma\\ 1\\ \cos\gamma\end{Bmatrix} \qquad h(\gamma) = \begin{Bmatrix}-\sin\gamma\\ 0\\ \sin\gamma\end{Bmatrix} \tag{2.8}$$

For convenience in subsequent derivations we will recast the deformation map into the following compact form:

$$\phi(\mathbf{X}) = \phi_o(S) + a_i(\mathbf{X})\mathbf{t}_i(S) \tag{2.9}$$

where $a_1 = X_3h(\gamma) + \psi_i\beta_ig(\gamma)$, $a_2 = X_2$, and $a_3 = X_3g(\gamma) - \psi_i\beta_ih(\gamma)$ can be viewed as the components of stretch of the base vectors.

Remark.– The above kinematic assumption is particular to the I–beam cross–sectional geometry and reflects finite torsional warping. The distortional warping terms are needed to obtain a reasonable distribution of shearing strains within the cross–section. This is quite important for a formulation in which local constitutive equations are used. The kinematics used here can be contrasted with those of Simo and Vu–Quoc (1989). There the warping is accommodated in a finite deformation context and is geometrically exact. However, the warping function is taken to be the one corresponding with the infinitesimal case. Since theirs is a stress resultant theory, the effect of making this assumptions does not show up in the geometry of beam deformation because the stress resultants, particularly the bishear, can be suitably defined so that the stress power of the stress resultants is identical to that of the 3–D continuum. However, the difference is implicit in the constitutive equations, which are also motivated by the infinitesimal theory.

2.1.2 Description of finite rotations

The orthogonal transformation $\Lambda(S)$ can be described in several ways. Among these are the Euler angles (with one of twelve conventions) and the Cayley–Klein parameters (or quaternions). Simo (1985) presents a novel parameterization in terms of quaternions with an updating procedure based on the exponential map to trace the evolution of the moving frame. Here we adopt the Euler angle representation. The well known singularity present in this parameterization is not expected to influence the problems of interest here.

The orthogonal transformation $\Lambda(S)$ can be derived as the product of the three (planar) rotation matrices $\Lambda_1(\theta_1(S))$, $\Lambda_2(\theta_2(S))$, and $\Lambda_3(\theta_3(S))$, where θ_1, θ_2 and θ_3 are the three Euler angles which we will use to parameterize the finite rotation. Following the *xyz* convention, the rotation matrix takes the form

$$\Lambda(S) = \Lambda_1(\theta_1(S))\Lambda_2(\theta_2(S))\Lambda_3(\theta_3(S))$$

$$= \begin{bmatrix} 1 & 0 & 0 \\ 0 & C_1 & -S_1 \\ 0 & S_1 & C_1 \end{bmatrix} \begin{bmatrix} C_2 & 0 & S_2 \\ 0 & 1 & 0 \\ -S_2 & 0 & C_2 \end{bmatrix} \begin{bmatrix} C_3 & -S_3 & 0 \\ S_3 & C_3 & 0 \\ 0 & 0 & 1 \end{bmatrix} \tag{2.10}$$

$$= \begin{bmatrix} C_2C_3 & S_1S_2C_3 - C_1S_3 & C_1S_2C_3 + S_1S_3 \\ C_2S_3 & S_1S_2S_3 + C_1C_3 & C_1S_2S_3 - S_1C_3 \\ -S_2 & S_1C_2 & C_1C_2 \end{bmatrix}$$

where the first rotation is the angle θ_3 about the initial X_3 axis, the second is the angle θ_2 about an intermediate X_2 axis, and the third is the angle θ_1 about the final X_1 axis. The notation: $C_i = \cos\theta_i(S)$, $S_i = \sin\theta_i(S)$, i=1,2,3 has been introduced to economize the notation.

2.1.3 Secondary warping due to torsion and transverse shearing

The warping of the cross-section due to torsion is composed of two parts: *(1)* a finite but plane rotation of the flanges in opposite directions (primary warping), as shown in Fig. 2.1, and *(2)* a superposed infinitesimal distortional warping displacement due to shearing of the flanges (secondary warping), as shown in Fig. 2.2. The first type of warping is characterized by the rotation angle γ, and is the finite deformation counterpart of the classical torsion warping function based on sectorial areas (Vlazov, 1961). The secondary warping is characterized by the warping intensities β_i which multiply the warping functions ψ_i. This mode of deformation is usually ignored in formulating beam theories. However, this warping component is important because it allows for a shear strain gradient, enabling the shear strain, and thereby shear stress, to vanish at the extreme fibers of the cross section. This mechanism also allows for a more realistic representation of the propagation of yielding through the cross-section. Again, this mode of warping is important mainly to short beams.

The secondary warping function associated with torsion is given by

$$\psi_1 = -\frac{\kappa_2 GA}{120EI_2} \begin{cases} 0 & \text{in web} \\ \frac{h}{2}\operatorname{sgn}(X_2)(2+\nu)[20X_3^3 - 3b^2X_3] & \text{in flange} \end{cases} \tag{2.11}$$

The secondary warping functions due to transverse shearing can be found as in Hjelmstad and Popov (1983) and have the explicit expressions:

$$\psi_2 = \frac{\kappa_2 GA}{120EI_2} \begin{cases} 0 & \text{in web} \\ (2+\nu)[20X_3^3 - 3b^2X_3] & \text{in flange} \end{cases} \tag{2.12}$$

$$\psi_3 = \frac{\kappa_3 GA}{120EI_3}\begin{cases}(2+\nu)[20X_2^3 - 3h^2X_2C_0] & \text{in web}\\ \frac{h}{2}\mathrm{sgn}(X_2)[60(2+\nu)X_3^3 - 120(1+\nu)b|X_3| + h^2C_1] & \text{in flange}\end{cases} \tag{2.13}$$

where, the constants, C_0 and C_1, are given by

$$C_0 = \frac{2 + 10m(1-2n^2) + \nu(1+5m(1-5n^2))}{(1+3m)(2+\nu)}, \qquad C_1 = \frac{4(1+15mn^2) + \nu(2+75mn^2)}{(1+3m)} \tag{2.14}$$

and G is the shear modulus, E is Young's modulus, and ν is Poisson's ratio. The function $sgn(x)$ takes values $sgn(x)=1$ if $x>0$, $sgn(x)=-1$ if $x<0$, and $sgn(x)=0$ if $x=0$. The geometric properties of the I-beam have been expressed in terms of the dimensionless parameters m, the ratio of gross flange area to web area, and n, the ratio of flange width to section depth:

$$m = \frac{2bt_f}{ht}, \qquad n = \frac{b}{h} \tag{2.15}$$

where h is the distance between the centroids of the flanges, t is the web thickness, b is the flange width, and t_f is the flange thickness, as shown in Fig. 2.3.

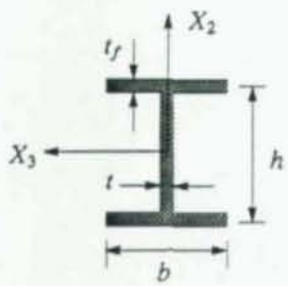

Fig. 2.3 Typical I-beam cross-section

The warping functions ψ_1 and ψ_2 are quite similar, differing only in sense (for transverse shearing the warping is symmetric with respect to the origin while for torsion it is antisymmetric) and in scaling (the torsion warping function has an additional factor of $h/2$). This similarity is a consequence of the symmetry of the section which leads to a simple mode for resisting primary warping torsion wherein the two flanges are sheared, as independent beams, in opposite directions.

For reference, we note that the standard cross-sectional properties: area, A, minor moment of inertia, I_2 (about the X_2 axis), and major moment of inertia, I_3 (about the X_3 axis), can be expressed in terms of m, n, h, and t as

$$A = ht(1+m), \qquad I_2 = \frac{h^3t}{12}mn^2, \qquad I_3 = \frac{h^3t}{12}(1+3m) \tag{2.16}$$

The two shear coefficients, κ_2 and κ_3, were given by Cowper (1966) as follows:

$$\kappa_2 = \frac{10(1+\nu)}{12+11\nu} \tag{2.17}$$

$$\kappa_3 = \frac{10(1+\nu)(1+3m)^2}{(12+72m+150m^2+90m^3)+\nu(11+66m+135m^2+90m^3)+30n^2(m+m^2)+5\nu n^2(8m+9m^2)} \tag{2.18}$$

Note that for zero Poisson's ratio κ_2 reduces to the familiar value of 5/6 (each flange is a rectangular section). The coefficient κ_3 has the approximate value of A_w/A, where A_w is the web area and A is the total area.

2.1.4 The constrained deformation gradient

The deformation gradient, reflecting the kinematic hypothesis, can be computed from the relationship $\mathbf{F} = \phi_{,I} \otimes \hat{\mathbf{E}}_I$. For the specific deformation map given by Eq. (2.9) the deformation gradient takes the form

$$\mathbf{F}(\mathbf{X}) = [\phi_0'(S) + a_i(\mathbf{X})\mathbf{t}_i'(S)] \otimes \hat{\mathbf{E}}_1 + a_{i,j}(\mathbf{X})\mathbf{t}_i(S) \otimes \hat{\mathbf{E}}_j \tag{2.19}$$

where the derivative of the position vector of the line of centroids is given by,

$$\phi_0'(S) = [1 + u'(S), \quad v'(S), \quad w'(S)]' \tag{2.20}$$

and the derivative of the moving basis is given by

$$\mathbf{t}_i'(S) = \Lambda'\hat{\mathbf{E}}_i = \Lambda_{,k}\theta_k'\hat{\mathbf{E}}_i = \frac{\partial\Lambda}{\partial\theta_k}\frac{d\theta_k}{dS}\hat{\mathbf{E}}_i \tag{2.21}$$

In the above expressions, a prime denotes differentiation with respect to S, *i.e.* $(\cdot)' = d(\cdot)/dS$, and subscripts following a comma denote differentiation with respect the coordinate indicated, *i.e.* $(\cdot)_{,k} = \partial(\cdot)/\partial X_k$. The notation $\Lambda_{,k}$ indicates the partial derivative with respect to the argument, $\partial\Lambda/\partial\theta_k$. The gradient of $a(\mathbf{X})$ is a matrix with components $a_{i,j}$ and has the explicit form:

$$\nabla a = \begin{bmatrix} X_3 h'(\gamma) + \psi_i[\beta_i' g(\gamma) + \beta_i g'(\gamma)] & \psi_{i,2}\beta_i g(\gamma) & h(\gamma) + \psi_{i,3}\beta_i g(\gamma) \\ 0 & 1 & 0 \\ X_3 g'(\gamma) - \psi_i[\beta_i' h(\gamma) + \beta_i h'(\gamma)] & -\psi_{i,2}\beta_i h(\gamma) & g(\gamma) - \psi_{i,3}\beta_i h(\gamma) \end{bmatrix} \tag{2.22}$$

The derivatives of the functions $g(\gamma)$ and $h(\gamma)$ with respect to S are given by the expressions

$$g'(\gamma) = -\begin{Bmatrix} \sin\gamma \\ 0 \\ \sin\gamma \end{Bmatrix}\gamma', \qquad h'(\gamma) = \begin{Bmatrix} -\cos\gamma \\ 0 \\ \cos\gamma \end{Bmatrix}\gamma' \tag{2.23}$$

2.1.5 Residual stresses

The distributions of residual stress adopted here are typical of steel I-sections fabricated by the hot rolling process. A polynomial expression is assumed as an analytical approximation of the residual stress pattern. Since residual stresses in a section are self-equilibrated, they must satisfy the following condi-

tions of statics: no resulting axial forces, and no resulting bending moment about two principal axes (Kitipornchai and Trahair, 1975*b*). The residual stress pattern considered here is shown in Fig. 2.4,

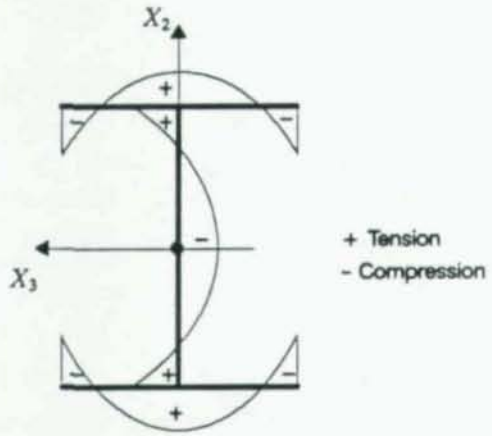

Fig. 2.4 Residual stress distribution for typical rolled section

wherein the flange tips and the central portion of the web are presumed in compression. The expressions for the residual stresses in the web and in the flange, σ_{rw} and σ_{rf} respectively, are given by:

$$\sigma_{rf} = a(c_1\xi^4 + c_2\xi^2 + 1)\sigma_0 \qquad \sigma_{rw} = a(c_3\eta^4 + c_4\eta^2 - 1)\sigma_0 \tag{2.24}$$

where a is the amplitude of the residual stress and σ_0 is the yield stress. The variations are expressed in terms of the normalized coordinates $\xi = X_3/b$, $\eta = X_2/h$, and the constants are given by the following relations

$$c_1 = \frac{88 - 28mn^2 + 80m}{(1.5n^2 + 2)m} \qquad c_2 = -\frac{22 + 5mn^2 + 36m}{(1.5n^2 + 2)m} \tag{2.25}$$

$$c_3 = -\frac{168 - 88mn^2 + 60n^2}{(1.5n^2 + 2)} \qquad c_4 = \frac{58 - 22mn^2 + 27n^2}{(1.5n^2 + 2)} \tag{2.26}$$

2.2 Equilibrium Equations, Weak Form

The local form for the static balance of linear momentum of a non-polar continuum is expressed by the equation (see, for example, Marsden and Hughes, 1983):

$$DIV\,\mathbf{P} + \varrho_0\,\mathbf{B} = 0\ ; \qquad \mathbf{X} \in B \tag{2.27}$$

where $\mathbf{P}$ is the first Piola–Kirchhoff stress tensor, ϱ_0 is the density in the reference configuration, $\mathbf{B}$ is the body force, and DIV is the divergence operator with respect to the reference coordinates $\{X_i\}$, *i.e.* the divergence of a second order tensor is has components $[DIV(\cdot)]_i = (\cdot)_{ij,j}$ in cartesian coordinates. Balance of angular momentum further implies the symmetry $\mathbf{PF}^t = \mathbf{FP}^t$.

In accordance with standard practice, we denote by ∂B_u that portion of the boundary where the deformation map is prescribed and by ∂B_t that portion of the boundary where the tractions $\bar{\mathbf{t}}$ are prescribed. The boundary value problem is well posed if $\partial B_t \cup \partial B_u = \partial B$ and $\partial B_t \cap \partial B_u = \emptyset$.

The local form of the equilibrium Eq. (2.27) can be expressed as a weak statement of equilibrium in the following way (Marsden and Hughes, 1983)

$$\hat{G}(\phi, \eta) \equiv \int_B \mathbf{P} : (D\mathbf{F} \cdot \eta)\, dV - \int_B \varrho_0 \mathbf{B} \cdot \eta\, dV - \int_{\partial B_t} \bar{\mathbf{t}} \cdot \eta\, dS = 0 \tag{2.28}$$

for any kinematically admissible variation η which satisfies the displacement boundary conditions. The variation of the deformation gradient has been denoted by $D\mathbf{F} \cdot \eta$ and is computed with the formula for the directional derivative as

$$D\mathbf{F}(\mathbf{X}, \mathbf{u}(S)) \cdot \eta = \frac{d}{d\epsilon}[\mathbf{F}(\mathbf{X}, \mathbf{u} + \epsilon\eta)]_{\epsilon=0} \tag{2.29}$$

where $\mathbf{u}(S) = \{u, v, w, \theta_1, \theta_2, \theta_3, \gamma, \beta_1, \beta_2, \beta_3\}$ is the vector of generalized displacements and $\eta(S)$ is the variation in $\mathbf{u}(S)$.

Since the kinematic hypothesis effectively obliterates the contribution of St. Venant torsion, the effect must be reintroduced to capture this effect. Formally, we accomplish this by augmenting the weak form as follows

$$G(\phi, \eta) \equiv \hat{G}(\phi, \eta) + \int_B \tau_{sv}\, (D\Gamma_{sv} \cdot \eta)\, dV \tag{2.30}$$

where τ_{sv} is the stress couple associated with St. Venant torsion, Γ_{sv} is the generalized strain conjugate to τ_{sv}, and $D\Gamma_{sv} \cdot \eta$ is the variation in strain. We note that the above construction is more an expedient than an axiomatic necessity. A more refined kinematic hypothesis can be written which contains a quadratic variation of displacement through the thickness of the contour which leads directly to a weak form containing the contribution due to St. Venant torsion (see, for example, Gjelsvik, 1981).

The appropriate strain measure for the St. Venant torsion is one which measures the rate of twist of the beam relative to the moving frame. To obtain an expression for the rate of twist consider the general expression for the curvatures of a finitely deformed beam (Simo, 1985):

$$\Omega(S) \equiv \left[\frac{d}{dS}\Lambda(S)\right]\Lambda'(S) = \begin{bmatrix} 0 & -\kappa_3(S) & \kappa_2(S) \\ \kappa_3(S) & 0 & -\kappa_1(S) \\ -\kappa_2(S) & \kappa_1(S) & 0 \end{bmatrix} \tag{2.31}$$

where $\kappa_1(S)$ is the torsional curvature and $\kappa_2(S)$ and $\kappa_3(S)$ are the flexural curvatures of the beam. The St. Venant torsional strain will be taken simply as $\Gamma_{sv} = \kappa_1(S)$, which clearly does not depend upon the cross sectional coordinates. From the expression for the finite rotation matrix, Eq. (2.10), we can compute the torsional curvature to be

$$\kappa_1(S) = (\cos\theta_2 \cos\theta_3)\theta_1' - (\sin\theta_3)\theta_2' \tag{2.32}$$

For configurations near the undeformed state the torsional curvature reduces to the expression $\kappa_1(S) = \theta_1'$ in accord with the linear theory. In the numerical implementation of the theory we will assume that the linear expression is adequate. For the problems studied here such an assumption is only a modest compromise, and is in line with the assumption made on the constitutive equations.

Since the St. Venant torsional strain measure does not depend upon the cross sectional coordinates, the second term in Eq. (2.30) can be explicitly integrated to give

$$G_{sv}(\phi, \eta) \equiv \int_B \tau_{sv} \, (D\Gamma_{sv} \cdot \eta) \, dV = \int_0^L m_{sv} \, (D\kappa_1 \cdot \eta) \, dS \tag{2.33}$$

where $m_{sv}(S)$ is the St. Venant torque resultant acting at a cross section. We will, however, assume that the stress couple is distributed uniformly along the contour of the section, in accord with the elementary theory, and integrate this term numerically over the cross section along with all of the other terms. In addition, we assume that the stress couple evolves according to an uncoupled constitutive equation and always remains in the elastic state. As a consequence, the explicit expression for the stress couple is $\tau_{sv} = GJ^*\kappa_1(S)$, where J^* is the distribution of torsion constant along the contour in the cross-section and is expressed as $t_f^3/3$ in the flange and $t^3/3$ in the web.

2.2.1 Linearized governing equations

The linearization of the weak form of equilibrium equation (2.28) about an intermediate configuration, $\hat{\phi} : B \to \mathbb{R}^3$, leads to to the expression (Marsden and Hughes, 1983)

$$L[\hat{G}]_{\hat{\phi}} = \int_B (D\mathbf{F} \cdot \eta)_{\hat{\phi}} : [\mathbf{S} \otimes \mathbf{1} + \mathbf{F}^t \frac{\partial \mathbf{S}}{\partial \mathbf{E}} \mathbf{F}]_{\hat{\phi}} : (D\mathbf{F} \cdot \Delta\phi)_{\hat{\phi}} \, dV + \hat{G}(\hat{\phi}, \eta) \tag{2.34}$$

where $\mathbf{1}$ denotes a unit matrix with components δ_{ij}. The subscript $\hat{\phi}$ designates that the argument is evaluated at the configuration $\hat{\phi} : B \to \mathbb{R}^3$ and $\Delta\phi : B \to \mathbb{R}^3$ is the incremental motion. The integral term in Eq. (2.34) gives rise to the tangent stiffness of the system, the first term being the geometric part and the last term being the material part. The constant term represents the so called out-of-balance force at the configuration and has the expression

$$\hat{G}(\hat{\phi}, \eta) = \int_B (\mathbf{P} : D\mathbf{F} \cdot \eta)_{\hat{\phi}} \, dV - \int_{\partial B_t} \bar{\mathbf{t}} \cdot \eta \, dS \tag{2.35}$$

The linearization of the St. Venant part of the weak form is carried out similarly:

$$L[G_{sv}]_{\hat{\phi}} = \int_0^L (D\kappa_1 \cdot \eta)_{\hat{\phi}} \, [\frac{dm_{sv}}{d\kappa_1}]_{\hat{\phi}} \, (D\kappa_1 \cdot \Delta\phi)_{\hat{\phi}} \, dS + G_{sv}(\hat{\phi}, \eta) \tag{2.36}$$

where the St. Venant out-of-balance is given directly by Eq. (2.33). The material tangent for the St. Venant part is $dm_{sv}/d\kappa_1 = GJ^*$ as mentioned previously. Clearly, $G(\hat{\phi}, \eta)$ vanishes if $\hat{\phi}$ is an equilibrium configuration.

We note that the deformation gradient $\mathbf{F}$ is completely defined in Eq. (2.19), and the directional derivative, $D\mathbf{F} \cdot \Delta\phi$ in Eq. (2.34), is as follows:

$$D\mathbf{F} \cdot \Delta\phi = \Delta\phi_0' \otimes \hat{\mathbf{E}}_1 + (\Lambda'\Delta a_i + a_i\Delta\Lambda')\hat{\mathbf{E}}_i \otimes \hat{\mathbf{E}}_1 + (\Lambda\Delta a_{i,J} + a_{i,J}\Delta\Lambda)\hat{\mathbf{E}}_i \otimes \hat{\mathbf{E}}_J \tag{2.37}$$

where $\Delta\phi_0' = [\Delta u', \ \Delta v', \ \Delta w']'$. The increment in the orthogonal transformation and its first derivative can be computed as $\Delta\Lambda = \Lambda_{,k}\Delta\theta_k$, and $\Delta\Lambda' = \Lambda_{,kl}\theta_k'\Delta\theta_l + \Lambda_{,k}\Delta\theta_k'$. The increment in the coefficients a (with components a_i) take the form:

$$\Delta a = \left[\psi g(\gamma)\Delta\beta_i + (X_3 h'(\gamma) + \psi\beta g'(\gamma))\Delta\gamma \ , \ \ 0 \ , \ \ \psi h(\gamma)\Delta\beta_i + (X_3 g'(\gamma) - \psi\beta h'(\gamma))\Delta\gamma \right]^t \tag{2.38}$$

and their derivatives ∇a (with components $a_{i,J}$) are given by

$$\Delta(\nabla a) = \begin{bmatrix} X_3\Delta h' + \psi_{,1}\{(\beta_i'\Delta g + \beta_i\Delta g') + (g'\Delta\beta_i + g\Delta\beta_i')\} & \psi_{,2}(\beta_i\Delta g + g\Delta\beta_i) & \Delta h + \psi_{,3}(\beta_i\Delta g + g\Delta\beta_i) \\ 0 & 0 & 0 \\ X_3\Delta g' - \psi_{,1}\{(\beta_i'\Delta h + \beta_i\Delta h') + (h'\Delta\beta_i + h\Delta\beta_i')\} & -\psi_{,2}(\beta_i\Delta h + h\Delta\beta_i) & \Delta g - \psi_{,3}(\beta_i\Delta h + h\Delta\beta_i) \end{bmatrix}^t \tag{2.39}$$

where the increment of functions $g(\gamma)$ and $h(\gamma)$ are defined as follows:

$$\Delta g(\gamma) = -h'(\gamma)\Delta\gamma \ , \qquad \Delta g(\gamma) = g'(\gamma)\Delta\gamma \tag{2.40}$$

and their first derivatives are given by

$$\Delta g'(\gamma) = -\begin{Bmatrix} \cos\gamma \\ 0 \\ \cos\gamma \end{Bmatrix}\gamma'\Delta\gamma - \begin{Bmatrix} \sin\gamma \\ 0 \\ \sin\gamma \end{Bmatrix}\Delta\gamma \ , \quad \Delta h'(\gamma) = \begin{Bmatrix} \sin\gamma \\ 0 \\ \sin\gamma \end{Bmatrix}\gamma'\Delta\gamma - \begin{Bmatrix} -\cos\gamma \\ 0 \\ \cos\gamma \end{Bmatrix}\Delta\gamma \tag{2.41}$$

The directional derivative $D\mathbf{F} \cdot \eta$, in Eq. (2.34), is the same as $D\mathbf{F} \cdot \Delta\phi$ except for the difference in directions $\Delta\phi$ and η.

2.2.2 Finite element discretization

Equation (2.34) has a form that is suitable for treatment by the finite element method. To carry out the solution, a knowledge of the current state of stress $\mathbf{S}_i$ and the material tangent $[\partial\mathbf{S}/\partial\mathbf{E}]_i$ is required. These tangent moduli can be obtained from the constitutive equations, which are discussed in the following chapter. We will obtain the solution from the equilibrium equations developed above by utilizing the finite element method. The beam is discretized into elements having 10 degrees of freedom at each of the 3 nodes of the element, one for each of the generalized variables.

Following standard procedures the generalized displacements $\mathbf{u}(S)=[u, v, w, \theta_1, \theta_2, \theta_3, \beta_1, \beta_2, \beta_3, \gamma]'$ are interpolated from the nodal displacements $\mathbf{U}=[\mathrm{U}, \mathrm{V}, \mathrm{W}, \Theta_1, \Theta_2, \Theta_3, \mathrm{B}_1, \mathrm{B}_2, \mathrm{B}_3, \Gamma]$, as

$$\mathbf{u}(S) = \sum_{i=1}^{N} h_i(S)\mathbf{U}_i \tag{2.42}$$

where $h_i(S)$ are the interpolation functions, $\mathbf{U}_i$ is the vector of nodal displacements at node i, and N is the number of nodes associated with each element. Inasmuch as the admissible variations lie in the space $H^1(0, L)$, C^0 continuity of interpolation is sufficient (see, for example, Strang and Fix, 1973). One should be aware, however, that the character of the solution for the warping intensities β_1, β_2, β_3, and γ is one of exponential decay, leading to boundary layer phenomena (*i.e.* rapid variations of the field variables over small distances) at points of restraint and point loadings. The ramifications of using C^0 shape functions for the warping intensities was considered by Hjelmstad (1987).

After introducing the interpolation of the nodal parameters, the expressions for the directional derivatives at each node can be put into matrix form as a linear transformation of the increments (or variations) as

$$D\mathbf{F} \cdot \Delta\phi = \mathbf{B}(\mathbf{X}, \mathbf{u}(S))\Delta\mathbf{U}, \qquad D\mathbf{F} \cdot \eta = \mathbf{B}(\mathbf{X}, \mathbf{u}(S))\eta \tag{2.43}$$

where, the rows of $\mathbf{B}(\mathbf{X},\mathbf{u}(S))$ are placed in one-to-one correspondence with the components of $D\mathbf{F} \cdot \Delta\phi$. The actual expression for the matrix $\mathbf{B}$ is extremely complicated, and hence will not be presented here. It is, however, straightforward to compute from the definitions given previously.

Using the above results we are lead to the standard discrete problem for the incremental nodal displacements $\Delta\mathbf{U}$.

$$\mathbf{K}_t\Delta\mathbf{U} = \mathbf{f}_t \tag{2.44}$$

where the tangent stiffness matrix is given by sum over all of the elements e as

$$\mathbf{K}_t = \sum_{e} \int_0^{L_e} \int_A \mathbf{B}^t \, [\mathbf{S} \otimes 1 + \mathbf{F}^t\mathbf{D}^{ep}\mathbf{F}]_\phi \, \mathbf{B} \, dA \, dS + \mathbf{K}_{sv} \tag{2.45}$$

where $\mathbf{K}_{sv}$ is the stiffness contribution from the St. Venant part of the weak form. The out-of-balance force has the expression

$$\mathbf{f}_t = \mathbf{F}_t - \sum_{e} \int_0^{L_e} \int_A \mathbf{B}^t : \mathbf{P}_\phi \, dA \, dS - \mathbf{f}_{sv} \tag{2.46}$$

in which $\mathbf{F}_t$ is the vector of currently applied nodal forces, dA is the element of integration over the cross-section, L_e is the length of element e, and the arguments of the summation are understood to be those quantities appropriate to that element. Again, $\mathbf{f}_{sv}$ is the residual force arising from the St. Venant term. The summation over the elements is taken to infer standard assembly procedures.

Since the stress $\mathbf{S}_\phi$ and the compliance $[\mathbf{D}^{ep}]_\phi$ generally vary nonlinearly over the cross-section due to inelasticity, the $X_2 - X_3$ dependence must be integrated over the cross-section A numerically. For the I-beam, the cross-sectional domain is subdivided into five regions: four half flanges and one web. Within

each region, Gaussian quadrature is employed and the total integral is taken to be the sum of the integrals over the five subregions. Reduced integration is used in the S direction to prevent shear locking effects (Hughes, 1987). The solution procedure is employed using the algorithm outlined in Table 2.1.

Table 2.1 Global solution algorithm

```
Initialize solution at t = t0
For each load step do
    While  |ft| > tol
        Form Kt , ft as follows:
            For each element e ;
                Compute deformation gradient F strains E
                Compute stresses by return mapping (Table 3.1)
                Compute element tangent stiffness matrix and residual force
                Assemble element matrices into global matrices
        Solve    Kt ΔU = ft
        Update   U ← U + ΔU
    Increment load step  t ← t + Δt
```

Chapter 3

A New Model for Cyclic Metal Plasticity

It is generally agreed that the inelastic behavior of mild steel can be approximately modeled with the classical plasticity theory with an associated flow rule. Finite element analyses of complex inelastic systems are often done with extremely simple constitutive models because they simplify the development of algorithms and they expedite computations. In a monotonic loading environment, material strain hardening effects are generally modeled with a simple isotropic hardening rule (expansion of the yield surface in stress space). In a cyclic loading and unloading environment, the anisotropic behavior of the material (*e.g.* Bauschinger's effect) is often modeled with a simple kinematic hardening rule (rigid translation of the yield surface in stress space).

It has been known for some time that these simple models do not represent real plastic behavior well, especially in the transient softening stage from the initial elastic unloading stage to the permanent softening stage for reversed loading. The first attempt to overcome the inadequacies of the simple hardening models goes back to Duwez (1935) who proposed the *mechanical sublayer model* wherein the (one dimensional) material is idealized as a series of friction elements with different friction coefficients and slip values. The basic idea of Duwez was subsequently extended by Bessieling (1953) and Iwan (1967). Mroz (1967) generalized the sublayer model to multiaxial states of stress by introducing a multi-surface model with fields of work-hardening moduli. Mroz's multi-surface model was simplified to a two surface theory by Krieg (1975) and independently by Dafalias (1975) and Dafalias and Popov (1975, 1976). The main idea behind the two surface models is that the elastoplastic modulus is determined from the distance of the stress point from the yield and bounding surfaces. A more refined approach to the bounding surface model was proposed by Petersson and Popov (1977) and Popov and Petersson (1978), wherein auxiliary surfaces between the yield and bound surfaces are used to interpolate a more realistic variation of the hardening moduli. Rees (1981, 1982, 1983) extended the idea of a kinematic hardening rule by expressing it in terms of a field of uniform hardening potentials. More recently, Rees (1984, 1987) has proposed the idea of using a multi-surface, equi-strain potential for the hardening.

While the more recent cyclic plasticity models represent real material behavior quite well, they are not well suited for large-scale computation. There is need for a computationally efficient model which possesses the advantages of these existing models. Such a model is developed in this chapter. The solution of the nonlinear constitutive equations will employ the consistent return mapping algorithm of Simo and Taylor (1985) in conjunction with a new kinematic hardening law which is generated from an isotropic hardening field at each stage of the cyclic loading. A monotonic tension or torsion test is all that is required to set the parameters of the model.

The chapter starts by laying the general foundation for the plasticity model. The details of some of the models mentioned above are reviewed and useful concepts are collected. The new cyclic plasticity model is then described along with the details of its implementation. Finally, the qualitative performance of the model is assessed by using it to simulate response for non-proportional loading histories which have been examined experimentally and are published in the literature.

3.1 Basic Framework for the Constitutive Equations

The equations of classical plasticity provide the basic framework for the development of the cyclic plasticity model used here. Assuming that the strains will generally be small, but that the motions will be finite, we cast the constitutive equations in terms of the second Piola–Kirchhoff stress tensor and its conjugate Lagrangian strain tensor. We adopt the fundamental hypothesis that the strains are made up of an elastic part and an inelastic part as follows:

$$\mathbf{E} = \tfrac{1}{2}(\mathbf{F}\mathbf{F} - \mathbf{1}) = \mathbf{E}^e + \mathbf{E}^p \tag{3.1}$$

where $\mathbf{F}$ is the deformation gradient. The stresses, $\mathbf{S}$, are given in terms of the elastic part of the strain and the initial elastic moduli, $\mathbf{D}$, as

$$\mathbf{S} = \mathbf{D}\mathbf{E}^e = \mathbf{D}(\mathbf{E} - \mathbf{E}^p). \tag{3.2}$$

The evolution of the inelastic strains can be expressed in terms of a plastic potential, for which purpose we adopt one of the von Mises variety:

$$\phi(\xi, \bar{\varepsilon}^p) = \tfrac{1}{2}\xi : \xi - \tfrac{1}{3}\kappa^2(\bar{\varepsilon}^p) \tag{3.3}$$

where $\xi = \mathbf{s} - a'$ is the effective stress, that is, the difference between the stress deviator $\mathbf{s} = \mathbf{S} - \frac{1}{3}tr(\mathbf{S})\mathbf{1}$ and the deviator a' of the backstress a. A yield surface can be described by the condition $\phi = 0$. Points inside the yield surface, $\phi < 0$, are elastic and points outside the yield surface are inadmissible. The radius of the yield surface is given by the function $\bar{\varepsilon}^p \rightarrow \kappa(\bar{\varepsilon}^p)$, which defines an isotropic hardening law in terms of the *equivalent plastic strain*:

$$\bar{\varepsilon}^p = \int_0^t [\tfrac{2}{3}\dot{\mathbf{E}}^p : \dot{\mathbf{E}}^p]^{1/2} dt \tag{3.4}$$

where $\dot{\mathbf{E}}^p$ is the plastic strain rate. With these definitions, the plastic strain can be expressed as an equation of evolution as

$$\dot{\mathbf{E}}^p = \lambda \frac{\partial \phi}{\partial \xi} \tag{3.5}$$

where λ is a plastic Lagrange multiplier which can be determined from the consistency condition. The elastoplastic loading/unloading (consistency) conditions can be expressed in standard Kuhn–Tucker form as

$$\phi \leq 0, \qquad \lambda \geq 0, \qquad \lambda\phi = 0. \tag{3.6}$$

Taking the rate form of Eq. (3.2), substituting the evolution equation for plastic strains, Eq. (3.5), and enforcing the consistency condition leads to the following rate equations for the evolution of stress

$$\dot{\mathbf{S}} = \Omega(\mathbf{S}, \mathbf{E}^p, a)\dot{\mathbf{E}} \tag{3.7}$$

where Ω is the fourth order elastoplastic tangent tensor, depending on the current state of stress, the plastic strain, and the backstress. The evolution equation for the backstress will be defined differently from the classical plasticity for the present cyclic plasticity model and will be described in section 3.4. The integration of the rate constitutive equations plays a central role in the numerical analysis of the beam model and will be discussed later.

3.2 Modeling of Isotropic Hardening

A model of nonlinear hardening law with a linear part and an exponential (saturation) part is adopted to describe the isotropic hardening in Eq. (3.3) as follows (Simo and Taylor, 1985).

$$\kappa(\bar{\varepsilon}^p) = \kappa_0 + K\bar{\varepsilon} + (\kappa_\infty - \kappa_0)[1 - e^{-\gamma\bar{\varepsilon}}] \equiv \kappa_0 + A(\bar{\varepsilon}^p) \tag{3.8}$$

where κ_0 is the initial radius of the yield surface, κ_∞ is the ultimate radius of the yield surface, K is the rate of linear hardening, and γ is the initial rate of exponential hardening. The parameter $\bar{\varepsilon}$ is a shifted equivalent plastic strain, allowing the modeling of a yield plateau, given by the expression

$$\bar{\varepsilon} = \begin{cases} 0 & 0 \le \bar{\varepsilon}^p \le \bar{\varepsilon}_{sh} \\ \bar{\varepsilon}^p - \bar{\varepsilon}_{sh} & \bar{\varepsilon}_{sh} \le \bar{\varepsilon}^p \end{cases} \tag{3.9}$$

where $\bar{\varepsilon}_{sh}$ is the length of the plastic plateau. The nonlinear isotropic hardening law is shown schematically for K=0 (no linear hardening) in Fig. 3.1

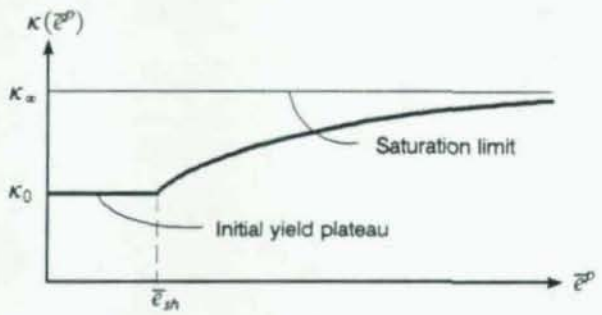

Fig. 3.1 Nonlinear isotropic strain hardening model

Popov and Petersson (1978) performed uniaxial experiments and torsion tests, and compared both results by plotting the effective stress and effective strain for both cases on the same graph. The agreement between the two curves was satisfactory in both the monotonic and cyclic cases. The use of effective stress and strain allows the hypothesis of a universal stress–strain curve applicable to any state of stress. One can use the stress–strain curve obtained from a monotonic tensile test on the virgin material to construct the universal curve. A field of loading surfaces can be constructed from the stress–plastic strain curve, taking the radii of the loading surfaces from the ordinates of the universal curve as shown in Fig. 3.2. Each surface in the stress space is assigned a particular value of equivalent plastic strain, as determined from the universal curve. The radii of the loading surfaces are computed as

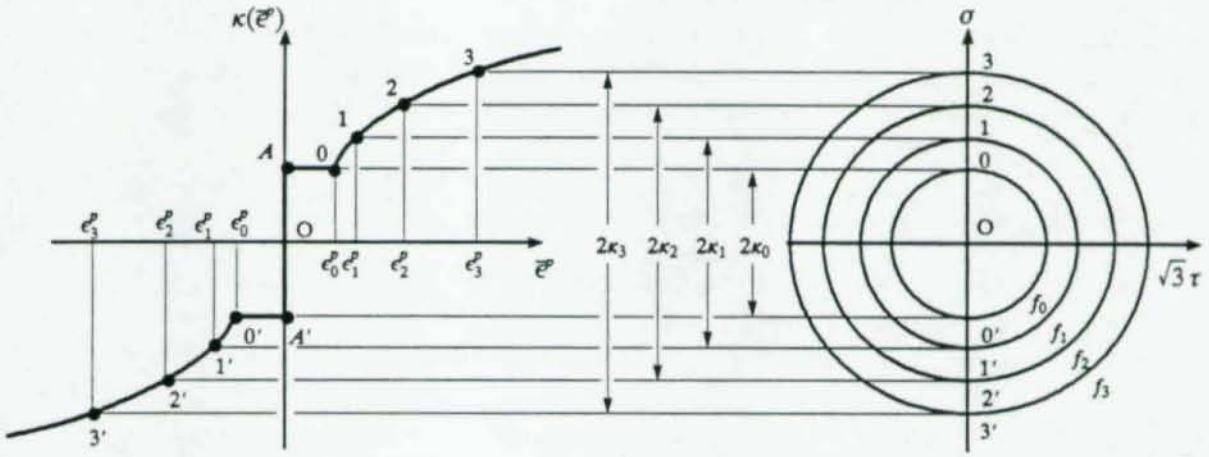

Fig. 3.2 Multi-strain potential representation for virgin state

$$f_q = \kappa(\bar{\epsilon}^p_q). \tag{3.10}$$

Figure 3.3 illustrates the concept of equivalence between corresponding stress-plastic strain paths and a uniaxial κ vs. $\bar{\epsilon}^p$ curve in a initial multi-strain potential field under a radial stress path OP in σ vs. $\sqrt{3}\tau$ space. It is convenient to obtain the uniaxial $\kappa - \bar{\epsilon}^p$ curve directly from a monotonic tension experi-

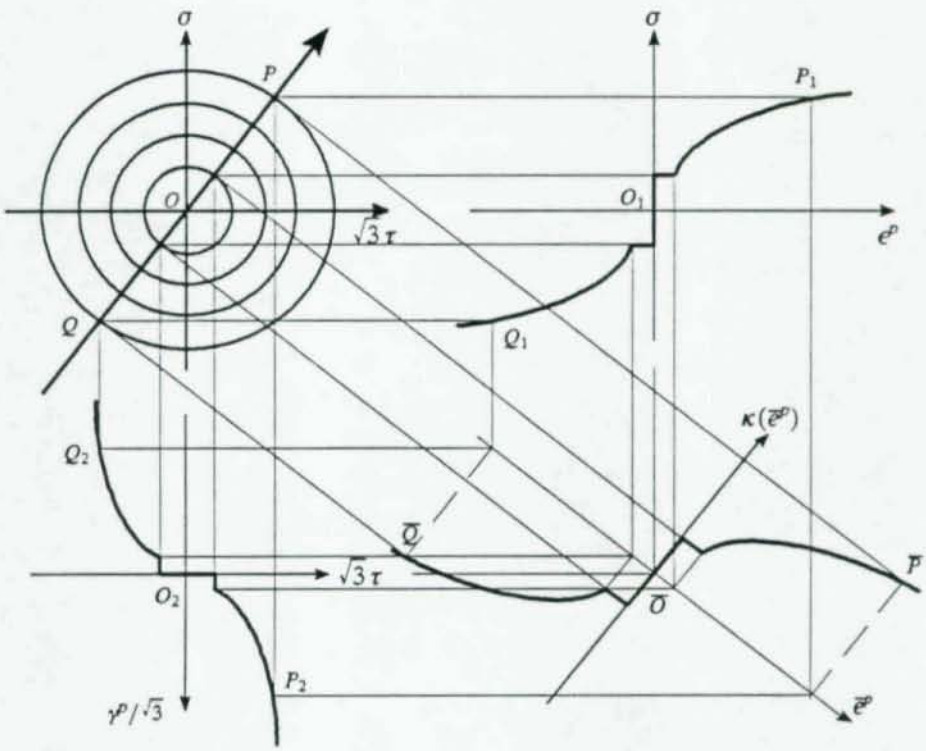

Fig. 3.3 Initial multi-strain potential field under a radial stress path OP in σ vs. $\sqrt{3}\tau$ space

ment because the normal stress and the extensional strain are identical to the effective stress and strain for the uniaxial case.

The next step is to define a rule to describe the inelastic state for the cyclic loading condition. In the monotonic loading condition, nonlinear isotropic hardening rules can be employed, while a more intricate hardening rule is needed to represent cyclic response.

3.3 Review of Kinematic Hardening Models for Cyclic Plasticity

Due to the complexity of nonlinear material behavior, many idealized models have been proposed. A combined isotropic–kinematic plasticity model, illustrated in Fig. 3.4, has often been adopted for applications in computational plasticity. The discrepancy between this simple model and experiments, however, is particularly pronounced on load reversal because real materials exhibit a phenomenon known as Bauschinger's effect. The simple kinematic hardening model also does not provide a smooth transition from the elastic to the fully plastic state, a phenomenon which is observed experimentally for most materials.

Many efforts have been made to improve the representation of cyclic material behavior. An early attempt may be traced to the sublayer model of Duwez (1935), with extensions by Bessieling (1953) and Iwan (1967). In this model, the material behavior is represented by some layers in parallel, each layer having a different yield strength. The model can replicate the transition softening stage between the elastic stage and virgin strain hardening stage for reversed loading much better than a kinematic hardening model can. This model has been generalized for multiaxial stress states by Mroz (1967), who introduced the concept of a field of work-hardening moduli which was defined by the configurations of surfaces with constant plastic tangent moduli. The surfaces in Mroz's model correspond to the sublayers in the uniaxial case. During plastic flow, the yield surface translates, contacts, and pushes the adjacent loading surfaces. The plastic modulus at any instant during plastic flow is the value associated with the outermost moving surface. On load reversal, the surfaces sequentially disengage, as shown in Fig. 3.5.

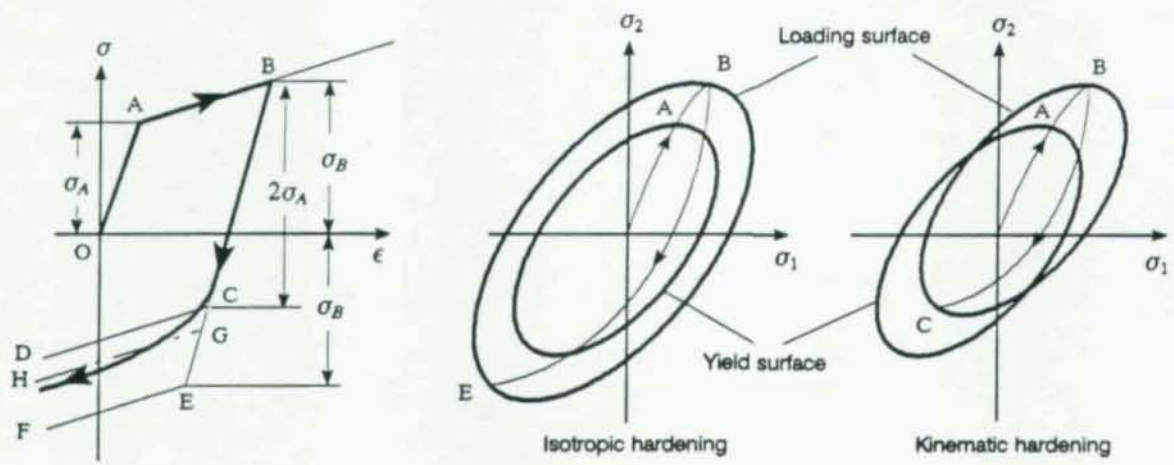

Fig. 3.4 Idealization of material behavior on load reversal

For nonproportional loading, the surfaces move by some prescribed rule such that the individual surfaces do not intersect but continuously contact and push each other. Although this model provides better representation of cyclic behavior than does the classical kinematic hardening model, many surfaces must be used to obtain the smooth behavior observed experimentally. This model has another difficulty associated with a proper choice for the parameters involved, especially for multiaxial response. These shortcomings notwithstanding, this model is the best known of the multi-surface representations of inelastic deformation.

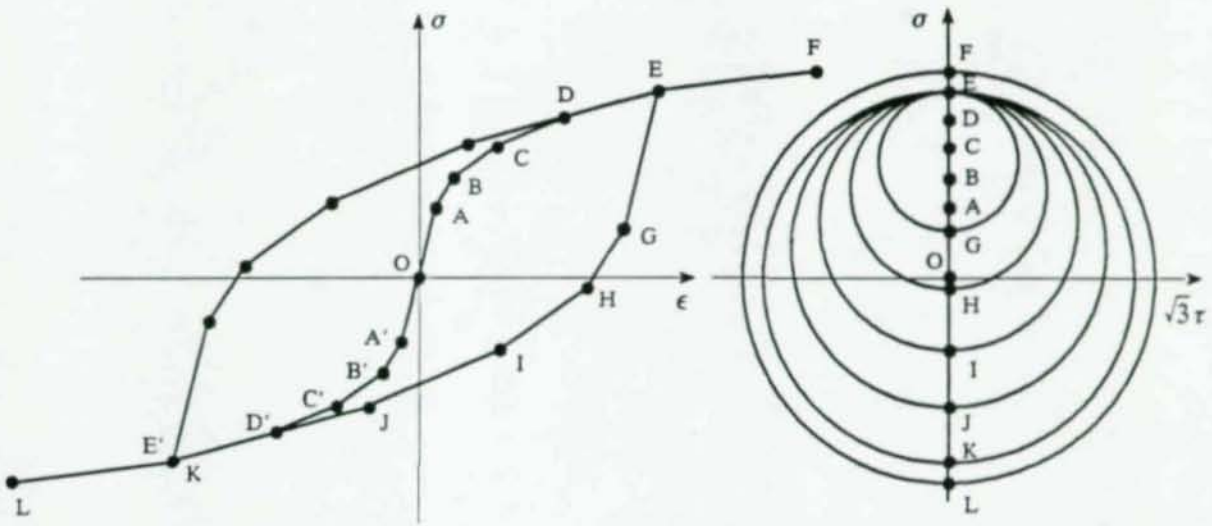

Fig. 3.5 Approximation of the stress-strain curve and the corresponding fields of work-hardening moduli for uniaxial cyclic loading (Mroz, 1967)

A modification of Mroz's fields of work-hardening model was proposed by Krieg (1975). This modified model, called the two-surface plasticity model, replaces all but two of the discrete surfaces of Mroz's model by a continuum of intermediate loading surfaces whose distribution is prescribed. The two surfaces are represented by an inner surface, called the loading surface, and an outer surface, termed the limit surface. Both the loading and limit surfaces can vary according to a combined isotropic and kinematic hardening behavior. The motion of the loading surface is identical to that of Mroz's model. This theory requires a memory of three vectors and three scalars, a small increase over the two vectors required for kinematic hardening alone. Independently, a more comprehensive and satisfying generalization of the concept of a two surface plasticity theory was proposed by Dafalias and Popov (1975). In this theory the concept of a bounding surface is introduced. This model also provides a smooth hardening model and relatively good computational efficiency, which was demonstrated from the almost exact prediction of the experimental data of cyclic uniaxial stress-strain curve. The yield region is constrained to move always within bounds, as shown in Fig. 3.6, where the bounding region is referred to as the bounding surface in the multiaxial case. The material behavior can be described by considering the plastic modulus E^p to be a function of two plastic internal variables, δ and δ_{in}, where δ is the distance from the active point on the loading surface to the bounding surface, and δ_{in} is the initial distance at the most recent initiation of yield and provides a memory of the most recent loading history associated with the previous

excursion in reverse plastic loading. The expression for the plastic modulus E^p suggested by Dafalias and Popov (1975, 1976) is

$$E^p = E_0^p + \frac{\delta}{\delta_{in} - \delta} h(\delta_{in}) \tag{3.11}$$

where E_0^p is the bounding value of plastic modulus, and $h(\delta_{in})$ is a shape parameter determined from experimental data. By projecting on the σ –axis and then generalizing in multiaxial stress space, the end points such as a' and b' become the yield surface, and the end points $\bar{a}$ and $\bar{b}$, the bounding surface, as shown Fig. 3.6. During the course of plastic deformation, the two surfaces translate simultaneously in the stress space, and in general, may also deform. During plastic deformation, the continually changing distance δ in stress space, between the stress state b' on the yield surface and the corresponding point $\bar{b}$ on the bounding surface, determines the value of the generalized plastic modulus in a manner analogous to the uniaxial case.

At the numerical implementation level, the above bounding surface model may give rise to an inaccurate results in some cases. Petersson and Popov (1977) took the uniaxial cyclic loading pattern shown in Fig. 3.7 to demonstrate the problem. If the load is reversed before any plastic flow occurs, the updating of the parameter δ_{in} will be done incorrectly. A number of these events in a cyclic loading history can significantly bias the plastic moduli. Petersson and Popov (1977) and Popov and Petersson (1978) generalized the Dafalias–Popov model by introducing intermediate surfaces between the yield and bound surfaces based on the experimental data. The intermediate surfaces were used for purposes of interpolation, and in principle are not related at all to those of the Mroz model. There is no basic change from the Dafalias–Popov model except for the introduction of the intermediate surfaces.

The initial stress–plastic strain curve can be defined with the aid of projections onto the stress axis using a pair of inclined bounding lines together with specified plastic strain increments, as shown in Fig. 3.8*(a)*. The plastic strain increments, ϵ_1^p, ϵ_2^p, ϵ_3^p, are chosen for equal stress increments, and the segment

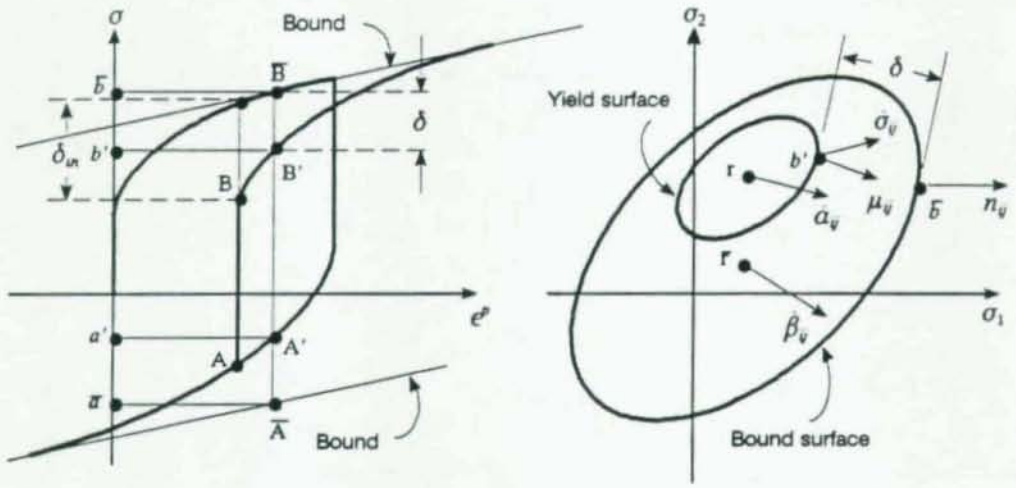

Fig. 3.6 The bounding surface model in uniaxial and multiaxial stress space (Dafalias and Popov, 1975)

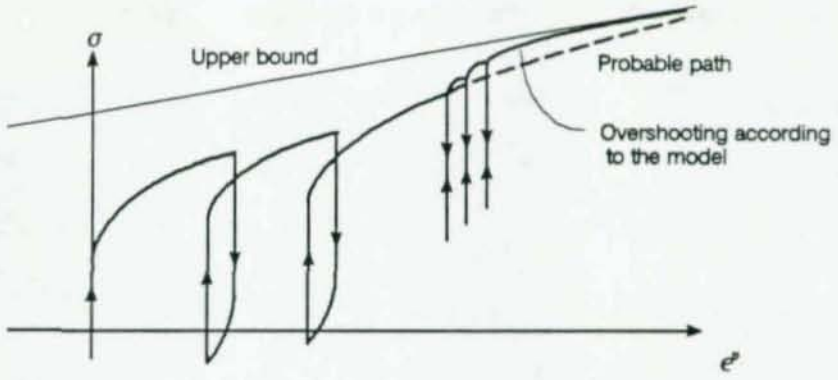

Fig. 3.7 Deficiency of the two-parameter model (Petersson and Popov, 1977)

AA' on the stress-axis defines the elastic range. For the multiaxial case, the hardening model is defined by the yield, bounding, and intermediate surfaces. First load reversal is illustrated in Fig. 3.8*(b)*. During a load reversal, a new stress-plastic strain path is generated by the points between the inclined lines and the decreased plastic strain increments. The inclined lines are parallel to the lower bounding line, and start from the stress points projected onto the stress-axis an equal distance in the opposite sense of plastic strain. A similar procedure is repeated during the subsequent load reversals, as shown in Fig. 3.8*(c)*, which brings in the history dependence of the cyclic process at each load reversal.

Instead of using this procedure for describing the loading surfaces and their translations at any stage of cyclic loading, Petersson and Popov (1977, 1978) made use of two different stress-strain curves obtained from uniaxial experiments. The first of these stress-strain curves is determined from a monotonic tensile test on the virgin material, and the other is half of a hysteretic loop with halved ordinates after several loading cycles. The monotonic hardening function κ_a, shown in Fig. 3.9*(a)*, is obtained from the virgin tensile stress-strain curve. The cycled hardening function κ_b, shown in Fig. 3.9*(b)*, can be systematically constructed as shown in Fig. 3.10. From the half hysteretic loop, an elastic region and the bounding lines can be easily determined. A generic point A on the curve at a horizontal distance $\Delta\epsilon^p$ from the origin is distance $2\kappa_i$ above the horizontal axis. Half the values of the quantities $2\bar{\kappa}$ and $2\kappa_i$ are used in the $\kappa_b - \bar{\epsilon}_i^p$ curve, and the vertical distances, 2κ, establish the bounding lines in the $\kappa_b - \bar{\epsilon}_i^p$ curve, as shown in Fig. 3.10*(b)*. By using the scalar weighting function W, shown in Fig. 3.9*(c)*, the surface size is approximated as

$$\kappa_i = W(\bar{\epsilon}^p)\kappa_a(\bar{\epsilon}_i^p) + [1 - W(\bar{\epsilon}^p)]\kappa_b(\bar{\epsilon}_i^p) \tag{3.12}$$

where W is a function of the total accumulated equivalent plastic strain $\bar{\epsilon}^p$ at the current time, whereas κ_a and κ_b are functions of an incremental equivalent plastic strain $\bar{\epsilon}_i^p$, accumulated since the last load reversal. The back stress of a loading surface is also assumed to be a function of $\bar{\epsilon}_i^p$, and each surface is associated with an unique value of $\bar{\epsilon}_i^p$. The weighting function can be fit to experimental data by a trial-and-error procedure. Once the sizes of loading surfaces are determined by the above procedure, their motions are updated during plastic flow. A restriction is also imposed to avoid intersections of the surfaces with each other. A numerical procedure is employed in updating the partial derivatives of κ_i and a_i with respect to the equivalent plastic strain $\bar{\epsilon}^p$ and its increment $\bar{\epsilon}_i^p$. Comparisons of theoretical predic-

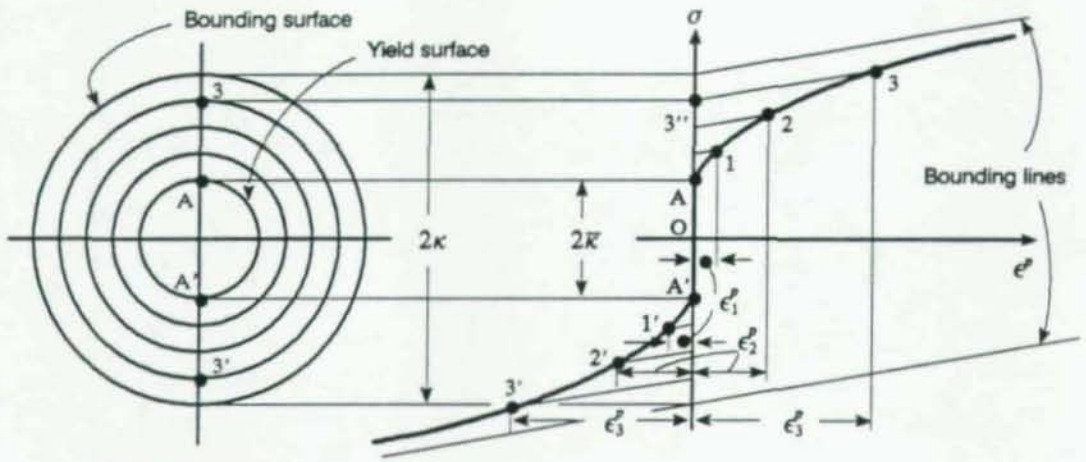

(a) Monotonic case

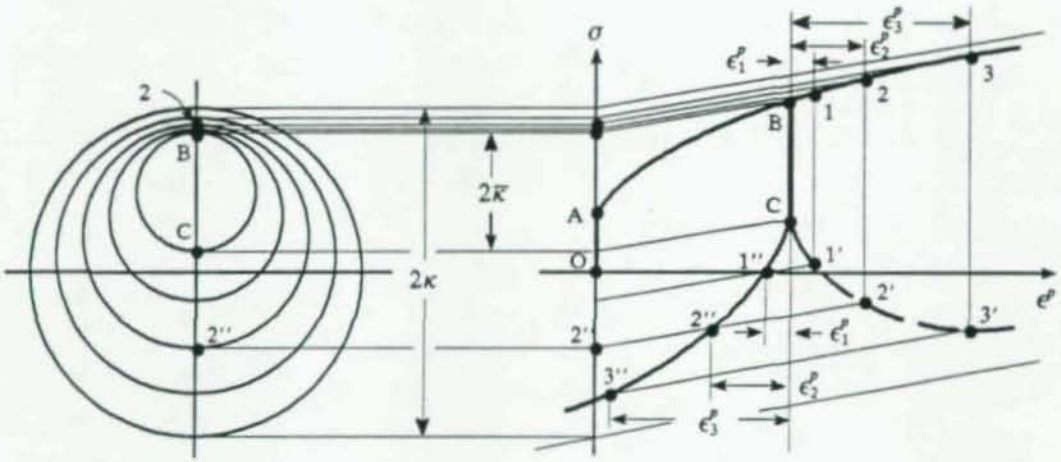

(b) First load reversal

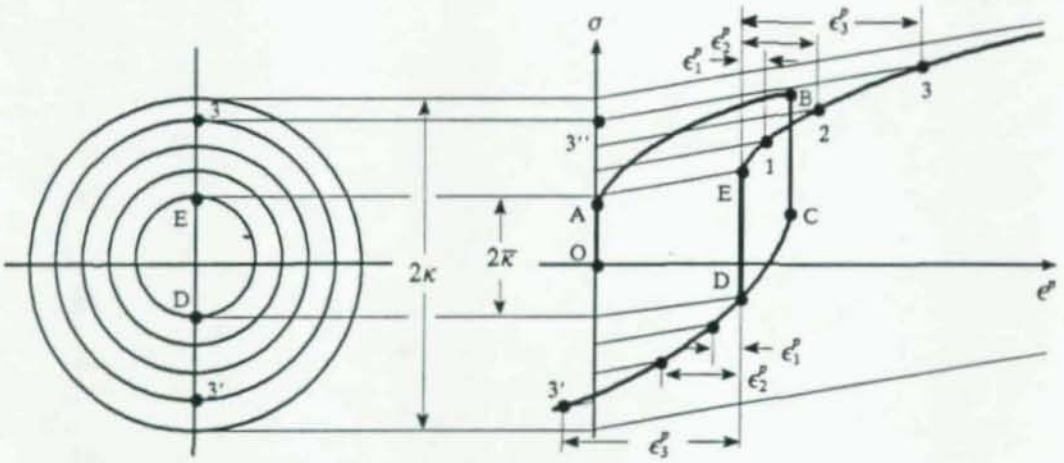

(c) First hysteresis curve

Fig. 3.8 Representation of constitutive relations (Petersson and Popov, 1978)

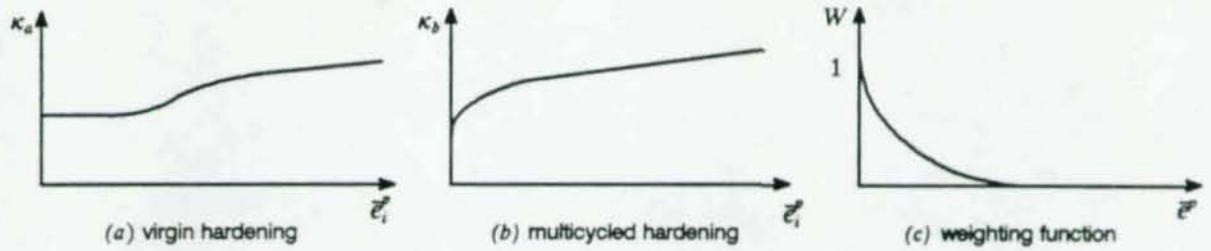

Fig. 3.9 Functions for defining surface sizes (Petersson and Popov, 1977 and 1978)

tions of hysteresis curves with the experimental ones were made for both the uniaxial tests, as well as for the torsional experimental experiments, and good agreement between the theory and experiments were found by Petersson and Popov (1977) and Popov and Petersson (1978).

Rees (1981, 1982, 1983) presented a combined hardening model for anisotropic materials in which the isotropic hardening potential remains tangential at the stress point to a yield surface which rigidly translates to the stress vector OP, as shown in Fig. 3.11. The field potentials, F_n, are identical to the anisotropic yield loci, f_n, only at initial yield ($f_0 = F_0$) when both enclose the elastic region. This model exhibits the Bauschinger effect and linear plastic strain paths under radially outward loading. Since both surfaces contact tangentially at points P_n, yield loci translate along the vector connecting O_n to P_n, which is identical to the modified Ziegler (1959) rule. Rees (1984, 1987) attributed the unrealistic prediction of the mechanical hysteresis and cyclic creep behavior to the undefined extent of anisotropy of a combined hardening rule, and introduced a multi-surface model which is especially representive of cyclic behavior under full anisotropic hardening. Another drawback of a combined hardening model might be its characterization of a field of isotropic potentials under repeated loading-unloading conditions. Some modifications to this model will be presented in the next section.

Rees' multi-surface model starts from the concept of an equi-strain potential in which each surface in stress space is assigned a particular value of equivalent plastic strain $\bar{\varepsilon}^p$. The Bauschinger effect and stress-strain hysteresis under cyclic loading can be realistically represented by this model, as shown in the

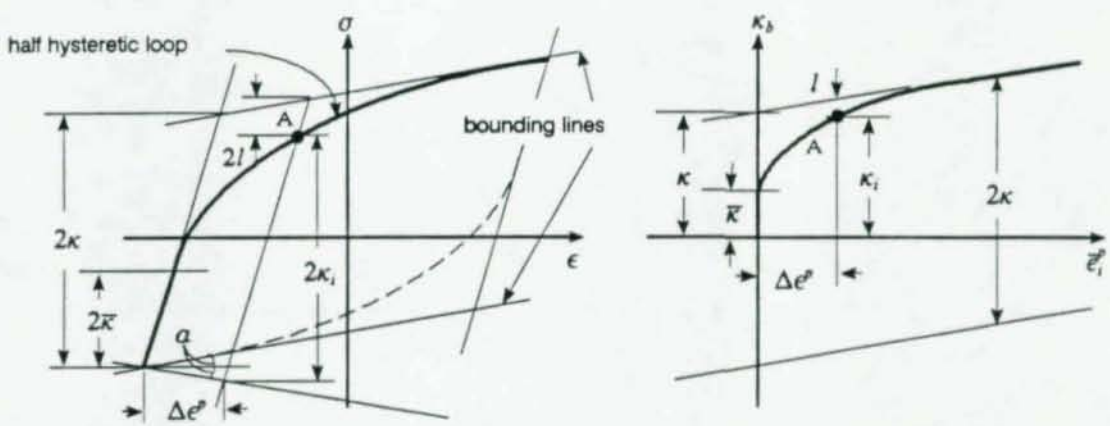

Fig. 3.10 Construction of multicycled hardening curve (Petersson and Popov, 1978)

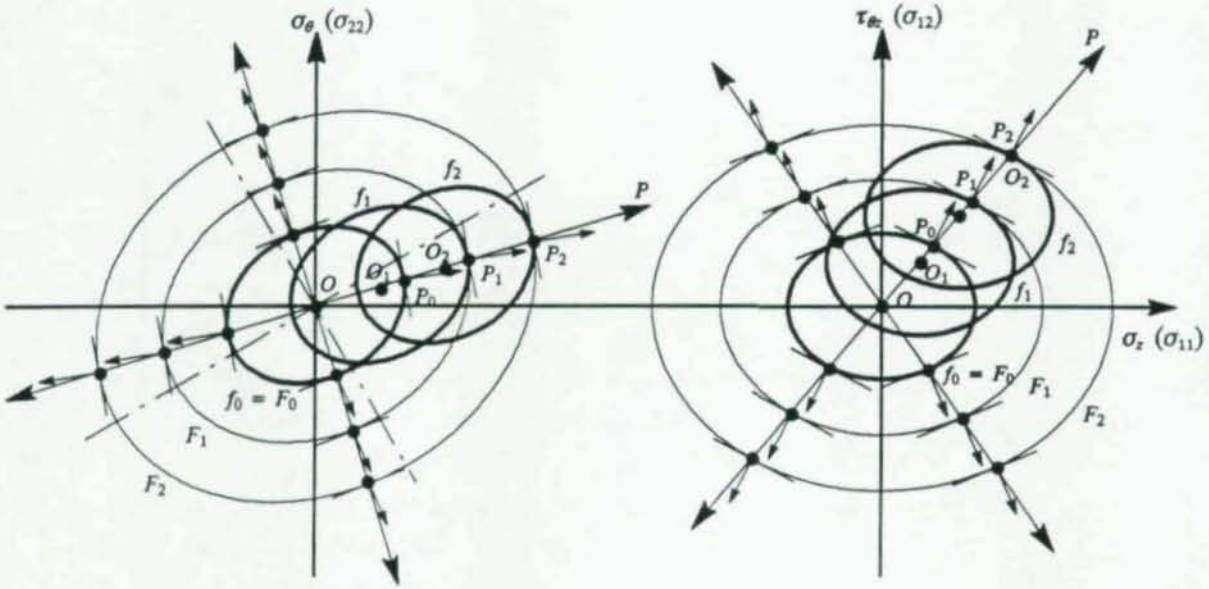

Fig. 3.11 Uniform-hardening plane-stress fields (F_n) showing anisotropic yield loci (f_n) for proportionate loading (Rees, 1981, 1982)

papers by Rees (1984, 1987). The unstrained state of the material is assumed to be isotropic, and the initial yield condition conforms to the von Mises yield criterion. The isotropic hardening rule, *i.e.* the representation of a multi-surface function, is the same as Eq. (3.6). The initial configuration of surfaces is continuously altered by translation during plastic deformation. The model can also be augmented to allow for contraction and rotation, as may be induced by anisotropic deformation. The contraction and translation function are scalar valued strain invariants which can be established from simple experimental tests in tension or torsion. Although the multi-surface model of Rees is powerful, it is difficult to implement in a computer code because the translations of all surfaces have to be traced at each loading step. The concept of this model will be used subsequently in the development of the new cyclic plasticity model.

3.4 Proposed Multiaxial Cyclic Plasticity Model

In the previous section, several cyclic plasticity models were reviewed. In this section a new multiaxial cyclic plasticity model is developed, taking advantage of the previous models. The concept of the universal stress-plastic strain curve and its determination from a uniaxial test are taken from the work of Petersson and Popov. We modify the procedure making it necessary only to have a uniaxial tension test to determine the hardening functions. Rees' idea of a combined hardening model will be employed for tracing the translation of a yield surface. If load reversal takes place after any plastic flow has occurred in the opposite sense, the field of equi-strain potentials will be replaced by new hardening functions, and the most recent backstress of the yield surface will be taken as the origin of the new field of equi-strain potentials. In each instance, the field of isotropic hardening potentials is obtained from the monotonic nonlinear isotopic hardening curve, Eq. (3.4), using the concept of Rees' multi-surface model. These

concepts will be employed in conjunction with the consistent return mapping algorithm developed by Simo and Taylor (1985) to numerically treat the constitutive equations.

A cyclic hardening function can be systematically obtained from the monotonic isotropic hardening curve, using the concept of Rees' multi-surface model as follows. A concentric configuration of von Mises surfaces centered at the stress origin is assumed for the unstrained material, as shown in Fig. 3.2, in which equi-strain potentials were chosen in equal stress increments for the equivalent plastic strain. We assign an equivalent plastic strain value to the qth equi-strain potential, f_q. For convenience, the potentials f_q are chosen at equal equivalent plastic strain increments rather than the equal stress increments shown in Fig. 3.2.

The subsequent multi-surface configurations in Fig. 3.12(b) are in the prestressed and prestrained state $(\bar{\sigma}_0, \bar{\varepsilon}^p_0)$. There is, of course, no translation of the multi-surface configurations in the stress state on the initial yield plateau. The subsequent configurations, f_q, are assigned new equivalent plastic strains, $\Delta\bar{\varepsilon}^p$. The forward and reversed equivalent yield stress points, and respectively, for a surface f_q, will be obtained by marking off the corresponding strain $\Delta\bar{\varepsilon}^p$ on either side of $\bar{\varepsilon}^p_0$ as shown in Figs. 3.12(a). As the translation of f_q is rigid, it follows that

$$\bar{\sigma}_f^q - \bar{\sigma}_r^q = 2\kappa_q \ , \tag{3.13}$$

where κ_q is the radius of the surface f_q and can be computed as follows:

$$\kappa_q = \kappa_0 + A(\Delta\bar{\varepsilon}^p) \tag{3.14}$$

$$\bar{\sigma}_f^q = \kappa_0 + A(\bar{\varepsilon}^p_0 + \Delta\bar{\varepsilon}^p) \tag{3.15}$$

From Eqs. (3.13), (3.14) and (3.15), the reversed equivalent yield stress point, $\bar{\sigma}_r^q$, will be as follows:

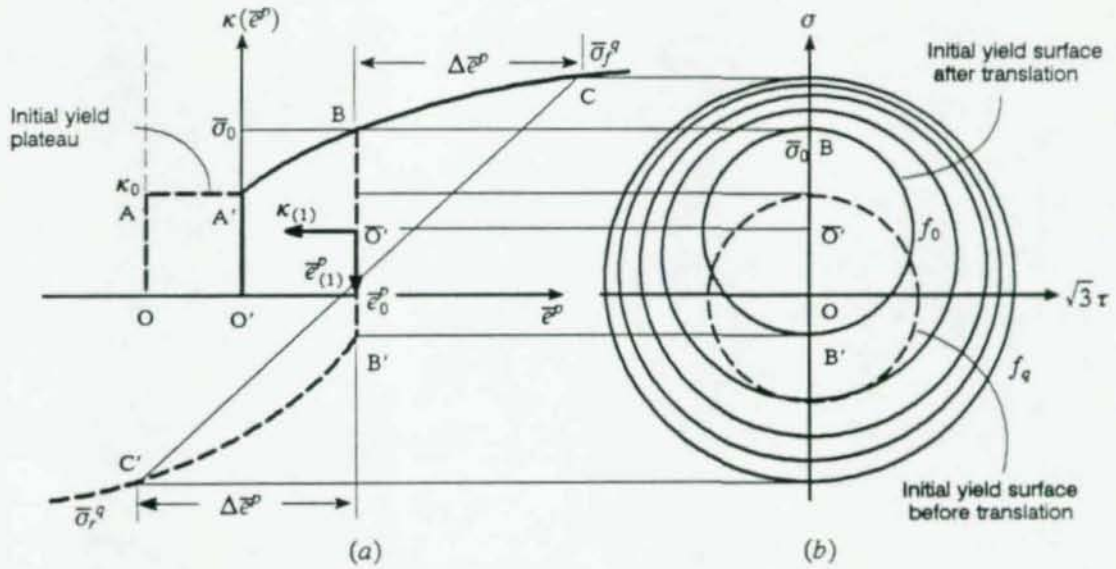

Fig. 3.12 Representation of initially prestrained material with the equi-strain model

$$\bar{\sigma}_r^q = -\kappa_0 + A(\bar{\varepsilon}_0^p + \Delta\bar{\varepsilon}^p) - 2A(\Delta\bar{\varepsilon}^p). \tag{3.16}$$

The predictions from Eq. (3.16) are consistent with Bauschinger's effect, as illustrated in Fig. 3.12(a). It can be seen that the curve of unloading, BB'C', is uniquely defined by the curve of primary loading, OAA'C . The segment BB' defines the elastic range in Fig. 3.12(a) which is the radius of the current yield surface in the two dimensional stress space, as shown in Fig. 3.12(b). The point $\bar{O}'$ is the center of the current yield surface. Choosing a new coordinate system $(\kappa_{(1)}, \bar{\varepsilon}^p_{(1)})$ with the origin at $\bar{O}'$, a new hardening curve, $\bar{O}'$B'C', can be found, which can be represented by the vertical distance between the center of the current initial yield surface, $\bar{O}'$, and the reversed equivalent yield stress point, C'. For the qth surface f_q we have

$$\kappa_{(1)}(\Delta\bar{\varepsilon}^p) = \bar{\sigma}_f^q(0) - \kappa_0 - \bar{\sigma}_r^q(\Delta\bar{\varepsilon}^p) = \kappa_0 + 2A(\Delta\bar{\varepsilon}^p) + A(\bar{\varepsilon}^p{}_0) - A(\bar{\varepsilon}^p{}_0 + \Delta\bar{\varepsilon}^p). \tag{3.17}$$

where $\bar{\sigma}_f^q(0)$ in Eq. (3.17) represents the equivalent stress at the point B in Fig. 3.12(a). Since the equivalent plastic strain is always positive, that is, it does not decrease during the plastic deformation, the actual relationship between $\bar{\varepsilon}^p$ and $\bar{\varepsilon}^p_{(1)}$ leads to the following:

$$\bar{\varepsilon}^p_{(1)}(\Delta\bar{\varepsilon}^p) = \bar{\varepsilon}^p(\bar{\varepsilon}_0^p + \Delta\bar{\varepsilon}^p) \tag{3.18}$$

If the current reversed stress at point B were to continue beyond point B', as shown in Fig 3.12, a new field of isotropic hardening potentials would be created as shown in Fig. 3.13. The new field of equi-strain potentials is created according to Eq. (3.17), and the new center of this field is the final center of the yield surface from the previous cycle. Each cyclic loading stage is represented by the sequential number m, as shown in Fig. 3.13, where m=0 means the initial field of equi-strain potentials.

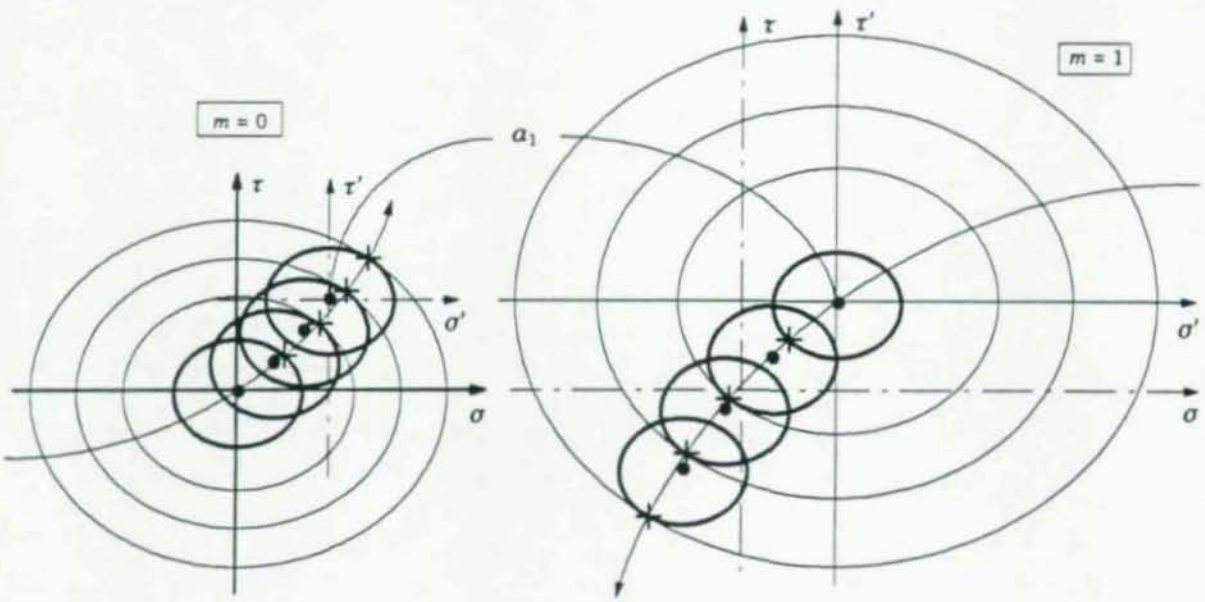

Fig. 3.13 Hardening plane stress fields

The center of the new field is referred to as the backstress, a, and is constant for each field of equi-strain potentials. Note that this definition of backstress is different from the one used with the traditional kinematic hardening model. If the stress path were to reverse again before reaching point B', the current field of isotropic hardening potentials would be retained; if the stress path passes point B', the field of isotropic hardening potentials is updated. The current stress point in or on the yield surface is constrained to lie in the updated yield surface, throughout the course of plastic deformation, according to the consistent return mapping algorithm of Simo and Taylor (1985). The updated stress point will be returned to the subsequent loading surface by a normal projection onto the yield surface which corresponds to the the mid-step time t_{n+a}, as shown in Fig. 3.16.

The motion of the yield surface in the proposed model is shown schematically in Fig. 3.14. Some restrictions are imposed to avoid the intersection of the yield surface with the loading surface: the yield surface may rotate to be tangential to the loading surface as they contact each other, however the shape and the size of the yield surface are assumed not to be changed during the course of plastic deformation. These surfaces are defined by the equations

$$f^k(S_n - \beta^{(k)}) = \kappa_0 , \qquad f^{k+1}(S_{n+1} - \beta^{(k+1)}) = \kappa_0 ,$$
$$F^k(S_n - a_{(m)}) = \kappa^{(k)}, \qquad F^{k+1}(S_{n+1} - a_{(m)}) = \kappa^{(k+1)}, \tag{3.19}$$

where κ_o is the size of the yield surfaces, f^k and f^{k+1}, and $\kappa^{(k)}$ and $\kappa^{(k+1)}$ are the radii of the loading surfaces F^k and F^{k+1}, respectively. Superscript $k+1$ represents the sequential number of the $(k+1)$th updated values of things such as the yield surface f^{k+1}, the loading surface F^{k+1}, the size of loading

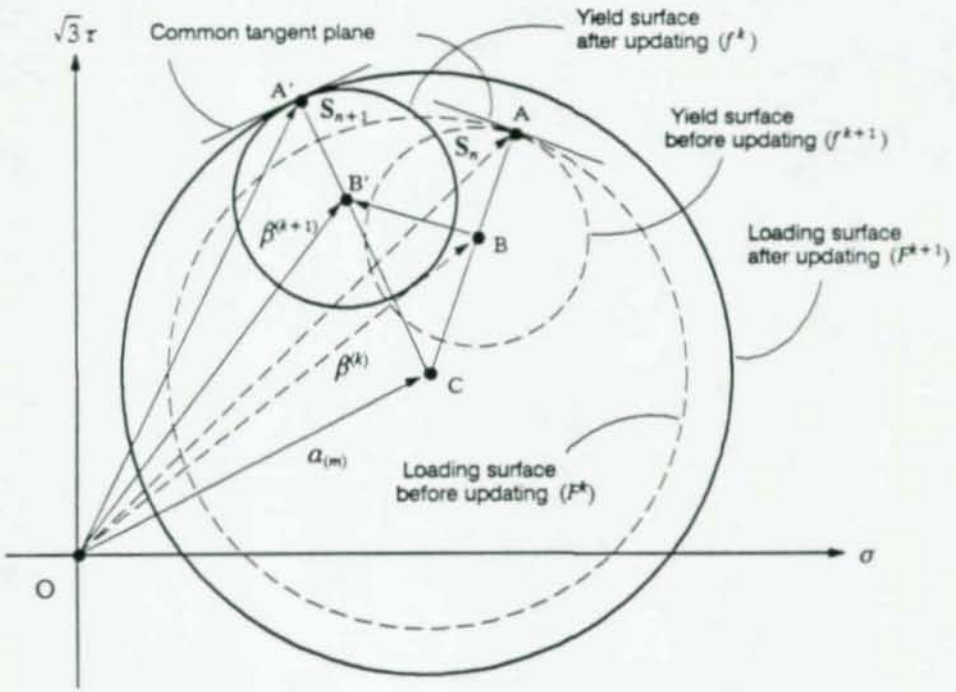

Fig. 3.14 Translation of yield surface to the subsequent loading surface

surface $\kappa^{(k+1)}$, and the center of the yield surface $\beta^{(k+1)}$. The backstress $a_{(m)}$ of the mth field of isotropic hardening potentials is constant during the mth cyclic loading stage. When the yield surface contacts to the loading surface at point A' from A, the center of the yield surface should move to the point B' along the straight line A'C from B. The relationship between the yield surface and the loading surface at the updated state is given by

$$\mathbf{S}_{n+1} - a_{(m)} = \frac{\kappa^{(k+1)}}{\kappa_0}(\mathbf{S}_{n+1} - \beta^{(k+1)}). \tag{3.20}$$

From this relation, the updated center of yield surface, $\beta^{(k+1)}$, can be computed as follows:

$$\beta^{(k+1)} = \mathbf{S}_{n+1} - (\mathbf{S}_{n+1} - a_{(m)})\frac{\kappa_0}{\kappa^{(k+1)}}. \tag{3.21}$$

The updated center of yield surface, $\beta^{(k+1)}$, will be the center of new field of equi-strain potentials, $a_{(m+1)}$, when the reversed stress continues to produce plastic deformation in the opposite sense.

The reversed yield points in the hysteretic loading condition are considered as illustrated in Fig. 3.15. Reloading occurs at the prestrain origin $\bar{\varepsilon}_1^p = \bar{\varepsilon}_0^p + \Delta\bar{\varepsilon}_0^p$, which was shifted from $\bar{\varepsilon}_0^p$, and the reversed yield points can be obtained from Eq. (3.16) by replacing $\Delta\bar{\varepsilon}^p$ by $\Delta\bar{\varepsilon}_0^p + \Delta\bar{\varepsilon}^p$ in the unloading state BB'C. The modified reversed equivalent yield stress point, C, in the unloading state, BB'C, in Fig. 3.15(*a*), is given by

$$\bar{\sigma}_r^q = -\kappa_0 + A(\bar{\varepsilon}_0^p + \Delta\bar{\varepsilon}_0^p + \Delta\bar{\varepsilon}^p) - 2A(\Delta\bar{\varepsilon}_0^p + \Delta\bar{\varepsilon}^p) = -\kappa_0 + A(\bar{\varepsilon}_1^p + \Delta\bar{\varepsilon}^p) - 2A(\Delta\bar{\varepsilon}_0^p + \Delta\bar{\varepsilon}^p). \tag{3.22}$$

Similarly, the forward equivalent yield stress point, C', in the reloading state, D$\overline{\text{O}}$'D'C', can be also obtained from Eqs. (3.13), (3.14) and (3.22)

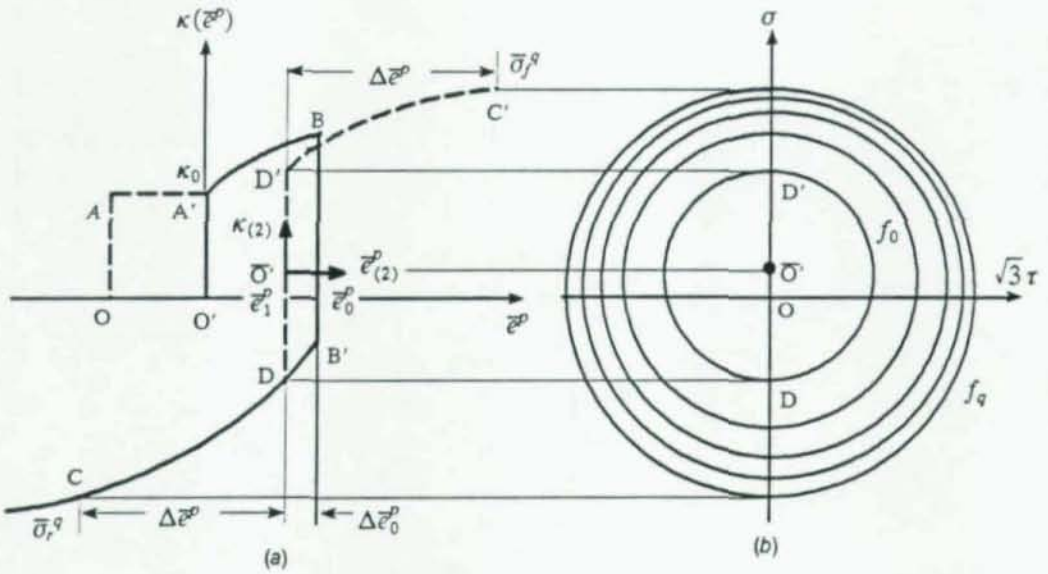

Fig. 3.15 Representation of equi-strain model for hysteresis

$$\bar{\sigma}_f^q = \kappa_0 + A(\bar{\varepsilon}_1^p + \Delta\bar{\varepsilon}^p) - 2A(\Delta\bar{\varepsilon}_0^p + \Delta\bar{\varepsilon}^p) + 2A(\Delta\bar{\varepsilon}^p). \tag{3.23}$$

Again, choosing a new coordinate system $(\kappa_{(2)}, \bar{\varepsilon}_{(2)}^p)$ with the origin at $\bar{O}'$, the curve $\bar{O}'D'C'$ can be obtained as the vertical distance between the forward equivalent yield stress point, C', of Eq. (3.23) and the center of the current initial yield surface, $\bar{O}'$.

$$\begin{aligned}\kappa_{(2)}(\Delta\bar{\varepsilon}^p) &= \bar{\sigma}_f^q(\Delta\bar{\varepsilon}^p) - (\bar{\sigma}_r^q(0) + \kappa_0) \\ &= \kappa_0 + A(\bar{\varepsilon}_1^p + \Delta\bar{\varepsilon}^p) - A(\bar{\varepsilon}_1^p) - 2A(\Delta\bar{\varepsilon}_0^p + \Delta\bar{\varepsilon}^p) + 2A(\Delta\bar{\varepsilon}^p) + 2A(\Delta\bar{\varepsilon}_0^p).\end{aligned} \tag{3.24}$$

From Fig. 3.15, the relationships among the equivalent plastic strains, $\bar{\varepsilon}^p$, $\bar{\varepsilon}_{(1)}^p$ and $\bar{\varepsilon}_{(2)}^p$, is

$$\bar{\varepsilon}_{(2)}^p(\Delta\bar{\varepsilon}^p) = \bar{\varepsilon}_{(1)}^p(\Delta\bar{\varepsilon}_0^p + \Delta\bar{\varepsilon}^p) = \bar{\varepsilon}^p(\bar{\varepsilon}_0^p + \Delta\bar{\varepsilon}_0^p + \Delta\bar{\varepsilon}^p). \tag{3.25}$$

Following the previous procedures, the strain hardening function under the general cyclic loading condition can be generalized as follows from the monotonic nonlinear isotropic hardening function.

$$\begin{aligned}\kappa_{(m)} = \kappa_0 &+ (-1)^m A(\bar{\varepsilon}^p{}_{m-1} + \Delta\bar{\varepsilon}^p) + (-1)^{m+1} A(\bar{\varepsilon}^p{}_{m-1}) + 2A(\Delta\bar{\varepsilon}^p) \\ &+ \sum_{j=0}^{m-2}[(-1)^{m+j+1}\, 2A(\sum_{i=j}^{m-2}\Delta\bar{\varepsilon}^p{}_i + \Delta\bar{\varepsilon}^p) + (-1)^{m+j}\, 2A(\sum_{i=j}^{m-2}\Delta\bar{\varepsilon}^p{}_i)]\ .\end{aligned} \tag{3.26}$$

where, $\bar{\varepsilon}^p{}_{m-1}$ is the equivalent plastic strain at the mth reversed loading condition, and $\Delta\bar{\varepsilon}^p{}_{m-1}$ is the distance between the equivalent plastic strains $\bar{\varepsilon}^p{}_{m-1}$ and $\bar{\varepsilon}^p{}_m$, and is given by

$$\bar{\varepsilon}^p{}_m = \bar{\varepsilon}^p{}_{m-1} + \Delta\bar{\varepsilon}^p{}_{m-1}\ . \tag{3.27}$$

As mentioned before, the subscript m indicates the sequence number of the reversed loading state. The value of 0 indicates no reversed loading condition, that is, the initial monotonic isotropic hardening state. Equivalent plastic strain values having negative integers of subscripts m and i have no meaning.

To implement the above model conveniently, some internal plastic variables are needed. These include the sequence number of the reversed loading state, the value of the equivalent plastic strain, the centers of yield surfaces, and the center of the field of isotropic hardening potentials. The most recent center of yield surface during previous cycle will be updated to the new center of field of equi-strain potentials. The yield criterion for the mth load reversal can be expressed as

$$\phi_{(m)} = \tfrac{1}{2}\xi_m : \xi_m - \tfrac{1}{3}\kappa_{(m)}^2(\bar{\varepsilon}^p) \le 0, \qquad \xi_m = s - \alpha'_{(m)} \tag{3.28}$$

where α_m is the mth deviatoric center of the field of equi-strain potentials and is constant under the mth cyclic loading state.

3.5 Numerical analysis of the constitutive equations

From a computational standpoint, the elastoplastic problem is treated as strain controlled in the sense that the stress history is obtained from the strain history by means of an integration algorithm

(Moss, 1984). An effective integration procedure for the elasto-plastic problem is to employ return mapping algorithms (Simo and Taylor, 1984). In what follows, a consistent return mapping algorithm (Simo and Taylor, 1985) will be used for the integration scheme of constitutive equations.

A locally plane stress condition in the web and flange elements is assumed, in the spirit of the thin-walled beam approximation, with the concomitant elastic stress-strain relations. The components of elastic stress, strain, and elastic tangent modulus are as follows.

$$\mathbf{S} = [S_{11}, S_{1s}]', \quad \mathbf{E}^e = [E_{11}, E_{1s}]', \quad \mathbf{D} = \begin{bmatrix} E & 0 \\ 0 & G \end{bmatrix} \tag{3.29}$$

where S_{1s} and E_{1s} are the shear stress and strain, respectively, and they depend on the direction at the subelement of I-section.

$$\begin{aligned} S_{1s}(web) &= S_{12}, \quad S_{1s}(flange) = S_{13}, \\ E_{1s}(web) &= E_{12}, \quad E_{1s}(flange) = E_{13}. \end{aligned} \tag{3.30}$$

The basic idea of the algorithm used here is to project the elastoplastic equations onto the subspace defined by the plane stress condition, and there construct a return mapping algorithm by applying the generalized midpoint rule as graphically shown in Fig. 3.16, which illustrates how stresses are updated. An essential step in the algorithm is the computation of consistent elastoplastic tangent moduli, which preserves the quadratic asymptotic rate of convergence of Newton's method (Simo and Taylor, 1985).

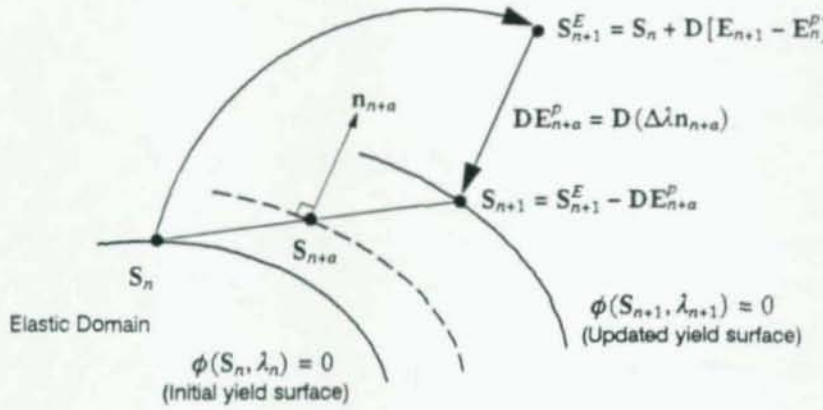

Fig. 3.16 Geometric interpretation of the generalized midpoint rule

A step-by-step implementation of the consistent returning mapping algorithm is summarized together with generalized kinematic hardening rule in Tables 3.1, 3.2 and 3.3. Substituting Eq. (3.31) into the linearized equation of equilibrium (2.34) reduces the latter to a system which is now linear in the incremental motion $\Delta\phi$ and provides a basis for an iterative solution procedure.

Table 3.1 Consistent return mapping algorithm for plane stress

(*i*) Update strain tensor and compute trial elastic stresses.

$$\mathbf{E}_{n+1} = \mathbf{E}_n + \nabla^S \mathbf{u}, \quad \mathbf{S}^E = \mathbf{D}(\mathbf{E}_{n+1} - \mathbf{E}^p_n), \quad \eta^E = \mathbf{S}^E - \alpha_{(m)}, \quad \zeta^E = \mathbf{S}^E - \beta^{(k)}.$$

(*ii*) Check the trial elastic stresses for yielding state under the *m*th cyclic loading stage from **Table 3.2**.

(*iii*) Solve $\phi(\lambda) = 0$ for λ, enforcing consistency condition at t_{n+1} from **Table 3.3**.

(*iv*) Compute modified elastic tangent moduli : $\Xi(\lambda) = [\mathbf{D}^{-1} + \lambda\ \mathbf{Q}]^{-1}$

where, $\mathbf{Q} = \frac{1}{3}\begin{bmatrix} 2 & 0 \\ 0 & 6 \end{bmatrix}$: mapping matrix from the plane stress subspace to the deviator subspace

(*v*) Update stresses, plastic strains and back-stresses of yield surface.

$$\eta_{n+1} = \Xi(\lambda)\mathbf{D}^{-1}\eta^E_{n+1}\ , \qquad \mathbf{S}_{n+1} = \eta_{n+1} + \alpha_{(m)}\ , \qquad \mathbf{E}^p_{n+1} = \mathbf{E}^p_n + \lambda \mathbf{Q}\eta_{n+1}\ ,$$

$$\bar{\varepsilon}^p_{n+1} = \bar{\varepsilon}^p_n + \sqrt{\frac{2}{3}}\lambda\bar{\phi}(\lambda), \qquad (\bar{\phi}(\lambda) \text{ from Table 3.3.})$$

$$\beta^{(k+1)} = \mathbf{S}_{n+1} - (\mathbf{S}_{n+1} - \alpha_{(m)})\frac{\kappa_0}{\kappa^{(k+1)}}. \quad \text{from Eq. (3.21)}$$

(*vi*) Compute consistent elastoplastic tangent moduli :

$$\left[\frac{\partial \mathbf{S}}{\partial \mathbf{E}}\right]_{n+1} = \Xi - \frac{(\Xi\mathbf{Q}\eta_{n+1})(\Xi\mathbf{Q}\eta_{n+1})^t}{\eta^t_{n+1}\mathbf{Q}\Xi\mathbf{Q}\eta_{n+1} + \gamma_{n+1}} = \Omega_{n+1} \qquad (3.31)$$

where, $\gamma_{n+1} = \frac{2}{3}\dfrac{(\kappa^{(k)}_{(m)})'_{n+1}}{1 - \frac{2}{3}(\kappa^{(k)}_{(m)})'_{n+1}\lambda}\eta^t_{n+1}\mathbf{Q}\eta_{n+1}$

Table 3.2 Check of the trial stresses for yielding state under the *m*th cyclic loading stage

$|\phi^E| = |\frac{1}{2}\eta^E : \eta^E - \frac{1}{3}\kappa^2_{(m)}| \le 0?$ ($\kappa_{(m)}$ from Eq. (3.26))

YES : Check the stresses state for the current yield surface.

$|\psi^E| = |\frac{1}{2}\zeta^E : \zeta^E - \frac{1}{3}\kappa^2_0| \le 0?$

YES : • Update the current strains and stresses, and QUIT

NO : • Update the center of the new field of isotropic hardening potential from the center of the current yield surface, $(\beta^{(k)}_{(m)} \rightarrow \alpha_{(m+1)})$.

• Set $\alpha_{(m+1)} = \alpha_{(m)}$, and compute $\eta^E = \mathbf{S}^E - \alpha_{(m)}$.

• GO TO (*iii*) in Table 3.1.

NO : GO TO (*iii*) in Table 3.1.

Table 3.3 Determination of plastic Lagrange multiplier

(a) $$\overline{\phi}^2(\lambda^{(k)}) = \frac{\frac{2}{3}(\eta_{11}^E)^2}{(1+\frac{2}{3}E\lambda^{(k)})^2} + \frac{2(\eta_{12}^E)^2}{(1+2G\lambda^{(k)})^2}$$

(b) $$\bar{e}^{p(k)}_n = e^{p(k-1)}_n + \sqrt{\frac{2}{3}}\,\lambda^{(k)}\overline{\phi}(\lambda^{(k)})$$

(c) $$\phi(\lambda^{(k)}) = \frac{1}{2}\overline{\phi}^2(\lambda^{(k)}) - \frac{1}{3}\kappa^2(\bar{e}^{p(k)}_n)$$

(d) $$\lambda^{(k+1)} = \lambda^{(k)} - \frac{\phi(\lambda^{(k)})}{\phi'(\lambda^{(k)})}$$

$$\phi'(\lambda^{(k)}) = -(1-\tfrac{2}{3}\kappa'\lambda^{(k)})\left[\frac{\frac{4}{3}E(\eta_{11}^E)^2}{(1+\frac{2}{3}E\lambda^{(k)})^3} + \frac{4G(\eta_{12}^E)^2}{(1+2G\lambda^{(k)})^3}\right] - \tfrac{2}{3}\kappa'\overline{\phi}^2(\lambda^{(k)})$$

(e) If $|\frac{\phi}{\phi'}| > \text{tol}$, then $k \leftarrow k+1$ and go to (a)

3.6 Numerical examples of proposed cyclic plasticity model

An application of the proposed plasticity model for representing random uniaxial cyclic loading behavior is shown in Fig. 3.17. It is assumed that the mechanical properties of the material are alike in tension and compression. Curves OABC and OA'B'C' are monotonic tension and compression curves, respectively, in the virgin state. The yield plateau, the strain hardening region, and the Bauschinger's effect can be easily identified. The consideration of the yield plateau seems to be very important in steel structures, as most regions of the structure remain in the elastic state and a substantial part of the rest is more or less on the yield plateau, even near failure of the structure. After yielding, a series of load reversals and reloadings is randomly applied: the solid curve is the loading process, while the dashed curve represents the loading path if loading continues. It can be seen that the dashed curves approach the monotonic tension and compression curves. Curve DD' shows that load reversal takes place before any plastic flow occurs in the opposite sense and this demonstrates this plasticity model can exclude unrealistic overshooting. No point returns to the same place after a complete cycle, but rather undershoots the initial point.

In addition to the uniaxial cyclic loading behavior as shown in Fig. 3.17, the behavior of nonproportional loading path is needed to examine the plasticity model. The biaxial strain–stress response can be represented by four kinds of diagrams: axial strain vs. shear strain, axial stress vs. shear stress, axial strain vs. axial stress, and shear strain vs. shear stress, where both the total strain and plastic strain histories are considered in the axial strain vs. shear strain diagram. In Figs. 3.18 and 3.19, two kinds of strain–stress histories are presented: One under a 90 degree out-of-phase tension–torsion strain–controlled cycling and the other under a square path of strain–controlled cycling. Experimental results for these cases can be found in the report by Doong (1989). The predictions of the analytical plasticity model can be found to be very similar to those of experimental results, qualitatively. A major discrepancy between analytical predictions and experimental results may come from the different material properties such as the elastic and shear moduli, the yield strength, and the type of strain hardening, *etc.* Another nonproportional cyclic strain path is applied as shown in Fig. 3.20. Experimental results for this case can be found in

Lamba and Sidebottom (1978). These predictions of the analytical plasticity model also seem to be qualitatively similar to those of experimental results.

From the overall qualitative similarity between the above predictions of analytical plasticity model and the experimental results under the uniaxial and biaxial strain-controlled paths, the current cyclic plasticity model would appear to be reliable.

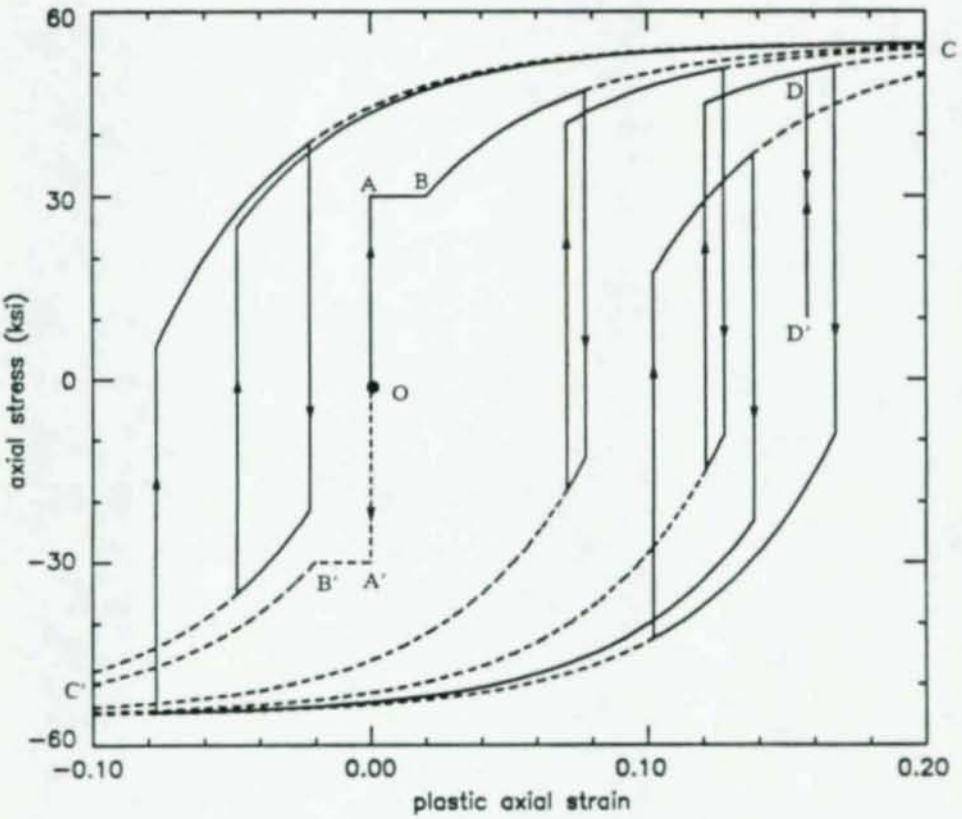

Fig. 3.17 Uniaxial random cyclic loading behavior

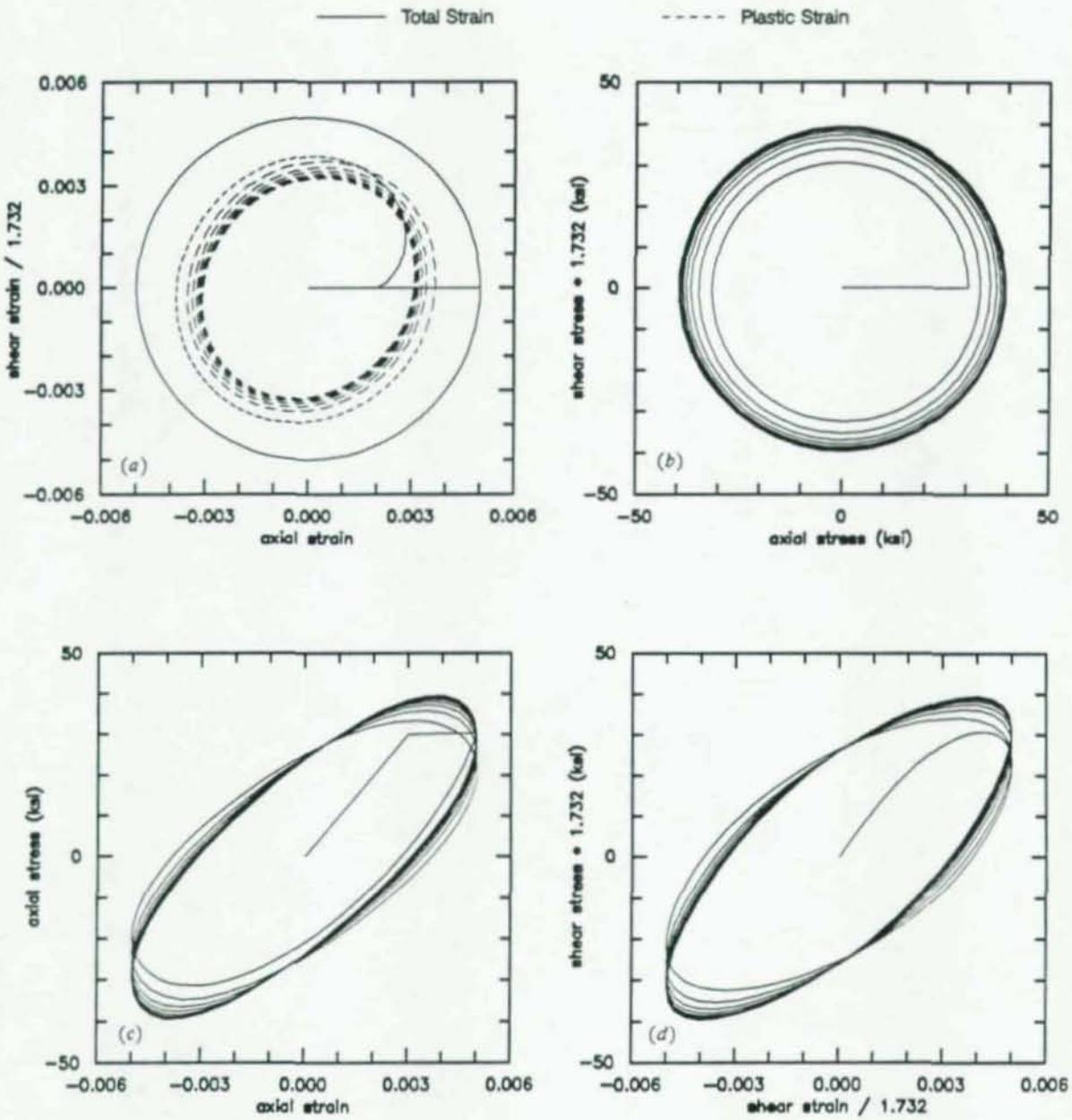

Fig. 3.18 Strain-stress history under 90 degree out-of-phase tension-torsion strain-controlled cyclic loading behavior (Doong, 1989)

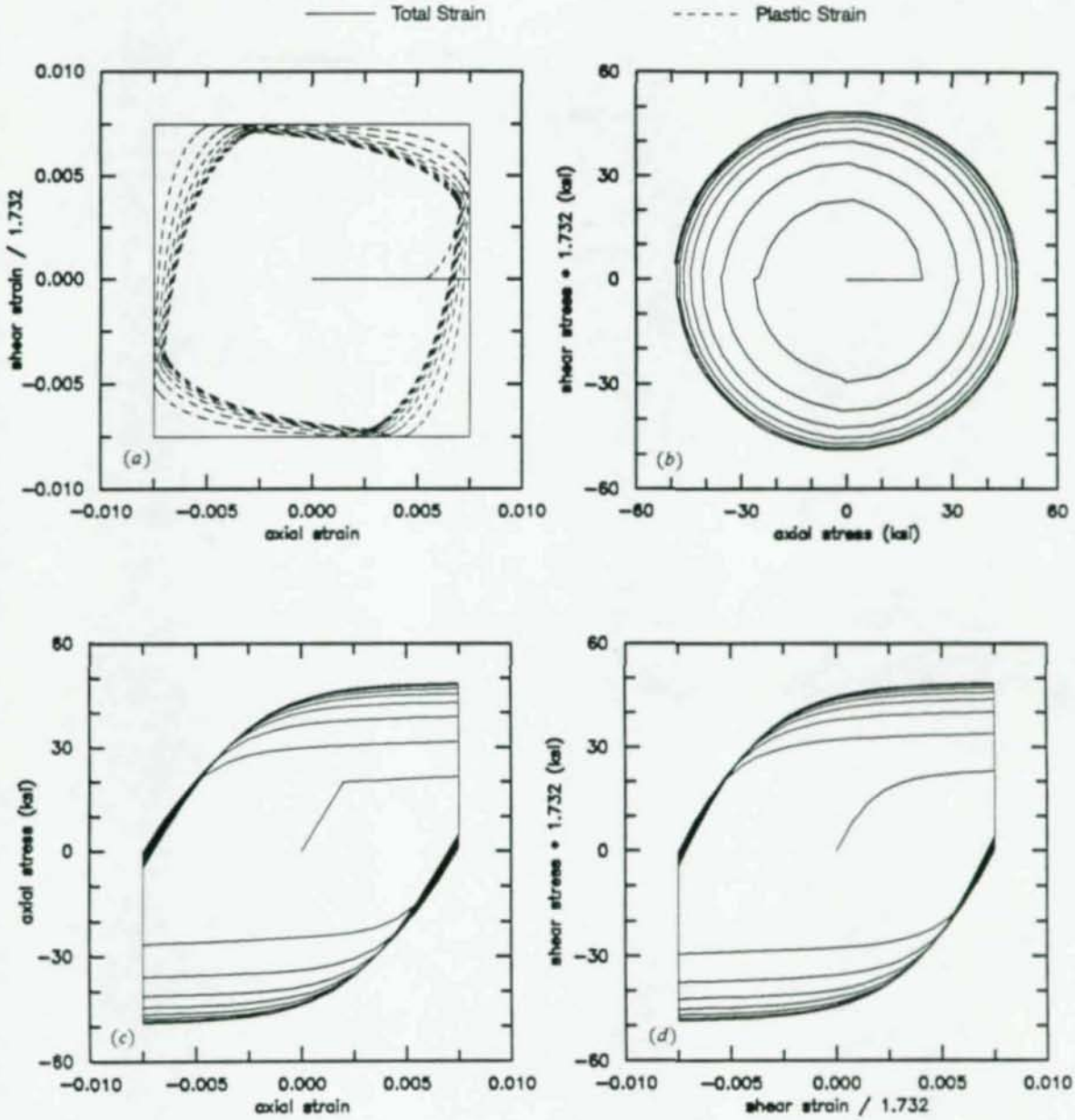

Fig. 3.19 Strain-stress history under one-square path strain-controlled cyclic loading behavior (Doong, 1989)

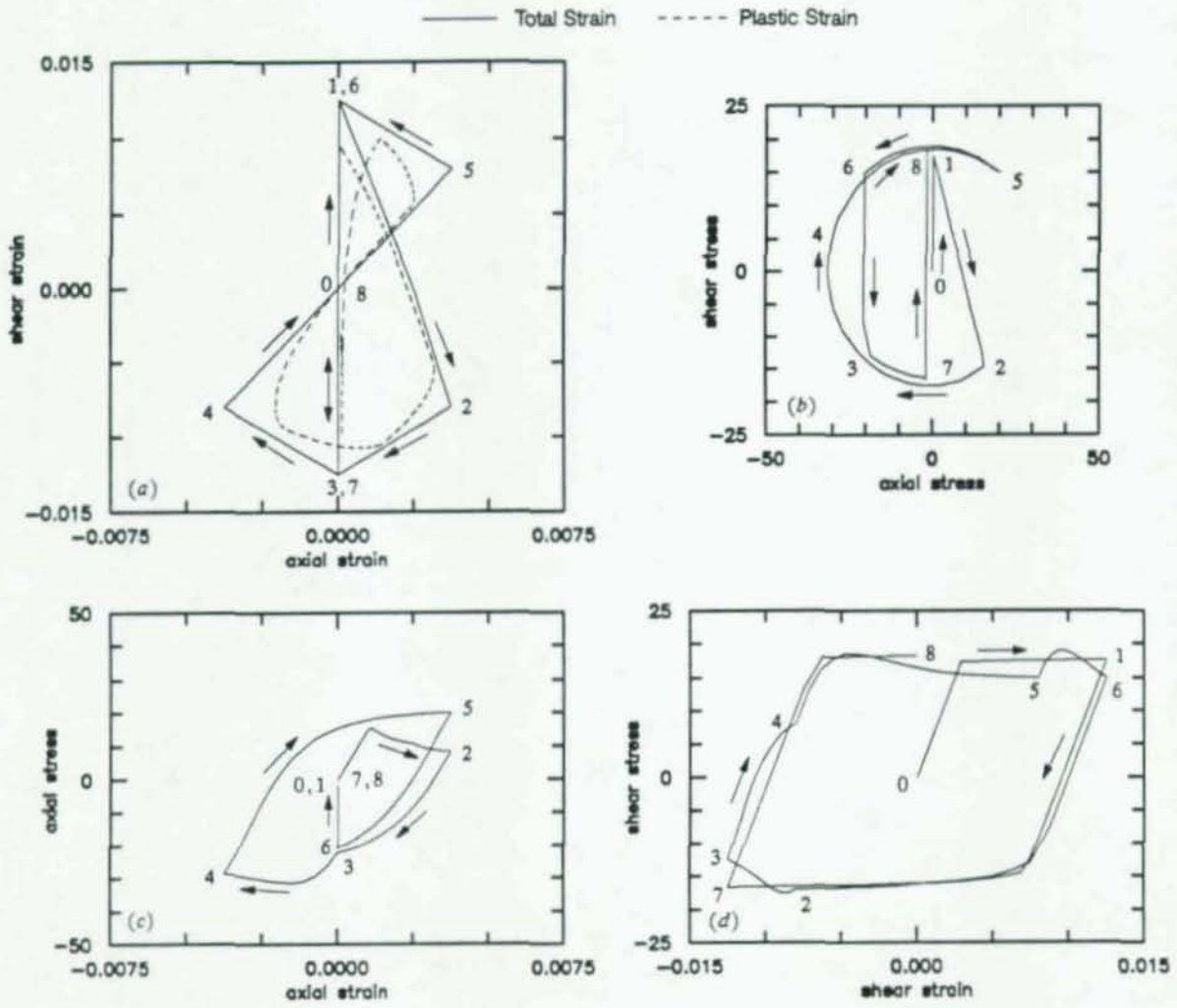

Fig. 3.20 Cyclic nonproportional loading paths behavior (Lamba and Sidebottom, 1978)

Chapter 4

Experiments on the Cyclic Buckling of Short I-beams

The results of experiments on the cyclic, inelastic, lateral buckling and post-buckling response of short beams are presented in this chapter. Experimental tests of five propped cantilever beams subjected to a cyclically reversing point load acting near the fixed end were carried out in the laboratory at the University of Illinois at Urbana-Champaign. The experiments included both unbraced and braced systems with similar loading histories. The results of the experiments are presented here along with a detailed analysis of the experimental configuration.

The experimental program described herein is clearly limited in scope. Consequently, it is difficult to put the results into proper perspective. To ameliorate this condition we provide a thorough analysis of the experiments using the finite deformation, inelastic beam model developed in earlier chapters. Chapters 5, 6, and 7 are devoted to various analytical parameter studies on the model tested in the laboratory. The analyses that follow including *(a)* elastic linearized buckling analyses, *(b)* inelastic limit load analyses, and *(c)* an inelastic cyclic load analysis similar to the loading program used in the experiments. The parameter studies should help to provide a frame of reference for evaluating the experimental results. The parameter studies are organized around a *standard* case which was optimized to be a close approximation of the response exhibited by the unbraced test specimens. The standard analytical model is documented at the end of this chapter.

4.1 Experimental Procedure

In the present section we describe the details of the experimental program, including the testing arrangement, the dimensions of the test pieces, and the instrumentation used to measure the response.

Testing configuration and loading apparatus.- The testing configuration used in these experiments is shown schematically in Fig. 4.1. Translation, rotation, and warping were restrained at one end of the test piece (hereafter called the *fixed end*). Vertical and lateral translation and torsional rotation were restrained at the other end while axial extension and flexural rotations were unrestrained. The fixed

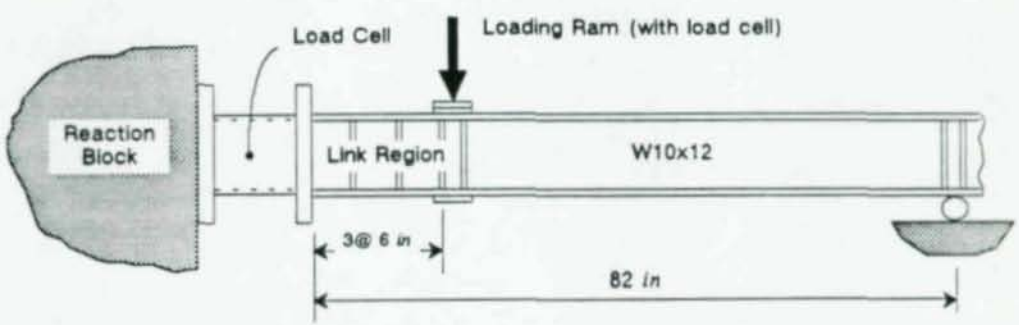

Fig. 4.1 Experimental test configuration

end was realized by welding the end of the test piece to a rigid end plate, bolting that end plate to the end plate of the load cell, and bolting the other end of the load cell to a massive concrete reaction block. Because of the presence of the load cell, the fixed end actually had a finite flexibility. The support flexibility was determined from elastic level tests and accounted for in the data analysis phase.

It is well known that the height of the load with respect to the shear center of the beam has a significant effect on the buckling response of the system. The point of load application for cyclically reversing loads depends strongly on the load transfer mechanism. The load transfer mechanism chosen for the tests is shown schematically in Fig. 4.2. The load was applied to the specimen by a hydraulic actuator which reacted against an overhead frame. The ram was endowed with a universal joint at both ends of its length and hence did not provide restraint to the specimen. The ram load was transferred to the specimen through a collar which was prestressed so as to act as a unit with the test piece. The integrity of the prestressing was verified for each of the tests. The collar received the ram through a universal clevis having a center 4.5 *in* above the top flange. The clevis bearing had a diameter of 3 *in* and hence the point of action of the load was approximately 3 *in* above the top flange for the push direction and 6 *in* above the top flange for the pull direction.

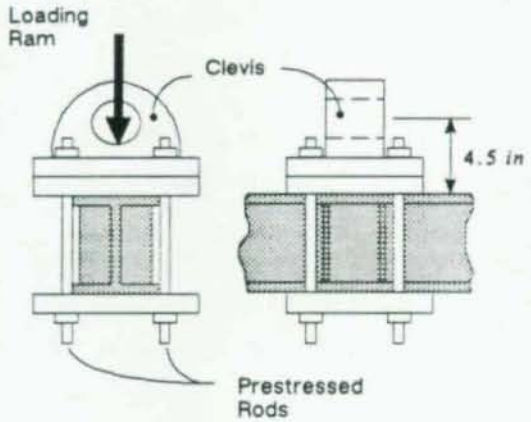

Fig. 4.2 Load transfer mechanism

In most practical applications, the brace-to-beam connection would be accomplished through a gusset plate or similar connection in which the load is transferred directly to the flange where the connection is made. In such a circumstance, the point of load transfer from the brace to the beam is always on that side of the beam. While the loading mechanism used in these experiments does not model any specific detail, it preserves the important *one-sided* nature of the practical application.

The tests were carried out under displacement control using the ram extension as the control displacement. A complete sweep of the instruments was made at intervals 0.1 *in* of ram extension.

Specimen properties.– All five of the test pieces had the same nominal cross-sectional geometry, a W10x12 section, and the same nominal material properties, ASTM A36 steel. Three of the five specimens were cut from one piece, the other two from a second piece. The material properties of the two pieces were determined by uniaxial tension tests, with two coupons taken from the web and one from each of the flanges. The material properties (designated as A and B) are listed in Table 4.1. One can

Table 4.1 Material properties

	Material Set A		Material Set B	
	Web	Flange	Web	Flange
Yield Strength (*ksi*)	46.3	47.5	48.2	46.7
Ultimate Strength (*ksi*)	68.3	67.9	68.4	67.7
Ultimate Elongation	0.20	0.20	0.20	0.16

observe that the strength of the steel greatly exceeded the nominal value, but the material was highly ductile.

The cross-sectional dimensions of the test pieces were measured and the values are given in Table 4.2. Observe that the half flange widths were not equal. Although the measured values are within standard mill tolerances, the imperfections caused a measurable torsional response to a loading acting in the plane of the web. The measured response indicates that the direction of initial rotation, and thereby the direction of rotational buckling, was determined by the geometry of the flange imperfections.

The configuration of a typical specimen is shown in Fig. 4.1. To prevent web buckling due to high transverse shear, fitted transverse web stiffeners were placed at approximately 6 *in* intervals in the region of the beam between the load and the fixed end in accordance with the recommendations of Hjelmstad and Popov, (1983). Transverse stiffeners were also placed at the point of load and at the point of support at the far end of the specimen to prevent web crippling at regions of concentrated force transfer. The specimen was welded to the massive end plate with full penetration grove welds. The flanges were prepared for welding by beveling them at 45 degrees. To insure weld integrity, a fillet weld was made on the back side of each flange. The web of each specimen was fillet welded on both sides, directly to the end plate.

Lateral bracing arrangements were of three varieties: (1) No lateral bracing, (2) Lateral bracing near the top flange, and (3) Lateral bracing near the bottom flange. The lateral bracing method used is shown in Fig. 4.3. The brace was pinned at both ends, attaching to one of the stiffeners under the load approxi-

Table 4.2 Measured section properties

Material Location		Material Set A	Material Set B
Half Flange Width (*in*)	1	2.070	1.880
	2	1.890	2.030
	3	2.030	2.083
	4	1.990	2.030
Half Flange Thickness (*in*)	1	0.220	0.212
	2	0.199	0.227
	3	0.196	0.213
	4	0.210	0.200
Depth (*in*)		9.841	9.851
Web Thickness (*in*)		0.177	0.179

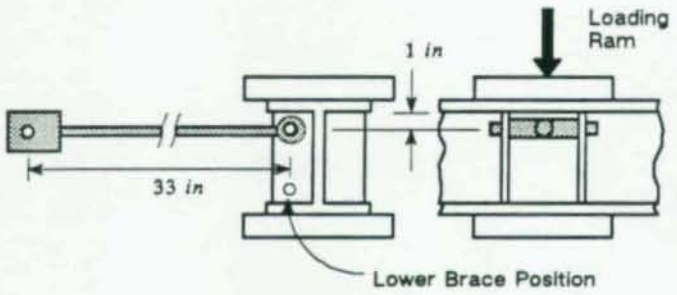

Fig. 4.3 Lateral bracing arrangement

mately 1 *in* away from the nearest flange. A summary of the distinctive features of each test are given in Table 4.3, which records the initial sense of the load, the bracing arrangement and the material used.

Response Measurement.– A load cell capable of measuring axial force, biaxial shear forces, biaxial bending moments, and torque resided between the specimen end and the reaction block (Fig. 4.1). A uniaxial load cell located in the loading ram measured the applied force. The force measurements rendered the test configuration statically determinate.

Displacements of certain points on the specimen were measured with linear variable differential transformers (LVDTs) deployed as shown in Fig. 4.4. The displacement measurements monitored the motion of the specimen in the plane normal to the axis of the beam, at the point where the load was applied. The motion at the *fixed* end and the extension of the loading ram were also monitored. The LVDTs were connected to rods which were 28 *in* long and had universal joints on both ends to allow free movement. As such, these instruments measured the change in length of a line connecting a point on the specimen and a stationary ground point.

The experimental data were acquired in digital form using a low speed electronic data acquisition system. The scan rate was approximately 25 channels per minute. Care was exercised to ensure that the system was steady during each scan.

Loading program.– Each of the five tests were similar in the sense that the specimen geometry was the same and the position of the load was the same. The important differences among the tests included differences in the character of lateral bracing, and slight differences in the loading histories.

The loading programs used in these tests consisted of cycles of applied load and was executed by controlling the ram extensions. The imposed displacement history for each of the five specimens is shown schematically in Fig. 4.5, in which each bar represents a continuous movement of the ram head (*i.e.* one

Table 4.3 Summary of test configurations

Specimen	Initial Loading	Bracing Arrangement	Material Set
1	pull	none	A
2	push	none	B
3	push	top	A
4	push	bottom	A
5	push	top	B

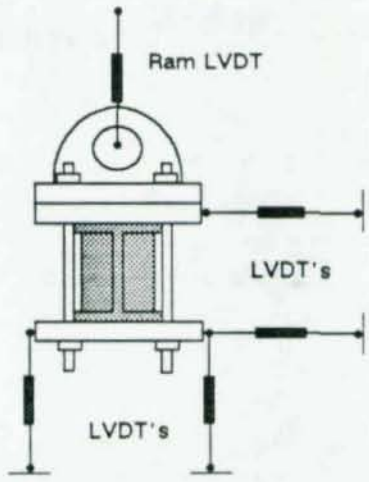

Fig. 4.4 Displacement response measurement at point of load

half cycle). Notice that specimen 1 began with a pull (stabilizing) half cycle while the others began with a push (destabilizing) half cycle.

4.2 Experimental Results

Narrative descriptions of the five tests.– The following paragraphs give a narrative account of each of the five tests. These descriptions begin by documenting the first observed phenomena (generalized buckling, local buckling, material yielding, and fracture), and reference these occurrences to a cogent graphical representation of the response history. Discussions of each specimen will reference a plot of load versus ram extension and a plot of load versus specimen rotation at the point of load. For simplicity, the ram displacement is called simply vertical displacement, which is approximately true for the point where the ram attaches to the loading collar. Vertical displacement of the specimen as a whole has no meaning. One should note that the plots of load versus ram displacement have not been corrected in any

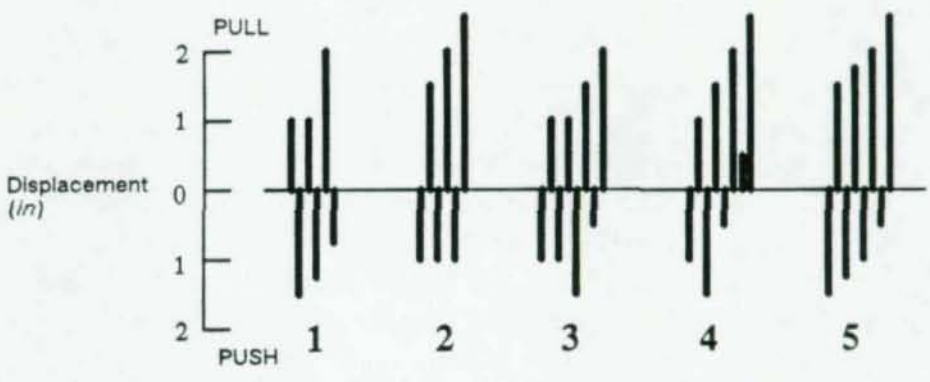

Fig. 4.5 Loading sequence for the five specimens

way for support flexibility. In their present form, the abscissa and ordinate are conjugates in the sense that the area enclosed under the graph represents the energy input to the system.

In the descriptions of the individual tests the following convention will be employed for describing the location of local events such as local buckling of the elements of the beams. To distinguish right from left we shall assume that the observer stands at the pinned end of the test piece and looks toward the fixed end. Local buckling generally involves a flange which can be located on the right or left; top or bottom of the beam; and may occur at the fixed end, at the point of load inside the link region, or at the point of load outside the link region. When buckling is described as inside or outside the link region it should be understood that reference is to regions at the point of load. Typical load point designated (*A*, *B*, *etc.*) are often indicated in the descriptions of the responses of the specimens. These load points are defined in Fig. 4.11. and are discussed in the section on general observations on cyclic response.

Specimen 1.– Specimen 1 was unbraced and the force was applied in the pull direction first. The force–deformation characteristics of Specimen 1 are shown in Fig. 4.6.

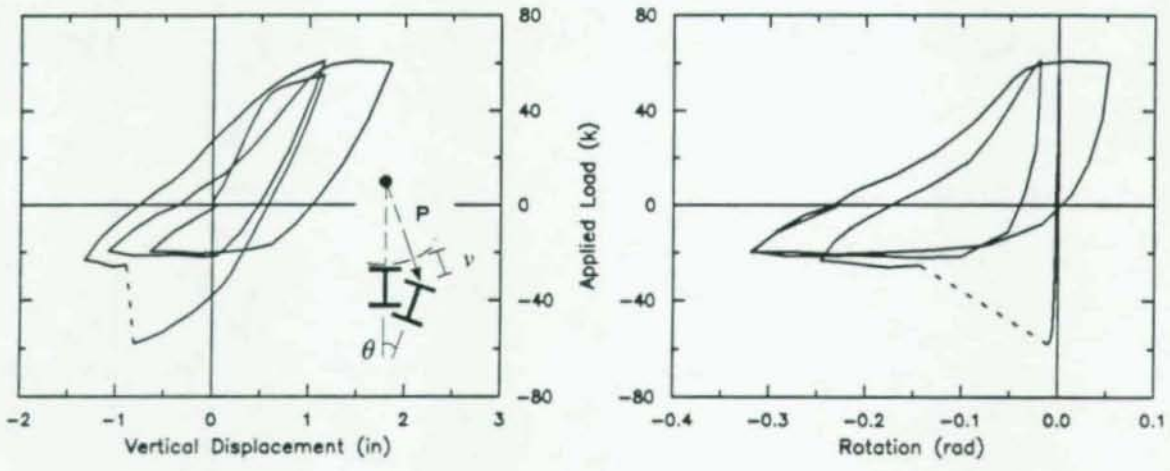

Fig. 4.6 Cyclic load response for specimen 1 (Hjelmstad and Lee, 1990)

Generalized yielding was evident during the first pull cycle at a load level of approximately 50*k*. Displacement was increased to 1.15 *in* in this direction with no evidence of generalized buckling, local buckling, or flange yielding. Upon reviewing the data it appears that there was some torsional movement due to the fact that the load was not perfectly placed. However, the torsional motion was not discernible to the naked eye.

Flange yielding at the point of load and at the fixed end was noted during the first push excursion. At incipient buckling (load point *B*) there was a small amount of local flange buckling noticed on the top right flange, outside the link region. Dramatic snap–through buckling took place immediately after load point *B* was passed. While the vertical movement (the control displacement) was on the order of hundredths of an inch the top flange moved laterally about 1.25 *in* while the bottom flange remained essentially stationary (lateral bracing would have had little effect if it were placed on the bottom flange). The specimen lost more than half of its load carrying capacity after buckling. Forcing in the push direction continued with little change in the load sustained. Loading continued until a vertical displacement of approximately 1.25 *in* was achieved. At maximum push displacement (load point *C*) only slight flange

buckling had occurred, indicating that local buckling was not necessary to accommodate the large lateral motions. The initial flange buckle outside of the link region had increased slightly in amplitude.

The loading was reversed and the specimen was pulled back to a positive displacement of 1.15 *in* Buckling did not occur in the pull direction, but considerable strain hardening accrued and the specimen was nearly straightened.

The loading was reversed again to push. The specimen buckled again, but was unable to sustain a load greater than the post buckling load of the previous push cycle.

A substantial local flange buckle, accompanied by web buckling, formed in the lower right flange outside the link region, and the response curve changed from concave upward to concave downward during the second pull excursion. A force in excess of 60*k* was sustained prior to slight lateral buckling of the specimen. Buckling in the pull direction was apparent from lateral movement of the specimen; however, the limit point was quite flat and hence little loss of carrying capacity resulted.

At the end of the test the specimen had substantial local bucking both outside the link region and at the flange–end plate connection on the top right side. Coupled flange and web buckling had occurred. While amplitudes of local buckling were high, there was no visual evidence of weld distress.

Specimen 2.– Specimen 2 was also unbraced and the initial loading was in the push direction. The response of the specimen to the imposed loads is shown in Fig. 4.7.

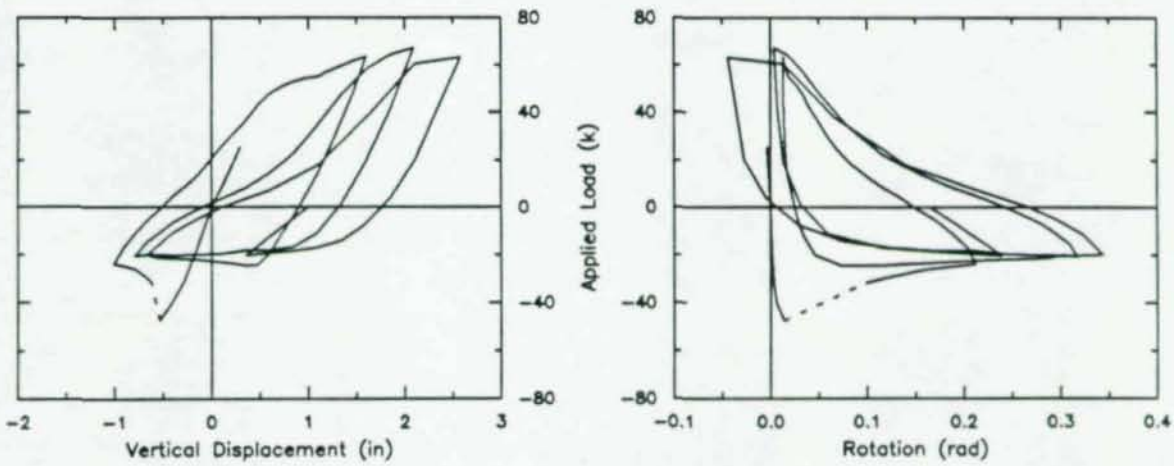

Fig. 4.7 Cyclic load response for specimen 2 (Hjelmstad and Lee, 1990)

At incipient buckling, lines of loosened mill scale indicated that yielding had taken place, albeit to a modest degree, even in the web region. There was no evidence of flange local buckling either inside the link region or outside it. The specimen snapped to a twisted position during the first inelastic excursion in the push direction (load point *A*). The value of the buckling load was observed to be a bit lower than Specimen 1 which was yielded in the pull direction before buckling. Several data points were measured on the downhill side of the post–buckling curve, giving a good indication of the shape of the post–buckling response characteristic. At the extreme push displacement (load point *B*) only slight buckling of the top right flange inside the link region was evident.

Generalized yielding commenced at a load of about 50k in the first excursion in the pull direction, followed by considerable strain hardening. The local buckle in the flange had straightened at maximum pull, and a new buckle formed at the top left flange at the fixed end.

When the specimen buckled again in the second push excursion, the top right flange buckle had reappeared, the flanges at the fixed end had yielded, and the top left flange buckle at the fixed end had straightened.

At load point *G*, significant buckling had occurred at the bottom left flange outside the link region and at the top left flange at the fixed end. Web buckling outside the link region was also evident. At this point, the loading collar had rotated about the axis of the loading ram.

Specimen 3.– Specimen 3 was braced at the top flange and initially loaded in the push direction. The response of Specimen 3 is shown in Fig. 4.8.

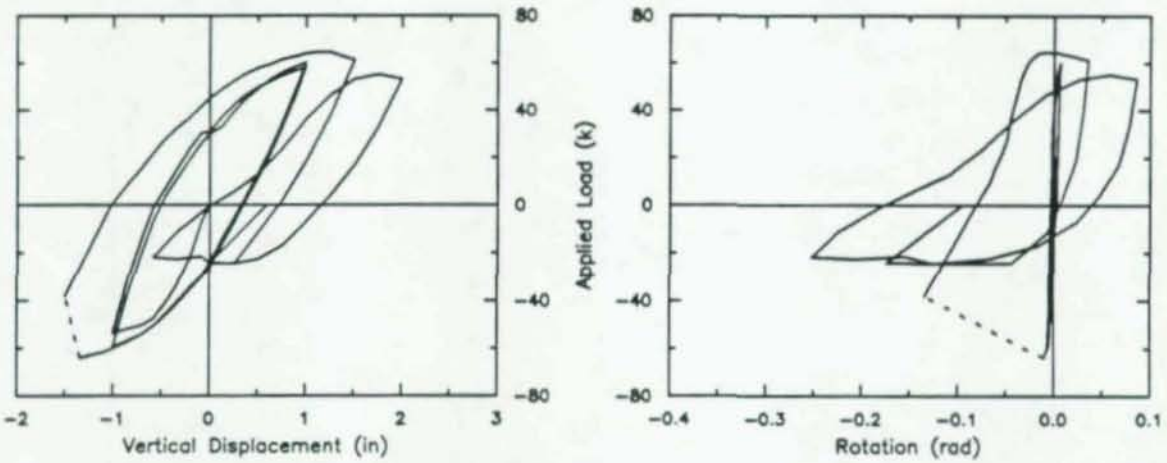

Fig. 4.8 Cyclic load response for specimen 3 (Hjelmstad and Lee, 1990)

Generalized yielding and subsequent strain hardening, without local or lateral buckling, took place during the first excursion in the push direction and reversed with no apparent distress. Flange yielding outside the link region was noted at load point *B*. Two cycles were completed without buckling.

Just prior to load point *E*, slight local buckling was observed in the top left flange outside the link region. Dramatic snap-through buckling of the specimen and the bracing rod occurred simultaneously, at load point *E*. Local buckling of the top right flange outside the link region and local buckling of the upper half of web in this same region also occurred in conjunction with the lateral-torsional buckling of the specimen.

The specimen was unloaded, the buckled bracing rod was removed, and loading was resumed in the pull direction without bracing.

The specimen exhibited a limit point in the third pull excursion (just prior to load point *G*). As expected, the post-buckling loss of load carrying capacity was slight. Antisymmetric local buckling of the bottom left and right flanges outside the link region with compatible local buckling of the adjacent web accompanied the post-limit loss of load. Substantial local buckling of the bottom left flange inside the link region and the top flange at the fixed end was also noted.

Pronounced local buckling of the top flange at the fixed end was observed prior to general lateral buckling in the fourth push excursion. Buckling in the fourth pull cycle showed a considerable loss in load carrying capacity.

Specimen 4.– Specimen 4 was braced at the bottom flange and was initially loaded in the push direction. The response of Specimen 4 is shown in Fig. 4.9.

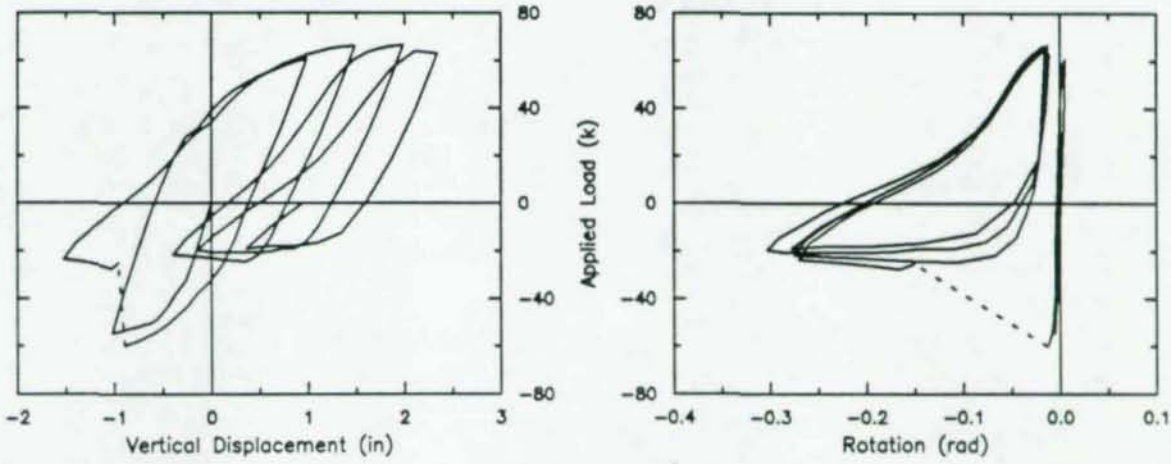

Fig. 4.9 Cyclic load response for specimen 4 (Hjelmstad and Lee, 1990)

The specimen achieved generalized shear yielding in the first push excursion without buckling. The specimen buckled during the second push excursion at a load level greater than its initial yield load. The increase in capacity can be attributed to strain hardening accrued during the previous yielding cycles. Upon buckling, the load carrying capacity of the specimen dropped to the asymptotic level of approximately $20.5k$. Subsequent load cycles demonstrated increasing capacity in the pull direction due to strain hardening and repeated achievement of the asymptotic buckling capacity in the push direction.

Prior to initial buckling there was no visual evidence of local buckling, but considerable yielding had taken place in the top and bottom flanges outside the link region, adjacent to the applied load. No yielding had taken place inside the link region. Slight local buckling occurred in the top flange inside the link region after generalized lateral buckling had occurred and motion was still in the push direction. Local buckling of the top flange at the fixed end occurred as the specimen approached its maximum load in the second pull cycle. The amplitude of the local flange buckles increased considerably as the loading progressed. It would appear that the flange buckles did not significantly affect either the maximum pull capacity nor the asymptotic push capacity.

Specimen 5.– Specimen 5 was braced at the top flange and loaded in the push direction first. The first cycle covered a 50% greater displacement than the other four specimens. The response of Specimen 5 is shown in Fig. 4.10.

Buckling occurred during the first cycle well after shear yielding and considerable strain hardening of the web had taken place. Due to the brace, the drop in carrying capacity after buckling was not as dramatic as in previous tests. Unlike previous tests, the buckling in the second push cycle exhibited a

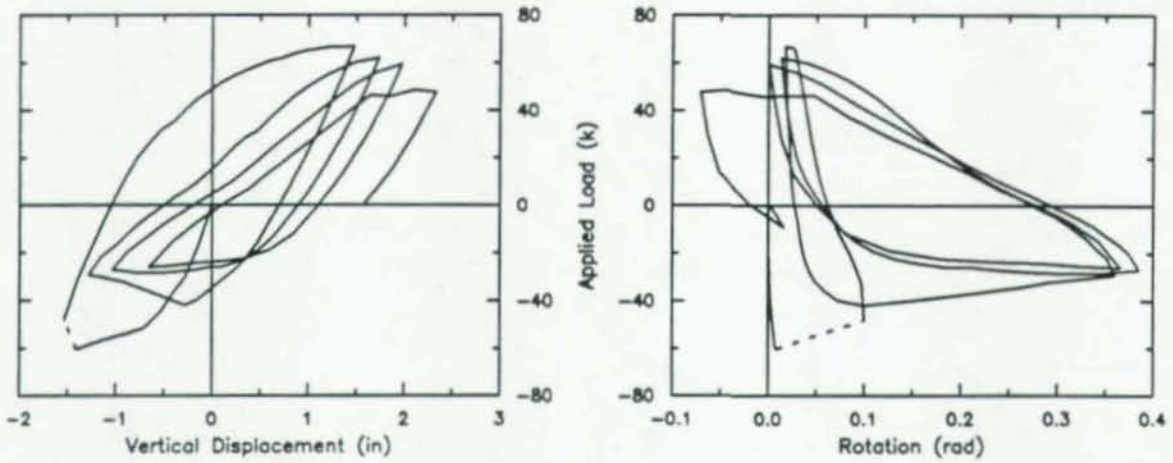

Fig. 4.10 Cyclic load response for specimen 5 (Hjelmstad and Lee, 1990)

limit load with degrading post-limit response. The post-limit response in this cycle approached an asymptotic buckling capacity of $28.5k$, a value somewhat larger than the unbraced tests.

There was no evidence of local buckling at initial lateral buckling. The first flange local buckling occurred on both sides of the loading collar during the first pull excursion. Flange buckling was accompanied by web buckling outside the link region. The local buckling of this specimen was more intense than in the other specimens because of the restraint provided by the brace. The local buckles helped to accommodate the large specimen rotations at the point of load whereas lateral movement of the section had accomplished the same thing for the unbraced specimens. Failure of the specimen in the fourth pull cycle was due to complete fracture of the bottom flange at the fixed end.

4.3 General Observations on Cyclic Lateral-Torsional Buckling

Several qualitative observations can be made about the cyclic response of short beams based upon these tests. Most of the qualities of the response are attributable to the effect of geometry of load placement with respect to the test piece. Clearly, the response in the pull direction is quite different from the response in the push direction when the load does not act at the shear center, since for either direction of lateral motion a pushing force tends to amplify rotational motion, while a pulling force tends to diminish rotational motion.

In this section we discuss the general aspects of cyclic lateral buckling that were observed in the tests. The discussion will refer to Fig. 4.11, which represents a typical cyclic response of a beam like those tested in the present program. Load points A through F are identified for a cycle which includes initial buckling, subsequent straightening by pulling in the opposite direction, followed by a subsequent buckling.

Initial Buckling and Post-Buckling.- Since initial buckling in a cyclic test is like a monotonic buckling test, one would expect that observations made in previous research on monotonic lateral buckling would apply to the present situation. However, the buckling and post-buckling response of short beams is quite different from the response observed in existing lateral buckling tests of longer beams.

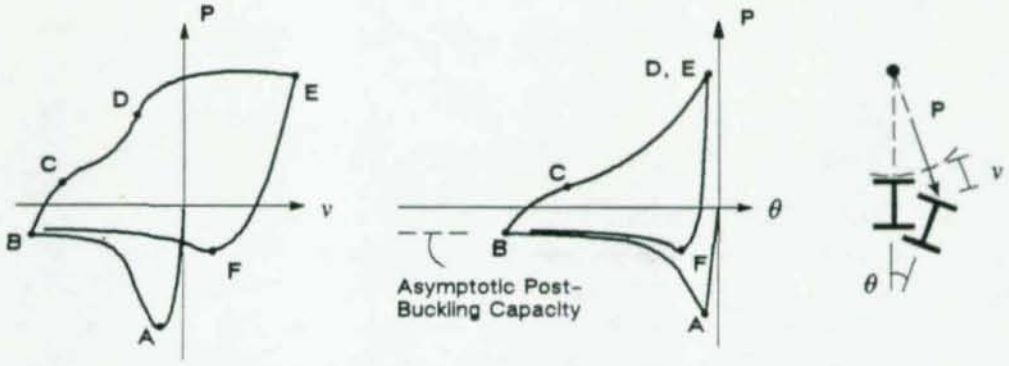

Fig. 4.11 Typical lateral buckling response

Specifically, lateral buckling of short beams exhibits a severe limit load with rapidly descending post buckling degradation. The existence of an asymptotic post-buckling strength is more apparent for short beams than it is for longer beams.

One might expect that estimates of the limit load could be made with existing analytical techniques. However, several phenomena are important to the behavior of cyclically loaded short beams which are at odds with the assumptions generally used in deriving analytical values of lateral buckling loads. Due to the cyclic nature of the loads, it is possible to sustain an inelastic loading in the pull direction prior to a push loading. Such an occurrence would have several ramifications: (*a*) the residual stress pattern would be altered from that of a virgin beam, (*b*) a residual (hogging) deformation would be induced, (*c*) some straightening of initial rotational imperfections would occur, (*d*) the material would strain-harden from its virgin state, and (*e*) softening of the material tangent modulus (Bauschinger's effect) would take place. One would expect that effects *a*, *c*, and *d* might act to strengthen the beam against buckling, whereas effects *b* and *e* might tend to lower buckling resistance. For extremely short beams (the test pieces in the present experiment are arguably such beams), the limit load is very nearly equal to the shear yield capacity of the beam. The effect of beam length will be thoroughly investigated analytically in the following Chapter 5.

Comparison of the buckling loads of specimens 1 (pull first) and 2 (push first) would indicate that the favorable factors dominate, and that strain-hardening has the greatest influence. It is difficult to assess the extent to which rotational imperfections were straightened. However, it should be noted that these imperfections were relatively large in the test specimens because of the poor tolerances on the rolling of the flanges (see Table 4.2). On the other hand the initial rotational imperfections were quite small as compared to those left by severe lateral buckling. No information was obtained from these tests to quantify the effect of residual stresses and Bauschinger's effect.

Buckling in the push direction was a snapping phenomenon which was difficult to control experimentally even under displacement control. Consequently, the post-buckling slopes (shown in Figs. 4.6 through 4.10 as dotted lines) represent the straight line between the pre-buckling state and the nearest stable post-buckling state, not the actual post-buckling behavior. Specimen 2 gives the best indication of the shape of the post-limit response. The response approaches a non-zero asymptotic post-buckling capacity, as shown in Fig. 4.11, which is sustainable under repeated cycles of loading.

Pull Response.– Four distinct regions of response are exhibited upon reversed loading in the pull direction from a push buckled state. The first stage (BC in Fig. 4.11) comprises elastic recovery from loading in the opposite direction. The second stage (CD) consists of straightening of residual twist left by inelastic buckling. The response curve stiffens during this stage because the initial flexible untwisting gives way to stiff planar bending as the residual lateral and torsional deformations diminish. The third stage (DE) consists of generalized yielding in the pull direction.

In the third stage it is possible to experience lateral buckling. However, such buckling is always accompanied by severe local buckling and often tearing of the flanges. In these cases some post-buckling degradation would occur prior to load point E. Pull buckling did not occur in the tests until late in the loading program, usually long after push buckling had shaken down into behavior which did not exhibit a limit load. The most important ramification of pull buckling is its association with failure by fracture in the flange welds. The local buckling which is invariably associated with pull buckling can lead to low cycle fatigue in the regions of high cyclic curvature reversals. When the stresses and strains associated with lateral motion accrue, the possibility of material tearing is quite high. While push buckling is also associated with significant local buckling in the latter stages, the sustained loads are considerably smaller, offering some protection from ultimate failure.

Buckling in Subsequent Cycles.– A beam reloaded in the push direction, after it has buckled once and straightened, suffers from several effects that tend to weaken it: (*a*) The beam might not be well straightened, even with considerable yielding in the pull direction. The residual imperfection decreases the magnitude of the limit load in the next push cycle. (*b*) The pull cycle can leave the beam permanently bowed from yielding. Initial camber is known to have an important effect on the lateral-torsional buckling capacity of a beam. The situation worsens under cyclic loading because buckling commences earlier in each subsequent push cycle, and the torsional motion of buckling does not counteract the residual cambers. Consequently, the beam creeps cyclically in the pull direction. (*c*) Material softening (Bauschinger's effect) may also weaken the subsequent buckling behavior.

Subsequent lateral-torsional buckling can demonstrate a limit load type of response (load point F in Fig. 4.11). However, the limit load is generally dramatically diminished from the initial buckling load. In the tests reported here, only Specimen 5 exhibited a second limit load which was more than marginally greater that the asymptotic post-buckling load. Specimen 5 was braced at the top flange and hence post-buckling deformations were controlled to a greater degree than for the other specimens. These observations would suggest that the residual deformation is the most important factor affecting subsequent buckling behavior.

When the point of loading is closer to the shear center the push and pull responses will tend to look more like each other. Therefore, care must be exercised in extrapolating the results of these experiments to cases in which the point of loading is closer to the shear center. For the case of loading exactly at the shear center, symmetry would indicate the same behavior in both the push and pull directions. Experimental evidence is lacking, but one might expect that under a shear center loading, unstable behavior would be exhibited in both directions albeit with much less severe post-buckling degradation.

Table 4.4 presents a summary of the specimen response features. The table gives initial buckling loads, the cycle in which initial buckling occurred, the asymptotic post-buckling capacity, the maximum pull load, and the energy dissipated throughout the loading program. The energy dissipation is history dependent, and insofar as each specimen underwent a slightly different history, the values are not di-

Table 4.4 Summary of experimental results

Specimen	Buckling Load (k)	Buckling Cycle	Asymptotic Push Buckling (k)	Maximum Pull Load (k)	Energy Dissipation (in-k)
1	57.8	1st	21.4	61.0	260
2	47.4	1st	20.5	67.3	225
3	63.9	3rd	22.0	64.7	380
4	59.9	2nd	20.5	66.9	350
5	60.2	1st	28.5	66.9	420

rectly comparable. They do, however, provide a qualitative indication of the ductility and toughness of the test specimen.

Influence of Local Buckling.– Local buckling in steel members generally refers to buckling of individual plate segments such as a flange or web, and may occur independently or in conjunction with generalized buckling such as lateral-torsional buckling. The kinematic feature that distinguishes local buckling from generalized buckling is that generalized buckling takes place without deforming the cross-sectional geometry whereas local buckling deforms only the cross-section. For extremely thin-walled members (e.g. as in cold formed steel sections) the coupling between local and generalized buckling is quite important and has been the subject of extensive research (Vlasov, 1961). This coupling has been largely ignored for the I-sections used in heavier building construction.

The theoretical models which have been used to study lateral-torsional buckling are universally based upon the hypothesis that cross-sectional shape remains invariant as the beam deforms; precluding local buckling effects. Lateral buckling experiments have indicated that generalized buckling usually precedes local buckling in slender beams, even for elastoplastic buckling. The present tests suggest that the same is largely true for the push buckling of extremely short beams; however, slight local buckling of the flanges was noted at or prior to buckling in Specimens 1 and 3. Local buckling commenced shortly after generalized buckling in the other tests. Based upon observations made during the tests, it would appear that local flange buckling is not necessary to accommodate the large rotations of the beam. Assuming cross-sectional invariance for analytical purposes appears to be reasonable for short members, but the effects of coupled flange buckling and lateral-torsional buckling need further investigation. As mentioned above local buckling is strongly coupled with generalized pull buckling in short beams (probably longer ones too).

Local buckling generally degrades the performance of structural members in a cyclic load environment. Local buckling in a cyclic load environment often leads to tearing of material in the zones where local curvatures are high due to cyclic changing of the buckled shape. Consequently, local buckling directly limits the ductility of steel members under cyclic loading through low cycle fatigue. Documented examples of low cycle fatigue caused by local buckling are plentiful. For example, local buckling of the wall was found to cause significant degradation in the axial buckling of tubular struts (Zayas, Popov, and Mahin, 1980). Web buckling in shear beams shows limit-load behavior which is arrested by the formation of a tension field. Eventual failure of these beams is caused by tearing in the high curvature zones of the web (Hjelmstad and Popov, 1983).

Local buckling was observed in all of the test specimens in the current study. Flange buckling with little web deformation was the most common mode of local buckling, but in some cases flange buckling

was accompanied by significant web buckling. The location of initial local buckling varied, sometimes occurring at the fixed end, sometimes at the point of load inside the link region, and sometimes at the point of load outside the link region. As the loading program progressed the amplitude of local buckling increased dramatically, often becoming as large as the half flange width. In the latter portions of the loading program local buckling was generally distributed among all candidate regions (*i.e.* highly compressed flanges and adjacent webs).

The importance of local buckling in the cyclic post-buckling response of the test pieces is difficult to determine from these (or any other) experiments. Slight local buckling was present at the point of lateral buckling in some, but not all, specimens. This observation would suggest that the value of the limit load is not strongly affected by local buckling, a hypothesis which can be explored analytically. In some of the specimens local buckling was still slight after snapping through to the post-limit asymptotic load. Since the asymptotic buckling capacity was achievable under repeated cycling, in which the amplitude of local buckling grew dramatically, it would appear that this asymptotic load level, and thus the post-buckling response, was not strongly affected by the amplitude of local buckling. The experimental data also suggest that local buckling does not always affect the response of the beams in the pull direction, as yielding pull loads were repeatable in the presence of considerable local buckling. If deformations are large enough, local buckling will generally lead to pull lateral buckling.

Influence of Lateral Bracing.– One of the main parameters investigated in this series of tests was the effect of lateral bracing at the point of loading. An idealized bracing system was configured to restrain lateral motion, but not rotation, at either the top flange (load point) or the bottom flange as shown in Fig. 4.3. Specimens 1 and 2 had no lateral bracing, Specimens 3 and 5 had top flange bracing, and Specimen 4 had bottom flange bracing. The effects of lateral bracing are discussed below.

The most favorable location for bracing is the top flange, since the top flange is compressed under the unstable push loading. However, in certain applications it might be costly to implement such a bracing arrangement. As an example consider the eccentrically braced frames shown in Fig. 1.1. The links would be subjected to a bottom flange loading. Bracing is often done with joist beams which are more shallow than the main beam. Since it is desirable to use these joists to provide a level floor surface, they would frame into the main beam at the top flange, providing bracing at the flange opposite the loaded flange. Specimen 4 was tested to determine if far-flange bracing is effective in controlling lateral buckling.

The responses of Specimens 3 and 5 show that near-flange bracing effectively controls, but does not preclude, lateral-torsional buckling. Lateral buckling of Specimen 3 did not occur until the third push cycle, whereupon the brace buckled simultaneously. Specimen 5 buckled during the first cycle, but snap-through was controlled by the lateral bracing allowing a load of 50*k* to be sustained in the buckled configuration. (Specimen 3 had less post-buckling resistance because the brace was buckled. The brace was completely removed from Specimen 3 after it buckled). Specimen 5 showed a limit load of 28.5*k* in the second buckling cycle, and the asymptotic buckling capacity was 35% higher than the other specimens.

Specimen 4 did not buckle until the second cycle, indicating that far-flange bracing has some effect on the response of the system. However, the post-buckling characteristics of Specimen 4 were similar to the unbraced specimens. One can conclude that far-flange bracing is only marginally effective at improving the response of laterally buckling beams. It is interesting to note that the lateral motion of the bottom flange was small for both of the unbraced specimens in the post-buckling regime, indicating that the

center of rotation during lateral buckling was near the bottom flange. Under these circumstances one would expect bottom flange bracing to be ineffective. However, the location of the center of twist will be different for different cross-sectional geometries. The specimens tested may be a coincidental worst case for far-flange bracing.

The buckling of the brace in Specimen 3 is particularly significant in that it gives us information on inadequate lateral bracing. The brace was made of 3/4 *in* threaded steel rod, was 33 *in* long, and was pinned at both ends. Hence, the ratio of the area of the brace to the area of the compression flange is approximately 0.45. The brace easily meets the requirements of strength and stiffness proposed by Lay and Galambos (1966). The buckling load of the brace was about 5% of the squash load of the compression flange (*i.e.* $\sigma_0 b t_f$, much greater than the 2–2.5% traditionally suggested for such applications). The brace buckled simultaneously with the beam and can therefore be considered undersized.

It would be difficult to make specific recommendations about lateral bracing of short beams based on the experiments, however, the following observations seem appropriate:

(*a*) Since the beam can adjust its center of rotation, single point bracing (or any bracing which approximates it) is far less effective than bracing which also provides rotational restraint. If single point bracing must be used, then bracing of the flange closest to the point of load transfer is superior to any other position. It seems prudent in the case of eccentrically braced frames to brace at the point of load with full rotational restraint.

(*b*) Traditional estimates of the required size of the bracing member are inadequate for short beams, possibly by a factor of two. However, in typical applications the size of the brace often far exceeds the minimum required to resist buckling.

The important thing to remember is that short beams represent an extreme case of lateral buckling, and that the cyclic load environment presents some fundamentally different phenomena beyond the monotonic loading case. The design of these elements requires due regard of these extremes.

4.4 Analytical Model of the Test Specimens

In order to put the experiments into proper perspective, we will further explore the behavior of the propped cantilever beams by perturbing the constitutive and geometric parameters of the theoretical model. These parameter studies will be described in the following three chapters. It is important to execute the perturbations about a configuration of the analytical model which represents the experiments well. This *standard* model was determined by adjusting the parameters (within the constraints of measured values) until reasonable correspondence with the experiments was attained. The standard model will be the basis of all future parameter studies and is presented in this section.

The values of the parameters are given in Table 4.5. The total length of the beam, L, is taken to be 82 *in* and the distance from the fixed end of the beam to the point of load, l, is taken to be 20 *in*, as measured in the experiments. The dimensions of the cross section of the beam are taken equal to the measured values of the test piece. The elastic moduli of the material are set to values generally accepted for steel while the yield strength and ultimate strength are as measured in the material tests. The load transfer mechanism is idealized using a rigid link as shown in Fig. 4.12. The point of load application is a distance $\bar{a}$ above and $\bar{e}$ to the right of the shear center. The standard value of the load height is taken to be the distance from the shear center to the center of the loading clevis as measured in the experiments.

Table 4.5 Dimensions and properties of the standard model

Section dimensions (*in*)		Member properties (*in*)		Material properties (*ksi*)	
Depth, h	9.82	Length, L	82.00	Youngs modulus, E	30,000
Width, b	4.00	Load position, l	20.00	Shear modulus, G	12,000
Web thickness, t	0.18	Height of load, $\bar{a}$	9.41	Yield strength, σ_0	48
Flange thickness, t_f	0.20	Eccentricity of load, $\bar{e}$	0.01	Ultimate strength, σ_u	69

The rigid link is modeled with a finite deformation box-section beam element. The element is made very stiff and remains in the elastic state throughout the loading histories. The validity of modeling the load position in this manner should be clear. The kinematics of the analytical model are referred to the line of centroids, which coincides with the line of elastic shear centers, only for convenience. Because the model is formulated in terms of stress components, the constitutive equations are treated locally, obviating the need for keeping track of the instantaneous location of the inelastic shear center. Stress resultant beam theories rely crucially on knowing the location of the shear center, but they do so only to get the constitutive equations correct.

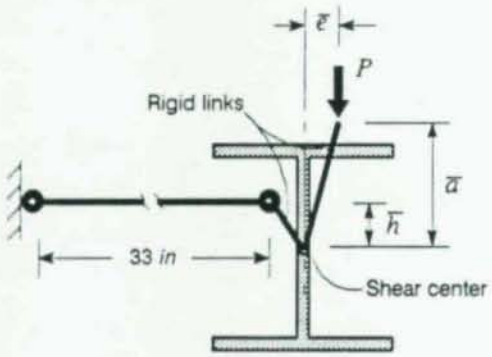

Fig. 4.12 Idealized load transfer and bracing mechanism

The finite flexibility of the fixed end, due to the presence of the load cell, is examined in Chapter 6. Since the load cell used in the experiments was a circular tube, its torsional flexibility is negligible in comparison with that of the test piece I-section. On the other hand, the flexural flexibility of the load cell was on the same order as the test piece. The load cell is modeled with a box section in the analytical studies as shown in Fig. 4.13. The length of load cell is designated as l_c. The box section is a reasonable model of the load cell because it has a similar ratio of torsional to flexural stiffness and was much easier to implement numerically than a circular beam. In Chapter 6, various end flexibilities are examined by changing the length and cross-sectional dimensions of the load cell.

The effects of lateral bracing are examined in Chapter 7. The lateral bracing arrangement was idealized as shown in Fig. 4.12. The position of the brace was enforced by placing a rigid link (modeled with the box section) between the shear center and the brace point as shown. The brace was pinned to the

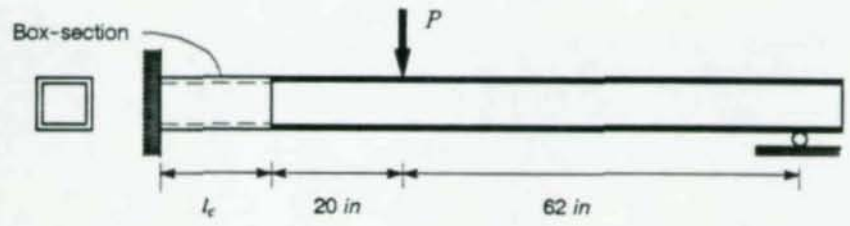

Fig. 4.13 Idealization of test beam with load cell

rigid link and either pinned or fixed at the support. In the parameter studies the brace elevation $\bar{h}$ was varied while the length of the brace and its lateral position (about 1 *in* left of the web) were held fixed.

In addition to the properties listed in Table 4.5, the following constitutive parameter values also characterize the standard model: *(a)* the equivalent plastic strain at the onset of strain hardening, $\bar{\varepsilon}_1^p$ = 0.0235 and *(b)* the nonlinear isotropic hardening moduli of the exponential hardening model, $K = 0$ and $\gamma = 25$. The values of the constitutive parameters were approximated based on the experimental tensile tests. The hardening moduli will be the same for all parameter studies.

The analyses were carried out with displacement control at the point of load. The vertical displacement and rotation at the shear center under the point of load are used to characterize the displacement history in the parameter studies.

4.5 Validity of the Proposed Analytical Model

In this section we present the cyclic response of the standard model as evidence that it represents the phenomena observed in the experiments well. In particular, we note that most of the typical features noted in the experiments are reproduced faithfully by the analytical model. Only qualitative comparisons between analysis and the experiments are made because the measurements of the movement of the fixed end in the experiments were not sufficient to produce an accurate model of the end flexibility.

The cyclic inelastic response for the standard model (without load cell), under the load history of test Specimen 2, is shown in Fig. 4.14. Observe that the qualitative behavior is well represented by the analytical model, particularly the initial buckling response, the recovery and yielding in the pull direction, and subsequent push buckling.

ince the analytical model is based on a beam-type kinematic hypothesis, the analytical model is unable to represent local buckling of the web or flange elements. In view of the fact that the model reproduces nearly all aspects of the cyclic load response of short beam, except possibly the final failure mode, one can conclude that local buckling plays a secondary role in the response of these systems. In particular, the asymptotic post-buckling capacity is not affected by the local buckling. It would appear that proper modeling of the finite rotation of the cross-section is sufficient to accurately capture the lateral buckling and post-buckling response of these beams. The excellent qualitative correlation between analysis and experiment lends credence to the model and to the parameter studies that follow.

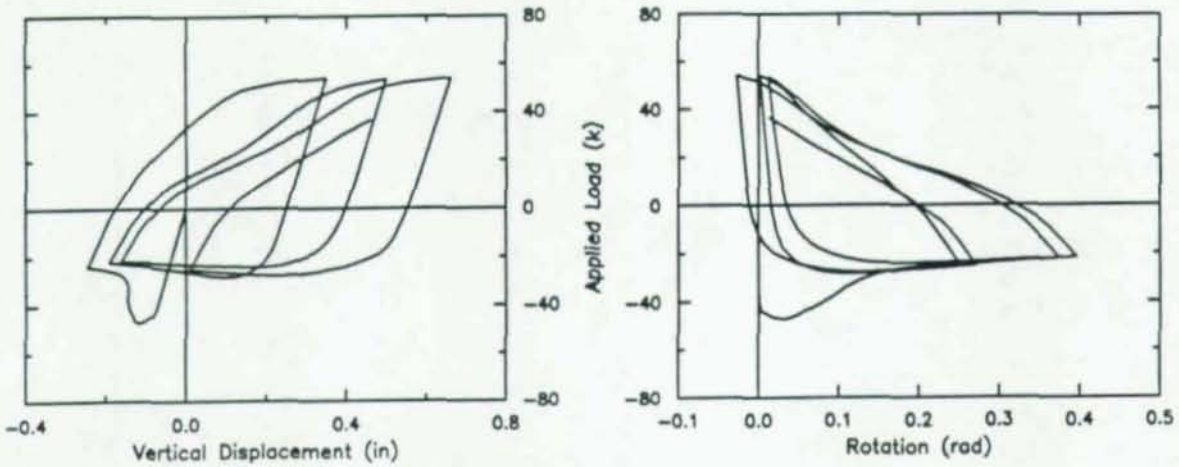

Fig. 4.14 Cyclic load response for the standard model

Chapter 5

An Analytical Study of the Parameters Affecting the General Response of the Test Specimens

The general cyclic lateral buckling response of the test specimens without end flexibility and lateral bracing is examined in this chapter. Parameters studied include constitutive parameters, residual stresses, geometrical imperfections due to the eccentricity of loading, cross-sectional dimensions, total length, locations of load, and remote boundary conditions. The response of the systems with perturbed parameters are compared with the response of the standard model described in the previous chapter. The configuration of a standard model is shown in Figs. 4.13 and 4.12, and its properties and dimensions are listed in Table 4.5.

5.1 Effect of Constitutive Parameters

Several constitutive parameters are expected to have an important effect on the buckling resistance of beams. Among these are the yield strength, the length of the yield plateau, and the strain hardening parameters. These parameters are important because yielding tends to reduce the beam's resistance to buckling, especially for short beams. The following parameter study is designed to assess the importance of these material parameters for both cyclic and monotonic loading conditions.

The material properties of the standard model are as follows: yield strength (σ_0 or κ_0) = 48 *ksi*, ultimate strength (σ_u or κ_∞) = 69 *ksi*, and equivalent plastic strain at the onset of strain hardening ϵ_{sh} = 0.0235. Ultimate strengths 69 *ksi*, 79 *ksi*, and 89 *ksi* correspond to yield strengths 48 *ksi*, 58 *ksi*, and 68 *ksi*, respectively (except for the perfectly plastic case), which means the shape of the strain hardening curve is the same regardless of the value used for the yield strength. Kinematic hardening employed in the proposed cyclic plasticity model was automatically included in all cases, except where this parameter is explicitly studied. Fig 5.1 describes the above mentioned constitutive parameters.

As expected, the yield strength influences the initial buckling load and post-buckling capacity of the beams, as shown in Figs. 5.2(*a*,*b*). While the responses of initial-buckling are the same for the strain

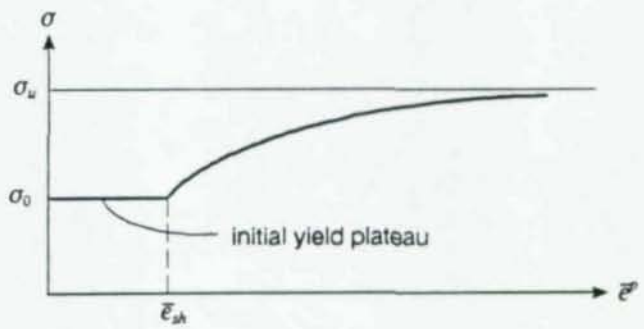

Fig. 5.1 Description of the constitutive parameters

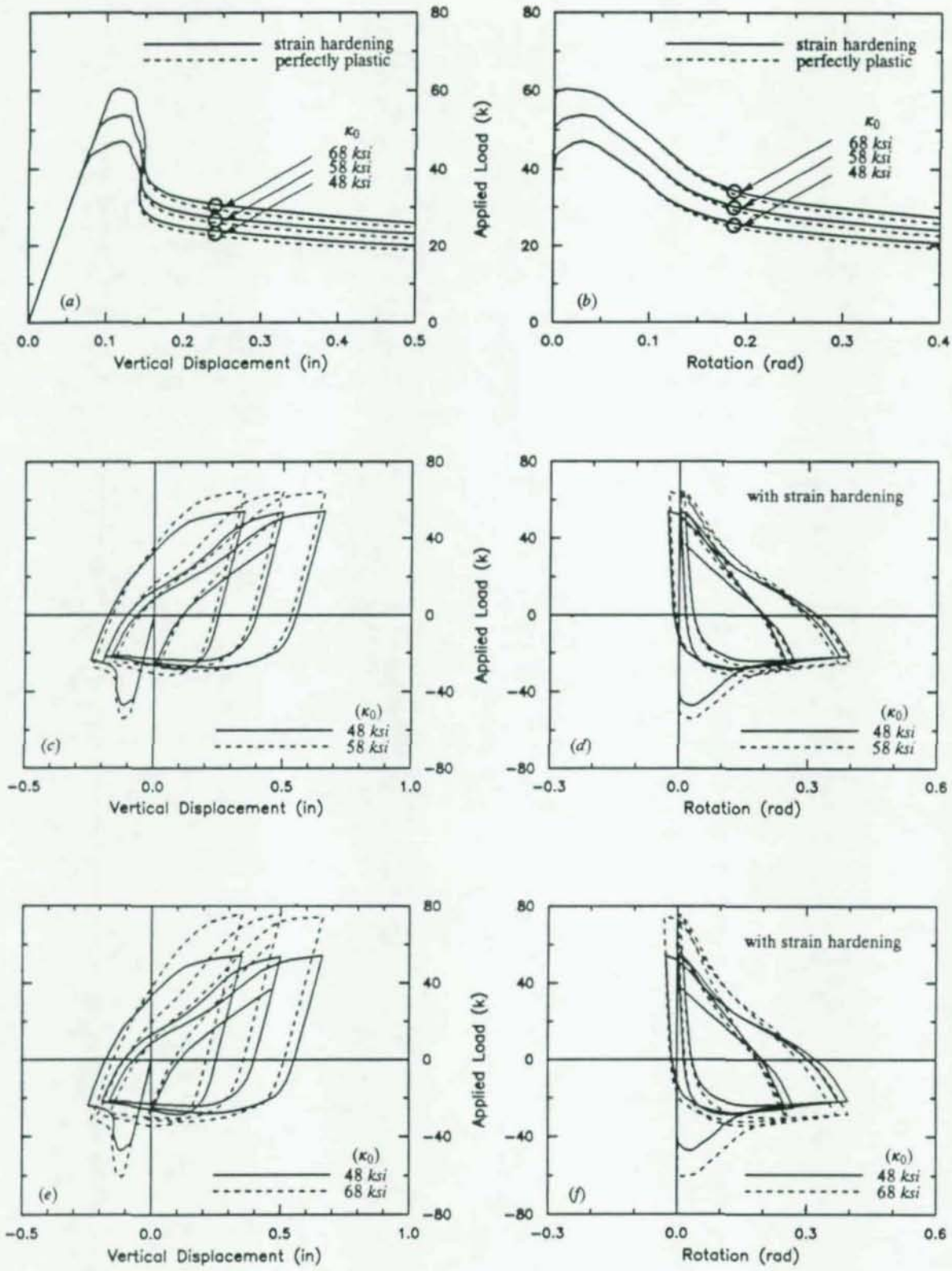

Fig. 5.2 Effect of yield strength: 48, 58, 68 *ksi*

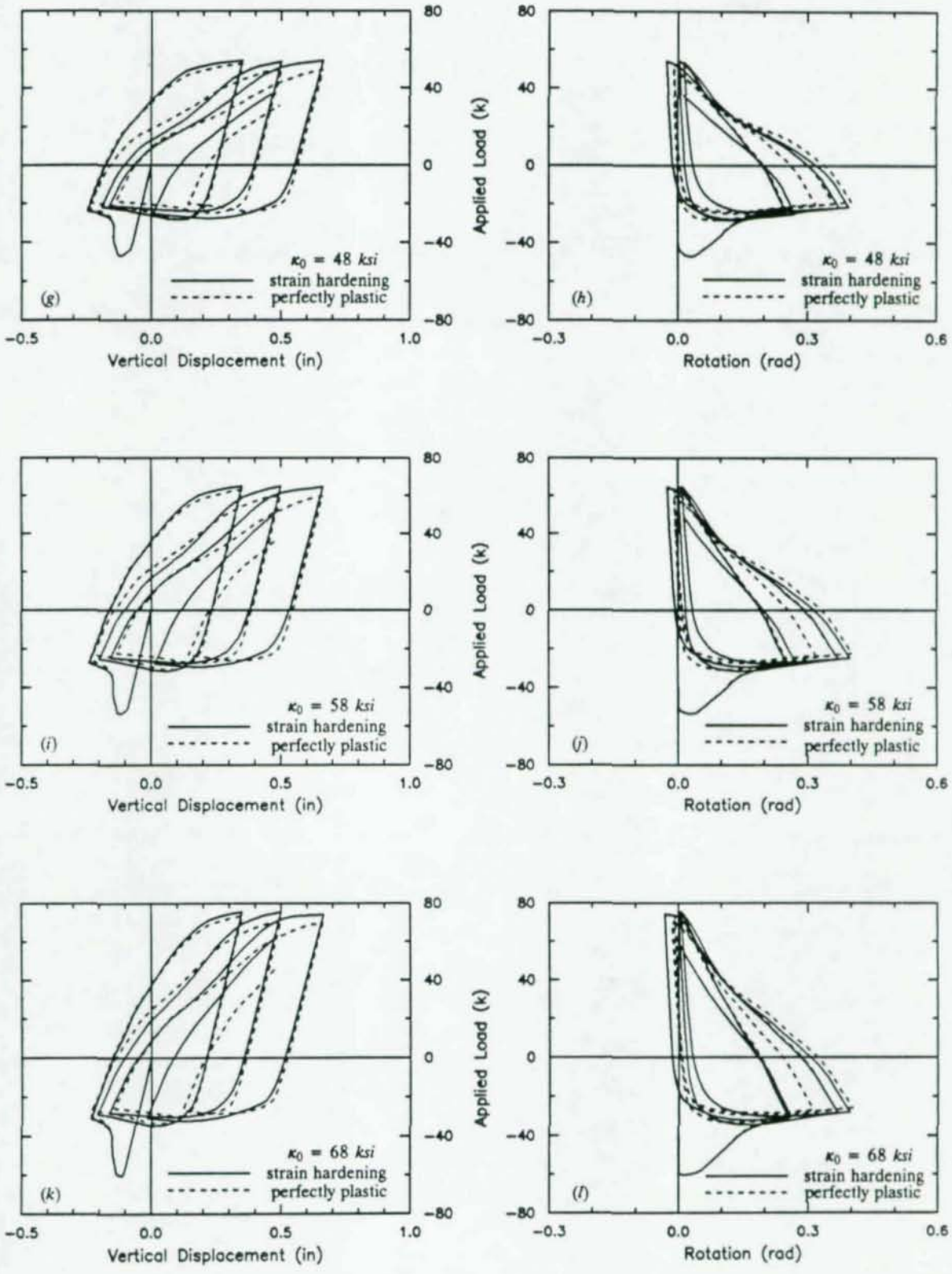

Fig. 5.2 *(cont.)* Effect of yield strength: 48, 58, 68 *ksi*

hardening case as for the perfectly plastic case at the same yield strength, the post-buckling capacity of the strain hardening case is larger than that of the perfectly plastic case for the same yield strength. The differences between them are almost the same regardless of the yield strength. The response curves of the perfectly plastic case and the strain hardening case in the post-buckling regime do not coalesce at large deformation because strain hardening has its greatest influence there. Judging from these observations, yield strength has a preponderant influence on the initial-buckling load and the post-buckling behavior. Initial-buckling generally occurs before strain hardening starts and hence strain hardening affects only the post-buckling response. Figs. 5.2(*c–f*) show the influence of each yield strength on cyclic response. As yield strength increases, pull yield load and asymptotic post-buckling capacity also increase notably.

Differences in the cyclic responses between the strain hardening and the perfectly plastic cases are illustrated in Figs. 5.2(*g–l*). The latter case has a slightly smaller pull load and asymptotic post-buckling capacity than the former one in the first cycle. The difference becomes smaller with additional cycling. Observe that yield strength also has an influence on the cyclic response even in the perfectly plastic case and the effect of strain hardening on the response to cyclic loading.

The influence of the length of the initial yield plateau is examined in Figs. 5.3(*a,b*). The response (including strain hardening) without an initial yield plateau has a slightly larger initial buckling load than any case with an initial yield plateau. The post-buckling responses are bounded above by the case with no plateau and below by the perfectly plastic case (infinite length plateau) for the entire range of monotonic behavior. The response curves for various plateau lengths do not converge on each other at large deformation probably because of strain hardening. Initial buckling occurs while most of the yielded material is on the yield plateau at plastic strains less than $\bar{\varepsilon}_i^p = 0.01175$, as evidenced by the fact that the responses for cases having a yield plateau greater than this value are identical at buckling. The effects of length of the initial yield plateau on the cyclic response of the test beams are examined in Figs. 5.3(*c,d*). The standard case ($\bar{\varepsilon}_i^p = 0.0235$) is compared with the case in which there is no yield plateau in Figs. 5.3(*c,d*). As noted previously the initial buckling load is slightly larger than with no plateau. Because strain hardening manifests earlier in this case the pull yield load and subsequent buckling loads also tend to be greater than the case that has a yield plateau. The observations are reinforced by comparing the other bounding case (perfectly plastic) with the standard case (Figs. 5.2(*g,h*)). In general, one might conclude that the effects of the length of the yield plateau are minor.

Figures 5.4(*a,b*) show the influence on the cyclic buckling response of the kinematic hardening model used to simulate cyclic plasticity here. Due to the change in the way Bauschinger's effect is modeled in the absence of kinematic hardening, notable differences in the response during the pull recovery from buckling can be seen. The response of kinematic hardening reduces the carrying capacity at comparable levels of deformation. Kinematic hardening also reduces the subsequent buckling loads. Qualitatively comparing these results with the cyclic load response of test specimen 2 in the experiments (Fig. 4.7), one can recognize the importance of kinematic hardening to the model.

5.2 Effect of Eccentrically Placed Load

Systems which exhibit limit loads with unstable post limit behavior are generally senstive to geometric imperfections. One of the important geometric imperfections in the propped cantilever test system is

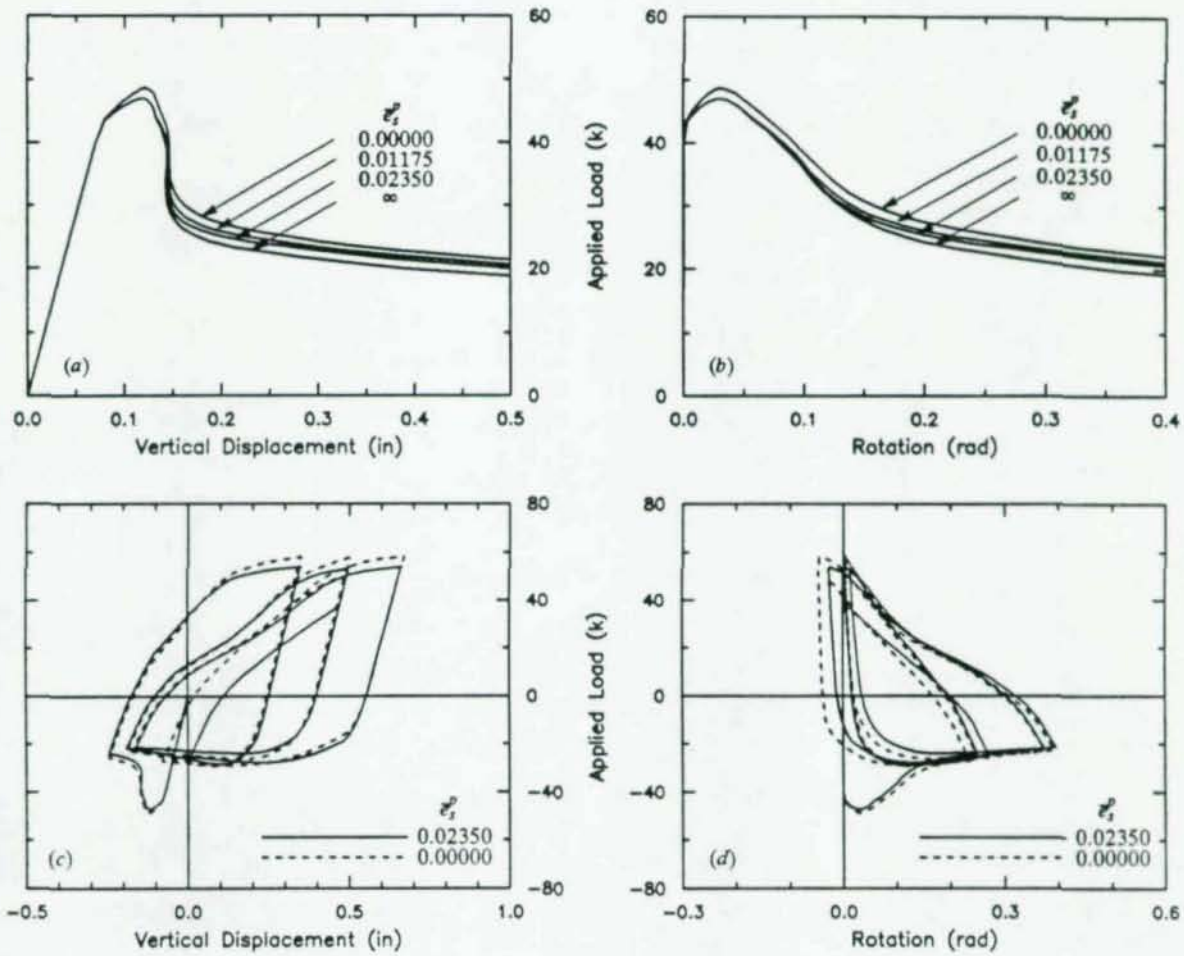

Fig. 5.3 Effect of length of initial yield plateau

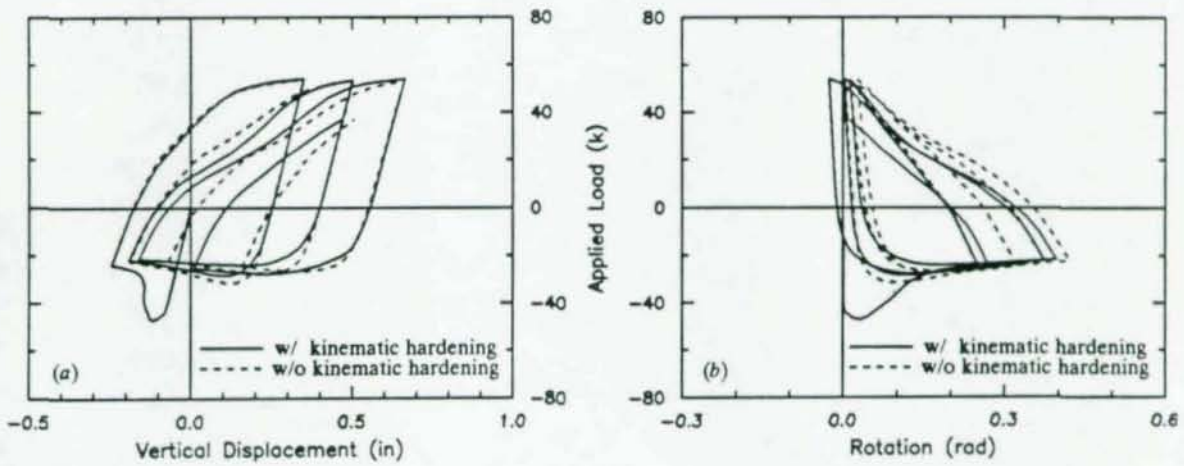

Fig. 5.4 Cyclic load response for kinematic hardening with isotropic hardening

eccentricity of the line of action of the load with respect to the shear center (and centroid) of the cross-section (Fig. 5.5). An eccentrically placed load will promote rotation of the cross-section prior to the buckling and will therefore reduce the magnitude of the limit capacity. In this section we examine the effect of eccentric placement of load on the monotonic and cyclic response of the test system.

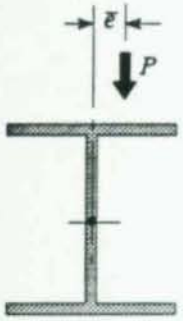

Fig. 5.5 Eccentricity of load position

In general, it is impossible to achieve perfect placement of load in a physical test, although every effort was made to do so in the tests reported here. In nature, even a perfect system will buckle if it passes through a bifurcation point. A perfect numerical model will not necessarily do so. In the studies performed here values of the eccentricity smaller than 0.01 *in* gave identical response of the system with respect to lateral buckling. Therefore the 0.01 *in* eccentricity is adopted as the *perfect* system for the analytical model. This value is designated e_0 in the subsequent study. Comparison of the *perfect* analytical model with the experiments would indicate that perfect load placement was nearly achieved in the experimental system.

The results of initial monotonic buckling with values of eccentricity of e_0, $5\,e_0$, $10\,e_0$, $20\,e_0$ and $50\,e_0$ are shown in Figs. 5.6(*a*,*b*). One can observe a considerable reduction in limit capacity for the modest eccentricities examined. The sharp limit response with sudden loss of capacity prevalent at small eccentricities begins to disappear at large eccentricities. One could surmise that the limit-type behavior would disappear entirely for a large enough eccentricity. For all values of eccentricity the post-buckling capacity is the same, even though for large eccentricities considerable deformations are required to achieve it. The tendency toward the same post-buckling capacity highlights the fundamental importance of this resistance parameter to the general response of these systems.

The cyclic response of the beams with initial load eccentricities is illustrated in Figs. 5.6(*c*-*f*), covering eccentricities of e_0, $10\,e_0$ and $50\,e_0$. One can observe that these eccentricities play a minor role in the cyclic response, the extent of influence being directly related to the magnitude of the eccentricity. This loss of memory of the initial eccentricity is expected for systems like these which experience considerable yielding.

5.3 Effect of the Height of the Load Point

It is well known that the height of the load with respect to the shear center of the cross-section has a significant effect on the linear elastic lateral buckling load. One would also expect it to have an important

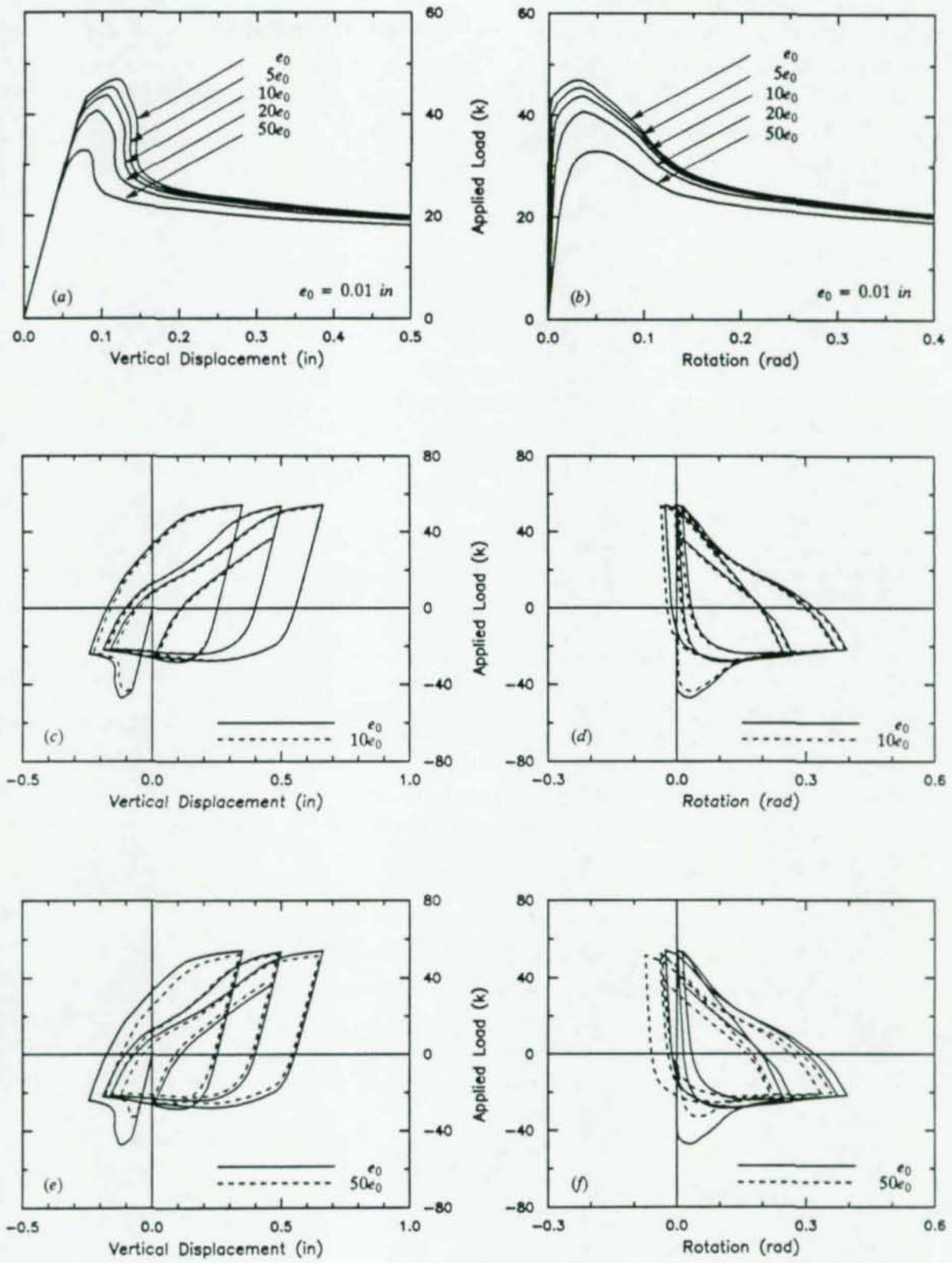

Fig. 5.6 Effect of horizontal eccentricity of load

influence on the inelastic buckling response. The effect of the height of the load on the elastic linearized buckling loads for the test configuration is shown for both pull and push loading directions in Fig. 5.7. In the experiments, the height of the load, measured from the center of the clevis was approximately 9.4 *in*. This value is taken as the standard value for the present parameter study which examines the response for both cyclic and monotonic loading conditions. A rigid link was used to apply the load remote from the shear center, as shown in Fig. 4.12.

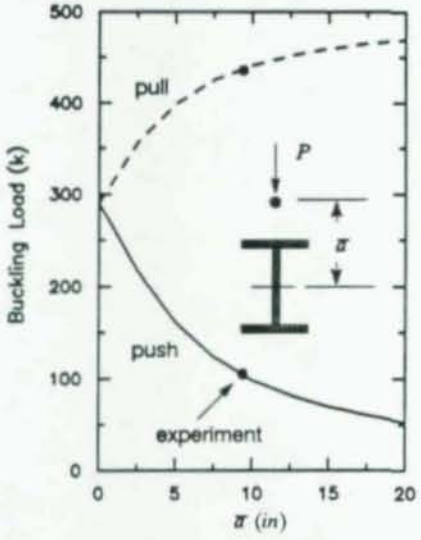

Fig. 5.7 Effect of height of load on linearized buckling load

The monotonic buckling and post-buckling response curves for the propped cantilever for load heights of 5, 8, 9.4, 11 and 14 *in* are shown in Figs. 5.8(*a*,*b*). As expected, the initial-buckling load and post-buckling capacity increase with a decrease in in the height of load, and the rate of loss of post-buckling capacity is lessened as the height of load decreases. The response curves of post-buckling do not coalesce at large deformation. Buckling is quite delayed for a load height of 5 *in*. One would thus expect that the beam would be more reluctant to buckle as the load is applied nearer to the shear center. Response to loads applied in the pull direction are expected to be stable.

The effects of load height on cyclic response are shown in Figs. 5.8(*c*-*f*). The height of 5 *in* is compared with the standard case in (*c*,*d*) while the height of 14 *in* is compared with the standard case in (*e*,*f*). There is virtually no difference in the pull yield load, but the asymptotic post-buckling response is greatly influenced by the height of the load. The height of the load application has a significant influence on the limit load, the post-buckling response at large deformation, and the response to subsequent cyclic loading.

5.4 Effect of the Load Location along the Beam Length

The propensity of a beam to buckle laterally is directly related to the distance of the potentially destabilizing force from a point where torsional motion is restrained. In design this distance is often called the *laterally unsupported length*. Qualitatively, the torsional stiffness accrues linearly with length from St. Venant resistance and cubically with length from warping torsion resistance for an elastic beam.

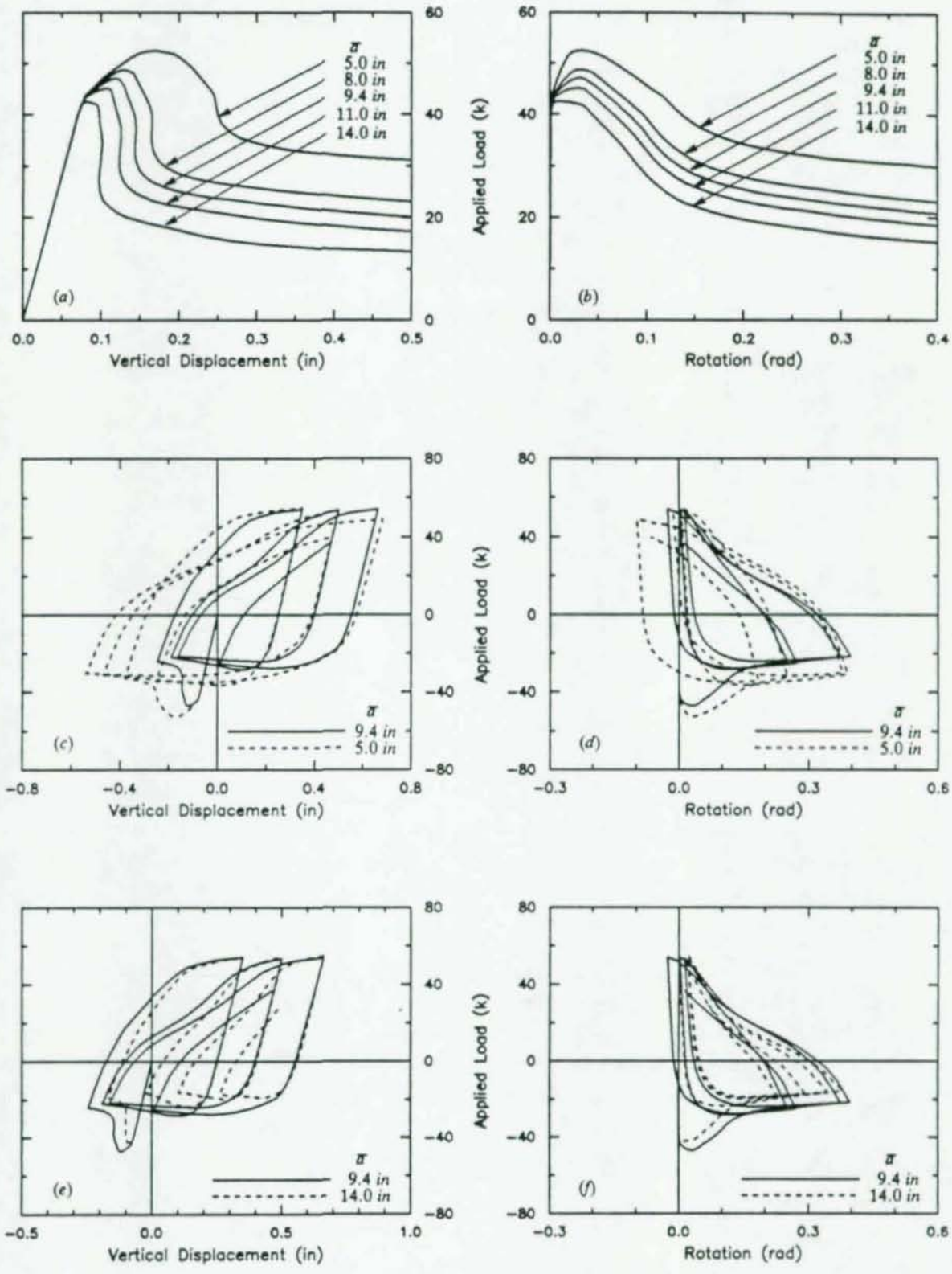

Fig. 5.8 Effect of height of load application

For short beams the warping torsional stiffness becomes so great as to practically preclude buckling. This tendency is illustrated in Fig. 5.9 which gives the linearized buckling load as the position of the load is varied over the entire length of the propped cantilever beam. Here, the minor length, l, can roughly be considered the unsupported length of the beam. As the point of loading approaches the supports the linearized buckling load becomes large, indicating less propensity toward buckling. The beam loaded remote from the supports shows a relatively great propensity to buckle. The length of beams examined herein lie in the transition range between clearly long beams and short beams which are generally reluctant to buckle.

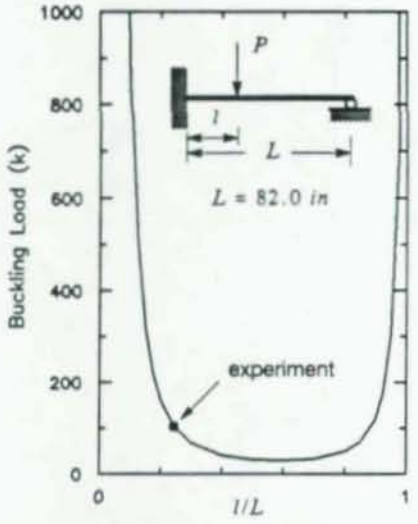

Fig. 5.9 Effect of location of load on linearized buckling load

The purpose of the present section is to put the buckling of short beams into the wider context of longer beams which are more common in applications and which have been more thoroughly studied. There is basically one issue at stake here: Even if a beam is able to reach its fully plastic capacity, might it yet buckle and thereby suffer important design consequences. These issues are examined in the sequel both for monotonic and cyclic loading.

As expected, the location of load along the length of the beam has a great influence on the initial-buckling load and the post-buckling response, as shown in Figs. 5.10(a,b). The limit point can be seen to be sharper as the location of the load approaches the middle of beam, and initial buckling is delayed as the location of the load approaches the fixed end. The response curves of post-buckling do not coalesce at large deformation. The dot symbols (•) on the monotonic response curves (Figs. 5.10(a,b,g)) represent the points where the loading direction changes from push to pull in the cyclic loading histories.

The beam of length l = 15 *in* exhibits a strong reluctance to buckle. However, as shown in Fig. 5.10(g) even this short beam buckles at a vertical displacement of over 1 *in*. For the cyclic loading history this beam survives the first cycle without buckling but buckles in the second cycle, demonstrating that inelastic cycling greatly increases the tendency for a beam to buckle. Since a great degree of strain hardening had occurred prior to buckling, the subsequent push and pull capacities were greater than the comparison beam (l = 20 *in*). However, buckling did have a typically debilitating effect.

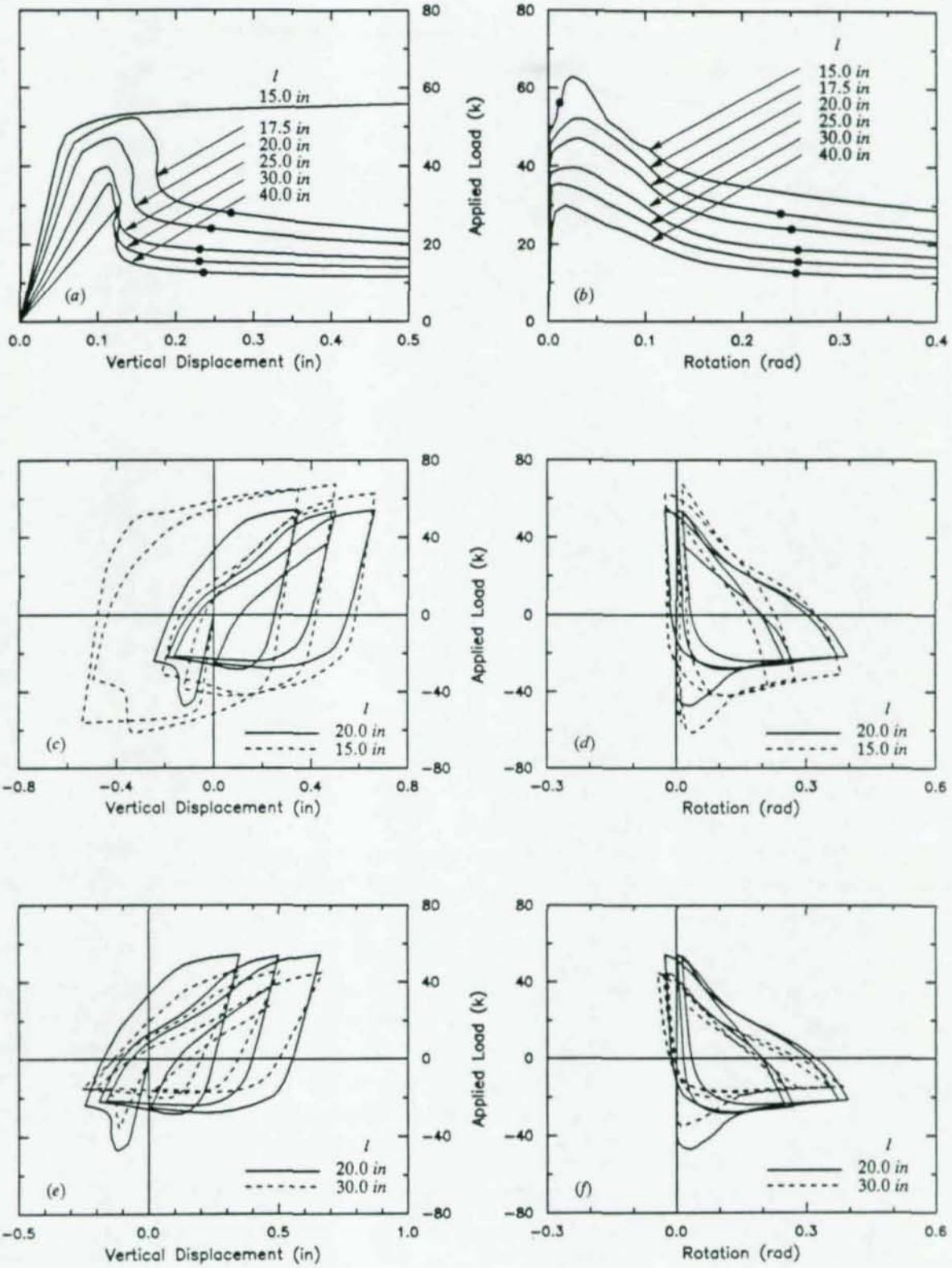

Fig. 5.10 Effect of the location of the load along the length of the beam

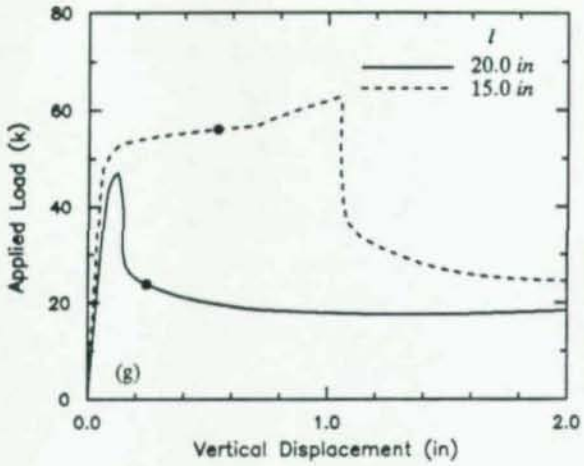

Fig. 5.10 *(cont.)* **Effect of the location of the load along the length of the beam**

The cyclic response of a longer beam (l = 30 *in*) is compared with the standard (l = 20 *in*) in Figs. 5.10(e,f). While the 30 *in* beam clearly exhibits inferior behavior, the qualitative aspects of response are similar for the two cases.

5.5 Effect of Cross-Sectional Dimensions

Resistance to lateral buckling clearly depends upon the geometric properties of the beam. In particular, the cross-sectional dimensions are expected to strongly influence the behavior. The W10x12 section examined in the experiments is geometrically similar to many of the available "*beam*" type sections in the W18 and deeper classes, which are characterized by deep webs with relatively narrow flanges. For short beams a great deal of the resistance to buckling comes from warping resistance which is dominated by the major moment of inertia of the flanges and the distance between them. Consequently, beam depth and flange width can be considered the most important geometric properties of the beam.

In this section we present a parameter study which is designed to assess the effect of width and height of the cross-section both for monotonic and cyclic loading conditions. Since a variation of the cross-sectional dimensions with no change of length would give exaggerated results, the total lengths of the propped cantilever are chosen to give the same elastic deflection at the point of loading as that of the standard case. All the dimensions of the beam studied are described in Table 5.1. Note that for the height of beam 1.5 times that of the standard case the height of load application is increased accordingly. The dot symbols have the same meaning as those of the previous study.

The monotonic buckling response for a beam of depth 9.8 *in* (standard) and width of 4, 5 and 6 *in* are given in Figs. 5.11(a,b,g). The cyclic response of these cases is given in Figs. 5.11 (c–f). One can observe that initial buckling is delayed by increasing the ratio of width to height of the cross-section without a change in the depth. There is a dramatic delay in initial buckling at the width of 5 *in*, and at the width of 6 *in* the beam does not buckle until well into the strain hardening regime. One remarkable feature of the monotonic response is that the load versus rotation curves are nearly parallel for the three

Table 5.1 Description of cross-sectional dimensions

h (*in*)	b (*in*)	L (*in*)	l (*in*)	$\bar{a}$ (*in*)
9.8	4.0	82.0	20.0	9.4 *(standard case)*
9.8	5.0	85.4	20.8	9.4
9.8	6.0	88.3	21.5	9.4
14.7	4.0	114.6	27.9	11.9

cases, despite the differences in vertical displacements. The asymptotic post-limit capacity also increases with the width of the beam.

Contrary to the case of variation in the width, changing the depth results in a relatively small change in the limit load, as shown in Figs. 5.12(*a–d*). However, the deeper beam exhibits a much sharper limit point than the standard case. The post-limit response curves converge right after initial buckling for monotonic loading, and the asymptotic post-buckling capacity is almost the same for both. The load-rotation curves are nearly identical for the two cases.

The cyclic responses of the two cases are shown in Figs. 5.12(*c,d*). A peculiar feature can be noted in the first pull yielding region wherein a limit load occurs in the pull direction. Otherwise, the deeper section behaves like the shallower beam in the cyclic regime. One might conclude that increasing the flange width is an effective way to control buckling whereas increasing depth is not.

5.6 Effect of Total Length and Ratio of Load Location to Total Beam Length

The total length of the beam and the location of the load along the length are two other important geometric parameters. The location of load along the length of the beam has already been discussed, but it must also be considered in the study of different length beams. The effect of beam length will be examined in this section. Figure 5.13 shows the effect of total length with a constant ratio of the load location to the total beam length, l/L = 20/82, and the effect of the total length with constant location of load, l = 20 *in*, respectively, on the elastic linearized buckling loads. The effect on the linearized buckling load of the load location along the beam length (with constant total length, 82 *in*) can be found in Fig. 5.9. The buckling load is quite sensitive to these parameters with the shorter beams showing a reluctance to buckle. The experimental values of these parameters, shown on the sketch as dots, are generally in the transition region. In this section we study these parameters for both cyclic and monotonic loading cases.

The limit load and asymptotic post-limit capacity decrease rapidly with an increase of the total length of the beam, at the constant ratio, l/L = 20/82, as shown in Figs. 5.14(*a,b*). The post-limit degradation of capacity decreases as the total length of beam increases, with flexible beams hardly showing a limit point. As shown in Figs. 5.14(*c,d*), there is a great decrease of pull yield load and and asymptotic post-buckling capacity in cyclic loading response.

Figures 5.15(*a,b*) show the monotonic behavior of the beam for various total lengths but with a constant location of load at l = 20.0 *in*. In contrast to the previous case, initial buckling load and asymptotic post-buckling capacity do not decrease very rapidly with an increase in length. Also the limit point does not get sharper with an increase of the total length. This aspect might be anticipated from Fig.

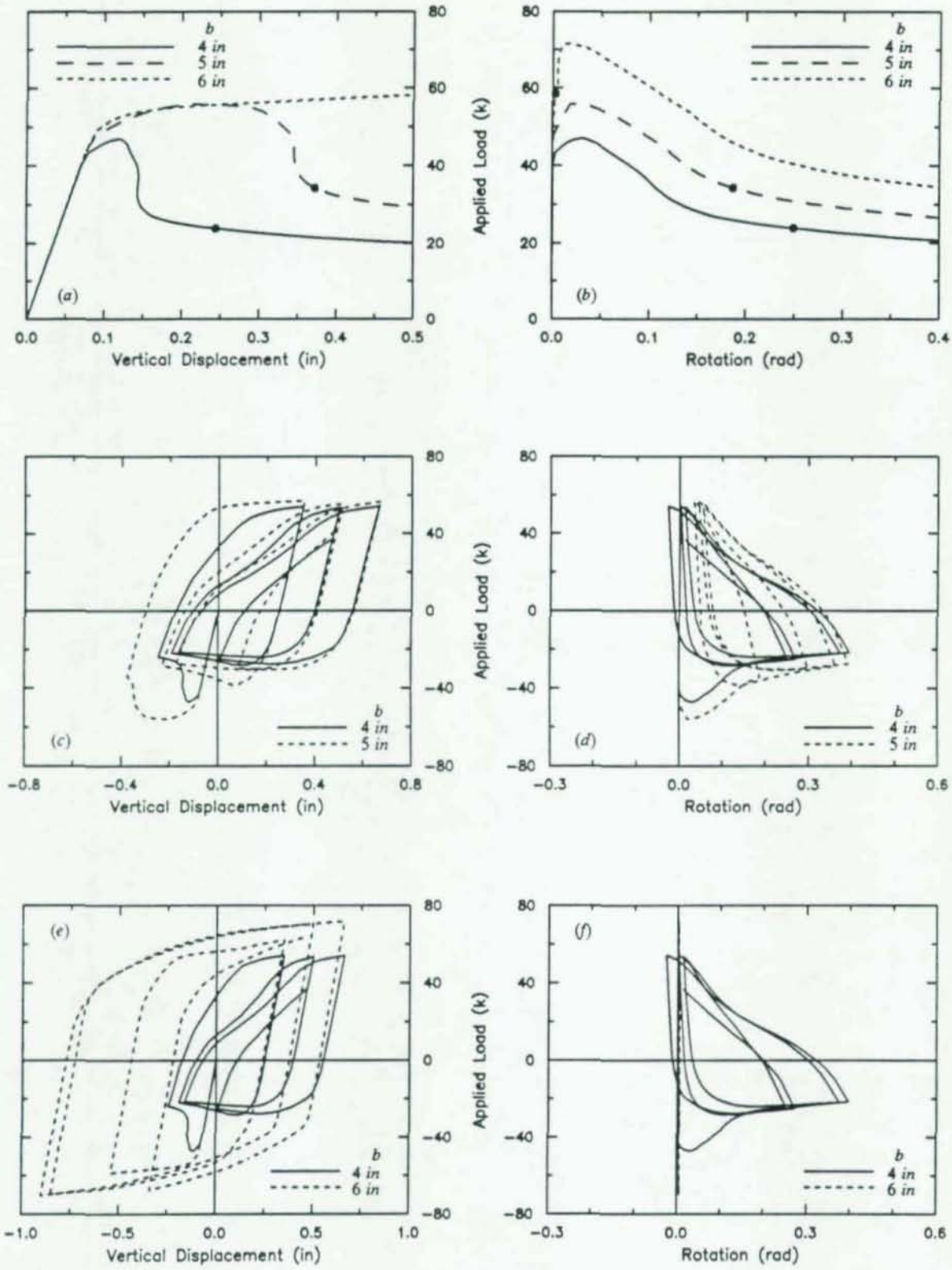

Fig. 5.11 Response of beams with standard depth and various flange widths

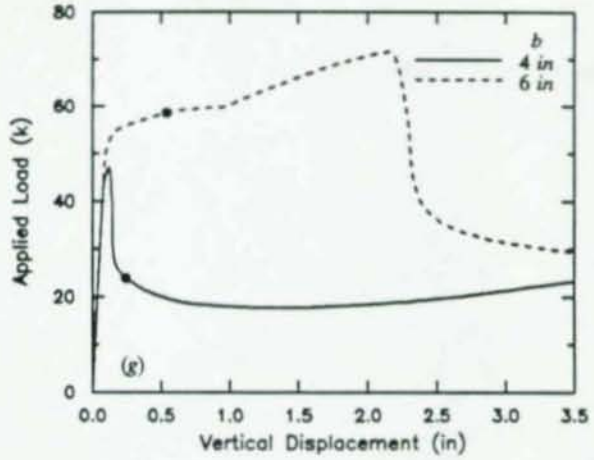

Fig. 5.11 *(cont.)* Response of beams of standard depth and various flange widths

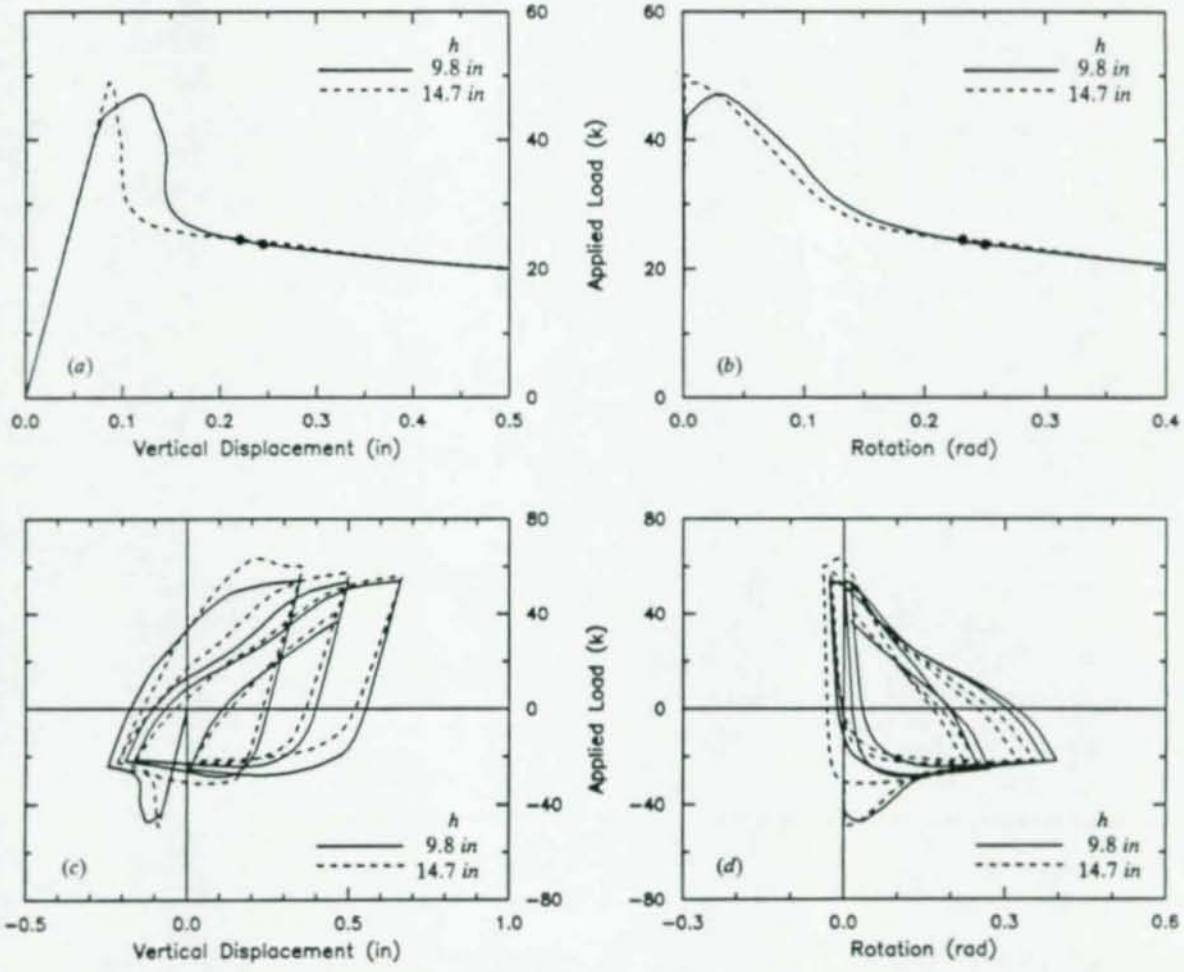

Fig. 5.12 Response of beams of standard width and various depths

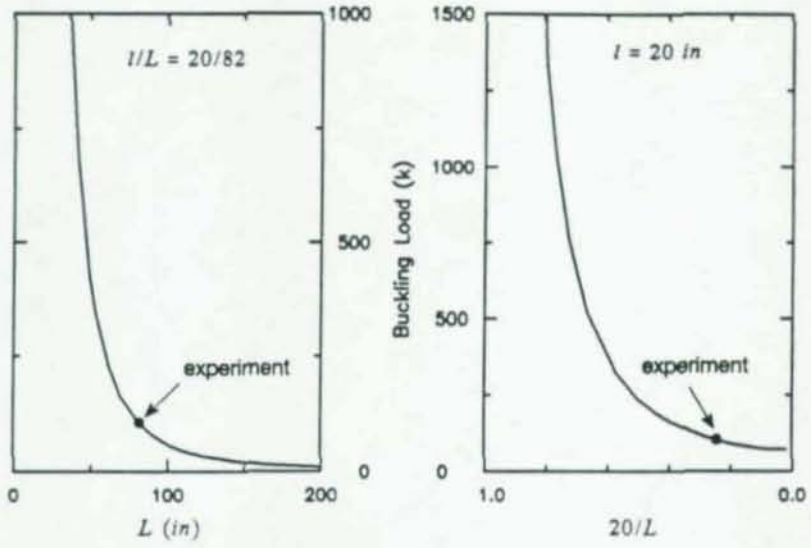

Fig. 5.13 Effect of ratio of location of load to total length of beam on elastic linearized buckling loads

5.13(*b*), where the experimental value of this case is on a less sensitive region of the curve than the previous study.

The response to cyclic loading is shown in Figs. 5.15(*c–f*). While the asymptotic post–buckling capacity shows no difference from that of the standard case, the pull yield load decreases and the sharpness of the limit point disappears, as the total length of beam increases with constant location of load. From these observations the total beam length has a great effect on the initial–buckling, and the load location has the predominant influence on large deformation behavior and cyclic response.

5.7 Effect of Residual Stresses

Residual stresses have long been recognized as having an important influence on the inelastic buckling of beams and columns. The beam stiffness is reduced by early yielding due to the presence of residual stresses, increasing the propensity to buckle. The pattern of residual stresses is well established for virgin sections, but this pattern may be changed by cyclic inelastic straining. Therefore we must reexamine our understanding of the effects of residual stresses for cyclic loading conditions.The pattern that exists in the cycle prior to buckling will determine the buckling characteristics of the beam for the subsequent cycle. A study of the influence of the distribution of residual stresses on beam buckling is made for both monotonic and cyclic loading conditions. A basic polynomial residual stress pattern is used for the analytical approximation, as shown in Fig. 2.4, and the maximum values range from 0 to σ_0 in steps of $0.25\sigma_0$ without changing the pattern.

Since yielding with residual stresses occurs well before initial buckling, the limit capacity decreases and the limit point blunts with an increase in the maximum value of residual stresses, as shown in Figs. 5.16(*a,b*). The response curves in the post–buckling range coalesce at large deformation. There is no difference in the asymptotic post–buckling capacity and pull yield load on the cyclic loading response.

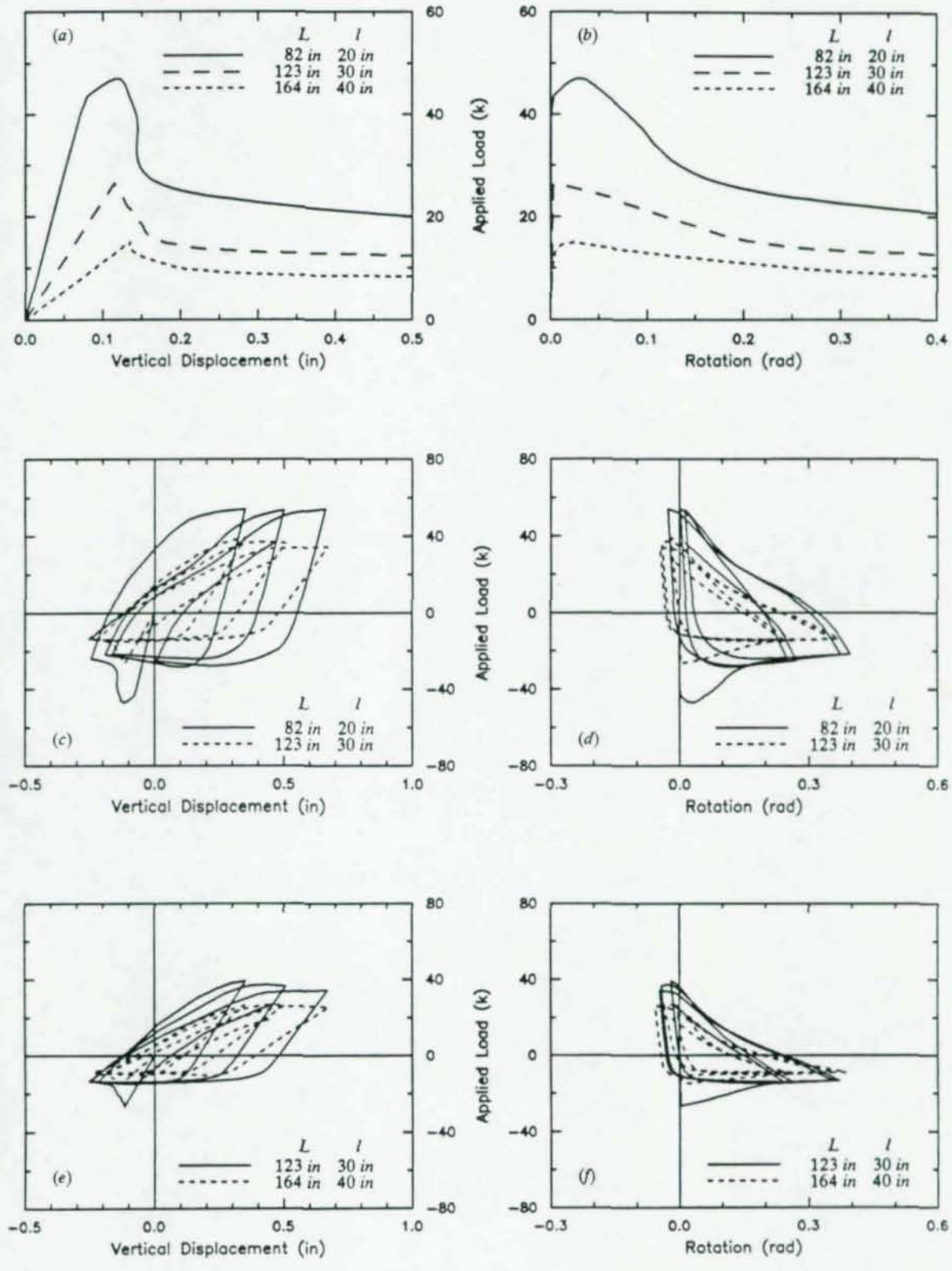

Fig. 5.14 Effect of changing the total length of the beam with l/L = 20/82

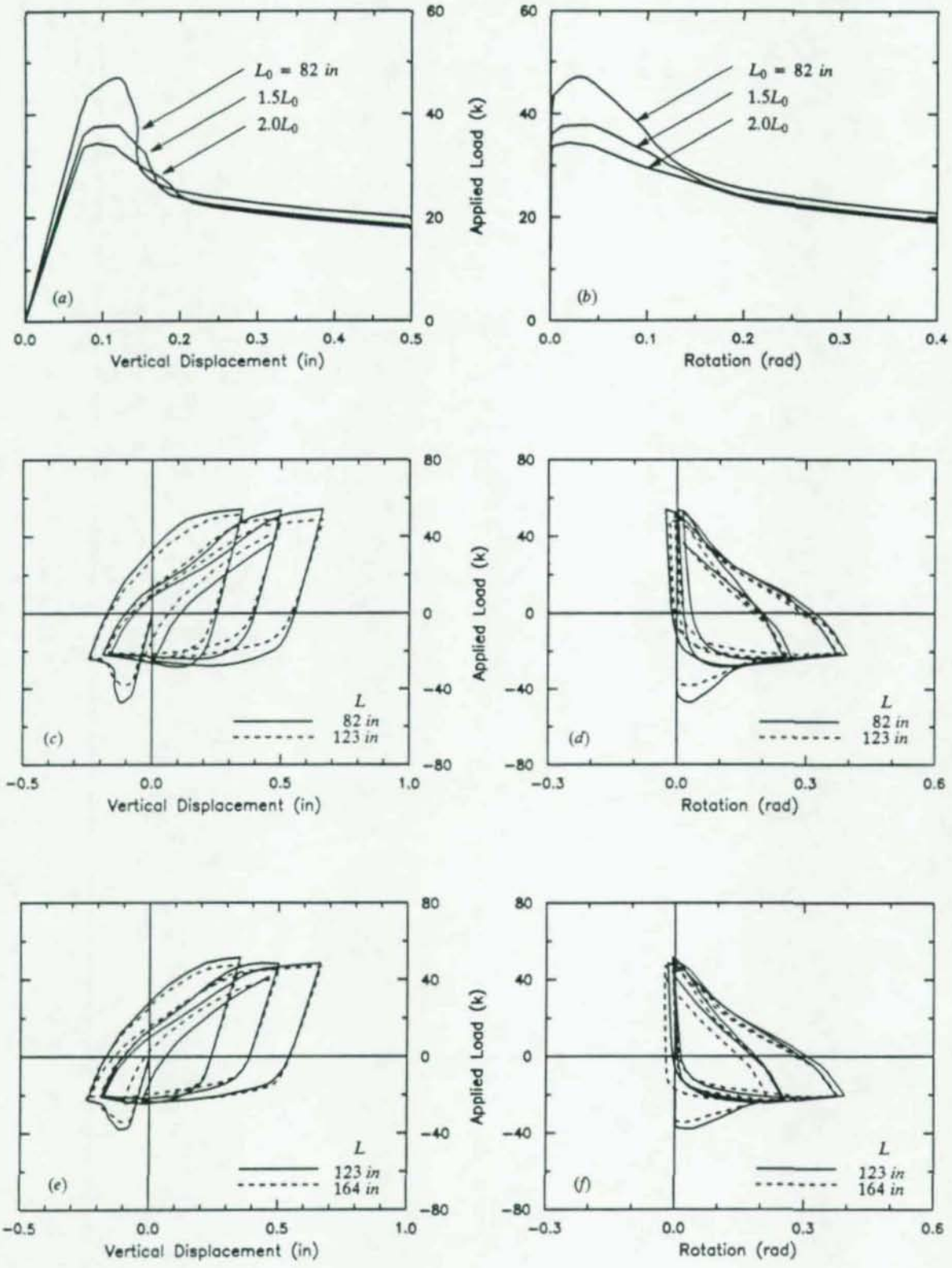

Fig. 5.15 Effect of changing the total length of the beam with l = 20 *in*

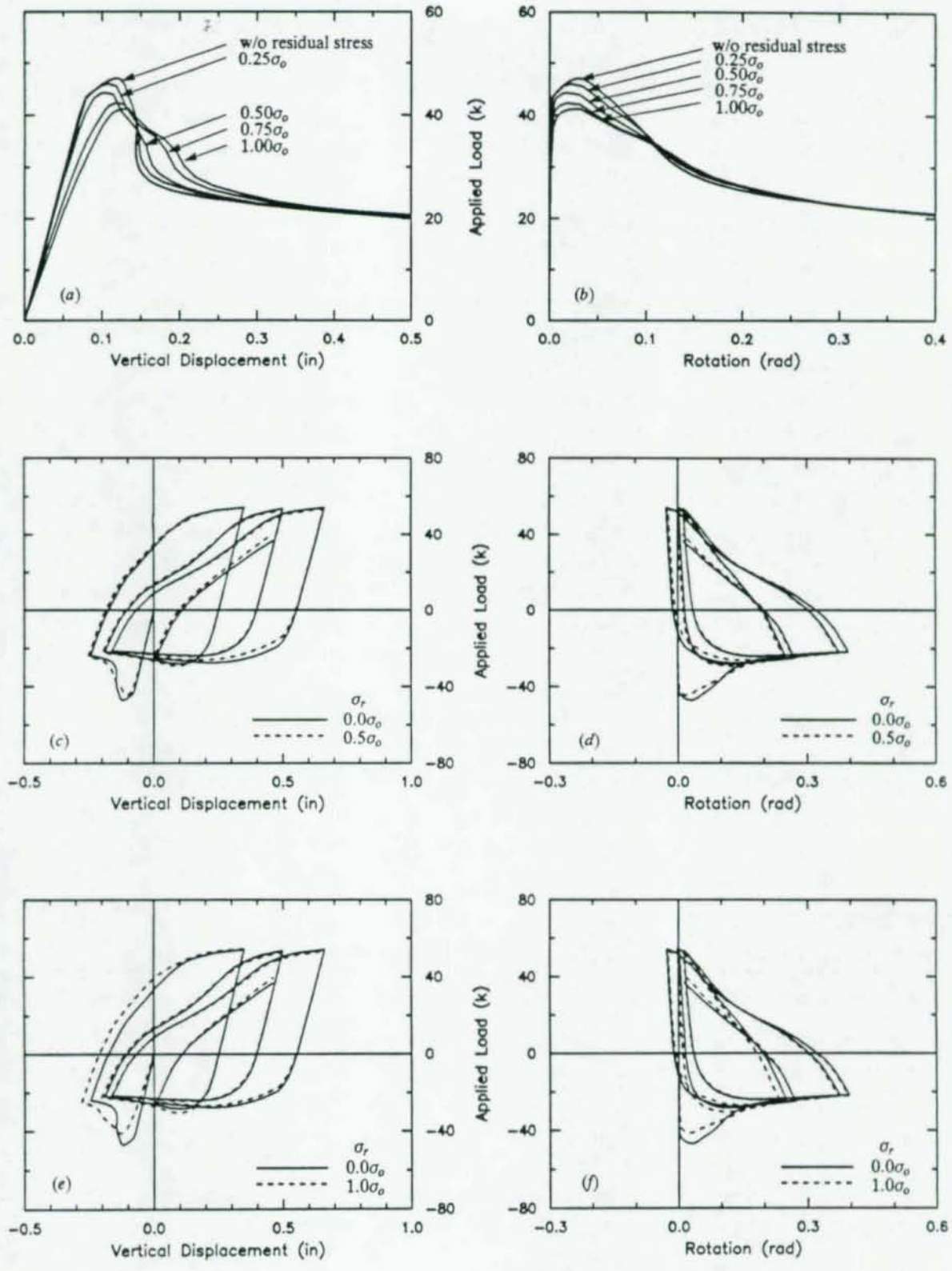

Fig. 5.16 Effect of residual stresses

This feature indicates that the residual stresses have no effect on large deformation behavior. They also have little effect on response to cyclic loading as shown in Figs. 5.16(*c–f*). Even though there are some differences at and after initial buckling, compared with the response of the standard case, the response seems to be almost recovered through the straightening of the residual twist left by inelastic buckling. Judging from this observation, the effect of the residual stresses is weaker than the influence of the residual twist of the beam left by the buckling.

5.8 Effect of Right End Boundary Condition

The degree of fixity at the boundary remote from the load is important to the buckling behavior. The clean support conditions realizable in an analytical environment are difficult to implement experimentally. Consequently, the end conditions in the experiment are unknown and need to be examined. Three idealized right end boundary conditions are considered here: *simple* (translation and torsional rotation fixed), *torsional warping* (simple plus warping fixed), and *fixed* (all fixed). These ideal conditions should give insight into the boundary conditions that existed in the experiments. A study of the effect of the right end boundary conditions is made for both monotonic and cyclic loading conditions. The boundary condition of the standard model is the simple support.

As expected, initial-buckling and subsequent post-buckling capacities increase as right end fixity is increased, as shown in Figs. 5.17(*a,f*). Torsional warping restraint delays initial buckling and increases limit capacity. For the fixed support, the limit capacity increases much more over the simple support than does the addition of only torsional warping restraint but initial buckling occurs at almost the same vertical displacement as the simple case. This difference in buckling behavior could be attributed to the difference in initial stiffness. The load-rotation curves are nearly parallel and have different asymptotic post-buckling capacities. The pull yield load and asymptotic post-buckling capacity of the fixed support are much greater than those of the simple support condition. However, qualitative aspects of response for the three cases are similar for cyclic loading. From these observations, it can be recognized that restraint of torsional warping helps resist the initial buckling only, while full fixed has an effect on the response throughout the cyclic load history.

5.9 Summary

The general behavior of the test specimens with respect to various constitutive, topologic, and geometric parameters has been examined in this chapter. The main observations are summarized as follows:

(1) **Effect of constitutive parameters.–** The effect of material yield strength has a strong impact on the limit capacity. However, the limit capacity appears simply to be proportional to the material yield strength. Initial buckling generally occurs before the onset of strain hardening for the current loading history. Most yielded zones remain on the yield plateau for a little while after initially buckling, but some points reach strain hardening with increased cycling. The influence of Bauschinger's effect, as realized through the kinematic hardening parameter of the current cyclic plasticity model, was also found to be important to cyclic response.

(2) **Effect of eccentrically placed load.–** The limit capacity is very sensitive to slight horizontal load eccentricities. However, only large initial load eccentricities have an effect on large deformation post-buckling behavior and subsequent cyclic response.

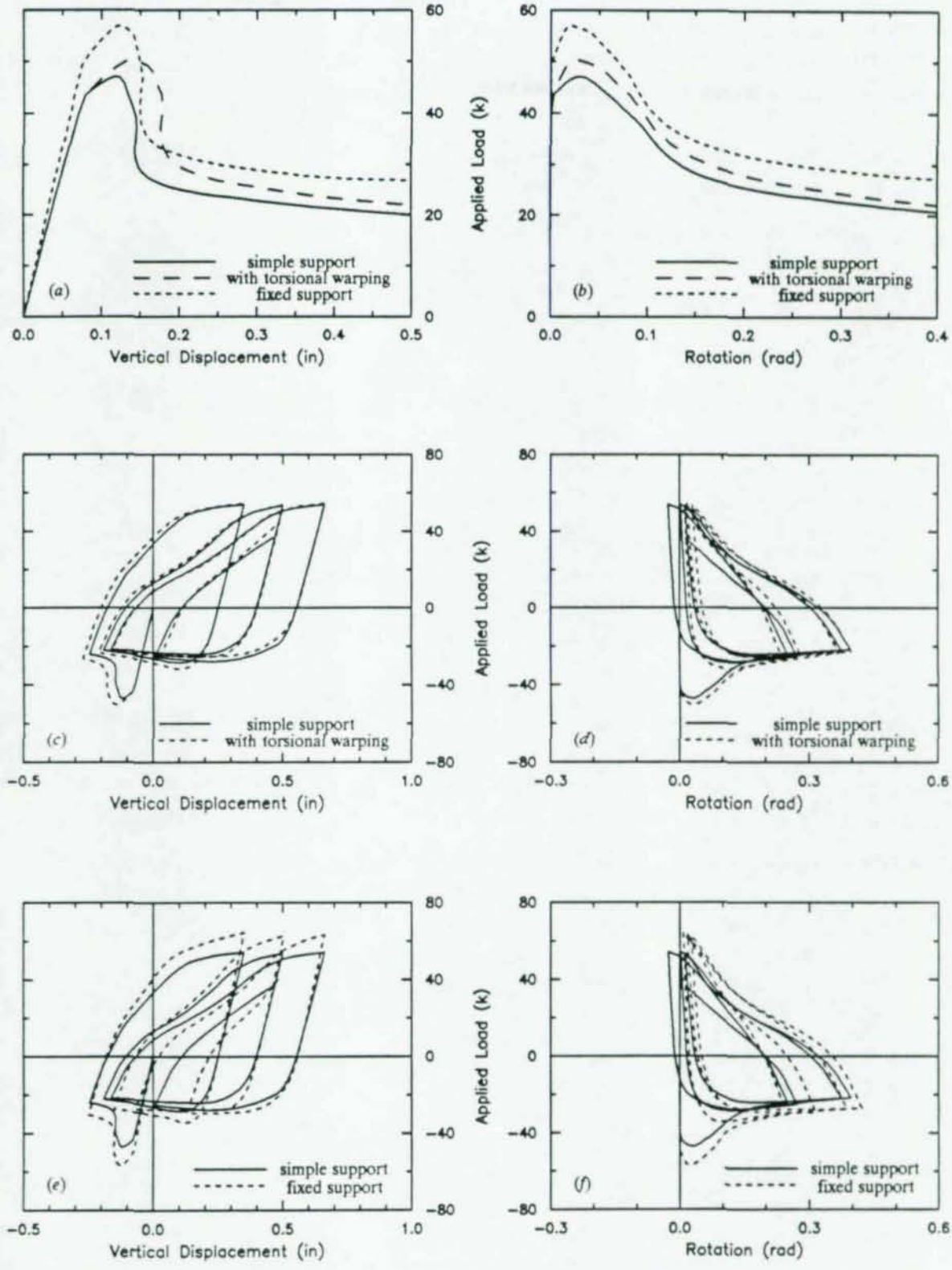

Fig. 5.17 Effect of the boundary conditions on the right end

(3) **Effect of the height of load application.**– Initial buckling capacity and asymptotic post–buckling capacity is very sensitive to the height of the load. The limit capacity and post–limit capacity increase with a decrease of the height of load application. The buckling of the beam is delayed as the application of load approaches the shear center of the cross–section of beam in the push direction of load. The beam is quite reluctant to buckle when the load is applied near the shear center, and is generally stable in the pull direction.

(4) **Effect of the load location along the beam length.**– The location of load along the length of beam significantly influences the initial–buckling load, the asymptotic post–buckling capacity, and pull yield load. Initial buckling is delayed as the location of the load moves toward the fixed end, even to the point of occurring *after* the first cycle in the cyclic loading condition in the current displacement history if the load is close enough to the fixed end.

(5) **Effect of cross–sectional proportions.**– The depth of the beam has much less impact on the initial buckling capacity, large deformation post–buckling behavior, and subsequent response to cyclic loading than does the flange width. The importance of warping resistance for short beams is a plausible explanation for this observation.

(6) **Effect of total length and ratio of load location to total beam length.**– Both the total length (with constant ratio of the location of load to the total length) and the ratio of the distance of the load from the fixed end to the total length (with constant location of load) have a large influence on the limit capacity. The total length (with constant ratio of the location of load to the total length) also has a large effect on the asymptotic post–buckling behavior under cyclic loading.

(7) **Effect of residual stresses.**– The residual stresses have an influence on the limit capacity of the beam, but have no effect on large deformation post–buckling behavior and subsequent response to cyclic loading. The influence of the residual stresses is apparently overshadowed by the effects of the residual twist in the beam left after inelastic buckling.

(8) **Effect of the boundary condition at the right end.**– The fixity of the end remote from the load affects the limit capacity, the pull yield load, and the asymptotic post–buckling capacity. Clearly full fixity has a greater effect than does the addition of only torsional warping restraint. However, the latter form of restraint has a surprisingly large amount of influence on initial buckling behavior.

Chapter 6

An Analytical Study of the Effects of End Flexibility and Pre-yielding on the Response of the Test Specimens

The "fixed" end of the propped cantilever beam in the experiments was actually flexible because of the existence of the load cell and the bolted connections between the test piece and reaction block. This added flexibility has an important influence on the response of this type of system. It is, for example, well known that the linearized buckling load of elastic systems is reduced by the presence of additional flexibility (the proof is in the Rayleigh quotient). It is also known that camber and pre-buckling deflections have an effect on the buckling response of a system. Some of the differences in response of the more flexible system will come from the presence of greater pre-buckling deflections.

In this chapter we study the effects of end flexibility on the behavior of the test specimens in order to make qualitative judgements about the comparison between experiments and theory and to generalize the experimental results. The end flexibility is modeled with a beam segment which can have properties different from the test span. The model is reminiscent of the load cell in the tests and thus will be called the "load cell" in the sequel, even though there is no need for a load cell in the theoretical model. The main difference between the load cell and the test span is the difference in the torsional rigidity. An element with a square tube cross-section (called *box-section* in the sequel), without warping degrees-of-freedom, is used to model the load cell (the load cell in the experiments was a circular tube). The response will also be compared with that of two beams having load cells of low torsional rigidity, either a beam with the same cross-section as the test piece or one with one quarter again as much depth. The cross-sectional dimensions of the model load cells are given in Table 6.1. The placement of the load cell is as shown in Fig. 4.13, and its length will be designated as l_c.

Another important influence on the buckling behavior of beams is the history of inelastic deformation. In particular, the initial buckling reponse of the test specimens seemed to be affected by pre-yielding from an initial pull loading. The beam properties which may be influenced by pre-yielding include the residual stresses and the initial camber of the beam as it enters the initial push buckling cycle. While the issue of pre-yielding is not directly related to end flexibility, it is studied here because we wish to examine the effect of end flexibility for beams which have no pre-yielding and for beams which do have pre-yielding.

In this chapter, the effect of end flexibility in the fixed end is examined for monotonic push and pull loading sequences as well as cyclic loading, varying the length and cross-sectional dimension of the load cell. The important effects of end flexibility are summarized in Section 6.4.

Table 6.1 Cross-sectional properties of the model load cells

Section Type	h (in)	b (in)	t (in)	t_f (in)	EI $10^6\ (in^2-k)$	GJ $10^3\ (in^2-k)$
box-section	6.0	6.0	0.5	0.5	2.16	1296
I-section 1	9.82	4.0	0.18	0.2	1.58	0.485
I-section 2	12.3	4.0	0.18	0.2	2.64	0.542

6.1 The Effect of End Flexibility on the Linearized Buckling Loads of the System

As before, we will use the elastic linearized buckling analyses as a point of departure in studying the effects of end flexibility on the buckling of the propped cantilever system. The linearized buckling load is interesting because it exhibits the effects of geometry on the equilibrium of the system apart from the effects of the constitutive model. One can thus learn a great deal about the stability characteristics from these analyses even though the system of interest exhibits inelastic buckling. This same reasoning lies at the heart of most design formulas for inelastic buckling. The linearized buckling analyses are useful for establishing a context for discussing stability, and become truly useful only when results on inelastic buckling are also examined. Inelastic buckling will be treated in the subsequent sections.

The presence of a load cell at the fixed end of the beam gives rise to essentially two effects: end rotation with concomitant in-plane vertical deflection from the rotational flexibility and end displacement with concomitant in-plane vertical deflection from translational flexibility. While the load cell couples these effects, it is instructive to examine them independently first. Figure 6.1 shows the effects of

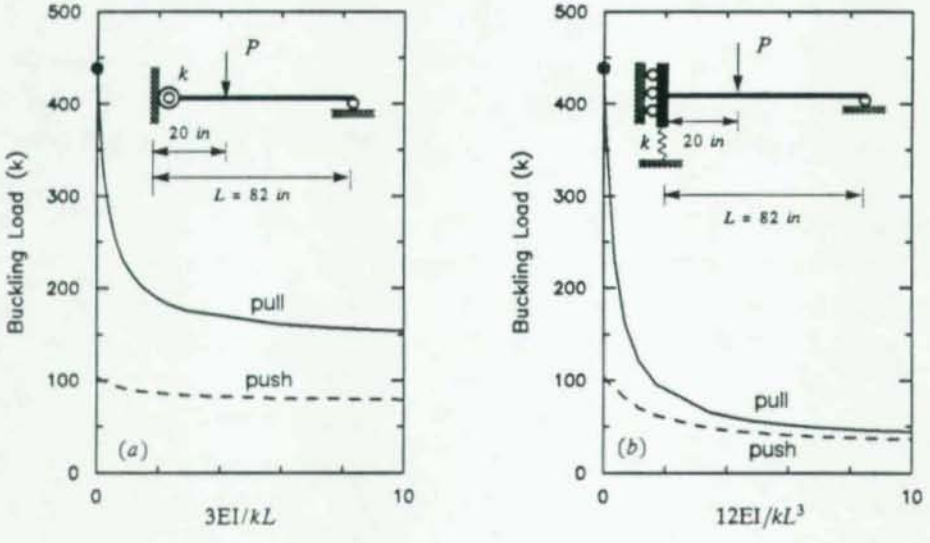

Fig. 6.1 Comparison of linearized push and pull buckling loads for end flexibility

(a) rotational flexibility in the absence of translational flexibility and *(b)* translational flexibility in the absence of of rotational flexibility on the elastic linearized buckling load of the propped cantilever system. For both of these cases the load is applied at the standard value of 9.4 *in* above the shear center of the cross-section. The length of the beam is $L = 82$ *in*, with load positioned at $l = 20$ *in* from the left end. The beam has the standard cross-section (W10x12) and the simple end resists vertical and lateral displacement, torsional rotation, and warping. Results are given both for the push (down) and pull (up) directions, and are expressed in terms of a nondimensional ratio of beam stiffness to spring stiffness.

The elastic linearized buckling load decreases with increased flexibility of the support, as expected, in both cases. One can again observe the effect of load height with respect to the shear center in the greater buckling loads for pull as opposed to push loading. Note the extreme sensitivity of the pull buckling load to end flexibility. For example, the system with a rotational spring has a value of 435 *k* for the rigid case, which decreases to a limiting value of about 150 *k* as the flexibility increases. The push load

case is not nearly so sensitive, going from about 105 k to a limiting value of 76 k. It is interesting to note that there is little difference between the push and pull buckling loads for a system with a relatively flexible translational spring. It is apparent that the translational flexibility has a much greater influence on the buckling load than does the rotational flexibility.

The load cell provides a coupled influence of rotational and translational flexibility. In fact, the linearized stiffness matrix for the rotational and translational degrees of freedom already defined is given by the expression

$$\mathbf{k} = \frac{2EI}{l_c^3}\begin{bmatrix} 2l_c^2 & 3l_c \\ 3l_c & 6 \end{bmatrix} \tag{6.1}$$

where l_c is the length of the load cell and the moment of inertia, I, is roughly proportional to the depth of the load cell cubed.

The variation of linearized buckling load with the length, l_c, and depth, h, of the (*box-section*) load cell is shown in Fig. 6.2. The properties of the test piece and loading are all held fixed at their standard

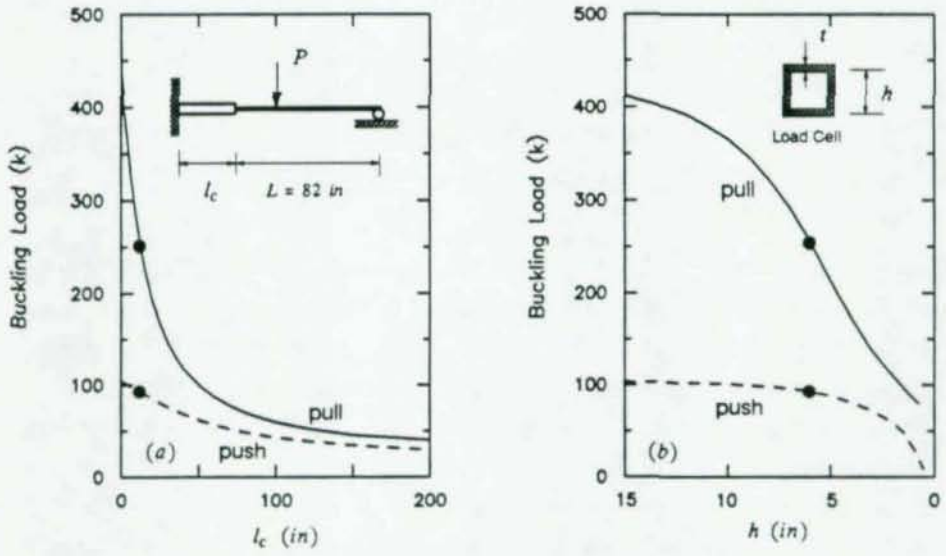

Fig. 6.2 Comparison of linearized push and pull buckling load for the model load cell

values as the two parameters indicated are varied. In *(a)* the cross-section of the load cell has depth h=6 *in* and thickness t=0.5 *in*, while in *(b)* the length of the load cell is l_c=12 *in*. The dots (•) on the curves indicate the standard value of the parameter. As in the case of the uncoupled springs, the buckling load with the load cell decreases rapidly with increasing flexibility, realized either by increasing the length of the load cell or by decreasing its depth. For long load cells it would appear that the translational flexibility controls the buckling behavior. This tendency is expected since the translational flexibility is proportional to l_c^3 while the rotational flexibility is proportional to l_c. For the short load cell (l_c=12 *in*) the push and pull buckling loads remain quite different for all values of h until h approaches zero. In general, the buckling load is not very sensitive to the depth of the load cell, particularly in the push direction of loading.

The differences in the buckling loads for the cases studied so far are due to differences in the planar stiffness of the system. Since torsion is the predominant mode of buckling deformation, one might suspect that the torsional stiffness of the load cell would have an influence on the buckling behavior. To examine the effect of the torsional stiffness of the load cell we consider the three cross-sections described in Table 6.1: the box-section of the previous studies and two I-sections of different depths. The variation in buckling load with the length of the load cell for push loading for these three load cells is shown in Fig. 6.3. The curve of *I-section 1* represents the response with a load cell with the same

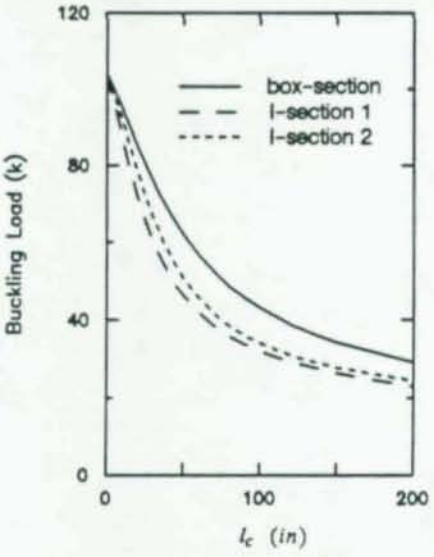

Fig. 6.3 Effect of torsional rigidity of the model load cell on the elastic linearized buckling load

cross-sectional dimensions as the test piece, while the curve of *I-section 2* represents the response with a load cell with an I-section 1.25 times as deep as the test piece. Table 6.1 shows the (in-plane) flexural and torsional rigidities of each cross-section. I-sections 1 and 2 have very small torsional rigidities (GJ) compared with that of the box-section, but have comparable flexural rigidities (EI). The flexural rigidity of *I-section 2* is even larger than that of the box-section. As expected, the lower is the torsional rigidity, the lesser is the buckling load. However, the torsional stiffness of the load cell appears to have a smaller influence on buckling than does in-plane flexibility. For short load cells, the differences in buckling loads are much less because of the influence of warping resistance in the I-beams.

6.2 The Effect of End Flexibility on the Monotonic Inelastic Response of the System

In the previous section the test piece and load cell were assumed to remain elastic during buckling. For the geometric dimensions considered here, elastic buckling will seldom, if ever, occur. Consequently, we must re-examine the buckling behavior in the light of inelastic material behavior. The constitutive parameters studied in Chapter 5 will not be as extensively studied here. Rather we will adopt the standard values to re-examine the effects of the length and depth of the load cell. In this section we consider the monotonic response both for push loading and for pull loading. The subsequent section is devoted to the consideration of cyclic loading.

6.2.1 Variation of Parameters for Pull Loading

We have established from the elastic analyses that pull loading is inherently more stable than push loading. One would expect this increased tendency toward stability to carry over to the inelastic case. In fact, one can reason that the inelastic case exhibits this characteristic more strongly because of the likelihood of generalized yielding intervening before buckling can take place. The relatively large inelastic deformations act to camber the beam into an even more favorable position for resisting buckling by moving the point of application of load further from the average line of shear centers of the system. For this reason we will generally consider pull loading to be stable, recognizing that buckling may take place at very large deformations.

The monotonic response of the beam/load cell system is shown in Fig. 6.4 for *(a)* various lengths, from l_c=0 (without load cell) to l_c=50, and *(b)* for various depths, from h=2 to h=∞ (without load cell), of the standard box-section load cell. One can observe generally the same behavior for both parameters.

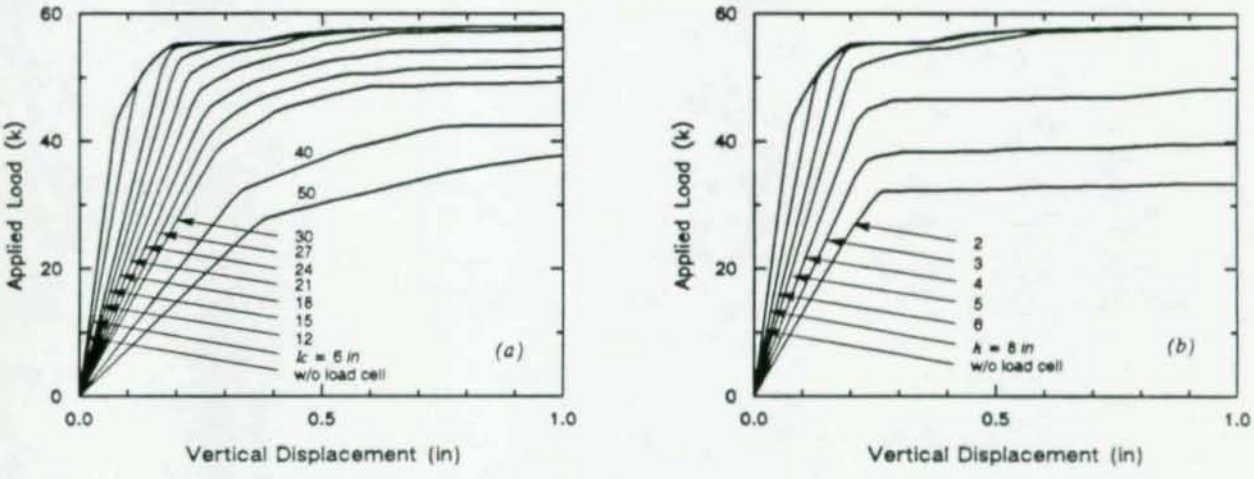

Fig. 6.4 Monotonic response for pull load with model load cell

For short load cell lengths and for deep load cell sections the initial stiffness is quite large, giving way to a yield plateau on which the resistance remains approximately constant. For parameter values which make the system more flexible, greater deformations are required to achieve the full plastic capacity. The limit capacity for long or shallow load cells is reduced because of yielding of the load cell rather than the beam itself. The limit capacity of the system can be reasonably predicted by simple plastic theory to be

$$P_o = \begin{cases} V_b + \dfrac{M_b}{L-l} & \text{for beam yielding} \\ \dfrac{M_c}{l+l_c} + \dfrac{M_b(L+l_c)}{(l+l_c)(L-l)} & \text{for load cell yielding} \end{cases} \tag{6.2}$$

where V_b and M_b are the shear and bending capacities of the beam, respectively, M_c is the bending capacity of the load cell, L is the length of the beam, l is the distance between the end of the beam and the point of load, and l_c is the length of the load cell. The beam mechanism equations assume that the short beam segment yields in pure shear while the load cell mechanism assumes that the load cell yields in pure flexure.The capacities taken from Fig. 6.4 *(finite element model)* are plotted along with the values

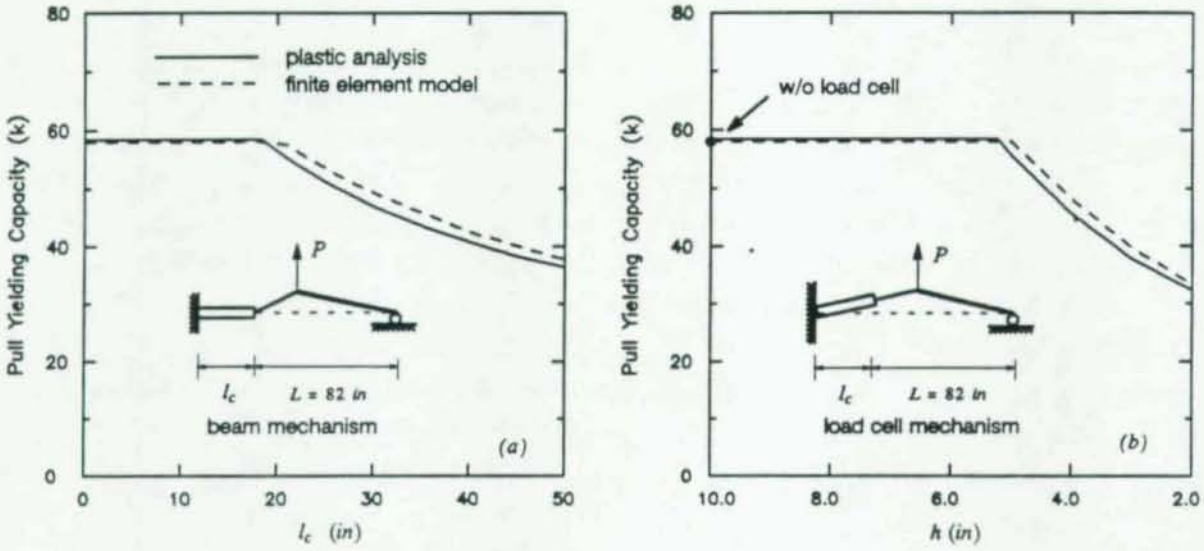

Fig. 6.5 Pull capacities for various load cell dimensions

from Eq. (6.2) (*plastic analysis*) in Fig. 6.5 which also shows the two possible collapse mechanisms. The parameter value determining which of the two mechanisms controls can be found by equating the two expressions in Eq. (6.2). For the values used here the transition occurs at l_c=18 *in* and h=5 *in*. The curve is flat for the beam mechanism because the load cell plays no role. As one would expect, the capacity drops as the length of the load cell increases and as the depth decreases. The pull response for the system having an I-section for the model load cell is compared with the box-section load cell of depth h=5 in Fig. 6.6. The responses are qualitatively similar.

6.2.2 Variation of Parameters for Push Loading

Unlike pull loading, push loading is generally unstable, showing a limit load with declining post-limit behavior. The main difference between elastic and inelastic buckling is that the latter exhibits a limit load

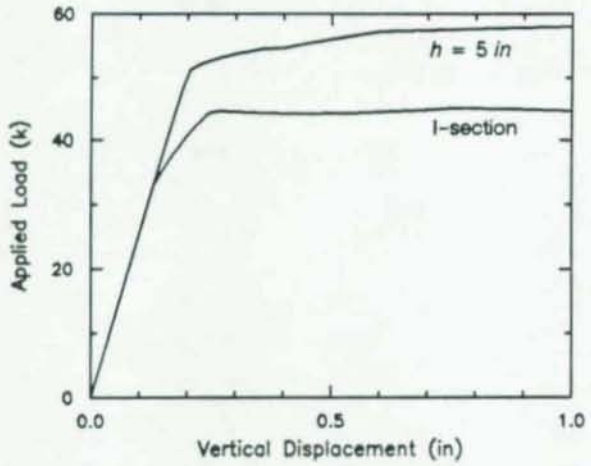

Fig. 6.6 Monotonic response for pull load with I-section load cell

with unstable post-buckling behavior whereas the former exhibits stable post-buckling behavior. One might expect that the effects of end flexibility for the inelastic case would be qualitatively similar to the elastic one, that is that end flexibility reduces the monotonic limit capacity. We demonstrate through the parameter study in this section that such is not the case.

The monotonic response under push loading is studied for variations in the length of the model (standard *box-section*) load cell in Fig. 6.7 and for variations in the depth of the model load cell in Fig. 6.8. Several important features can be seen in the study of the variation of end flexibility. For short load cells, the system buckles laterally shortly after yielding initiates. For longer load cells, buckling does not take place until considerable yielding has taken place. This behavior can be explained by observing that for load cells of length 15 *in* and shorter the load cell remains elastic and yielding occurs in the beam. Loss of torsional stability is then governed by the reduced modulus of the yielded material in the beam. Load cells 18 *in* and longer yield before the beam, but since the load cell is a tube the yielding does not compromise the torsional resistance of the system to the same degree as the case in which beam yielding occurs. As a consequence, the system is able to deform inelastically in the plane of loading longer if the load cell yields. Note that for the systems with load cell yielding, buckling occurs with a snap back in vertical deflection to accommodate the rotation. The load versus rotation curves are remarkably similar for all of the systems for variations in load cell length, with all curves coalescing at a moderate value of the rotation. Significant differences in the load-rotation response can be seen for cases in which the depth of the load cell is less than 4 *in*. In these cases, the asymptotic post-limit capacity is strongly affected by the cross-sectional dimension of the load cell.

The influence of torsional rigidity of the load cell can be seen by examining Figs. 6.8(*e,f*), in which the system with I-section (*I-section 1*) load cell is compared with the system with 5x0.5 *in* box-section. The dimensions of the two sections are such that the in-plane elastic stiffnesses are the same. The length of the load cell is 12 *in*, so yielding of the box-section load cell rather than the beam end is expected. Since *I-section 1* is the same as the test piece, yielding is also expected in the load cell. The I-section load cell is deeper and thus it yields well in advance of the box section, and has a much smaller limit capacity. Interestingly, the post-limit behavior of the two systems is nearly identical. It is evident that the torsional stiffness of the load cell has an important influence on the monotonic buckling response of the system.

The limit loads for the various values of the parameters, taken from Figs. 6.7 and 6.8, are plotted against the values of the parameters in Fig. 6.9. Remarkably, the limit capacity of the system initially increases with an increase in flexibility. One possible explanation for this anomalous behavior is that, while torsional flexibility is reduced with these parameter variations, the main influence is a reduction in in-plane flexural stiffness. As the system becomes more flexible in the plane of loading, it can deflect more under smaller loads. With the load applied above the shear center, as it is for push loading, the in-plane deflection represents movement of the point of load application closer to the average line of shear centers of the system. Such a deflection would be favorable from the point of view of torsional stability. Eventually, the negative effect of reduction in torsional stiffness catches up with the positive effect produced by vertical deflection, and the limit capacity then decreases with increased flexibility as expected.

The variation of limit capacity with parameter values for pre-yielded beams is also shown in Fig. 6.9. The response of pre-yielded beams will be discussed in Section 6.3. Briefly, a pre-yielded beam is one

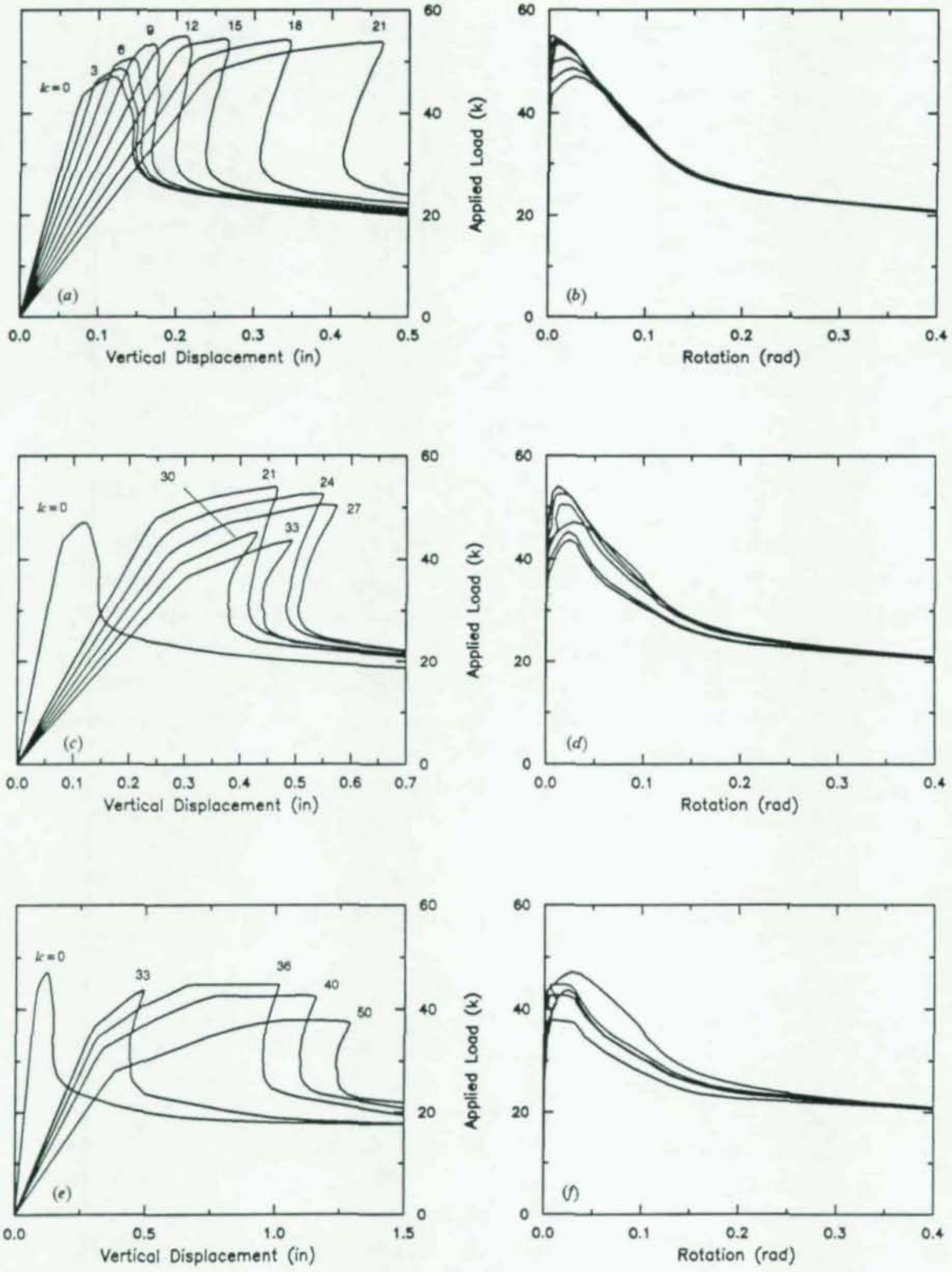

Fig. 6.7 Monotonic load response for push load for various lengths of the model load cell

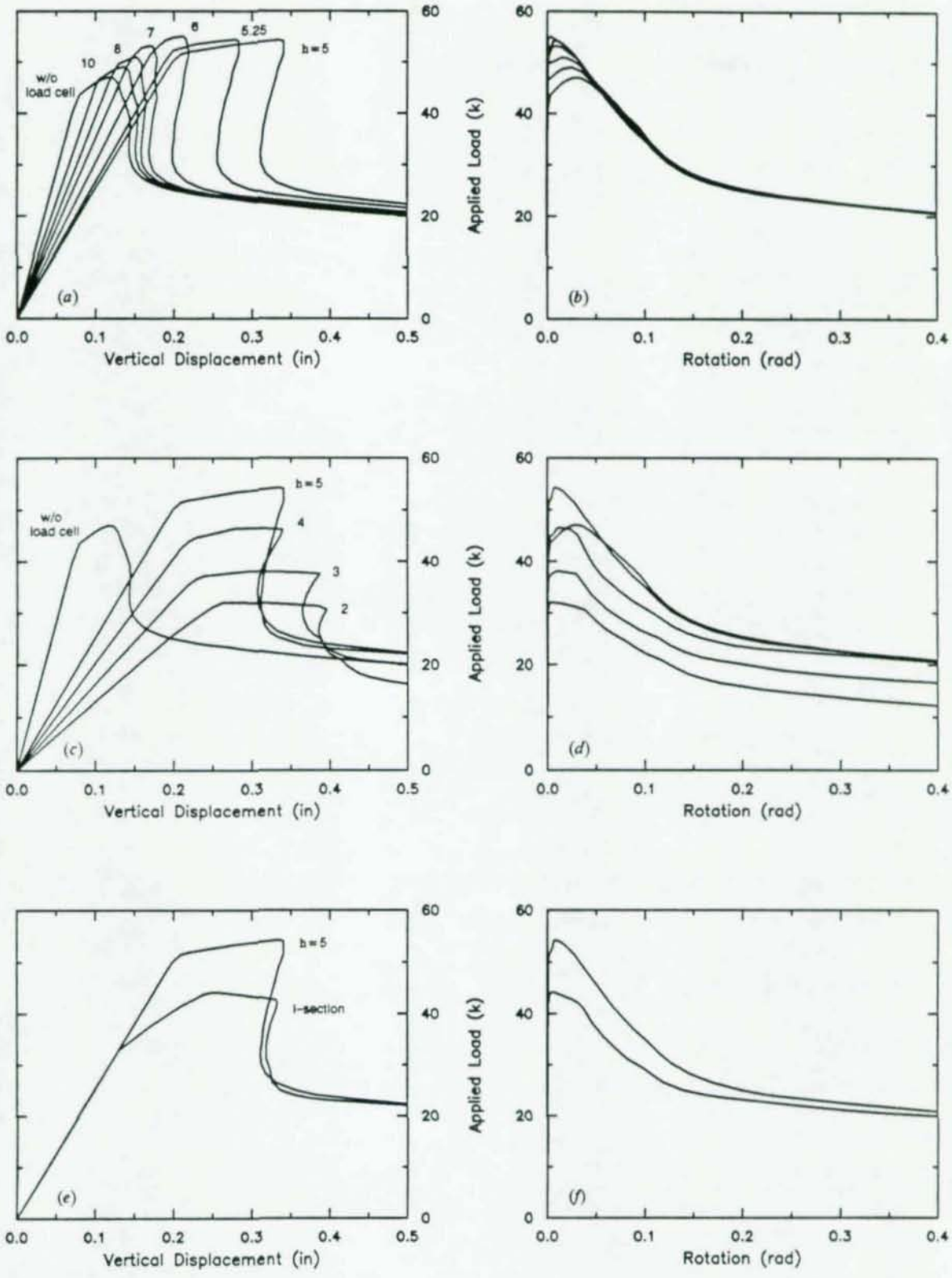

Fig. 6.8 Monotonic load response for push load for various depths of the model load cell

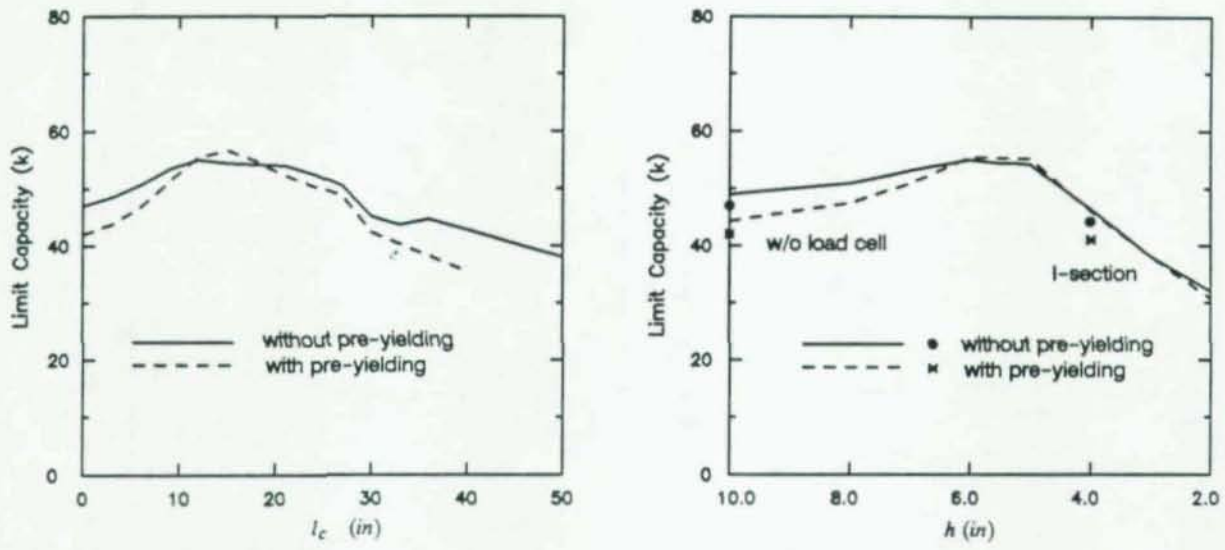

Fig. 6.9 Variation of limit capacity with end flexibility

which is first pulled to a prescribed value, generally causing yielding, and then pushed to its limit capacity. The difference in buckling response would therefore be a ramification of pre-yielding and might include material softening, residual stresses, and residual inelastic camber. The pre-yielded beams show the same anomalous tendency to increase strength with increasing end flexibility, but to a greater degree. The value of the parameter giving the maximum capacity is about the same for both virgin and pre-yielded beams.

6.3 The Effect of End Flexibility on the Cyclic Inelastic Response of the System

There are several features of the response to cyclic loading which transcend the linearized buckling and monotonic response studies. Among these are the hysteretic stability of the response, particularly in the pull regime, the rate of recovery from buckling when the load direction is reversed, and the ability of the system to dissipate energy. In this section we study the cyclic response of the propped cantilever beam while again varying the length and cross-sectional dimensions of the load cell in an effort to expose their influence on cyclic response. The influence of pre-yielding, whereby the cyclic loading program is started with an (possibly) inelastic pull half-cycle, is also examined.

The parameter studies are organized in essentially the same manner as the inelastic monotonic response studies. For each parameter variation, a complete cyclic response history is generated, and plotted along with the response history of the standard case. As before, both the vertical displacement response and rotation response are presented. The loading programs for all cases are the same, with the displacement history specified at the point of load application. Since the vertical displacement is reported at the shear center, the loading histories appear different but are not.

The influence of the length of the load cell on the cyclic response is shown in Fig. 6.10 for values of the length of $l_c = 0$ *(without load cell)*, 6, 12, 18, 21, 24, 27, 30, 33, 36, 40, and 50 *in*. Several interesting features of the response can be noted. For small values of the load cell length the increased flexibility is readily apparent in the initial buckling response as well as in the elastic unloading from the pull yielded

state. On the other hand the response curve for the pull direction of loading remains similar to the case without a load cell, particularly as full yielding develops in the pull direction. As the length of the load cell increases beyond 24 *in* this similarity begins to vanish because the flexible system is less able to reach the full yield value as it is still unwinding from the buckled state. Also at a length of 24 *in* the increased flexibility causes initial buckling to be delayed until the second cycle. In general, as the flexibility of the system increases, the response looks less characteristic of the short beam (because it is actually no longer a short beam), degenerating more and more toward flexible elastic response.

The influence of the cross-sectional dimension of the load cell on the cyclic response is shown in Fig. 6.11 for values of the depth of h=8, 5.25, 5, 4, and 2 *in*. In Figs. 6.11 *(k,l)* the cyclic response with *I-section 1* is compared to the cyclic response without load cell. The variation of the load cell dimensions has a similar effect to changing the load cell length. Pull yielding remains achievable for large values of depth, with degradation due to flexibility for depths of 4 *in* and less. The I-section load cell also shows a similar type of response.

If the load is applied in the pull direction first, the system can experience yielding before buckling. These loading cases are termed *pre-yielding*. The previous two parameter studies on end flexibility have been repeated for a loading history that includes pre-yielding and are shown in Figs. 6.12 and 6.13. As indicated in the previous section, pre-yielding has a noticeable effect on the subsequent buckling cycle because of the alteration of the residual stress pattern, the presence of residual cambering, and material softening. These effects generally act to reduce the limit capacity. After the initial buckling cycle, very little difference from the case without pre-yielding can be seen. This observation is not surprising since the important effects all relate in one way or another to material inelasticity and would tend not to be remembered as cycling progresses.

6.4 Summary

The linearized buckling analyses showed that the (elastic) buckling load of the propped cantilever beam is quite sensitive to the presence of in-plane end flexibility, exhibiting a sharp drop in capacity for small values of flexibility. Contrary to our intuition, which is generally based upon the results of linearized buckling analyses, the inelastic limit capacity of the system increases with an increase in the end flexibility for small values of flexibility. The optimal length and depth of load cell for the test pieces examined here were around l_c=12.0 *in* and h=6.0 *in*. Buckling is, on the whole, delayed by greater in-plane flexibility because the deformation demands on the flexible system are less than the rigid system. The presence of low torsional flexibility along with low flexural flexibility reduces the improvement obtained from flexural flexibility alone. Torsional flexibility at the fixed end greatly influences the buckling capacity of the beam, and has an effect on the large deformation behavior and the response to the cyclic loading.

Small values of flexibility influence only the initial buckling cycle of the cyclic loading response to any important degree. Subsequent response is quite similar to the rigid end case. The most important aspect of cyclic loading is that buckling will eventually occur at modest deformations if cycled enough times. This tendency to buckle may not be apparent from a monotonic analysis.

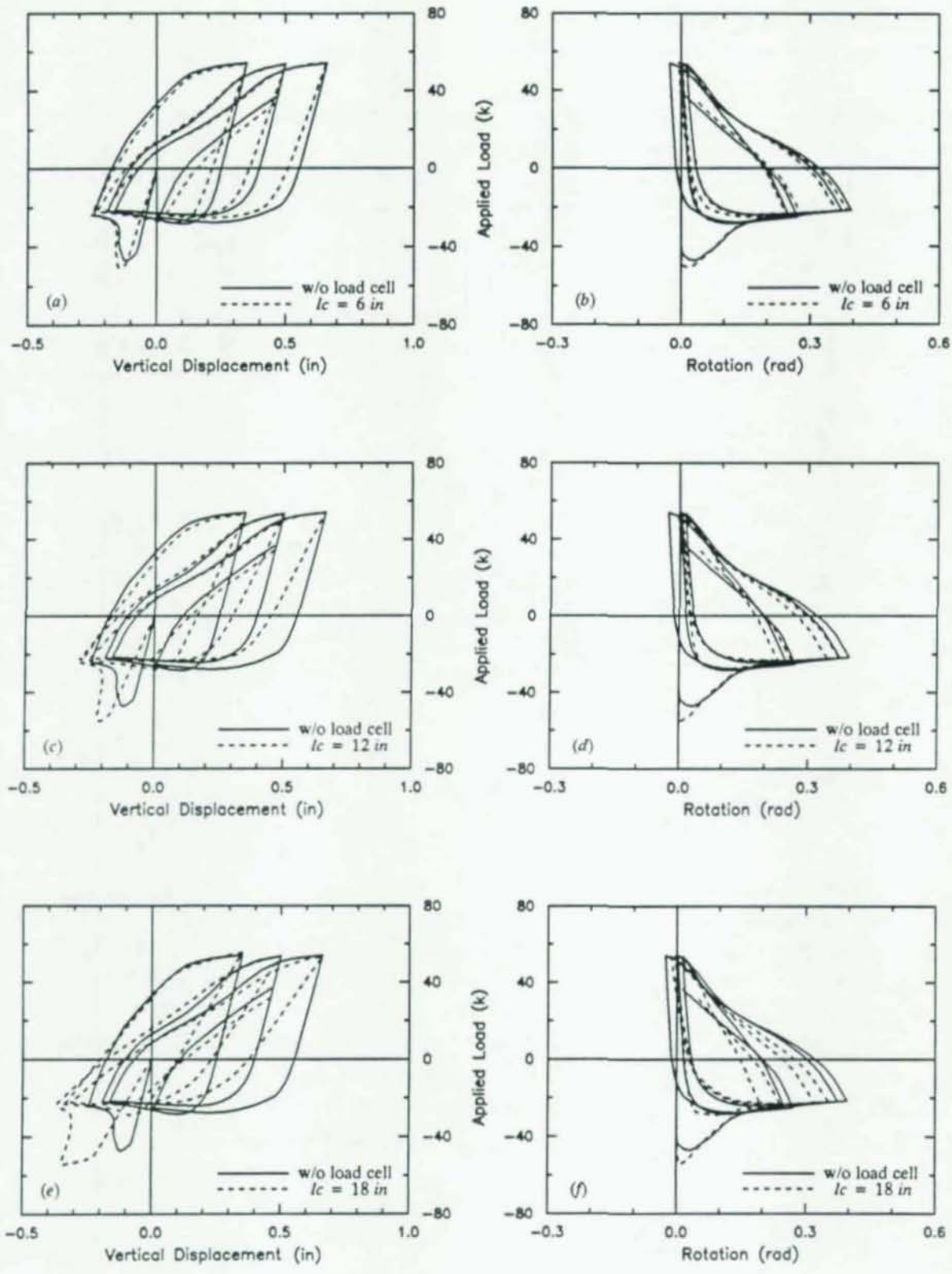

Fig. 6.10 Effect of load cell length on cyclic response (no pre-yielding)

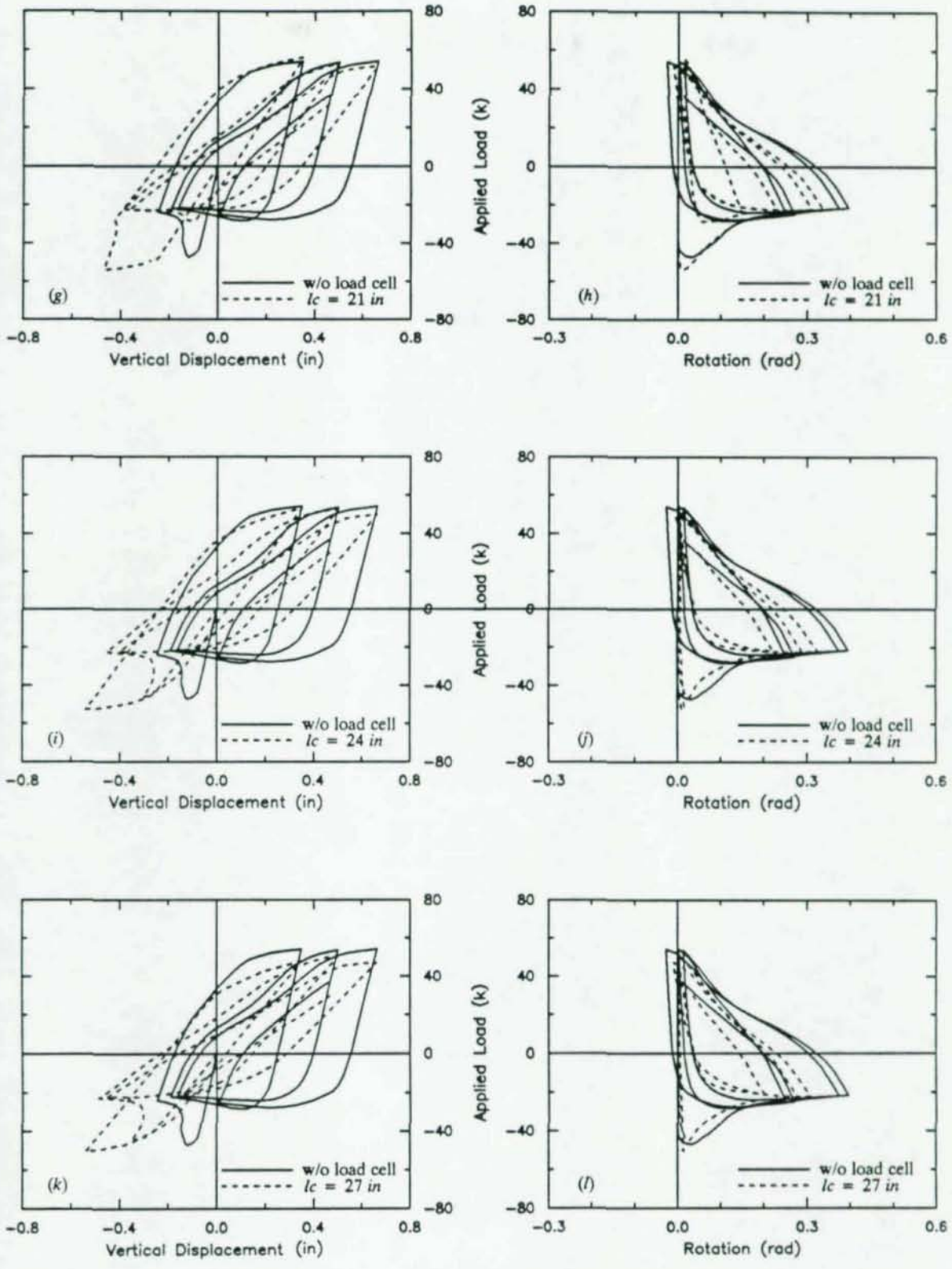

Fig. 6.10 *(cont.)* Effect of load cell length on cyclic response (no pre-yielding)

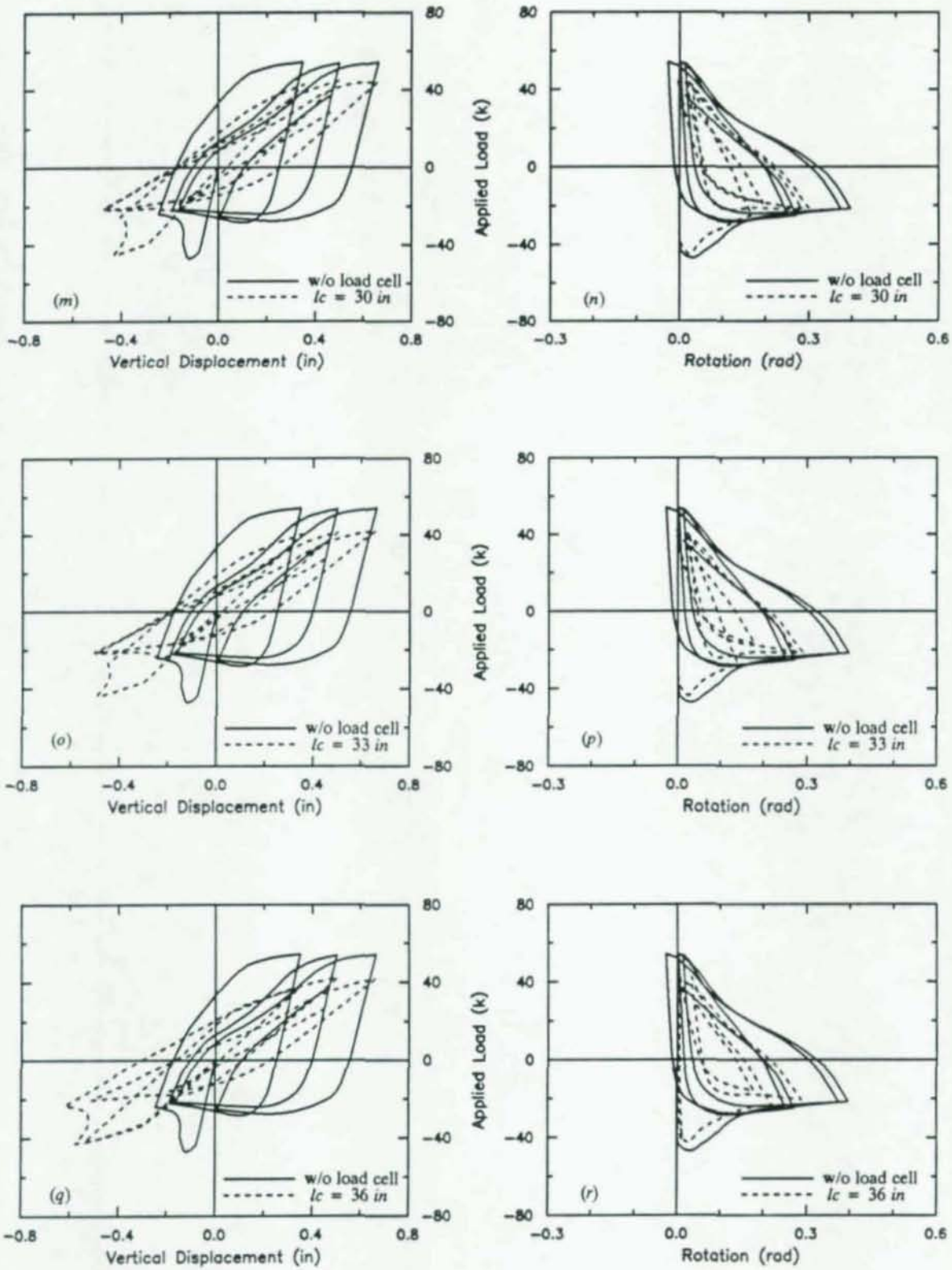

Fig. 6.10 *(cont.)* **Effect of load cell length on cyclic response (no pre-yielding)**

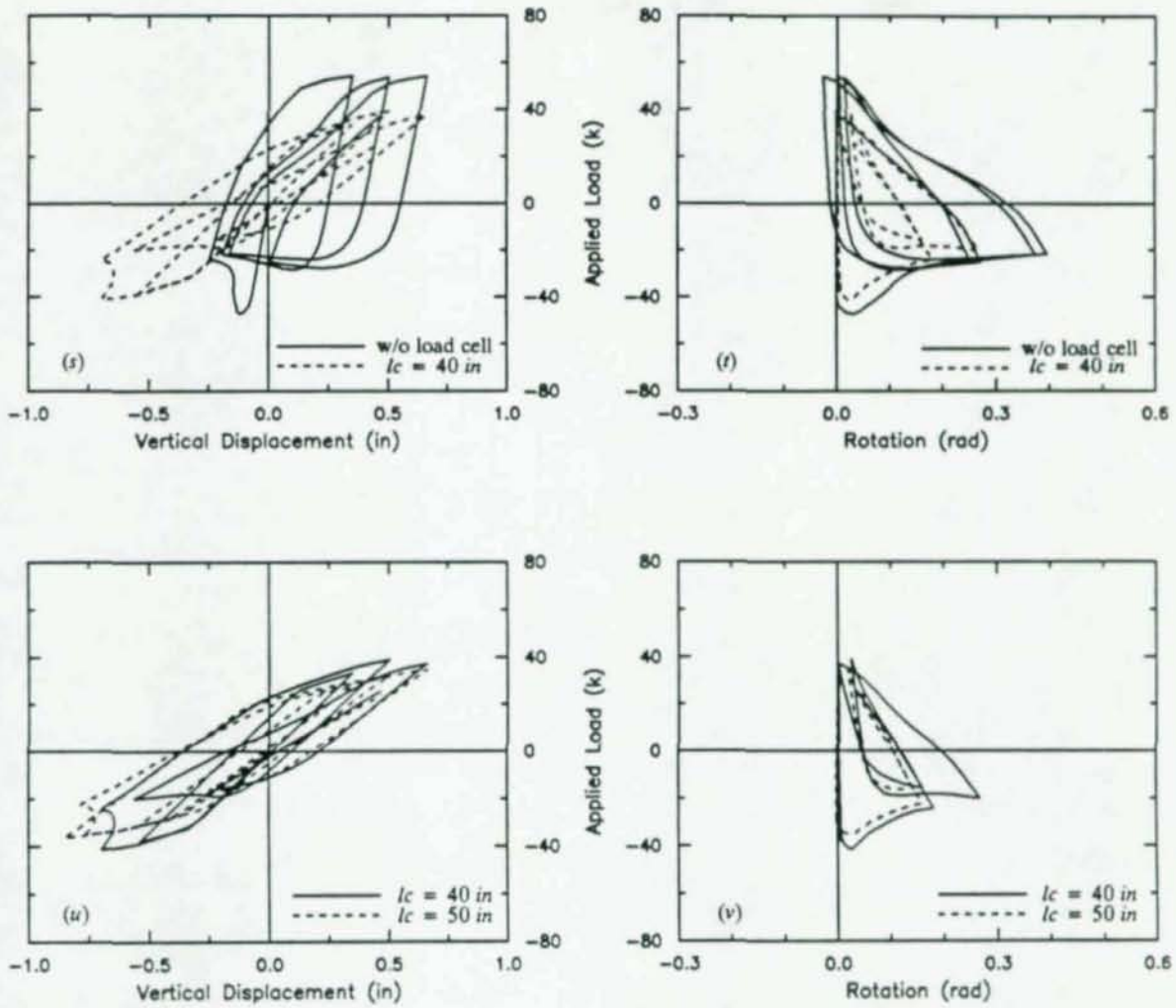

Fig. 6.10 *(cont.)* Effect of load cell length on cyclic response (no pre-yielding)

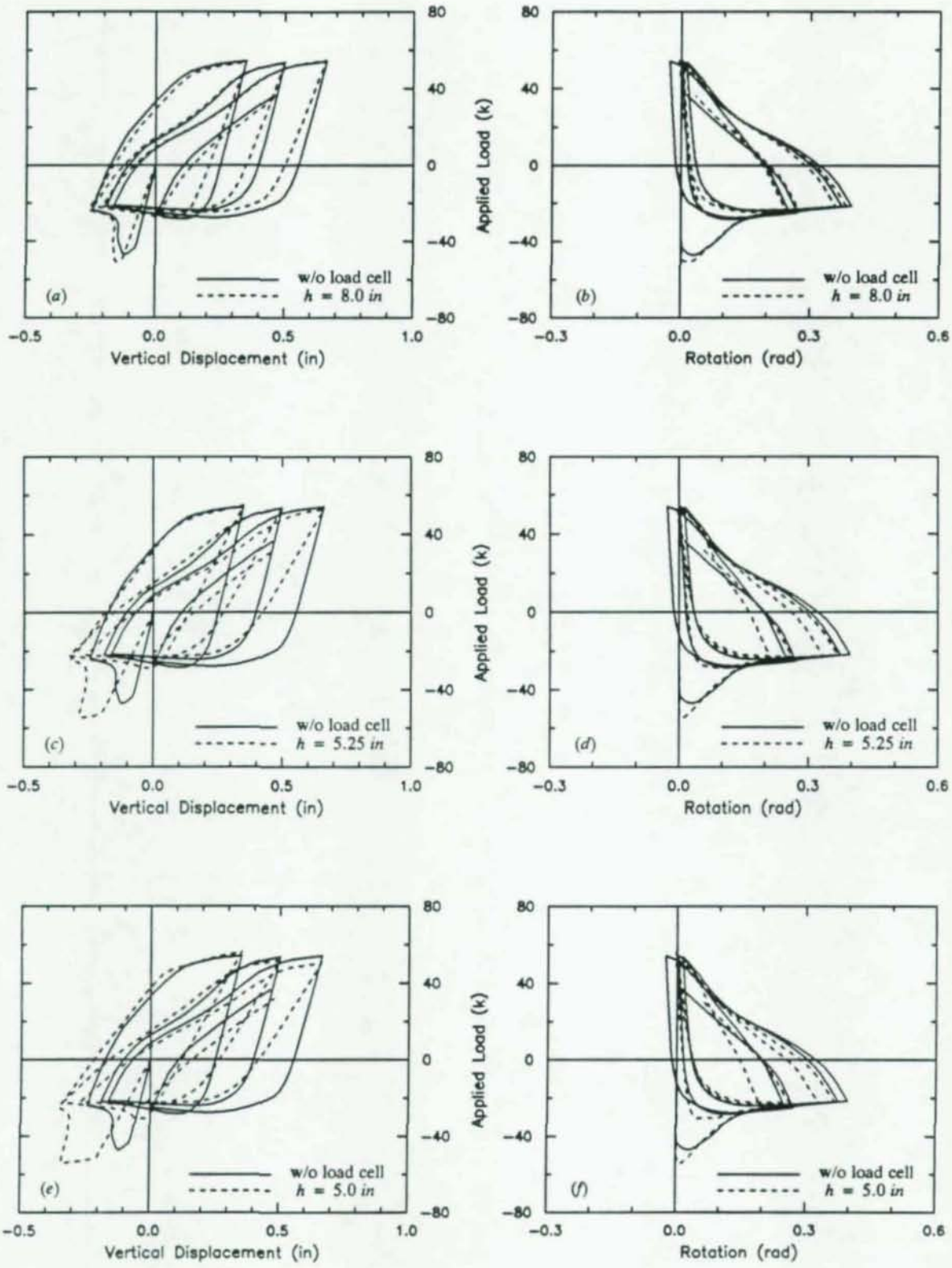

Fig. 6.11 Effect of cross-sectional dimensions of load cell on cyclic response (no pre-yielding)

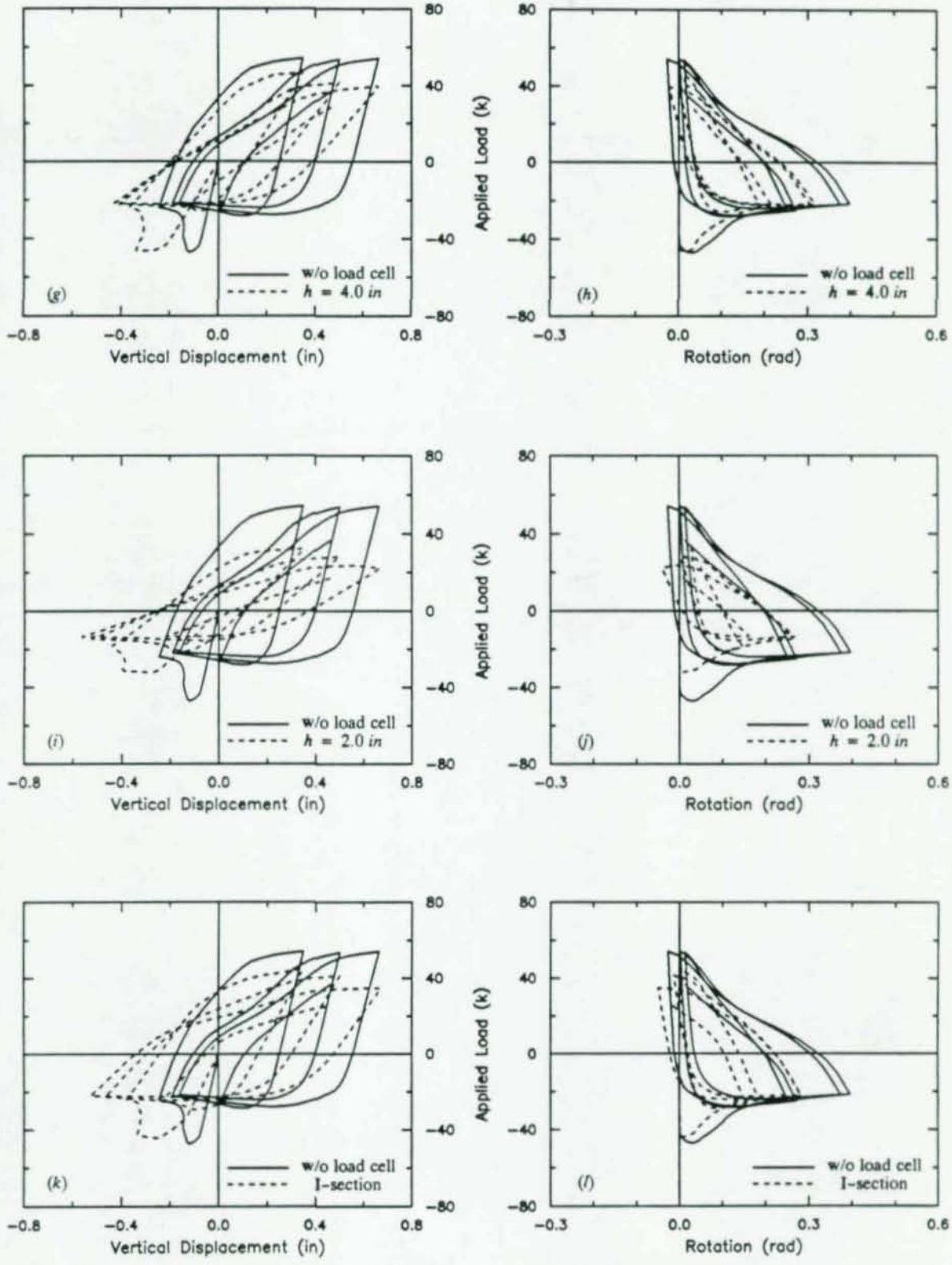

Fig. 6.11 *(cont.)* Effect of cross-sectional dimensions of the load cell on cyclic response (no pre-yielding)

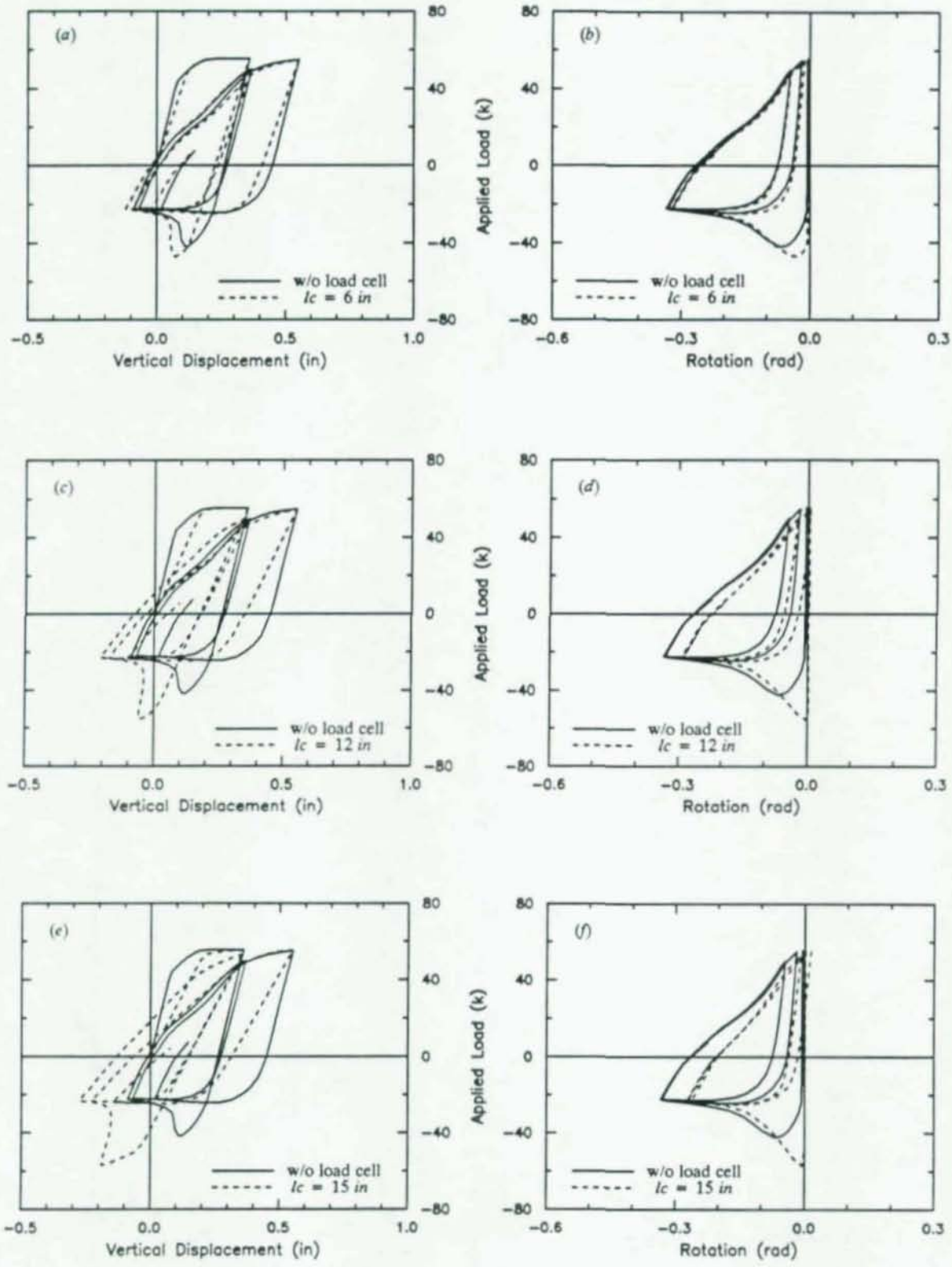

Fig. 6.12 Effect of load cell length on cyclic response (pre-yielding)

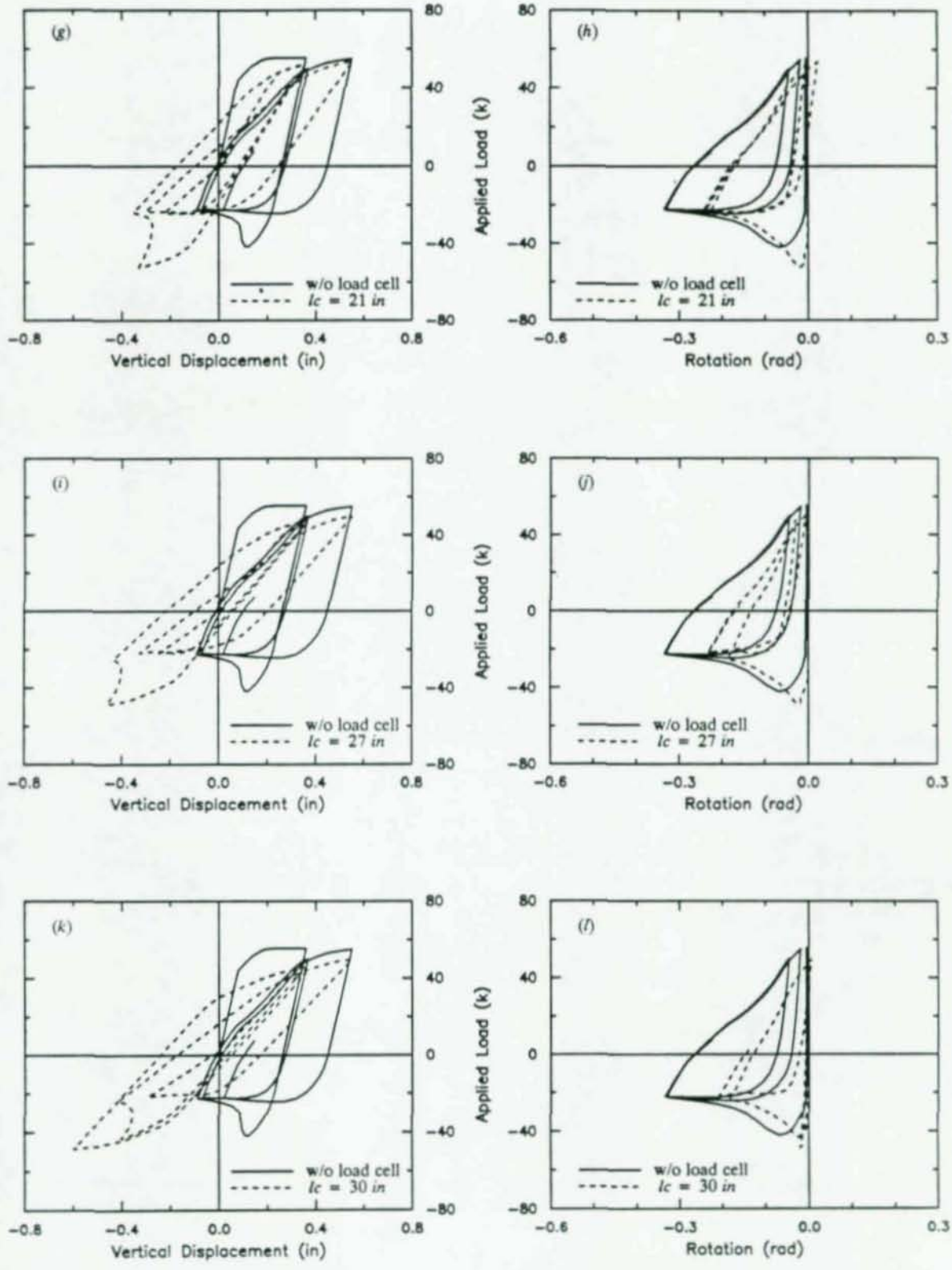

Fig. 6.12 *(cont.)* Effect of load cell length on cyclic response (pre-yielding)

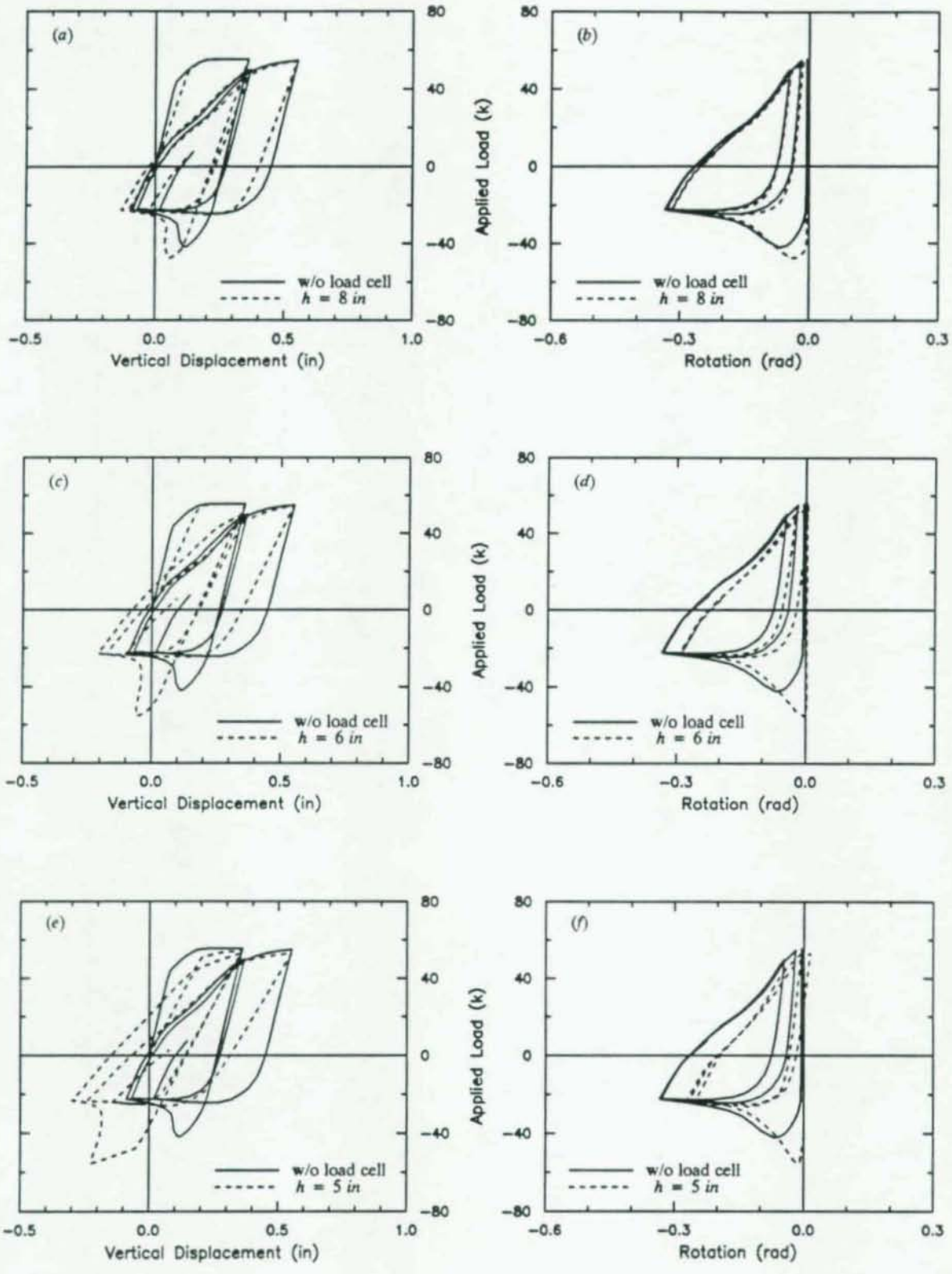

Fig. 6.13 Effect of cross-sectional dimensions of load cell on cyclic response (pre-yielding)

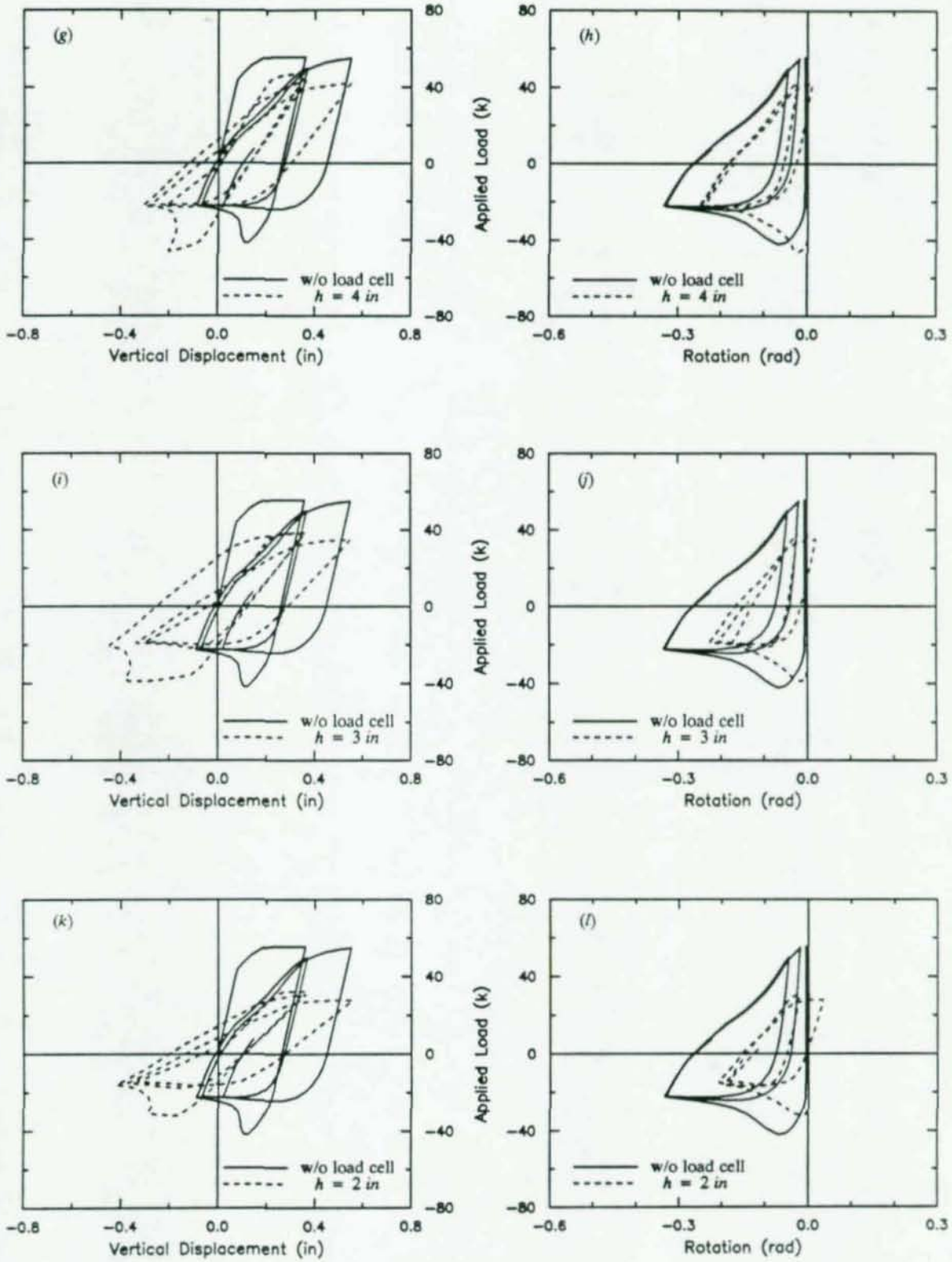

Fig. 6.13 *(cont.)* Effect of cross-sectional dimensions of load cell on cyclic response (pre-yielding)

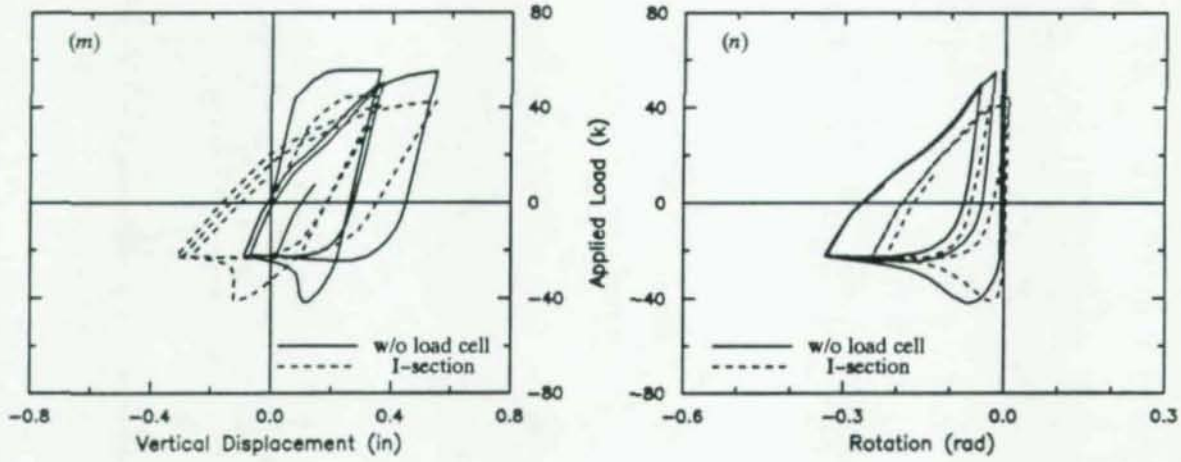

Fig. 6.13 *(cont.)* **Effect of cross-sectional dimensions of load cell on cyclic response (pre-yielding)**

Chapter 7

An Analytical Study of the Influence of Lateral Bracing on the Lateral Buckling of the Test Specimens

The primary mode of response of a beam which buckles laterally is lateral motion and rotation of the cross-section. If restraints are added to the system to prevent these motions, while at the same time allowing planar motion, the performance of a torsionally flexible system can be greatly improved. *Lateral bracing*, as it is called, has long been used in design practice to enhance the carrying capacity of I-beams and other sections which show a propensity toward lateral buckling. While design specifications address the issue of lateral bracing, essentially through the artifice of the so-called *laterally unbraced length*, the understanding of what constitutes adequate lateral bracing remains rather primitive.

Lateral bracing can be realized in a variety of ways, either through the attachment of discrete elements with axes perpendicular to the main member, or through the continuous attachment of a lateral restraining system such as a floor slab. In most practical circumstances the degree of fixity of the bracing member to the beam is not well known, making an assessment of the effectiveness of bracing difficult, if not impossible. These problems have hampered the development of rational design criteria for lateral bracing. Just as important parameters (such as the height of load action) are often not reflected in design formulae, many factors which are critically important to lateral bracing performance do not appear in design formulas. Some of these factors will be discussed herein for the application to short beams.

The lateral bracing system is an integral part of the beam/bracing system, and the response will depend upon the interaction of the two components. While this observation is true for all laterally braced systems, it is particularly important for the application to short beams because the in-plane forces can be quite large at incipient buckling. After buckling, a component of these large forces must be absorbed by the bracing system. If the strength of the brace is not sufficient to resist compressive buckling, then the brace/beam system buckles simultaneously. If the strength of the brace is sufficient to resist the induced forces without buckling, then the beam buckles into a shape which respects the persisting constraint. In many cases it may not be feasible to completely prevent buckling, but it may be important to delay it. In this chapter we examine bracing systems which are in that intermediate range where the brace itself is near its critical size. We consider only bracing against lateral motion and not against rotation; so even if the brace does not buckle, lateral buckling of the system may not be completely prevented.

A number of studies have been made on the effectiveness of various types of lateral restraint and on the strength and stiffness required to inhibit buckling of elastic beams. Mutton and Trahair (1973) investigated the stiffness requirements for midspan rotational and translational bracing of perfect, elastic beams acted upon by either top-flange loading or by shear-center loading. Nethercot (1973) also studied the effectiveness of translational and torsional restraints on simply supported elastic I-beams, focussing on the relationship between the height of the applied load and the geometric placement of the bracing system. Kitipornchai, Dux and Ritcher (1983) investigated the influence of the restraint location along the length of an elastic cantilever beam.

Lay and Galambos (1966) treated the problem of laterally bracing beams which have a propensity to buckle inelastically, and developed design criteria for cases in which the required plastic strain is high.

These rules are based on a rotational capacity consistent with the beam unbraced length slenderness ratio. They calculated a required cross-sectional area for axial strength where the stiffness of brace must be satisfied, and also indicated that flexural strength and stiffness requirements must be satisfied in addition to the axial strength and stiffness when the compression flange is braced.

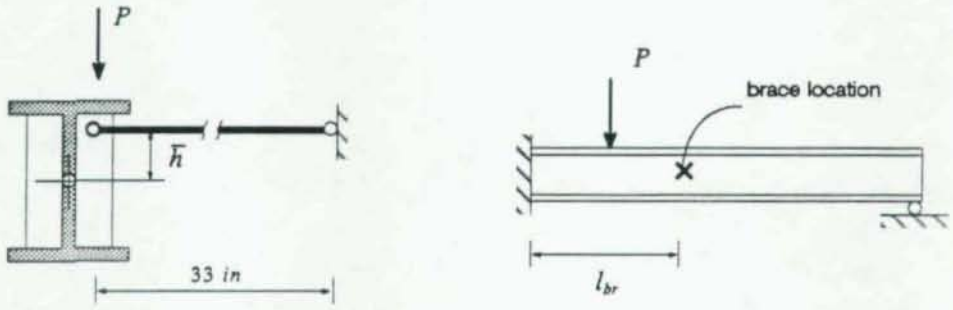

Fig. 7.1 Geometry of the lateral bracing system

In this chapter, the effect of adding a discrete translational bracing system, similar to that used in the experiments, to the test specimens is examined analytically. Figure 7.1 shows the position of the brace with respect to the cross-section and with respect to the beam axial coordinate. The influence of the height of the bracing above the shear center of the beam, the location of the brace along the length of the beam, and the strength and stiffness of the brace are examined through parameter studies with the analytical model. The brace positions examined in this study include $\bar{h}$ = 4.31, 3.81, 2.81, 1.81, 0.0, -1.81, -2.81, -3.81, and -4.31 *in*. The height of 3.81 *in* (-3.81 *in*) corresponds roughly with the brace position used in the experiments, that is, one inch below (above) the top (bottom) flange. Rectangular tube *(box)* sections, ranging in area from 0.032 in^2 to 0.128 in^2, are used here to analytically model the braces. Table 7.1 lists the properties of the braces examined in the main parameter studies. The braces used are quite slender, having $(A/I)_{br}$ = 24. The location of the brace along the length is varied from l_{br} = 15 *in* to 50 *in* in increments of 5 *in*.

Table 7.1 Properties of the lateral bracing members

t (*in*)	A_{br} (in^2)	$EI_3 = EI_2 = 0.6GJ$ ($in^2 - k$)
0.016	0.032	40
0.020	0.040	60
0.032	0.064	80
0.048	0.096	120
0.064	0.128	160

The brace configurations examined here consist of a brace on only one side of the beam. Depending upon the geometry of the initial lateral imperfection (which determines the direction of buckling), the brace will be either compressed (brace on the same side as the eccentricity) or tensed (brace on the opposite side of the eccentricity). Clearly, the response in these two cases will be different if the compressed brace buckles since the tensed brace cannot buckle. The effect of the position of the bracing with

respect to the side of the load eccentricity is also studied, using a fully nonlinear model for the brace as well as the beam to capture system buckling.

In the experiments, the bracing rods were pinned at both ends. Here we consider two brace models: one in which the brace is fixed at the end remote from the specimen and pinned to the specimen and the other in which the brace is pinned at both ends. In the latter case it is necessary to give the brace initial geometric imperfections in order to analytically model brace buckling. In the former case the deformation of the system before buckling causes flexure in the brace making it possible to buckle without initial geometric imperfections. Because the amplitude of the initial geometric imperfection of the brace may affect the response, the pin–fixed brace is employed for most of the parameter studies in this chapter. The two different brace boundary conditions are compared subsequently.

The main advantage of analytic modeling over experimental analysis is the ease with which different geometric configurations can be implemented. The geometric and material properties of the model beams studied in this chapter are the same as those used in the experiments and in the previous analytical studies. The fixed end is considered to be rigid for the purposes of these studies and the loading programs do not include pre–yielding. Standard values are used for the height and eccentricity of the applied load. The responses are compared to the (analytic) response of the test beam without bracing wherever possible.

The parameter study is organized in the following way: First the effect of brace location along the length of the beam is examined holding the brace size and bracing height fixed. The effect of brace size and bracing height are examined for bracing placed at the point of loading, first for a brace on the same side as the load eccentricity and subsequently for a brace on the opposite side of the load eccentricity. The effect of different brace cross–sectional types is then examined while holding the area of the brace and the location constant. Finally, the effect of end fixity conditions of the brace is examined. In each case inelastic monotonic and cyclic responses are considered.

7.1 The Effect of Brace Position along the Length of the Beam

The position of the load along the length of the beam is of fundamental importance to the buckling behavior. There are, of course, many possibilities for bracing arrangements and we will restrict our attention here to a single discrete brace placed somewhere in the span. It is perhaps obvious in the present case, with a single point loading, that the best brace location will be at or near the point of loading. In fact, many design specifications require lateral bracing at points of load (or at points where plastic hinges are likely to form) as a conservative precaution and in lieu of more rigorous knowledge. In this section we demonstrate that the above observation is true and make an effort to quantify the trade–off represented by other bracing locations.

The inelastic monotonic responses of the propped cantilever beam with bracing alternatively at l_{br} = 15, 20, 25, 30, 35, 40, 45, and 50 *in* are shown in Fig. 7.2 for the brace having area $A_{br} = 0.064\ in^2$ and bracing elevation $\bar{h} = 3.81\ in$. The response of the beam without lateral bracing is also shown in the figure for comparison. One can observe the clear superiority of bracing in the vicinity of the applied load. Interestingly, the response for bracing up to 10 *in* past the load point is nearly identical to the response for bracing at the load point. This observation makes sense because the load is located so near to the fixed end. One can also observe that there is virtually no improvement in behavior for bracing locations

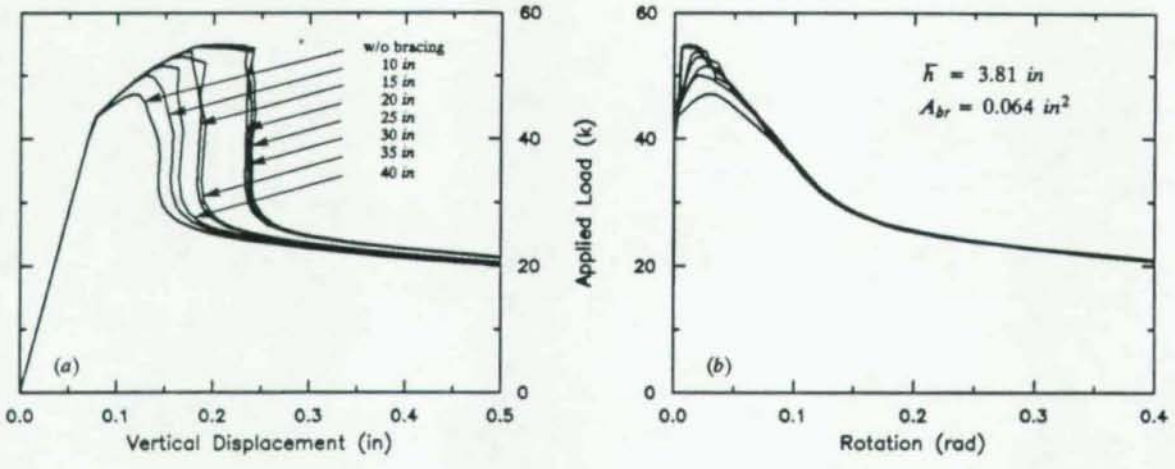

Fig. 7.2 Effect of the position of the load along the length of the beam

even moderately remote from the point of loading. In the sequel, the brace will be positioned at the point of loading.

7.2 The Effect of Brace Size and Elevation with Respect to the Shear Center

The primary parameters studied in this section are the size of the brace and its elevation with respect to the shear center of the cross-section. Since push loading is critical with respect to lateral stability, and since the top flange is in compression for this sense of loading, it is expected that bracing above the shear center will be most effective. We demonstrate the veracity of the previous assertion and make an effort to quantify the importance of this effect. The brace sizes are chosen to bracket the transition from cases where the brace remains straight while the beam buckles to cases where the brace and beam buckle simultaneously. The parameter domain is covered by alternatively varying brace size and brace dimension with results for both monotonic inelastic buckling and cyclic buckling. The responses for braces placed on the same side as the eccentricity (compression braces) are examined first and then compared to those of braces placed on the opposite side as the eccentricity (tension braces).

The effect of varying the size of the brace while holding the elevation fixed at 3.81 *in* is shown in Fig. 7.3. As the brace size increases both the limit capacity and the vertical deformation capability increase. Braces larger than $A_{br} = 0.096\ in^2$ allow the achievement of the full plastic capacity of the beam in planar bending before buckling. It is noted that for braces smaller than $0.096\ in^2$ the brace buckles in the plane in which it is bending, while those larger do not buckle. It is clear that this type of point bracing will delay but not prevent buckling. The load-rotation relationship is nearly independent of the brace size. The response curves for the cyclic loading cases demonstrate that after buckling the system behaves as if it had not been braced, even for relatively large braces. This same observation was noted in the experiments. The dot symbols (•) on the curves for monotonic loading response represent points of equal vertical displacement at the point of load application, and the point were the load direction is reversed in the first cycle of the cyclic loading.

The effect of varying the elevation of the brace while holding the area fixed at $0.040\ in^2$ is shown in Fig. 7.4. In *(a,b)* one can observe that the system exhibits higher limit loads and has greater vertical

deformation capability the higher the brace is placed above the shear center. The brace elevated to 4.31 *in* allows the beam to reach its full planar capacity before buckling. In *(c,d)* and *(e,f)* one can observe the ineffectiveness of bracing below the shear center. The fact that the response for an elevation of −1.81 *in* is identical to the response for the system without bracing indicates that during buckling the beams rotates about that point in the cross-section. It is interesting to note that the center of rotation remains fixed even in the presence of progressing inelasticity and large rotations. The cyclic responses again demonstrate the ineffectiveness of bracing in the post-buckling regime.

The combined effects of brace size and elevation are shown again in Fig. 7.5. In each plot, four different bracing sizes (A_{br} = 0.000, 0.048, 0.064, 0.080) are shown for a single value of the elevation. Each subsequent plot has a lower brace elevation ($\bar{h}$ = 4.31, 2.81, 0.00, −1.81, −2.81, −4.31). While this figure presents no new information, it helps to more clearly show the trade-off between brace size and brace elevation. Again, the ineffectiveness of bracing below the shear center is demonstrated.

The previous studies were for beams braced on the same side as the load eccentricity. Under these conditions, the brace is compressed at the point of buckling and, if it is slender enough, it will buckle too. We next examine the behavior of the system with brace buckling precluded by bracing on the opposite side of the eccentricity. The previous parameter variations are repeated for the opposite side bracing case. The responses of the two configurations are compared for the cyclic loading history.

Figure 7.6 shows the effect of brace area for a fixed elevation of 3.81 *in* for the case where the beam is braced on the opposite side as the eccentricity. Some important differences from the case with bracing on the same side as the eccentricity can be seen by comparing Fig. 7.6 with Fig. 7.3. For monotonic buckling, the responses for the smaller braces are quite similar to those of the present case. However, the tensile braces show a much greater vertical deformation capacity for the larger sized braces. One can also observe that the load-rotation curves for the tensile braces clearly depend on the brace size, even at large deformations, whereas the curves for the compression braces did not show this dependency. One consequence of this behavior is that the tension braced systems do not tend toward the same asymptotic post-buckling capacity. Comparing the cyclic responses of the two cases one can see the clear superiority of the tension brace. Note that the tension brace exhibits subsequent buckling loads which are greater than the asymptotic post-buckling capacity. This phenomenon was also observed in specimen 5 of the experiments. In spite of the better behavior, the tension braced system still shows only marginally better performance over the unbraced system in the post buckling range.

The effect of brace elevation for fixed brace area is shown in Fig. 7.7 for the case of opposite side bracing. These results can be compared with eccentric side bracing in Fig. 7.4. Considerable increases in the load carrying capacity and vertical deformation capability are gained by opposite side bracing for elevations above the shear center. Virtually no benefit accrues from opposite side bracing below the shear center. Again, opposite side bracing has a large effect on the first cycle of loading, but little effect in subsequent cycles. Most of the observations on the response carry over from the study on brace size. The two parameters are further studied in Fig. 7.8, wherein similar observations can be made. It is interesting to note that the brace buckles for the elevation of −1.81 *in* but does not for any other elevation studied.

7.3 The Effect of Brace Cross-Sectional Geometry

In the previous study the ratio of brace area to moment of inertia was held fixed. In this section we examine braces which have the same cross-sectional area but have different moments of inertia. Three

brace cross-sections are considered as outlined in Table 7.2. The first brace type is the box-section used in the previous study, with a depth of 0.5 *in* and a wall thickness of 0.032 *in*. The second brace type is an I-section with considerably larger major moment of inertia, but smaller minor moment of inertia than the box. The third brace type is a smaller box-section with one quarter the moments of inertia of the standard box-section.

Table 7.2 Properties of alternative brace types with equal same brace area

type	h (*in*)	b (*in*)	t (*in*)	t_f (*in*)	A_{br} (in^2)	EI_3 (in^2-k)	EI_2 (in^2-k)	GJ (in^2-k)
box	0.50	0.50	0.032	0.032	0.064	80	80	48
I-section	1.60	0.40	0.020	0.040	0.064	819	12.8	0.256
box	0.25	0.25	0.064	0.064	0.064	20	20	12

The monotonic buckling responses with the various braces are given for brace elevations of 4.31, 2.81, 0.00, -1.81, -2.81, and -4.31 *in* in Fig. 7.9. It is evident from this study that the axial stiffness, which is the same for all braces, is not an important influence on the limit capacity and vertical deformation capability of the system. Even though the I-section brace had the largest major flexural moment of inertia it buckled the soonest, because buckling in the minor direction occurred even before the beam buckled laterally. One can conclude that the limit load of the beam-brace system depends most significantly on the minor moment of inertia of the brace.

7.4 Effect of Brace End Fixity Conditions

In this section, we examine the influence of the end boundary conditions of the brace. An initial imperfection increasing linearly from zero at the ends to maxima of 0.003 *in* in the major direction and 0.0005 *in* in the minor one was used to induce buckling in the pin-pin brace. No imperfection was required for the pin-fixed brace because deformations due to bending were sufficient to drive the buckling mode. Figure 7.10 shows the influence of the two different brace boundary conditions for brace elevations of 3.81, -1.81, and -3.81 *in* with a (standard) cross-sectional area of $A_{br} = 0.064\ in^2$. While the initial buckling of pin-fixed brace is slightly delayed relative to that of the pin-pin brace for a brace elevation of 3.81 *in*, there is no difference between these two cases for braces below the shear center. The two end conditions lead to the same value of limit capacity and the same value of asymptotic post-buckling capacity.

Figure 7.11 shows the influence of different brace boundary conditions for various brace areas with braces elevated 3.81 *in* toward the top flange. The pin-fixed brace still shows an improvement in limit capacity of the beam with a small brace size, but the effect is clearly diminished as the size of the brace decreases. The pin-fixed brace does not buckle in the minor direction at the brace area of 0.096 in^2, while the pin-pin brace does.

Figure 7.11 *(e,f)* also demonstrates that the response is not sensitive to the magnitude of the initial imperfections chosen for the pin-pin brace. There is no visible difference in the behaviors with various (*major, minor*) initial imperfections of (0.003, 0.0005 *in*), (0.003, 0.0000 *in*), (0.002, 0.0005 *in*) and (0.001, 0.0005 *in*). The response of the system with a perfectly straight brace is also shown on this figure.

As expected, the perfectly straight pin-pin brace does not buckle and therefore provides more restraint against lateral buckling. This behavior is an artifact of the numerical model and illustrates the importance of proper analytical modeling in inelastic stability problems.

7.5 Summary

Lateral bracing is clearly effective in delaying buckling, but it does not necessarily prevent it and it has little impact on the post buckling response. In practice, since it is difficult to apply the load on the opposite side of the brace by intention, both sides of of the beam should be braced, as high above the shear center (toward the compressed flange) as possible. Lateral bracing below the shear center provided no benefit for the configuration studied here because the center of rotation during buckling was about 2 *in* below the shear center.

Minor flexural stiffness of bracing is the size parameter most important to the buckling response because simultaneous brace buckling seemed to cause the greatest difference in behavior. The most desirable location to brace along the beam is at or near the position of the applied load. The position of brace with respect to the side of the load eccentricity has a large effect on the limit capacity and the vertical deformation capability. It also has an effect on the large deformation behavior and the response to the cyclic loading. This difference in behavior can be attributed to the fact that a brace on the opposite side of the eccentricity will be tensed during lateral buckling of the beam and therefore will not buckle simultaneously.

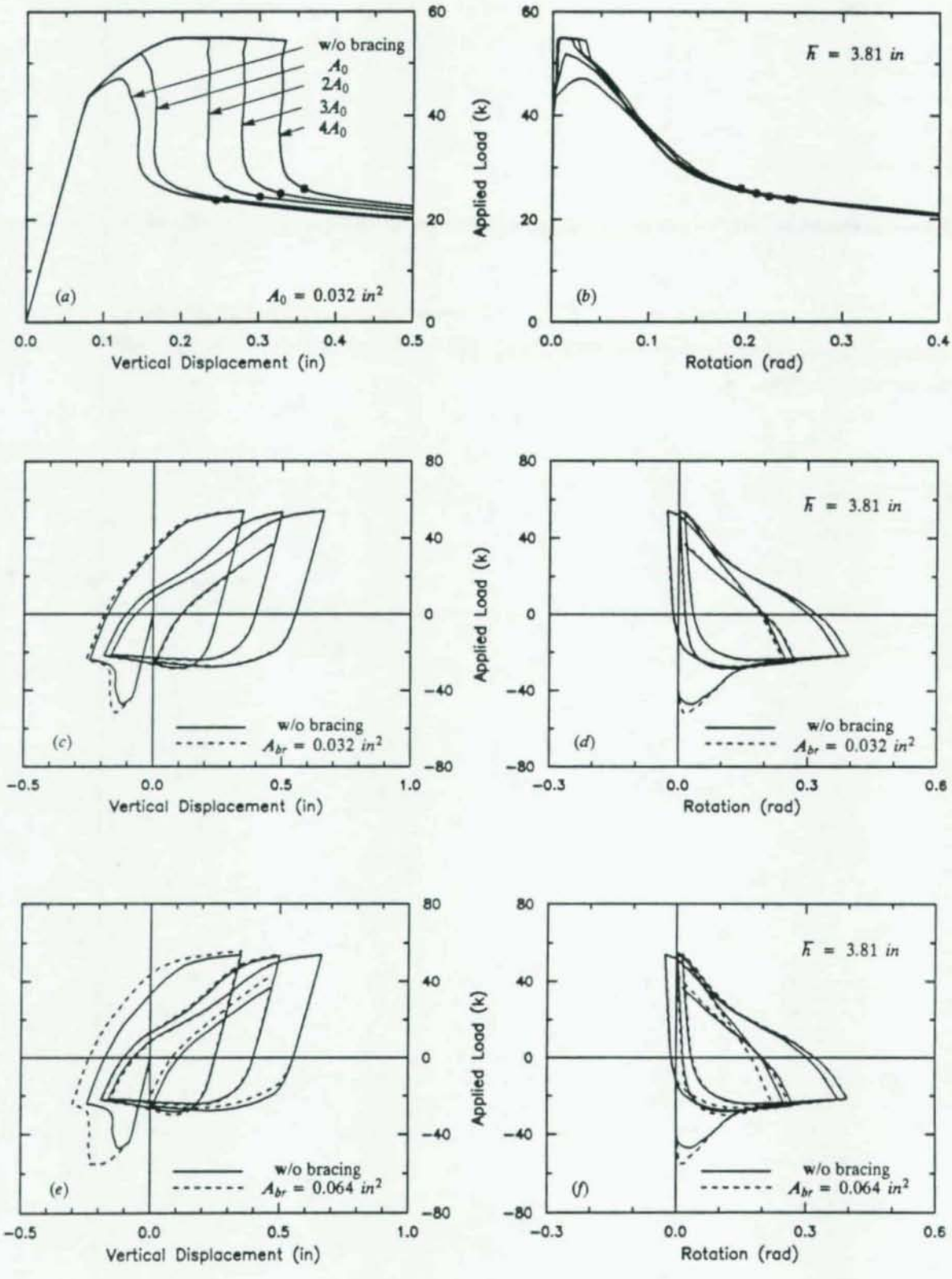

Fig. 7.3 Effect of brace size (eccentric side braced)

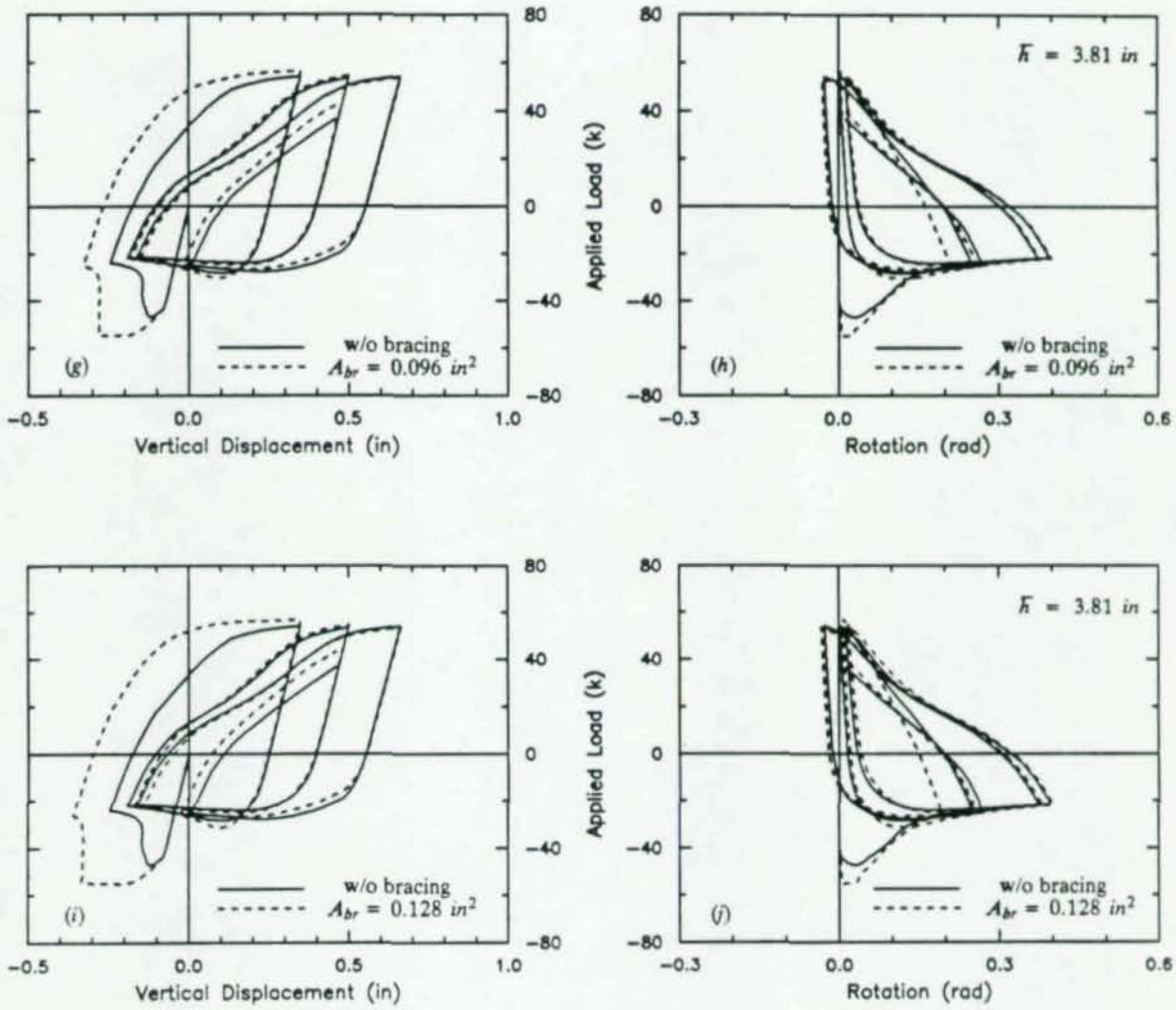

Fig. 7.3 *(cont.)* Effect of brace size (eccentric side braced)

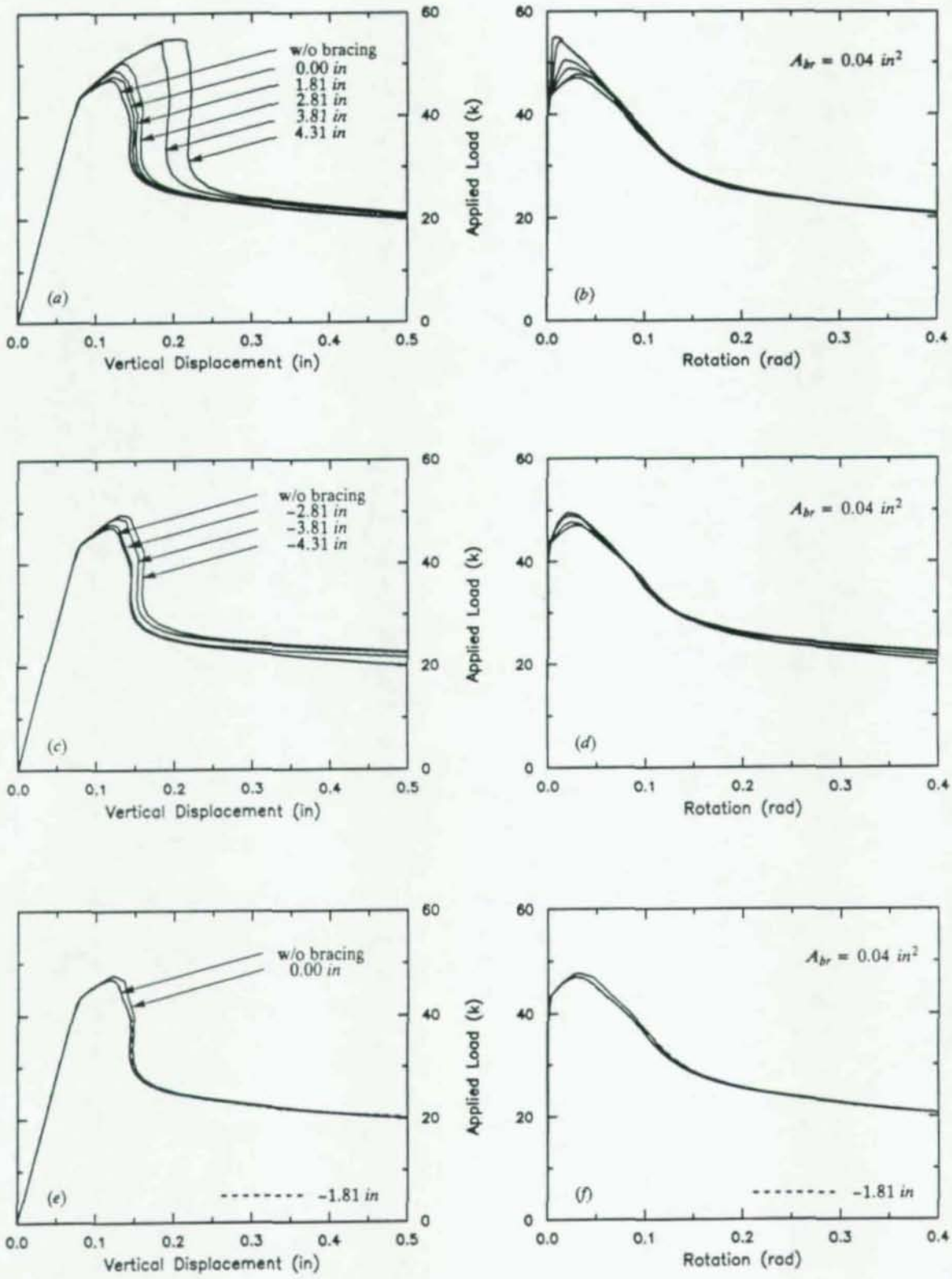

Fig. 7.4 Effect of brace elevation with fixed brace size (eccentric side braced)

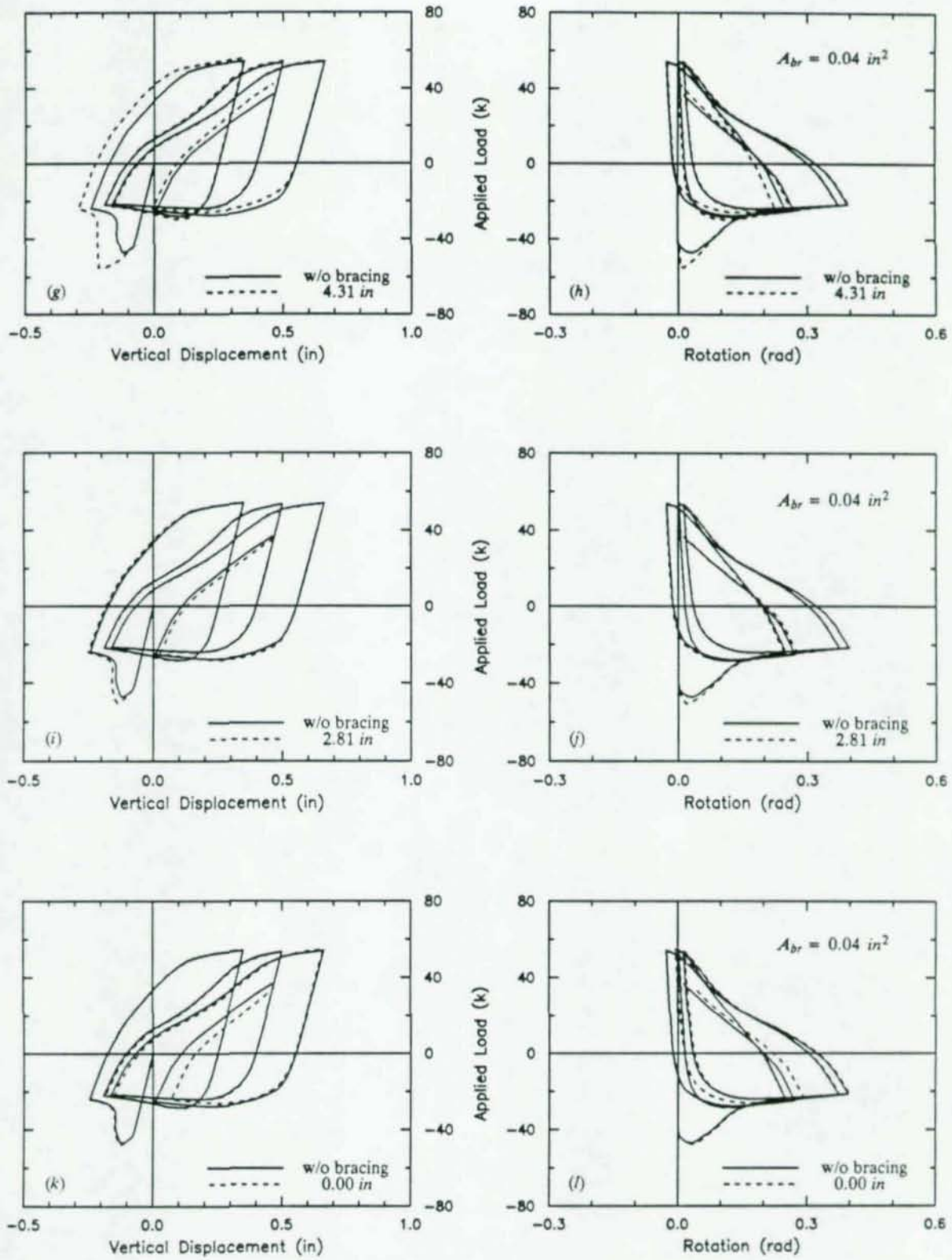

Fig. 7.4 *(cont.)* Effect of brace elevation with fixed brace size (eccentric side braced)

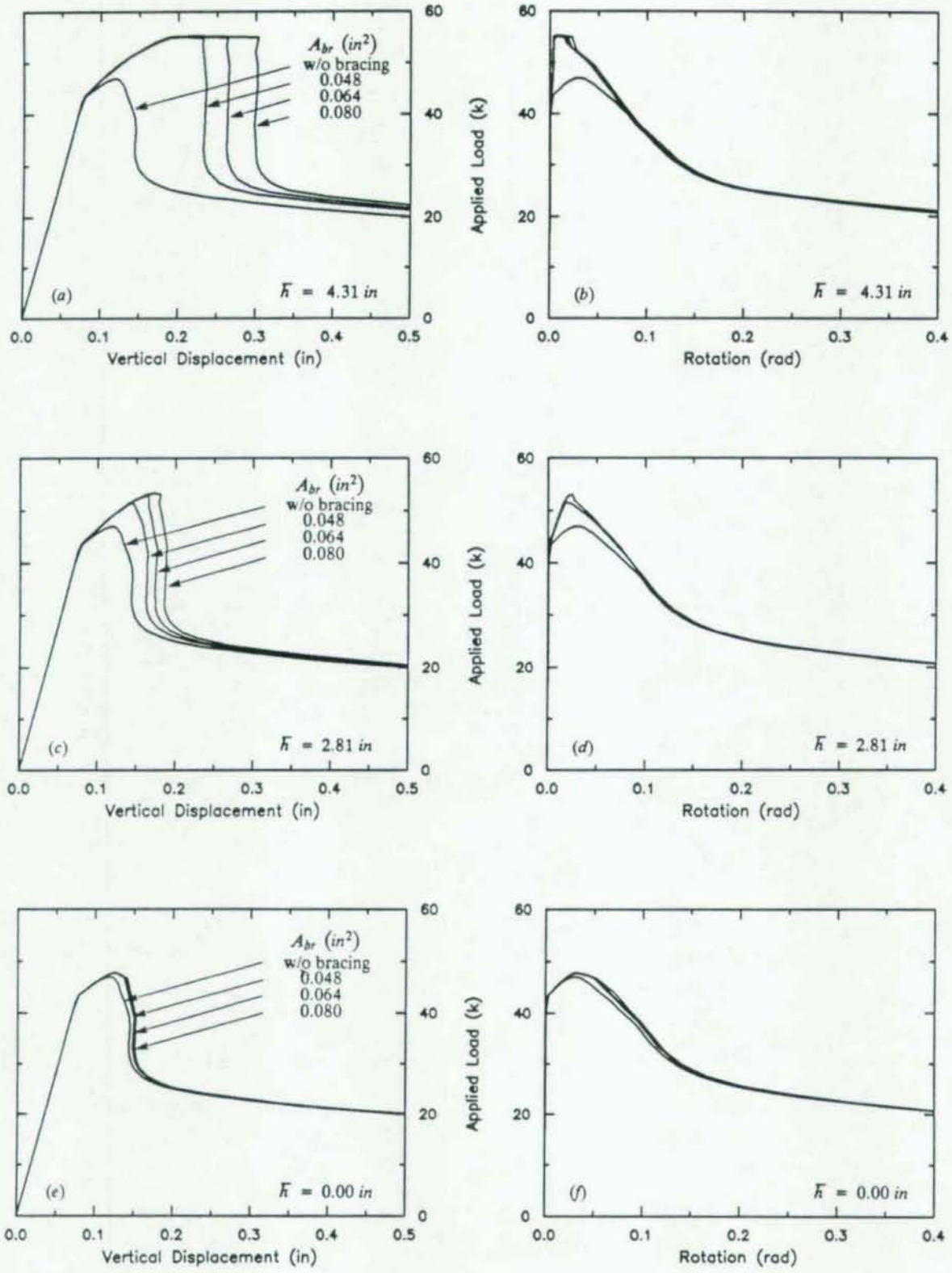

Fig. 7.5 Combined effects of brace size and brace elevation (eccentric side braced)

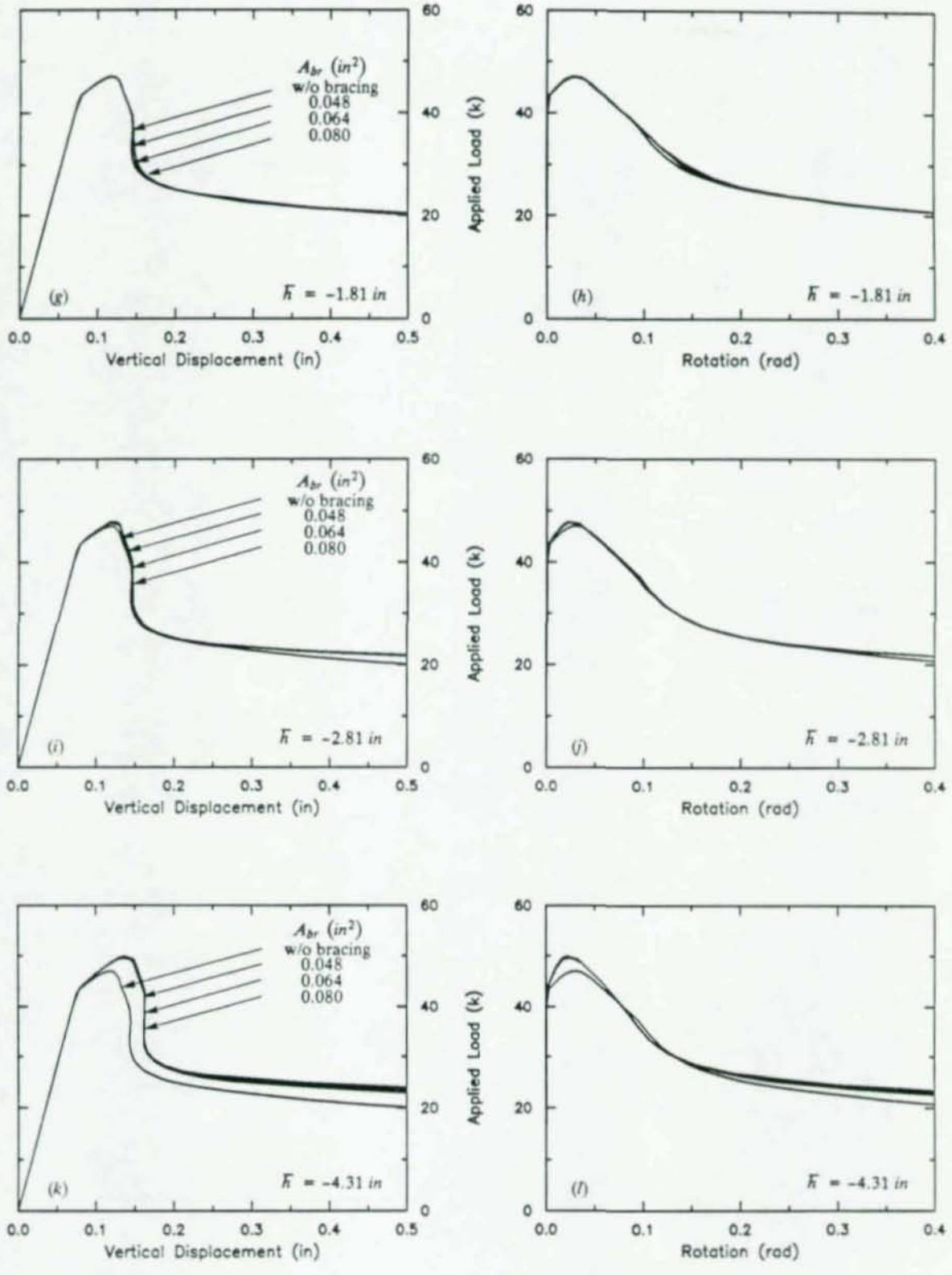

Fig. 7.5 *(cont.)* Combined effects of brace size and brace elevation (eccentric side braced)

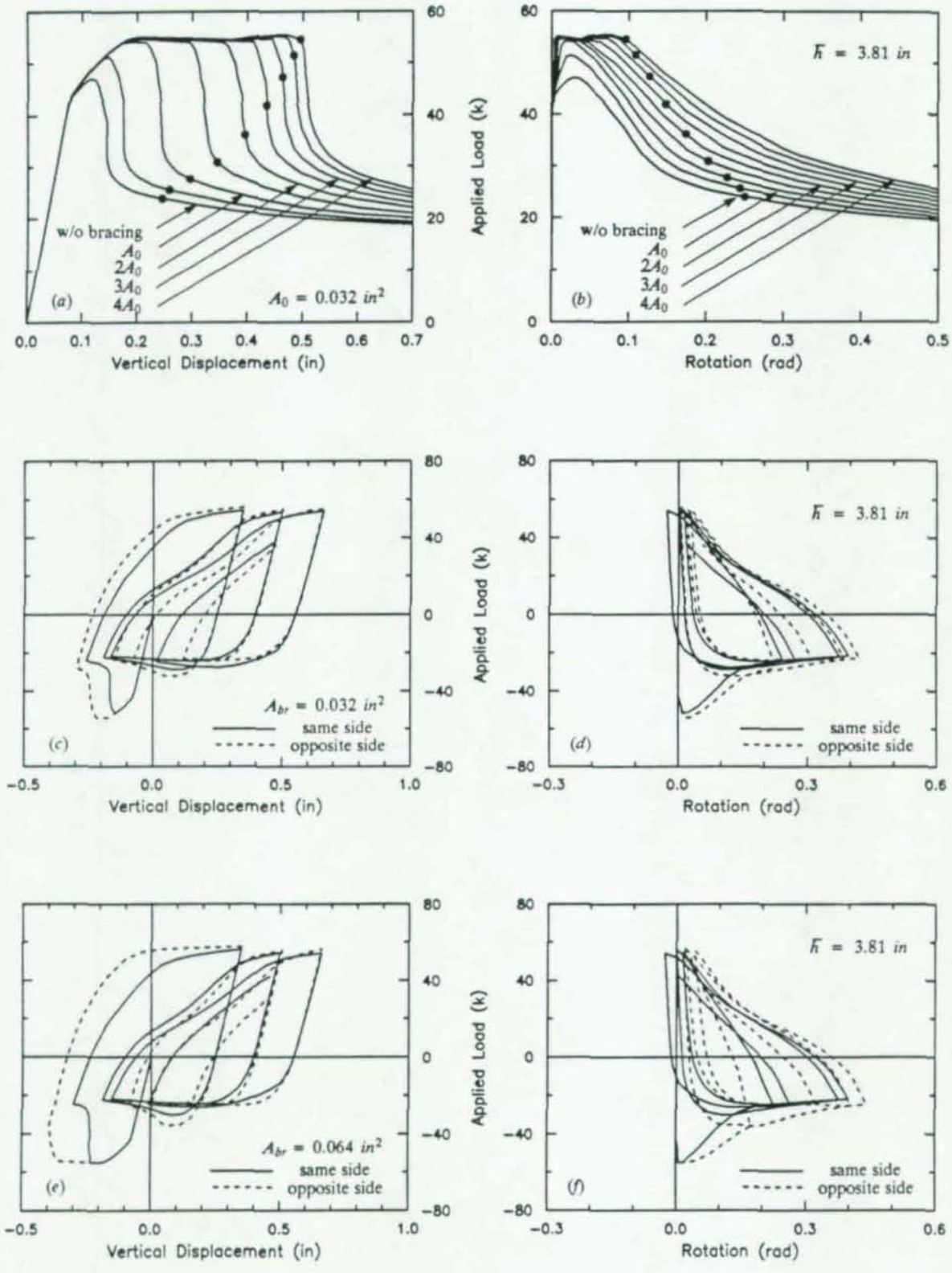

Fig. 7.6 Effect of brace size (opposite side braced)

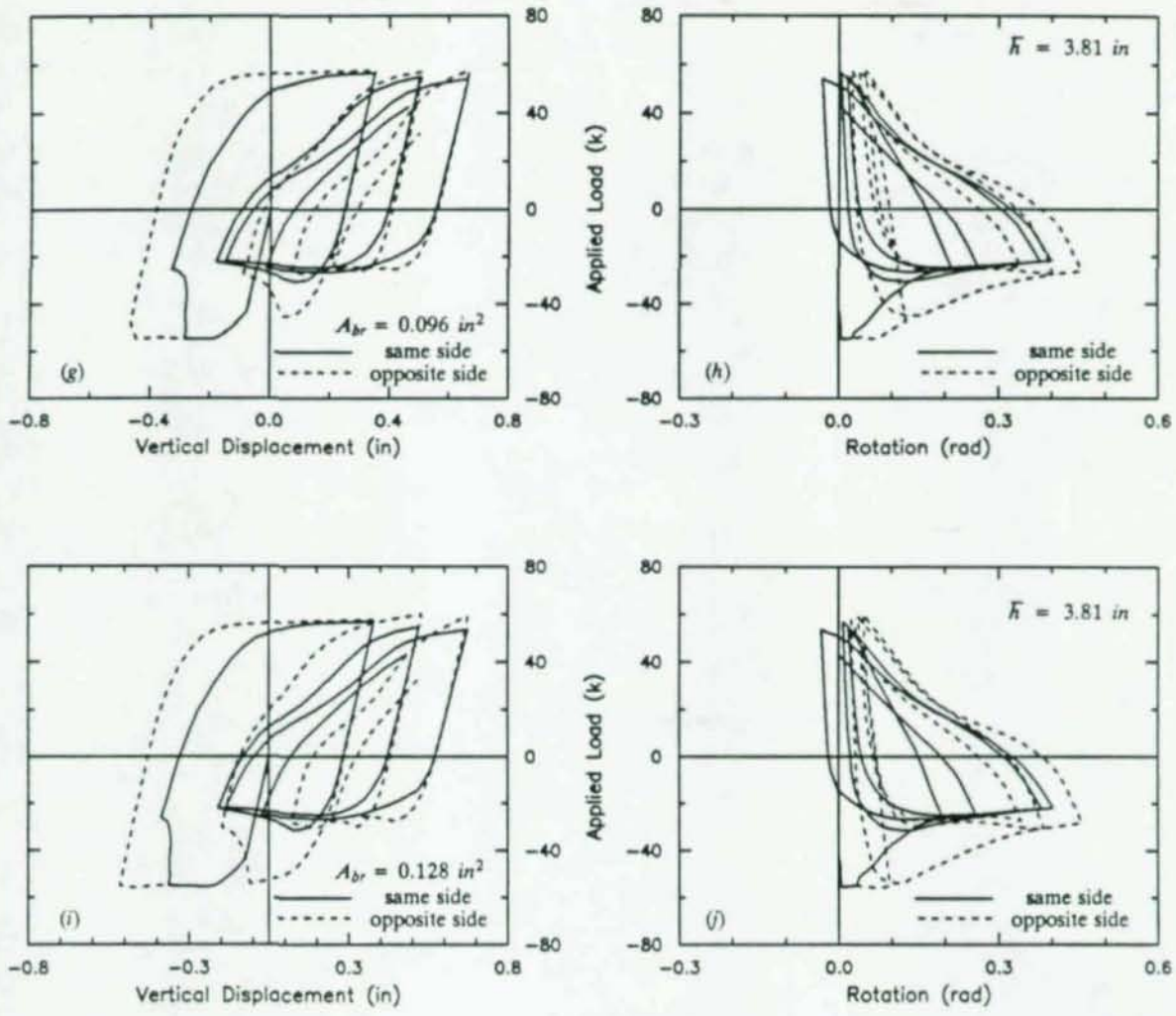

Fig. 7.6 *(cont.)* Effect of brace size (opposite side braced)

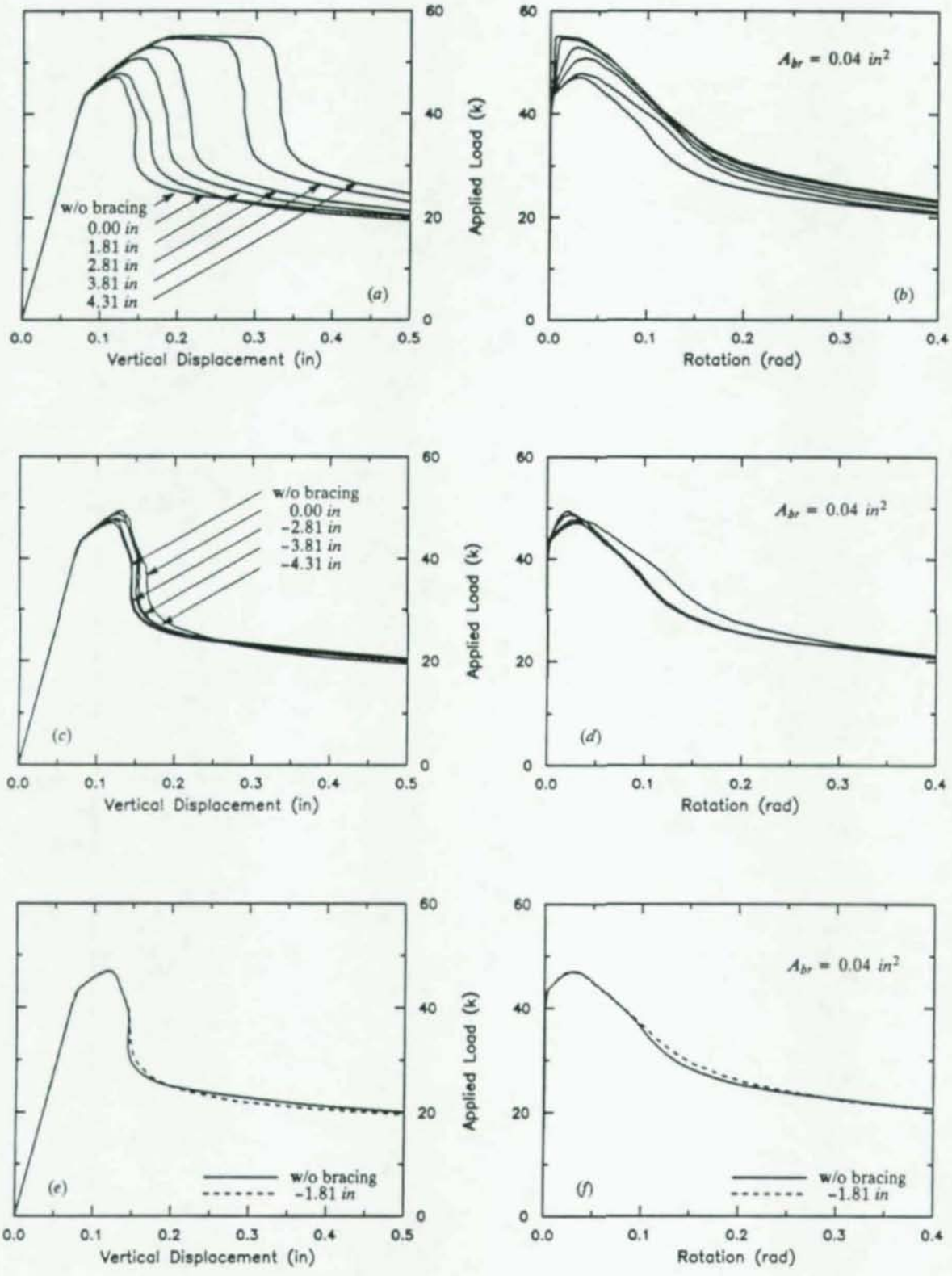

Fig. 7.7 Effect of brace elevation with fixed brace size (opposite side braced)

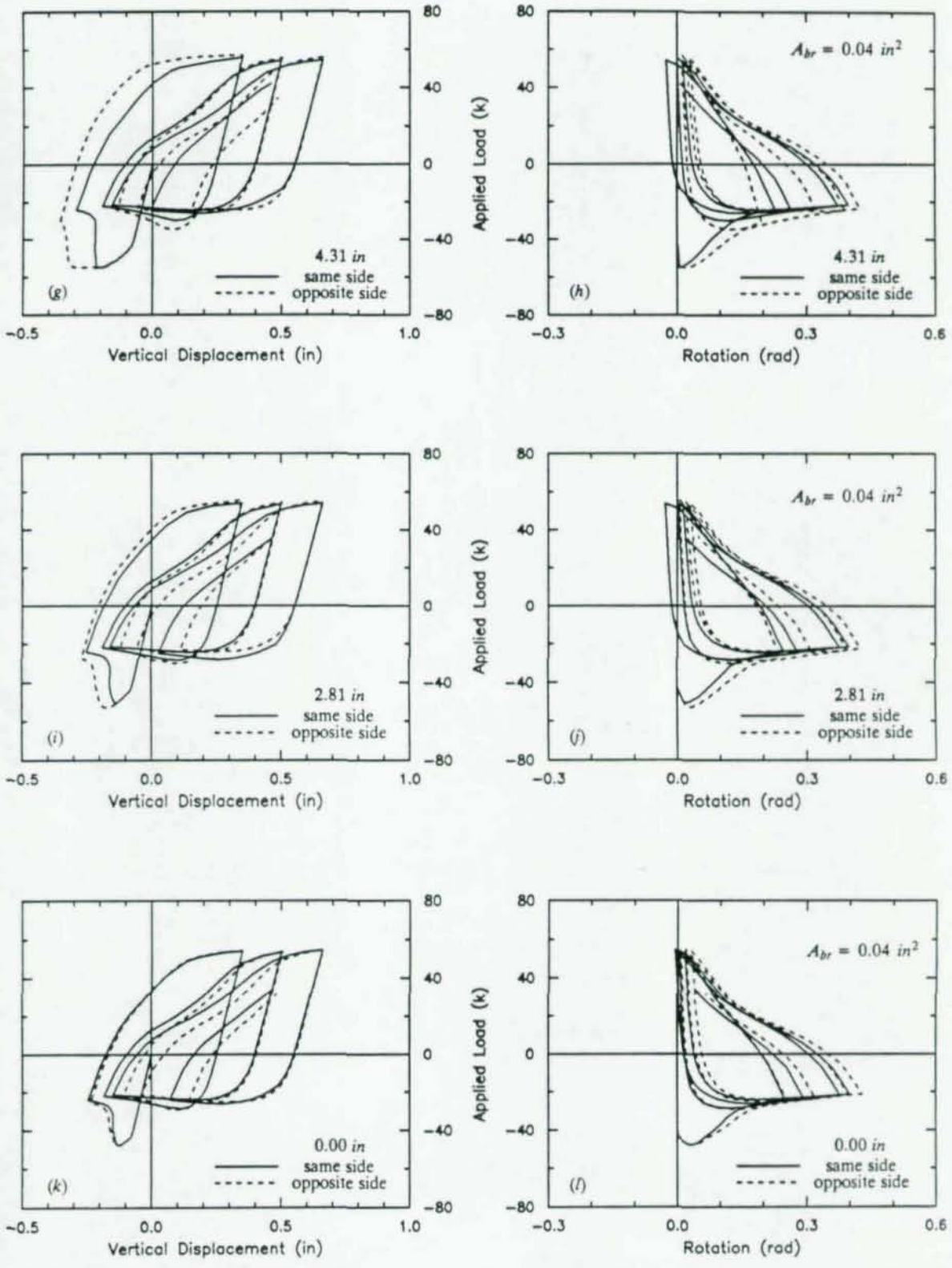

Fig. 7.7 *(cont.)* **Effect of brace elevation with fixed brace size (opposite side braced)**

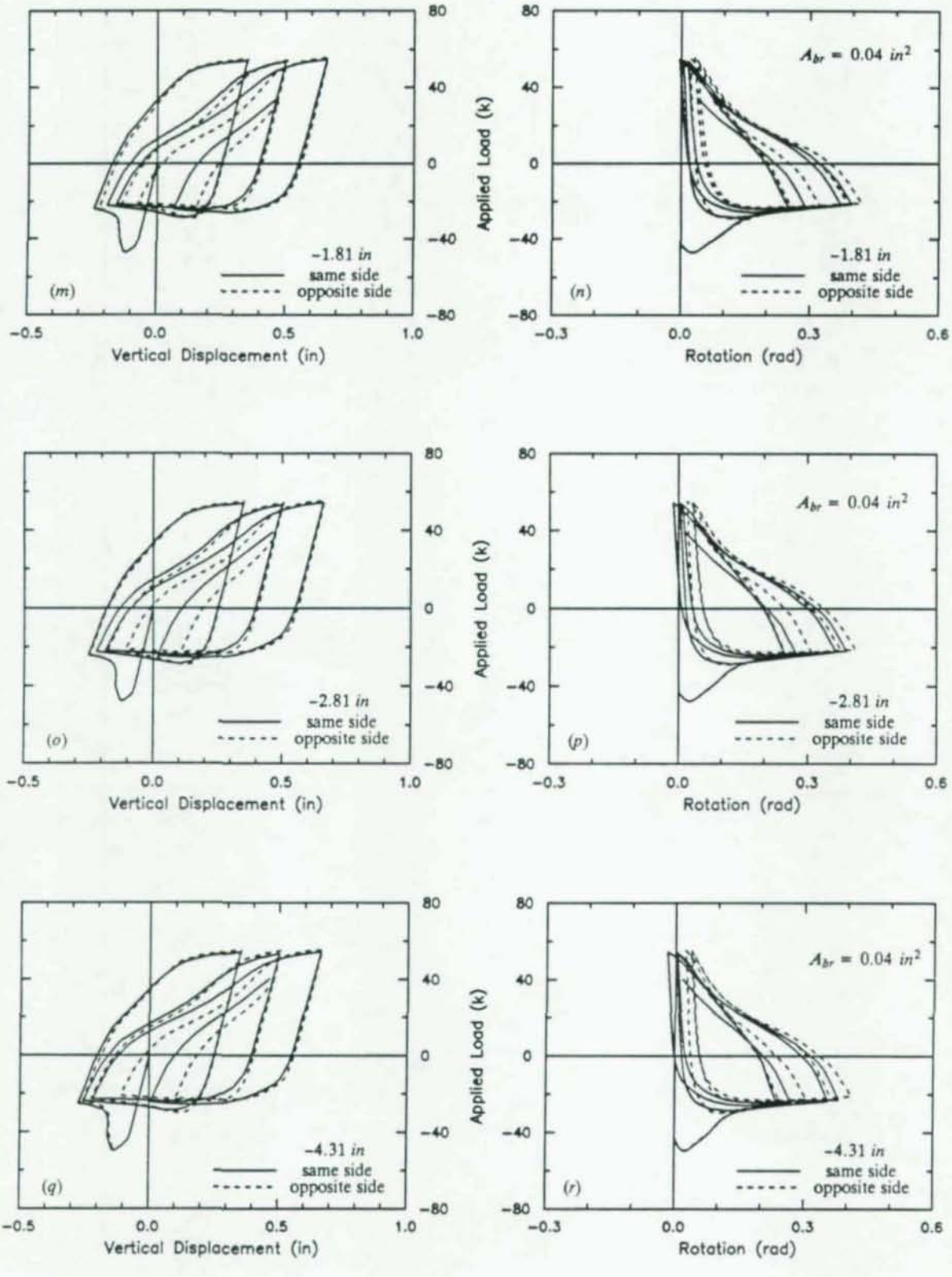

Fig. 7.7 *(cont.)* **Effect of brace elevation with fixed brace size (opposite side braced)**

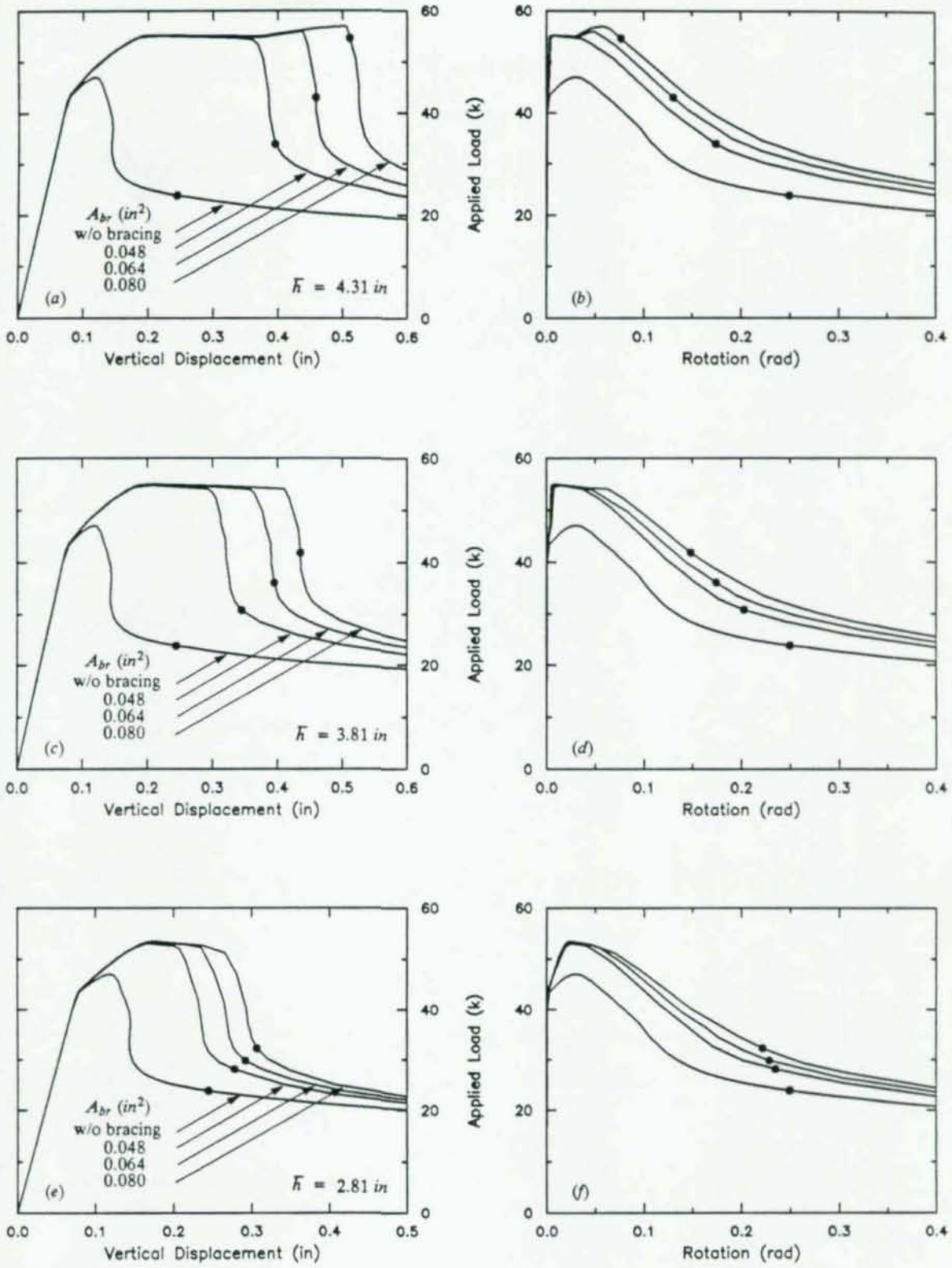

Fig. 7.8 Combined effects of brace size and brace elevation (opposite side braced)

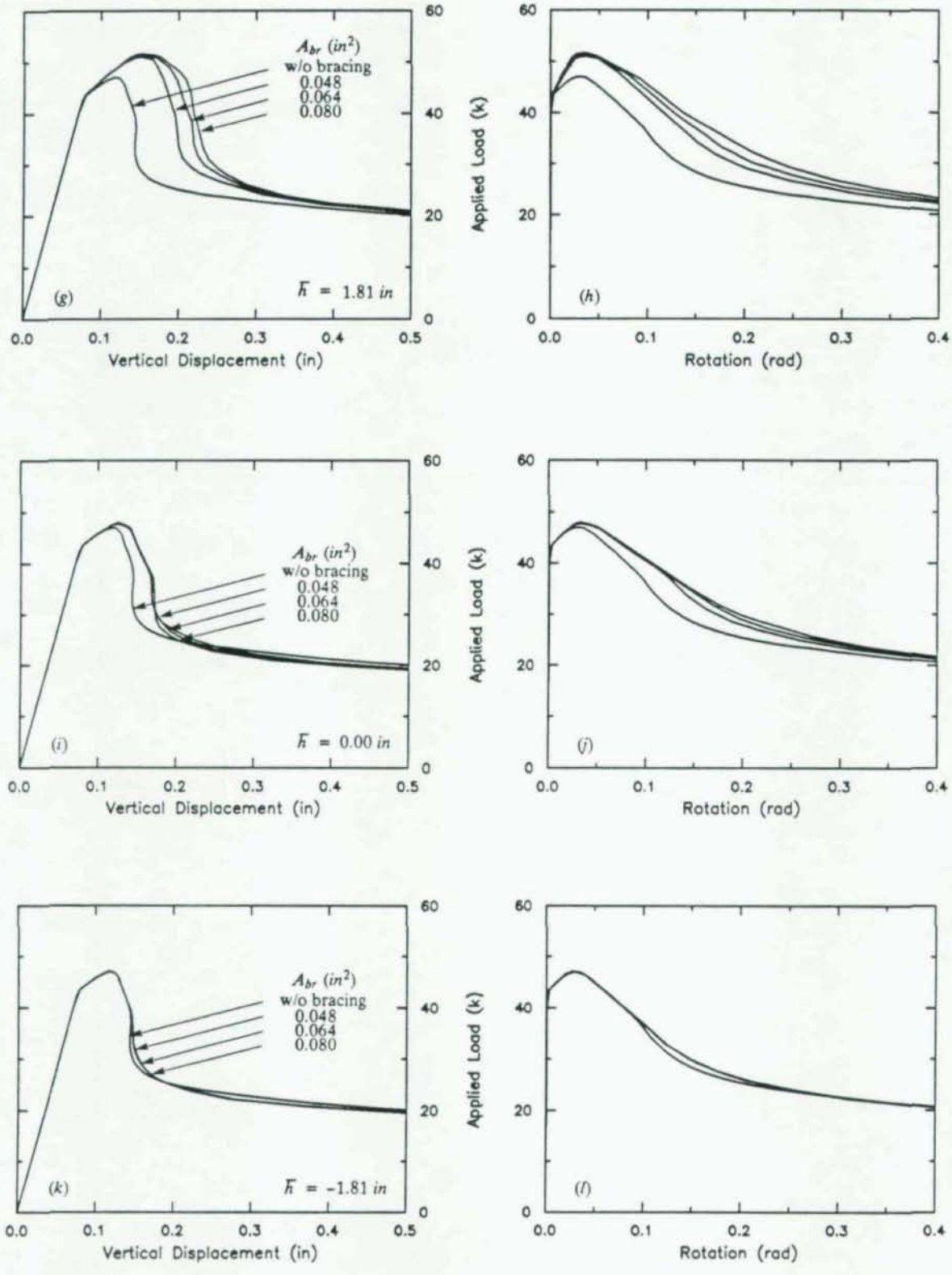

Fig. 7.8 *(cont.)* Combined effects of brace size and brace elevation (opposite side braced)

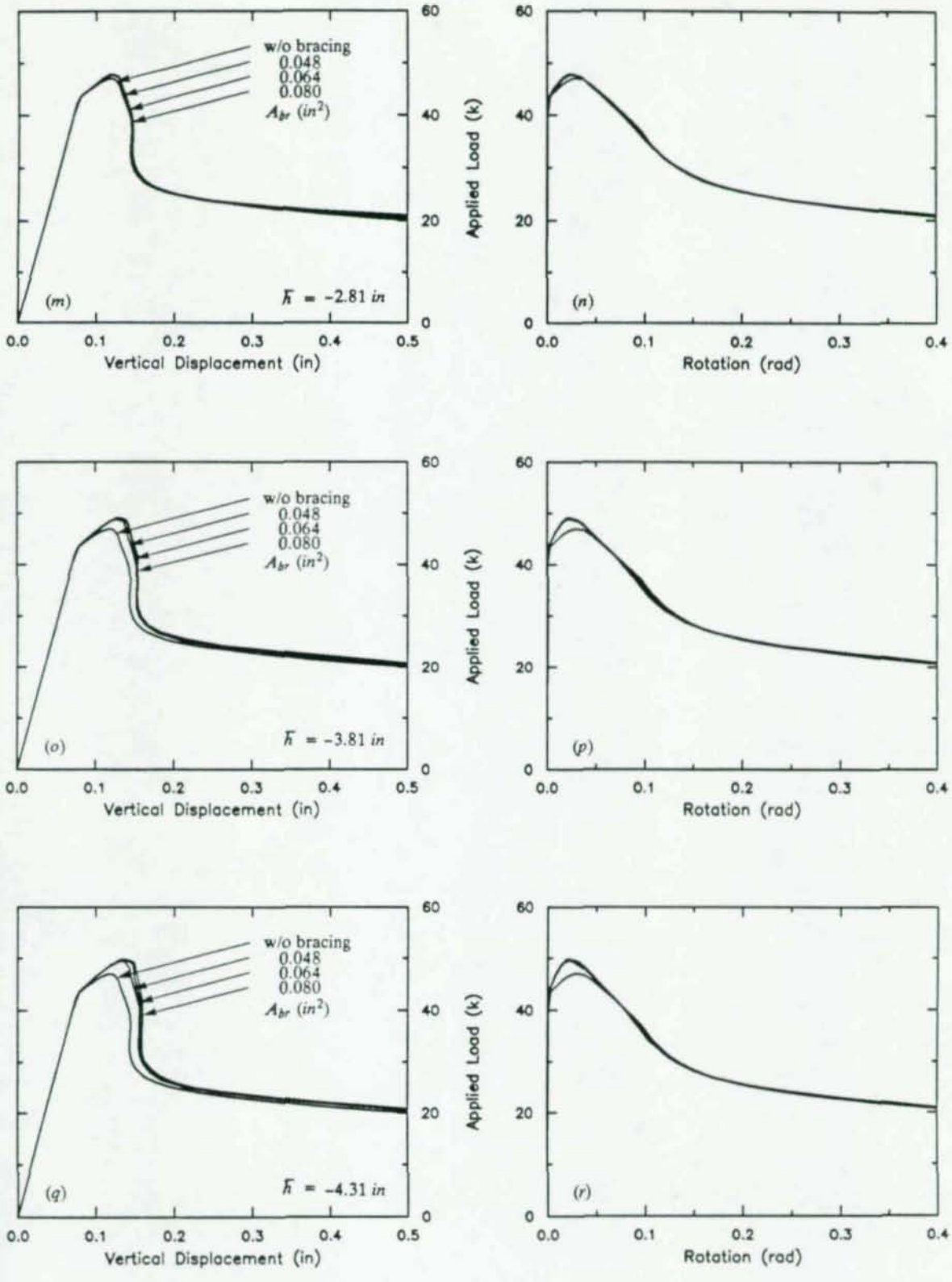

Fig. 7.8 *(cont.)* Combined effects of brace size and brace elevation (opposite side braced)

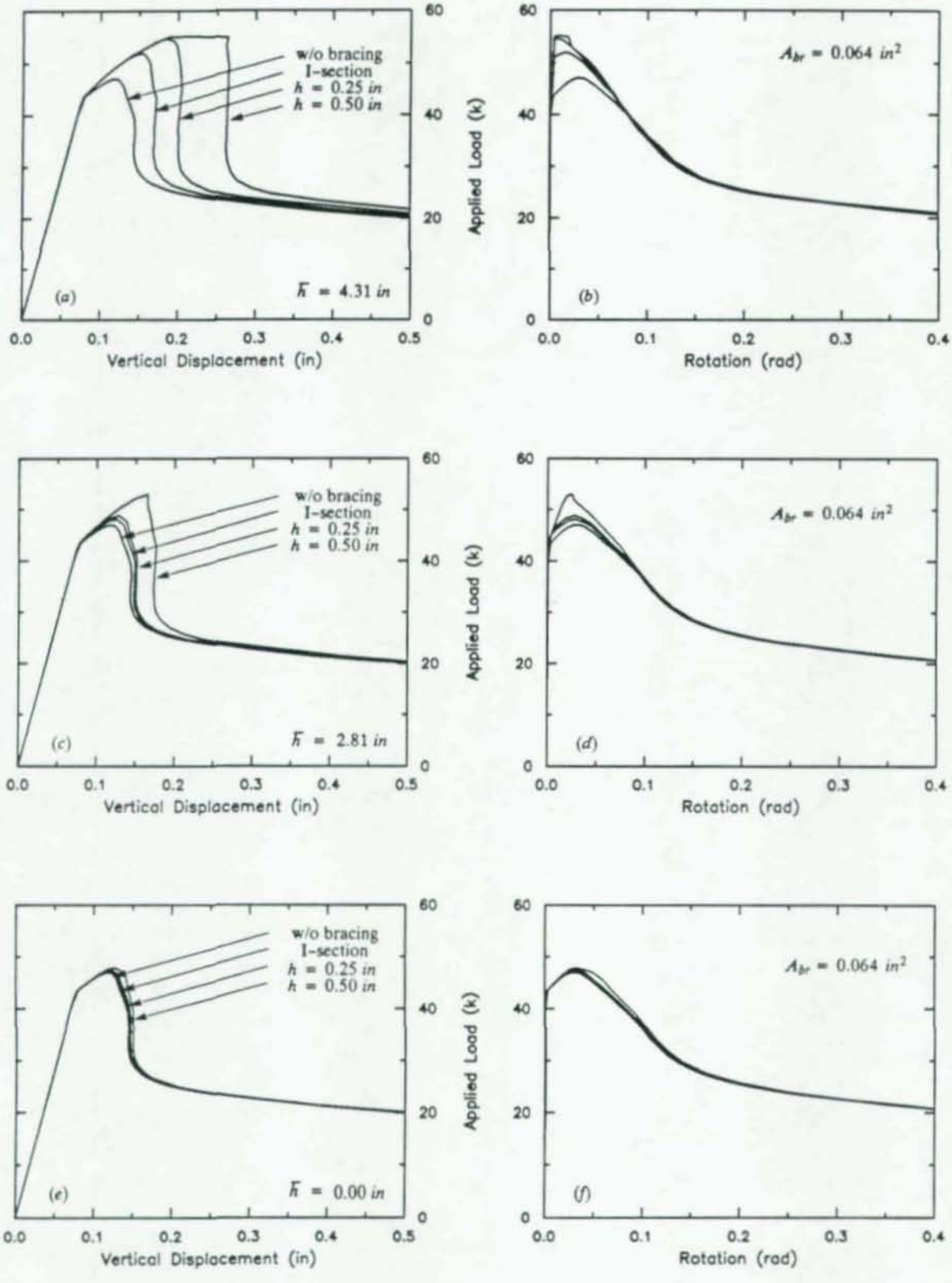

Fig. 7.9 Effect of different brace geometries (eccentric side braced)

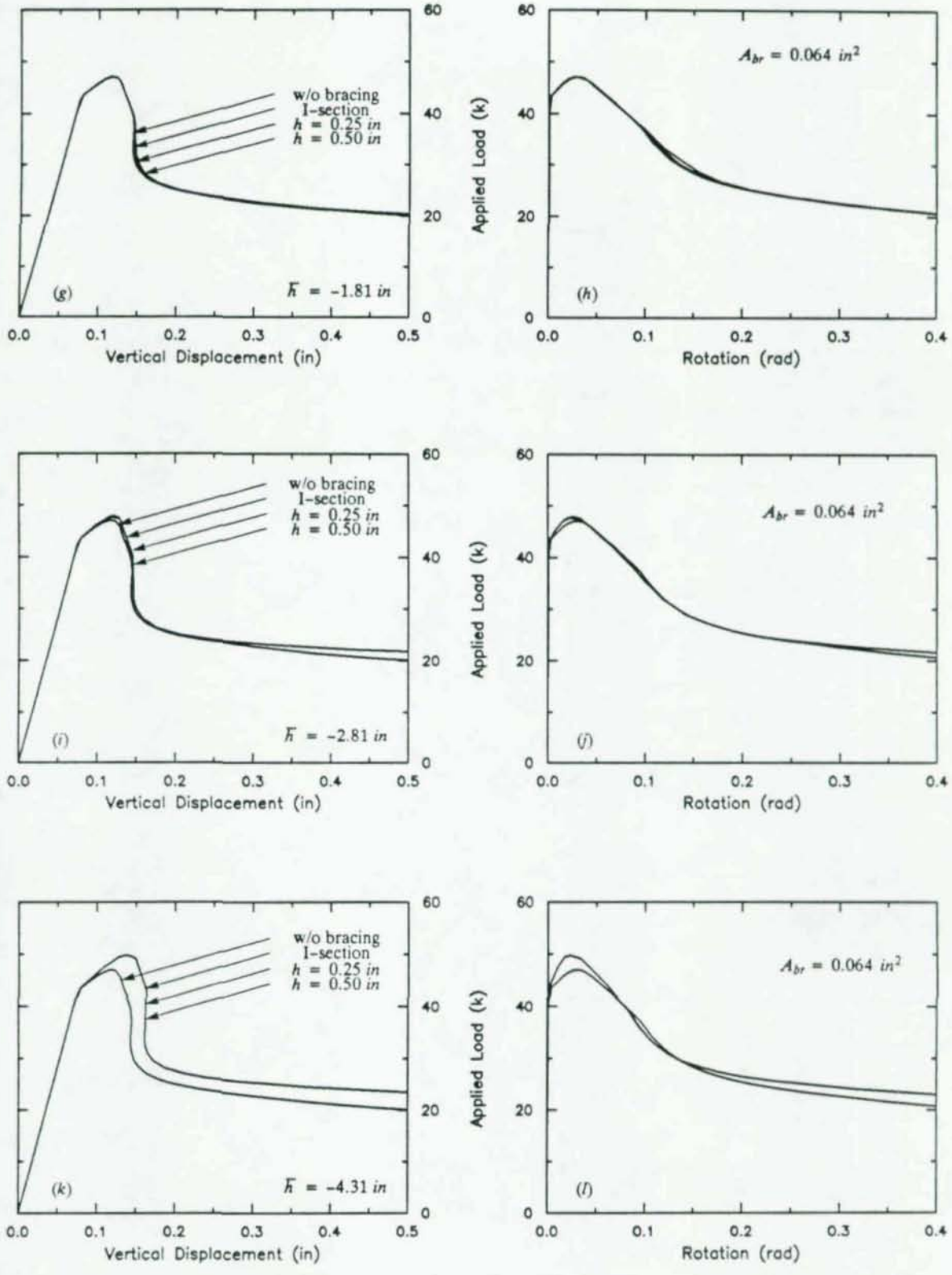

Fig. 7.9 *(cont.)* Effect of different brace geometries (eccentric side braced)

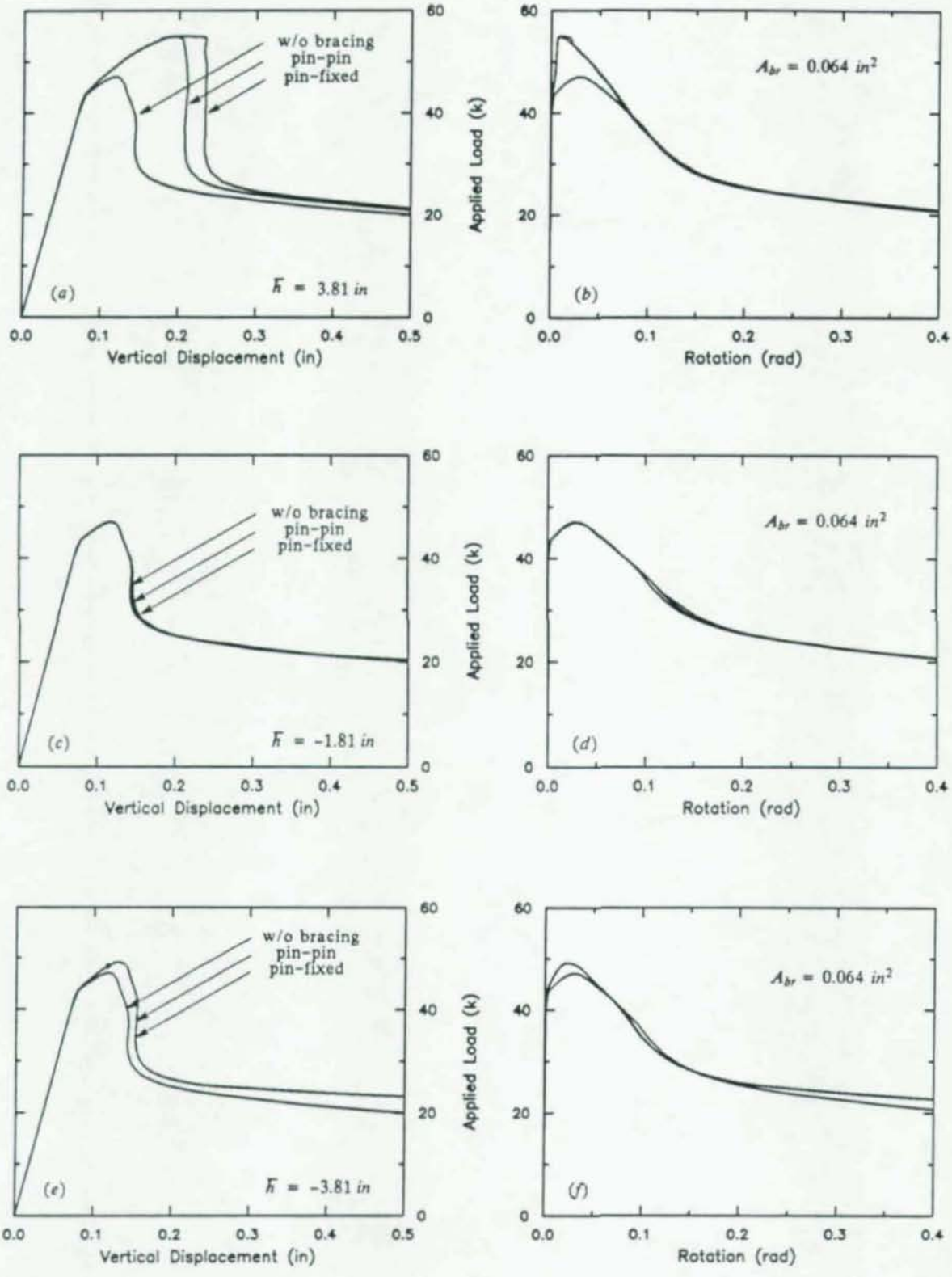

Fig. 7.10 Effect of brace end fixity conditions with brace elevation (eccentric side braced)

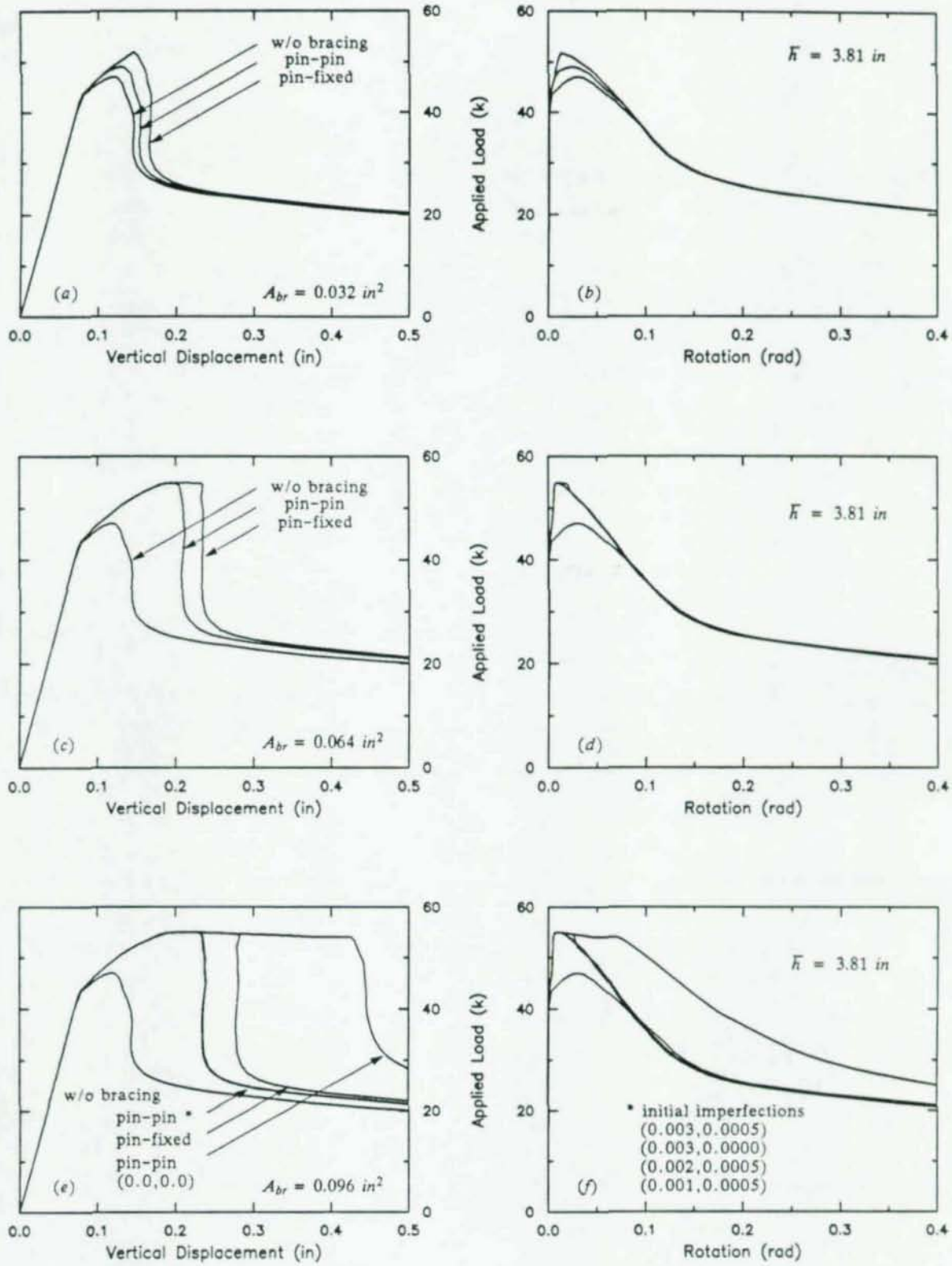

Fig. 7.11 Effect of brace end fixity conditions with brace size (eccentric side braced)

Chapter 8

Summary and Conclusions

The overall objective of this study was to develop insight into the lateral-torsional beam buckling problem. The specific emphasis of the research was on applications to short I-beams subjected to cyclically reversing loads. The study included five experiments on propped cantilever beams subjected to a cyclically reversing load applied near the fixed end. An analytical model was developed to perform extensive parameter studies to extend and help interpret the results of the experiments.

The experiments exposed several features typical of the cyclic lateral-torsional buckling of short I-beams. Those features include a sharp limit behavior with rapid loss of post-limit capacity loaded in the virgin state and an asymptotic post-buckling capacity which persists under cyclic loading. Three distinct regions of response in the pull direction were noted. It is presumed that each of these regimes relates to the progress in untwisting the inelastically buckled beam. The experiments also demonstrated the effects of lateral bracing on the cyclic lateral buckling of the test beams.

A geometrically nonlinear beam model, capable of tracking finite displacement, rotation, and cross sectional warping was developed and implemented in a general purpose finite element program. The beam kinematics include infinitesimal warping due to transverse shear and torsion superposed upon a finite torsional warping deformation. The primary warping due to torsion is the finite deformation generalization of the classical "sectorial areas" hypothesis due to Vlasov. The secondary warping due to transverse shearing of the flanges is included to properly represent shearing phenomena important to short beams. Numerical treatment of the problem was accomplished through an iterative procedure of first linearizing the equilibrium equations about an intermediate configuration and then solving the linear problem for the incremental motions. The updated configuration determined the strain state in a body, and the corresponding state of stress was found by solving the nonlinear constitutive equations. The essentially three-dimensional formulation was treated as a one-dimensional problem by numerically integrating the equations of motion over the cross-section. In this way one can completely trace local phenomena such as propagation of yielding through the cross-section. Because the governing equations are treated locally it is not necessary to track the location of the inelastic shear center or the elastoplastic interface of the beam cross section. In addition, the location of the applied loads are referred to the centroid of the cross section, simplifying the analysis of effects due to load position.

A new multiaxial cyclic plasticity model, suitable for large scale computation, was developed and implemented. The new model is a synthesis and extension of some of the most compelling concepts implicit in existing phenomenological cyclic metal plasticity models. One of the novel features of the present model is that once the isotropic hardening rule is approximated (*e.g.* from a monotonic tensile or torsion test) the kinematic hardening rule is automatically obtained as a consequence, significantly simplifying the physical testing needed to determine the model parameters. The proposed model was tested with proportional, non-proportional, uniaxial, and multi-axial load paths, for which experimental results are available in the literature. The model was found to be credible when compared with those experimental results. The plasticity model was implemented with a robust numerical scheme, using the consistent tangent concept in conjunction with a radial return mapping algorithm.

Comparison of the analytical and experimental results indicates that the analytical model is able to reproduce in a qualitative way all of the important features of cyclic lateral buckling of short beams. Consequently the analytical model was deemed reliable for carrying out the extensive parameter studies reported herein. The kinematic constraint imposed in constructing the analytical model precluded local buckling of the web and flange elements. Based on the observation that the analytical model qualitatively reproduces all aspects of the cyclic buckling response of the beams, we posit that local buckling is relatively unimportant to the overall lateral buckling response of short beams. Our one-dimensional, geometrically nonlinear beam model appears to be an eminently suitable framework for modeling the lateral buckling of I-beams.

In chapter 5 the general response of the test beams was examined through various parameter studies around a standard (control) configuration . A number of distinct features were found in these studies that should be of value in the design against lateral buckling of short beams. The following conclusions can be drawn from the general parameter studies:

(1) The yield strength of the material has a great influence on the initial lateral buckling capacity, the behavior at large deformation, and the response to cyclic loading. The characteristics of the yield plateau and strain hardening of mild steel strongly influence the post-buckling response but not the initial buckling. The details of modeling kinematic hardening were found to affect the response significantly. The current cyclic plasticity model did an adequate job of modeling the Bauschinger effect in cyclic response. Residual stresses have an influence on the limit capacity of a beam, but have no effect at large deformations nor in the response to cyclic loading. Residual stresses are less important in cyclic response because the residual twist in the beam left by buckling tends to overwhelm the influence of the residual stresses.

(2) The initial horizontal eccentricity of the load with respect to the shear center has a strong influence on the limit capacity of the beam but has little effect on the post-buckling response and the response to cyclic loading, except when the initial eccentricity is quite large. The limit load is very senstive to small load eccentricities. The height of the load with respect to the cross-section of the beam has a noticeable effect on both the limit capacity and asymptotic post-buckling capacity. Both capacities increase as the load is placed close to the shear center. Furthermore, for loads placed closer to the shear center, buckling is delayed. Pull loads (loads on the other side of the shear center) help stabilize the beam.

(3) The location of load along the length of beam also has a significant effect on the limit capacity, the post-buckling capacity, and the deformation at which buckling commences in a cyclic loading program. As the length of beam increases, the buckling capacity decreases. The proximity of the load to the fixed end is the most important influence on the lateral buckling capacity.

(4) A wide-section beam is better at resisting lateral buckling than is a deep-section beam. While a deeper beam can slightly improve the limit capacity, a wide-section delays or even prevents the lateral buckling of beam, because of the importance of warping resistance. Therefore, a wide I-beam would be more useful than a deep one in an application where lateral buckling resistance is important.

(5) The fixity of the end remote from the load has a great influence on the lateral buckling of the beam. Even the addition of torsional warping restraint to the simple support condition increased the buckling load dramatically. The fully fixed support had the highest limit load, but because of the increased stiffness, the beam tended to buckle at smaller deformations.

Unexpected results were obtained in chapter 6 from the parameter study concerning the influence of flexibility of the fixed end on the lateral buckling. The studies of the influence of flexibility of the fixed end on the lateral buckling of the beam allowed the following observation:

(6) One would expect that a beam with a perfectly fixed end would not buckle as readily as one with additional flexibility. However it was observed that some degree of end flexibility improves the lateral buckling limit capacity and delays buckling. A plausible explanation for this unexpected behavior is that bifurcation takes place from a deformed shape in which the applied load is lower than its initial position with respect to the average line of shear centers. The flexible end allows the more deflection under the load prior to lateral buckling, thereby increasing the buckling load over the fully fixed case. For large enough end flexibilities, the reduction in capacity due to the additional flexibility exceeds the increase gained from pre-buckling vertical displacement. This behavior was observed both for beams which were pre-yielded and those which were not. In practice, it might be helpful to increase the flexibility of the fixed end of a short beam to increase the limit capacity and delaying the buckling.

It is well known that lateral bracing is the best way to improve or delay lateral buckling of a beam. However, few previous investigations had been made into the inelastic lateral buckling of beams with a bracing system. Chapter 7 examined the influence of lateral bracing on the lateral buckling of beams. The following conclusions can be drawn from the parameter study on the inelastic lateral buckling with translational bracing system:

(7) The best level to place translational bracing in the cross section of beam is near the flange that is compressed by a push loading (the top flange in the experiments). Bracing placed below the shear center has little effect on lateral buckling. The center of rotation of the beams studied here was near the bottom flange, and remained fixed during lateral buckling, as evidenced by the ineffectiveness of bracing placed there.

(8) Flexural rigidity and axial strength of the bracing is important to the lateral buckling of beam. Increasing the flexural and axial stiffness has a greater effect on the lateral buckling of beam when the level of bracing is near the top flange.

(9) The 2% rule, traditionally used for the minimum brace size, does not automatically insure adequate strength of the brace, as it often does in applications involving lateral buckling of longer beams. It is clear from these studies that the brace size should, at the very least, depend on the position of the load and the position of the bracing in addition to the strength and stability properties of the the beam. Further research on the lateral bracing problem seems to be warranted.

(10) Another factor which influences the effect of bracing on the buckling of a beam is the manner in which the bracing resists lateral motion. Positioning the bracing on the opposite side of the eccentricity of the load delays buckling over the case in which the brace is positioned on the same side of the eccentricity because the brace is extended in the former case and cannot buckle. It is desirable to locate the brace at the point of the applied load or between

the applied load and the point of largest deflection. Bracing both sides of the beam may also be useful.

List of References

Anderson, J. M. and Trahair, N. S. (1972). Stability of monosymmetric beams and cantilevers. *ASCE J. Struct. Div.*, **98**(ST1). 269–286.

Antman, S. S. (1974). Kirchhoff's problem for nonlinearly elastic rods. *Quart. Appl. Math.*, **32**(3). 221–240.

Augusti, G. (1964). Experimental rotation capacity of steel beam–columns. *ASCE J. Struct. Div.*, **90**(ST6). 171–188.

Barsoum, R. S. and Gallagher, R. H. (1970). Finite element analysis of torsional and torsional–flexural stability problems. *Int. J. Numer. Meth. Engrg.*, **2**. 335–352.

Besseling, J. F. (1953). A theory of plastic flow for anisotropic hardening. Plastic deformation of initially isotropic material. *National Aeronautical Research Institute Report*, **S410**. Amsterdam.

Bleich, F. (1952). *Buckling strength of metal structures*. McGraw–Hill Book Company, Inc. New York, New York.

Bradford, M. A., Cuk, P. E., Gizejowski, M. A. and Trahair, N. S. (1984). Inelastic lateral buckling of beam–columns. *Research Report. No. R474*. School of Civil and Mining Engineering. The University of Sydney. Sydney, Australia.

Brown, P. T. and Trahair, N. S. (1968). Finite integral solution of differential equations. *Civil Engineering Transactions, Institution of Engineers, Australia*, **CE10**(2). 193–196.

Chen, W. F. and Atsuta, T. (1977). *Theory of beam columns, vol. II: space behavior and design*. McGraw–Hill Book Company, Inc. New York, New York.

Cowper, G. R. (1966). The shear coefficient in Timoshenko's beam theory. *J. Appl. Mech.*, **33**(2). 335–340.

Dafalias, Y. F. (1975). On cyclic and anisotropic plasticity. Ph.D Dissertation. Department of Civil Engineering, University of California, Berkeley.

Dafalias, Y. F. and Popov, E. P. (1975). A model for non–linearly hardening materials for complex loading. *Acta Mechanica*, **21**. 173–192.

Dafalias, Y. F. and Popov, E. P. (1976). Plastic internal variables formalism of cyclic plasticity. *J. Appl. Mech.*, **98**(4). 645–651.

Dibley, J. E. (1969). Lateral torsional buckling of I–sections in grade 55 steel. *Proceedings of the Institution of Civil Engineers*, **43**. 599–627.

Doong, S.–H. (1989). A plasticity theory of metals based on the dislocation substructures. *Report No. 148*, UILU–ENG 89–3602, Mechanical and Industrial Engineering. University of Illinois, Urbana.

Duwez, P. (1935). On the plasticity of crystalls. *Physical Review*, **457**. 494–501.

Fukumoto, Y. and Galambos, T. V. (1966). Inelastic lateral–torsional buckling of beam–columns. *ASCE J. Struct. Div.*, **92**(ST2). 41–61.

Fukumoto, Y. and Itoh, Y. (1981). Statistical study of experiments on welded beams. *ASCE J. Struct. Div.*, **107**(ST1). 89–103.

Fukumoto, Y., Itoh, Y. and Kubo, M. (1980). Strength variation of laterally unsupported beams. *ASCE J. Struct. Div.*, **106**(ST1). 165–181.

Galambos, T. V. (1963). Inelastic lateral buckling of beams. *ASCE J. Struct. Div.*, **89**(ST5). 217–241.

Galambos, T. V. (1980). Behavior of steel structures, in *Structural engineering and structural mechanics* (K. S. Pister, ed.). Prentice-Hall, Inc. Englewood Cliffs, New Jersey.

Galambos, T. V., ed. (1988). *Guide to stability design criteria for metal structures*, Fourth edition. John Wiley and Sons, Inc. New York, NY.

Gjelsvik, A. (1981). *The theory of thin-walled bars*. John Wiley and Sons, Inc. New York.

Goldstein, H. (1980). *Classical mechanics*, Second edition. Addison Wesley.

Hartmann, A. J. (1970). Experimental study of flexural-torsional buckling. *ASCE J. Struct. Div.*, **96**(ST7). 1481–1493.

Hartmann, A. J. (1971). Inelastic flexural-torsional buckling. *ASCE J. Engrg. Mech. Div.*, **97**(EM4). 1103–1119.

Hill, R. (1950). *The mathematical theory of plasticity*. Clarendon Press. Oxford.

Hinton, E. and Owen, D. R. J. (1980). *Finite elements in plasticity: theory and practice*. Pineridge Press. Swansea, Wales.

Hjelmstad, K. D. (1987). Warping effects in transverse bending of thin-walled beams. *ASCE J. Engrg. Mech.*, **113**(6). 907–924.

Hjelmstad, K. D. and Lee, S.-G. (1990). Lateral buckling of beams in eccentricity-braced frames. *Int. J. Constructional Steel Research*. To appear.

Hjelmstad, K. D. and Popov, E. P. (1983). Seismic behavior of active beam links in eccentrically braced beams. *Report No. UCB/EERC-83/15*. University of California, Berkeley.

Hodge, P. G. Jr. (1955). The theory of piecewise linear isotropic plasticity. *Proc. Coll. on Deformation and Flow of Solids*. Madrid. 147–169.

Hollinger, B. A. and Mangelsdorf, C. P. (1981). Inelastic lateral torsional buckling of beams. *ASCE J. Struct. Div.*, **107**(ST8). 1551–1567.

Horne, M. R. (1950). *Critical loading conditions in engineering structures*. Ph.D. thesis, Cambridge University. Cambridge, England.

Horne, M. R. (1954). The flexural-torsional buckling of members of symmetrical I-section under combined thrust and unequal terminal moments. *Quart. J. Mech. Appl. Math.*, 7(4). 410–426.

Hughes, T. J. R. (1987). *The finite element method: linear static and dynamic finite element analysis*. Prentice-Hall, Inc. Englewood Cliffs, New Jersey.

Hughes, T. J. R. and Pister, K. S. (1978). Consistent linearization in mechanics of solids and structures. *Computers & Structures*, **8**. 391–397.

Iwan, W. D. (1967). On a class of models for the yielding behavior of continuous and composite systems. *J. Appl. Mech.*, **34**. 612–617.

Kitipornchai, S., Dux P. F. and Richter, J. (1984). Buckling and bracing of cantilevers. *ASCE J. Struct. Engrg.*, **110**(9). 2250–2262.

Kitipornchai, S. and Trahair, N. S. (1975*a*). Buckling of inelastic I-beams under moment gradient. *ASCE J. Struct. Div.*, **101**(ST5). 991–1004.

Kitipornchai, S. and Trahair, N. S. (1975*b*). Inelastic buckling of simply supported steel I-beams. *ASCE J. Struct. Div.*, **101**(ST7). 1333–1347.

Kitipornchai, S. and Trahair, N. S. (1975*c*). Elastic behavior of tapered monosymmetric I-beams. *ASCE J. Struct. Div.*, **101**(ST8). 1661–1678.

Kitipornchai, S. and Trahair, N. S. (1980). Buckling properties of monosymmetric I-beams. *ASCE J. Struct. Div.*, **106**(ST5). 941–958.

Kitipornchai, S. and Trahair, N. S. (1986), Buckling of monosymmetric I-beams under moment gradient, *ASCE J. Engrg. Mech.*, **112**(4). 781–799.

Klöppel, K. and Unger, B. (1971). Eine experimentelle Undersuchung des Kippverhaltens von Kragträgern im elastischen und im plastischen Bereich Im Hinblick auf Neufassung des Kippsicherheitsnachweises der DIN 4114, *Der Stahlbau*, **40**(11). 321–329. **40**(12). 375–383.

Krieg, R. G. (1975). A practical two surface plasticity theory. *J. Appl. Mech.*, **42**. 641–646.

Lamba, H. S. and Sidebottom, O. M. (1978). Cyclic plasticity for nonproportional paths: Part 2 – Comparison with predictions of three incremental plasticity models. *ASME J. Engrg. Material and Technology*, **100**. 104–111.

Lay, M. G. and Galambos, T. V. (1965). Inelastic steel beams under uniform moment. *ASCE J. Struct. Div.*, **91**(ST6). 67–93.

Lay, M. G. and Galambos, T. V. (1966). Bracing requirements for inelastic steel beams. *ASCE J. Struct. Div.*, **92**(ST2). 207–228.

Lay, M. G. and Galambos, T. V. (1967). Inelastic beams under moment gradient. *ASCE J. Struct. Div.*, **93**(ST1). 381–399.

Lee, G. C. (1960). A survey of literature on the lateral instability of beams. *Welding Research Council Bulletin No.* **63**. 50–59.

Lee, G. C., Fine, D. S. and Hastreiter, W. R. (1967). Inelastic torsional buckling of H-columns. *ASCE J. Struct. Div.*, **93**(ST1). 295–307.

Love, A. E. H. (1944). *The mathematical theory of elasticity*. Fourth edition. Dover Publications, New York, New York. (Originally published in 1927 by Cambridge University Press).

Manheim, D. N. (1982). *On the design of eccentrically braced frames*. D. Engrg. thesis, University of California, Berkeley.

Marsden, J. E. and Hughes, T. J. R. (1983). *Mathematical foundations of elasticity*. Prentice-Hall, Inc. Englewood Cliffs, New Jersey.

Massey, C. and Pitman, F. S. (1966). Inelastic lateral stability under a moment gradient. *ASCE J. Engrg. Mech. Div.*, **92**(EM2). 101–111.

Moss, W. C. (1984). On the computational significance of the strain space formulation of plasticity theory. *Int. J. Numer. Meth. Engrg.*, **20**. 1703–1904.

Mroz, Z. (1967). On the description of anisotropic work-hardening, *J. Mech. Phys. Solids*, **15**, 163–175.

Mutton, B. R. and Trahair, N. S. (1973). Stiffness requirements for lateral bracing. *ASCE J. Struct. Div.*, **99**(ST10). 2167–2262.

Neal, B. G. (1954). The lateral instability of yielded mild steel beams of rectangular cross-section. *Philos. Trans. Royal Soc. London*, **242**(A.846). 197–242.

Nethercot, D. A. (1973). Buckling of laterally or torsionally restrained beams. *ASCE J. Engrg. Mech. Div.*, **99**(EM4). 773–791.

Ortiz, M. and Popov, E. P. (1982). A statistical theory of polycrystalline plasticity. *Proc. R. Soc. Lond.* A **379**. 439–458.

Petersson, H. and Popov, E. P. (1977). Constitutive relations for generalized loadings. *ASCE J. Engrg. Mech.*, **103**(4). 611–627.

Pinsky, P. M., and Taylor, R. L. (1980). A finite deformation formulation for elasto/viscoplastic beam structures, chapter 17 of *Computational methods in nonlinear mechanics*, (J. T. Oden, ed.). North Holland Publishing Co.

Pinsky, P. M., Taylor, R. L. and Pister, K. S. (1980). Finite deformation of elastic beams. *Proceedings IUTAM Symposium on Variational Methods in the Mechanics of Solids*, (S. Nemat-Nasser & K. Washizu, eds.). Pergamon Press. 115–120.

Popov, E. P. and Petersson, H. (1978). Cyclic metal plasticity: Experiments and theory. *ASCE J. Engrg. Mech. Div.*, **104**(6). 1371–1388.

Prager, W. (1956). A new method of analyzing stresses and strains in working hardening plastic solids. *J. Appl. Mech.*, **78**. 493–496.

Rajasekaran, S. (1971). Finite element analysis of thin-walled members of open sections. Ph.D. thesis, Department of Civil Engineering. University of Alberta. Edmonton.

Rees, D. W. E. (1981). A hardening model for anisotropic materials. *Experimental Mechanics*, **21**. 245–254.

Rees, D. W. E. (1982). On isotropy and anisotropy in the theory of plasticity. *Proc. Royal Society of London*, A **383**. 333–357.

Rees, D. W. E. (1983). The theory of scalar plastic deformation functions. *Z. angew. Math. Mech.*, **63**(6). 217–228.

Rees, D. W. E. (1984). A multi-surface representation of anisotropic hardening and comparison with experiment. *Proc. Inst. Mech. Engrs.*, **198C**(16) 269–284.

Rees, D. W. E. (1987). An experimental appraisal of equi-strain multi-surface hardening model. *Acta Mechanica*, **70**. 193–219.

Reissner, E. (1972). On a one-dimensional finite strain beam theory: the plane problem. *J. Appl. Math. Phys.*, **23**. 795–804.

Reissner, E. (1973). On a one-dimensional large-displacement finite-strain beam theory. *Studies in Applied Mathematics*, **52**. 87–95.

Roberts, T. M. (1981). Second order strains and instability of thin walled bars of open cross-section. *Int. J. Mech. Sci.*, **23**. 297–306.

Roberts, T. M. and Azizian, Z. A. (1983). Instability of thin walled bars. *ASCE J. Engrg. Mech.*, **109**(3). 781–794.

Roberts, T. M. and Azizian, Z. A. (1984). Instability of monosymmetric I-beams. *ASCE J. Struct. Engrg.*, **110**(6). 1415–1418.

Roeder, C. W. and Popov, E. P. (1978). Eccentrically braced steel frames for earthquakes. *ASCE J. Struct. Div.*, **104**(ST3). 391–412.

Simo, J. C. (1982). A consistent formulation of nonlinear theories of elastic beams and plates. *Report No. UCB/SESM-82/06*. University of California, Berkeley.

Simo, J. C. (1985*a*). A finite strain beam formulation: the three-dimensional dynamic problem, part I. *Comp. Meth. Appl. Mech. Engrg.*, **49**. 55–70.

Simo, J. C. (1985*b*). On the computational significance of the intermediate configuration and hyperelastic stress relations in finite deformation elastoplasticity. *Mechanics of Materials*, **4**. 439–451.

Simo, J. C., Hjelmstad, K. D. and Taylor, R. L. (1984). Numerical formulations of elasto-viscoplastic response of beams accounting for the effect of shear. *Comp. Meth. Appl. Mech. Engrg.*, **42**. 301–330.

Simo, J. C. and Ortiz, M. (1985). A unified approach to finite deformation elastoplastic analysis based on the use of hyperelastic constitutive equations. *Comp. Meth. Appl. Mech. Engrg.*, **49**. 221–245.

Simo, J. C. and Taylor, R. L. (1985*a*). Consistent tangent operators for rate independent elasto-plasticity. *Comp. Meth. Appl. Mech. Engrg.*, **48**. 101–118.

Simo, J. C. and Taylor, R. L. (1985*b*). A consistent return mapping algorithm for plane stress elastoplasticity. *Report No. UCB/SESM-85/04*. University of California, Berkeley.

Simo, J. C. and Vu-Quoc, L. (1986). A three dimensional finite-strain rod model: computational aspects, part II. *Comp. Meth. Appl. Mech. Engrg.*, **58**. 79–116.

Simo, J. C. and Vu-Quoc, L. (1989). A geometrically exact rod model incorporating shear and torsion-warping deformations. *Comp. Meth. Appl. Mech. Engrg.*, in press.

Sokolnikoff, I. S. (1956). *Mathematical theory of elasticity*. Second edition. McGraw-Hill Book Company, New York.

Strang, G. and Fix, G. J. (1973). *An analysis of the finite element method*. Prentice-Hall Inc. Englewood Cliffs, New Jersey.

Taylor, A. C. Jr., and Ojalvo, M. (1966). Torsional restraint of lateral buckling. *ASCE J. Struct. Div.*, **92**(ST2). 115–129.

Taylor, R. L. (1977). Computer procedures for finite element analysis, chapter 24 of *The finite element method*, 3rd Edition, by O.C. Zienkiewicz. McGraw-Hill Book Company (UK) Limited. London.

Timoshenko, S. P. and Gere, J. M. (1961). *Theory of elastic stability*. McGraw-Hill Book Company, Inc. New York, NY.

Trahair, N. S. (1969). Deformations of geometrically imperfect beams. *ASCE J. Struct. Div.*, **95**(ST7). 1475–1496.

Trahair, N. S. and Woolcock, S. T. (1973). Effect of major axis curvature on I-beam stability. *ASCE J. Engrg. Mech. Div.*, **99**(EM1). 85–98.

Vacharajittiphan, P., Woolcock, S. T. and Trahair, N. S. (1974). Effect of in-plane deformation on lateral buckling. *J. Struct. Mech.*, **3**(1). 29–60.

Vinnakota, S. (1977). Inelastic stability of laterally unsupported I-beams. *Computers & Structures*, **7**. 377–389.

Vlasov, V. Z. (1961). *Thin-walled elastic beams*. Israel program for scientific translations, ltd. Jerusalem.

Wang, C. M. and Kitipornchai, S. (1986). Buckling capacities of monosymmetric I-beams. *ASCE J. Struct. Engrg.*, **112**(11). 2373–2391.

Wilkins, M. L. (1964). Calculation of elastic-plastic flow, in *Methods of Computational Physics 3* (Alder *et al.*, eds.). Academic Press, New York, NY.

Winter, G. (1960). Lateral bracing of columns and beams. *Trans. ASCE*, **125**. 807–845.

Woolcock, S. T. and Trahair, N. S. (1974). The post-buckling behavior of determinate beams. *ASCE J. Engrg. Mech. Div.*, **100**(EM3). 151–157.

Yura, J. A., Galambos, T. V. and Ravindra, M. K. (1978). The bending resistance of steel beams. *ASCE J. Struct. Div.*, **104**(ST9). 1355–1370.

Zayas, V. A., Popov, E. P., and Mahin, S. A. (1980). Cyclic inelastic buckling of tubular steel braces. *Report No. UBC/EERC-80/16*. University of California, Berkeley.

Ziegler, H. (1959). A modification of Prager's hardening rule. *Quart. Appl. Math.*, **17**. 55–65.

Zienkiewicz, O. C. (1977). *The finite element method*. 3rd Edition. McGraw-Hill Book Company (UK) Limited. London.

Zuk, W. (1956). Lateral bracing forces on beams and columns. *ASCE J. Engrg. Mech. Div.*, **82**(EM3). 1032.1–1032.16.

Appendix A

Load Cell

A load cell capable of measuring the six stress resultant quantities was designed for the purposes of the tests reported herein. The load cell, which resided between the specimen end and the reaction block, was a circular tube 12 *in* long, with 9.6 *in* outside diameter and 0.445 *in* wall thickness. The tube was edge prepared and welded to 2 *in* thick end plates. These end plates were welded to a second set of 2 *in* thick plates which were used for bolting the load cell in place. The 4 *in* end plate thickness was necessary to insure a consistent stress transfer mechanism into the load cell which thereby insured a reliable measurement of load. The circular cross section was chosen because, within a thin-wall approximation, the circular shape does not experience cross sectional warping due to transverse shearing or twisting. The load cell was gaged with 90 degree strain gage rosettes (0.125 *in* gage length) placed at the quarter point stations along the length of the cell. At each station four rosettes were placed at 90 degree intervals around the circumference. The load cell configuration is shown in Fig. A.1. The response of each gage was measured independently during the load cell calibrations and the tests and the data were combined in the data reduction phase.

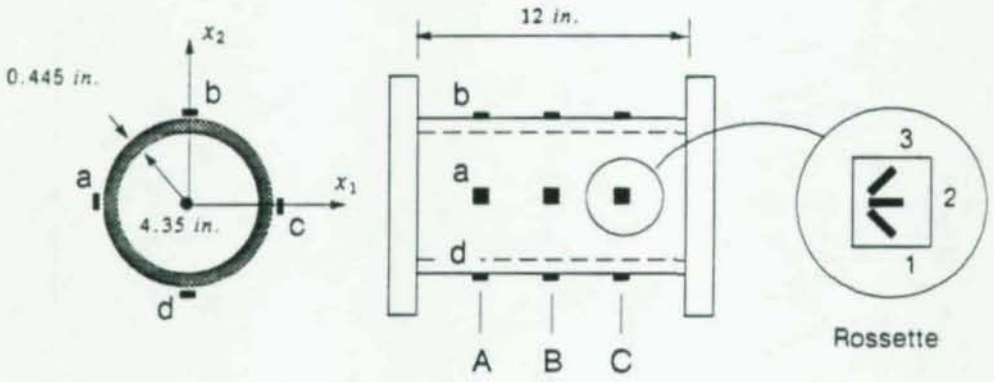

Fig. A.1 Load Cell Geometry

Two analytical models of the load cell were used in the calibration phase. First, the load cell was treated using the exact linear elastic solution to St. Venant's problem, *i.e.* a beam subjected to end loading (Sokolnikoff, 1956). Using this solution, one can write a relationship between the strains at a cross-section and the stress resultants acting there as follows:

$$\epsilon = \mathbf{B}\mathbf{R} \tag{A.1}$$

where $\epsilon = (\epsilon_1, \ldots, \epsilon_{12})$ is a vector of the 12 strain measurements at longitudinal station or cross section (Fig. A.1), $\mathbf{R} = (T,\ M_1,\ M_2,\ N,\ V_1,\ V_2)$ is the vector of six stress resultants, and $\mathbf{B}$ is the coefficient matrix given by the theory of elasticity. The strain gages are numbered clockwise around the circumference at a station starting with a-1 and ending with d-3. The nomenclature used for the stress resultants

is: T is the torque, M_1 is the flexural moment about the x_1 axis (horizontal), M_2 is the flexural moment about the x_2 axis (vertical), N is the axial force, V_1 is the shear along the x_1 axis, and V_2 is the shear along the x_2 axis.

Equation (A.1) is clearly overdetermined. The stress resultants can be determined from the strain measurements by a least square projection as

$$\mathbf{R} = [\mathbf{B}^t \mathbf{B}]^{-1} \mathbf{B}^t \epsilon \tag{A.2}$$

Interestingly, the coefficient matrix $\mathbf{B}^t \mathbf{B}$ is diagonal, making it possible to write an explicit formula for the stress resultants:

$$T = \frac{GJ}{2b}[-\epsilon_1 + \epsilon_3 - \epsilon_4 + \epsilon_6 - \epsilon_7 + \epsilon_9 - \epsilon_{10} + \epsilon_{12}] \tag{A.3}$$

$$M_1 = \frac{EJ}{4b(1+\nu^2)}[(1+\nu)(\epsilon_5 - \epsilon_{11}) - \nu(\epsilon_4 + \epsilon_6 - \epsilon_{10} - \epsilon_{12})] \tag{A.4}$$

$$M_2 = \frac{EJ}{4b(1+\nu^2)}[(1+\nu)(\epsilon_8 - \epsilon_2) - \nu(\epsilon_7 + \epsilon_9 - \epsilon_1 - \epsilon_3)] \tag{A.5}$$

$$N = \frac{EA}{4(1+\nu^2)}[(1+\nu)(\epsilon_2 + \epsilon_5 + \epsilon_8 + \epsilon_{11}) - \nu(\epsilon_1 + \epsilon_3 + \epsilon_4 + \epsilon_6 + \epsilon_7 + \epsilon_9 + \epsilon_{10} + \epsilon_{12})] \tag{A.6}$$

$$V_1 = \frac{GJ}{a}(\epsilon_4 - \epsilon_6 - \epsilon_{10} + \epsilon_{12}) \tag{A.7}$$

$$V_2 = \frac{GJ}{a}(-\epsilon_1 + \epsilon_3 + \epsilon_7 - \epsilon_9) \tag{A.8}$$

where E, G, and ν are Young's modulus, the shear modulus, Poisson's ratio respectively; b is the outside radius of the cylinder, A is the cross sectional area, J is the polar moment of inertia, and a is defined through the relationship

$$a = \frac{(3+2\nu)a^2 + (1+2\nu)b^2}{2(1+\nu)} \tag{A.9}$$

where a is the inside radius of the cylinder.

Equations (A.3)-(A.8) are inaccurate because end effects induced by welding the tube to the end plates, which precludes changes in the tube diameter, are important to the recorded strains. The St. Venant solution systematically ignores these end effects.

To estimate the end effects the load cell was modeled using shell finite elements to determine new coefficients, $\dot{\mathbf{B}}$, which account for the end restraint. While the coefficients have different numerical values, the form of $\dot{\mathbf{B}}$, (repeated values, zeros, etc.), is nearly identical to the elasticity solution of the St. Venant problem, $\mathbf{B}$. Hence, the St. Venant solution and the finite element solution concur on how to combine the information supplied by the gages, but not on the values of the gage factors. This observation simplifies the determination of scale factors by calibration in the sense that very few tests are required.

The number of tests can be further reduced through the symmetry properties of the load cell. Similar to the elasticity solution, the form used for calibration of the stress resultants at a cross section take the form:

$$T = a[-\epsilon_1 + \epsilon_3 - \epsilon_4 + \epsilon_6 - \epsilon_7 + \epsilon_9 - \epsilon_{10} + \epsilon_{12}] \tag{A.10}$$

$$M_1 = d(\epsilon_5 - \epsilon_{11}) + c(\epsilon_4 + \epsilon_6 - \epsilon_{10} - \epsilon_{12}) + b(-\epsilon_1 + \epsilon_3 + \epsilon_7 - \epsilon_9) \tag{A.11}$$

$$M_2 = d(\epsilon_8 - \epsilon_2) + c(\epsilon_7 + \epsilon_9 - \epsilon_1 - \epsilon_3) + b(-\epsilon_4 + \epsilon_6 + \epsilon_{10} - \epsilon_{12}) \tag{A.12}$$

$$N = e(\epsilon_2 + \epsilon_5 + \epsilon_8 + \epsilon_{11}) + f(\epsilon_1 + \epsilon_3 + \epsilon_4 + \epsilon_6 + \epsilon_7 + \epsilon_9 + \epsilon_{10} + \epsilon_{12}) \tag{A.13}$$

$$V_1 = g(\epsilon_4 - \epsilon_6 - \epsilon_{10} + \epsilon_{12}) \tag{A.14}$$

$$V_2 = g(-\epsilon_1 + \epsilon_3 + \epsilon_7 - \epsilon_9) \tag{A.15}$$

where a, b, c, d, e, f, and g are the calibration constants. The finite element solution gives some additional relationships among the constants. In particular it was found that $40b=d$, $3c=d$, and $3e=f$, leaving four independent constants to be determined by calibration. The constants were found from two calibration tests, the first a torque-free cantilever bending test about the horizontal axis (Fig. A.2, load position A) and the second a torsion and bending cantilever test about the horizontal axis (Fig. A.2, load position B). Ideally, two additional tests might have been performed. However, the axial forces in the test pieces were expected to be negligible and hence an axial calibration was not deemed necessary. Symmetry was used instead of a bending test about the vertical axis. The coefficients obtained from the horizontal axis test were used for bending and shear in the horizontal plane. The cantilever bending test is sufficient to calibrate both moment and shear in a single plane.

The calibration tests constants were determined by a least square error fit of the calibration data. The least square error procedure assumed that both the ordinate and the abscissa were subject to error. The unbiased value of the slope of the line under these conditions is given by

$$m = \frac{n(\mathbf{y}'\mathbf{y}) - (\mathbf{1}'\mathbf{y})^2}{n(\mathbf{x}'\mathbf{x}) - (\mathbf{1}'\mathbf{x})^2} \tag{A.16}$$

where $\mathbf{x}$ and $\mathbf{y}$ are the vectors of abscissa and ordinate data respectively, $\mathbf{1}$ is a vector of ones, and n is the number of measurements in the sample. In determining the calibration constants the contributions of stations A, B, and C were averaged before fitting the least square line. The excellent correlation present in the calibration data is evident in Fig. (A.3), which plots the expected and measured values of the stress resultants in the two calibration tests. There appears to be greater scatter for the torsion calibration in the bending tests, however the values of the torque were small for load position A, due only to imperfection in load placement. Similarly, there appears to be greater scatter in the moment and shear values for the

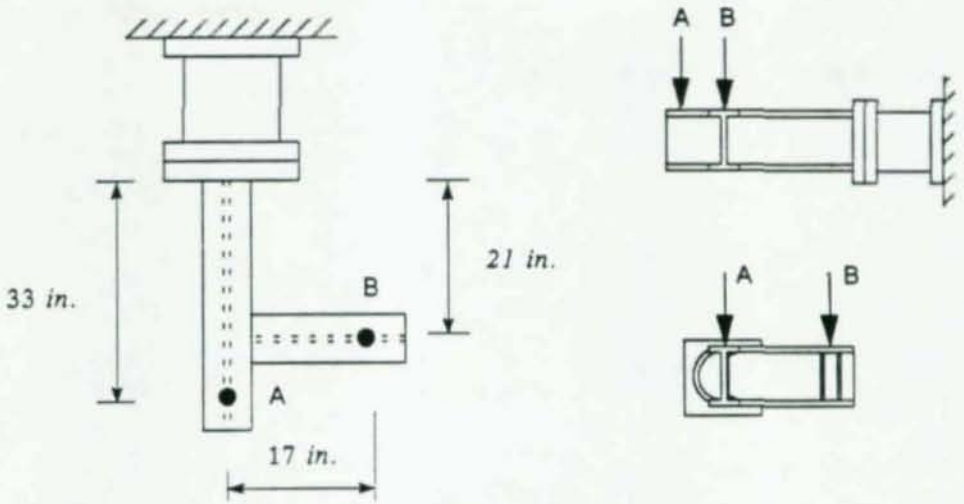

Fig. A.2 Load Points for Calibration Tests

torsion test, but the load levels were much smaller for this test than they were for the bending test. The values obtained are given in Table A.1 below.

Table A.1 Calibration Constants

a	152065 *in-k*
b	9388 *in-k*
c	125167 *in-k*
d	375500 *in-k*
e	*not calibrated*
f	*not calibrated*
g	33945 *k*

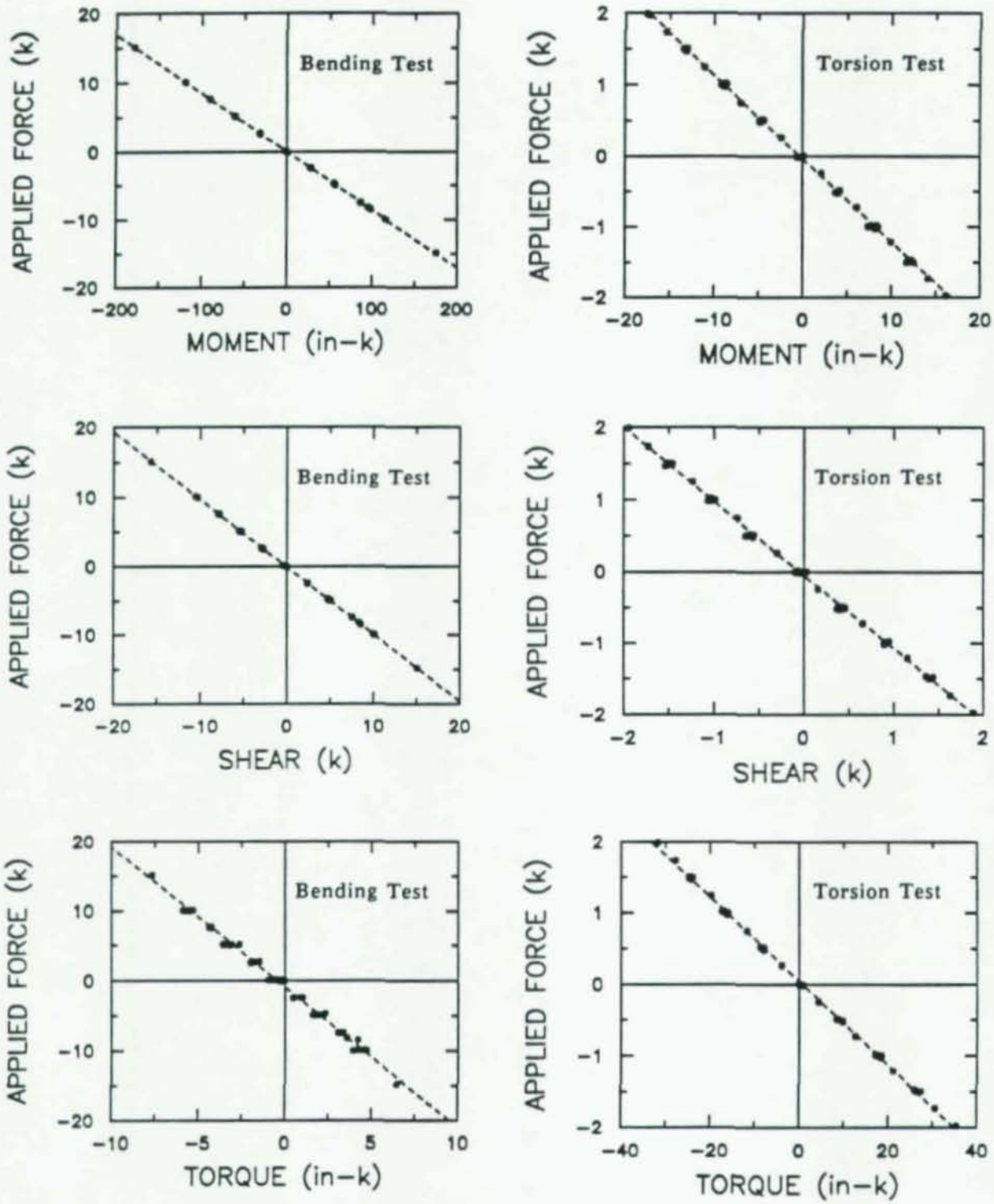

Fig. A.3 Calibration for Bending and Torsion Tests